Thèse n° 8158

Thermal transport beyond Fourier, and beyond Boltzmann

Présentée le 26 mai 2021

Faculté des sciences et techniques de l'ingénieur
Laboratoire de théorie et simulation des matériaux
Programme doctoral en science et génie des matériaux

pour l'obtention du grade de Docteur ès Sciences

par

Michele SIMONCELLI

Acceptée sur proposition du jury

Prof. D. Damjanovic, président du jury
Prof. N. Marzari, directeur de thèse
Prof. Ph. B. Allen, rapporteur
Prof. D. G. Cahill, rapporteur
Prof. M. Ceriotti, rapporteur

École
polytechnique
fédérale
de Lausanne

2021

A source of delight is uncovering down-to-earth or dramatic and sometimes beautiful examples of abstract mathematical ideas: the arcane in the mundane.

— Prof. Sir Michael Victor Berry

Dedicated to my family

Acknowledgements

The results presented in this thesis have been possible also thanks to the support of other people, to whom this section is dedicated.

I would like to express my sincere and deep gratitude to my advisor Prof. Nicola Marzari. Having him as a mentor has been a privilege far beyond what one might expect from his well known scientific achievements. The first thanks are for all the notions he has taught me in physics, materials science, and also management. Most importantly, I will be forever grateful to him for having shown me a critical approach towards science, and for having taught me the importance of envisioning and contextualizing research projects in the grand scheme of things. His dream-big attitude has been truly inspirational and will probably have long-lasting effects on my life. Finally, I thank him for having granted me trust and freedom, for the positive atmosphere that he has always promoted, for his encouragement and support, and for the honest, disinterested advices he has given me for career and life.

I would like to thank profoundly and sincerely Prof. Francesco Mauri, for having hosted me at University of Rome “La Sapienza” in January 2018, and for the many extremely instructive, enlightening, and direct discussions I had with him since then. His way of tackling challenging problems with enthusiasm, elegance, and pragmatism has been truly inspirational and will serve as a model to follow in the future. I also thank him for the support and for the genuine, disinterested advices he gave me during this PhD — all this has been incredibly helpful for my scientific work and much more.

A special thank goes to Dr. Andrea Cepellotti, for all the work done in collaboration and that has been as instructive as enjoyable. I also thank him for the suggestions he gave me about academic life.

I thank Prof. Gábor Csányi for his hospitality at University of Cambridge in February 2020. Also, I thank him for the guidance and support he provided for the next step in my professional life, and I look forward to the work to come.

I express my gratitude to Dr. Davide Campi for the useful discussions we had at the early stage of this work, which helped me to start working in the field of computational science. I thank Dr. Lorenzo Paulatto for having hosted me at the Institut de minéralogie, de physique des matériaux et de cosmochimie (Paris) in September 2017, and for his teachings in computational science. I thank (in chronological order) Norma Rivano, Enrico Di Lucente, and Giovanni Caldarelli for the useful discussions that emerged during their master theses, and for the projects that started from these and are currently ongoing.

I thank all the current and past members of the group of theory and simulation of materials at EPFL for the many interesting discussions and social activities that made my time in the research group enjoyable.

Finally, I thank all the friends who challenged me in trainings, races, or in profound philosophical discussions: their be-your-best-self attitude and growing mindset has motivated and inspired me, also for this work. I likewise thank all the friends who did not challenge me at all or with a completely different mindset, for having shown me other very important aspects of life, of work, and of their combination.

Lausanne, March 25, 2021 Michele Simoncelli

Abstract

This thesis explores the physics underlying thermal transport in solids, elucidating how current formulations can be extended to enlarge their domain of applicability.

The first part focuses on the microscopic description of heat conduction, and relies on the Wigner phase-space formulation of quantum mechanics to derive a unified theory of thermal transport, which can describe on the same footing crystals, glasses, and anything in between. Specifically, it is shown that there exists a general microscopic (quantum) equation for thermal transport that encompasses the emergence and coexistence of vibrational excitations in crystal and glasses. This formulation reduces to the Peierls' phonon Boltzmann transport equation in the limit of a "simple" crystal (*i.e.* one with phonon interband spacings large compared to the phonon linewidths), or to the Allen-Feldman formulation in the case of a harmonic glass. It is shown how the two established heat conduction mechanisms — namely the propagation of vibrational waves in anharmonic crystals elucidated by Peierls [Ann. Phys. 395, 1055–1101 (1929)] and the coupling of vibrational modes in harmonic glasses envisioned by Allen and Feldman [Phys. Rev. Lett. 62, 645–648 (1989)] — naturally emerge as limiting cases of this Wigner formulation. The generality of the approach makes it predictive also in the intermediate regimes — that are not described by either the Peierls or the Allen-Feldman limits — where both anharmonicity and disorder are relevant. Applications are discussed, demonstrating the capability to predict correctly the opposite trends of thermal conductivity in crystals and glasses. In particular, it is shown that this Wigner formulation solves the long-standing problem of understanding and predicting the ultralow, glass-like thermal conductivity of materials for thermal barriers or thermoelectric devices. Furthermore, we study the thermal properties of silica polymorphs such as crystalline α-quartz, vitreous silica, and the complex crystal meteoritic low tridymite, using these materials as paradigmatic test cases to investigate how the interplay between the quantum Bose-Einstein statistics of atomic vibrations, disorder, and anharmonicity affects thermal transport. We show the emergence of a phonon liquid signature in vitreous silica, with atomic vibrations having mean free paths that are mainly determined by the disorder length scale; we also predict the temperature-conductivity curve of meteoritic low tridymite to display an exotic, almost temperature-independent trend, which is intermediate between the decreasing trend of the crystalline polymorph α-quartz and the increasing trend of the glassy polymorph vitreous silica.

The second part of this thesis discusses heat hydrodynamics, *i.e.* the regime in which Fourier's diffusive heat equation fails and heat propagation becomes fluid-like. The hydrodynamic regime of thermal transport appears in crystals characterized by weak anharmonicity and simple primitive cells, conditions under which the Wigner formulation introduced here reduces to the Peierls-Boltzmann one. Therefore, the recently introduced relaxon kinetic theory for thermal transport [A. Cepellotti and N. Marzari, Phys. Rev. X 6, 041013 (2016)] can be employed to solve exactly the Peierls-Boltzmann equation, and to provide a closed-form solution as a sum over relaxons (*i.e.*, collective phonon excitations that are the eigenvectors of the collision operator appearing in the Peierls-Boltzmann equation). Relaxons have a well-defined parity, and only odd relaxons contribute to the thermal conductivity. It is shown that the complementary set of even relaxons determines another quantity — the thermal viscosity — that enters into the description of heat conduction, and is especially relevant for this hydrodynamic regime, where dissipation of crystal momentum by Umklapp scattering phases out. Such microscopic insight is used to coarse grain the integro-differential microscopic Peierls-Boltzmann equation into two mesoscopic “viscous heat equations”, which are partial differential equations for the temperature and drift-velocity fields that describe both the limit of Fourier’s diffusion and that of heat hydrodynamics, taking place, respectively, in the regime of strong or weak crystal momentum dissipation. Finally, a descriptor (the "Fourier deviation number") is introduced to capture the deviations from Fourier’s law due to hydrodynamic effects. These findings are showcased in a test case of a complex-shaped device made of graphite, obtaining remarkable agreement with the recent experimental demonstration of hydrodynamic transport in this material. It is also suggested that hydrodynamic behavior can appear in micrometer-sized devices made of layered hexagonal boron nitride around 75 K. Such mesoscopic formulation rigorously generalizes Fourier’s heat equation, extending the reach of physical and computational models for heat conduction also to the hydrodynamic regime.

Keywords: quantum heat transport, Wigner phase-space formalism, thermal conductivity, thermal viscosity, heat hydrodynamics

Riassunto

Questa tesi esplora la fisica alla base del trasporto termico nei solidi, estendendo il dominio di applicabilità delle teorie attuali.

La prima parte si concentra sulla descrizione microscopica della conduzione del calore. Utilizzando la formulazione di Wigner della meccanica quantistica nello spazio delle fasi, viene derivata una teoria unificata della conduzione del calore, che descrivere in modo accurato materiali con ordine strutturale perfetto (cristalli), materiali con struttura disordinata o amorfa (vetri), e i casi intermedi rappresentati da materiali parzialmente disordinati. In particolare, viene dimostrata l'esistenza di un'equazione microscopica (quantistica) per la conduzione del calore, dalla quale emerge la coesistenza delle diverse eccitazioni vibrazionali tipiche dei cristalli e dei vetri. Questa formulazione si riduce all'equazione di trasporto di Peierls-Boltzmann per i fononi nel limite di un cristallo "semplice" (cioè un cristallo in cui le bande fononiche sono ben separate, *i.e.* la distanza tra le bande è molto maggiore delle larghezze di riga dei fononi), o alla formulazione di Allen-Feldman nel caso di un vetro armonico. Viene mostrato come i due meccanismi noti di conduzione del calore — vale a dire la propagazione delle onde vibrazionali nei cristalli anarmonici discussa da Peierls [Ann. Phys. 395, 1055-1101 (1929)], e l'accoppiamento dei modi vibrazionali nei vetri armonici scoperto da Allen e Feldman [Phys. Rev. Lett. 62, 645-648 (1989)] — emergono in modo naturale come casi limite di questa formulazione di Wigner. La generalità dell'approccio lo rende predittivo anche nei regimi intermedi — che non sono descritti né dal caso limite di Peierls né da quello di Allen-Feldman — dove sia l'anarmonicità che il disordine sono rilevanti. Si discutono applicazioni di questa teoria unificata a vari materiali, dimostrando la capacità di questa nuova teoria di predire correttamente gli andamenti opposti della conducibilità termica nei cristalli e nei vetri. In particolare, si dimostra che questa formulazione di Wigner risolve il problema di capire e predire gli andamenti della conducibilità termica ultrabassa, simile a quella dei vetri, dei materiali per barriere termiche o dispositivi termoelettrici. Inoltre, vengono studiati polimorfi della silica quali quarzo α, silica amorfa, e tridimite meteoritica come casi paradigmatici per capire come l'effetto combinato della statistica quantistica di Bose-Einstein delle vibrazioni atomiche, del disordine e dell'anarmonicità influenza il trasporto termico. In particolare, viene mostrata l'emergenza del comportamento da "liquido fononico" nella silica amorfa, con vibrazioni atomiche che hanno cammini liberi medi determinati principalmente dalla scala di lunghezza del disordine; viene inoltre predetto che la curva temperatura-conducibilità della tridimite meteoritica mostra un andamento esotico, quasi indipendente dalla temperatura, che è intermedio tra l'andamento decrescente del polimorfo cristallino quarzo α e

l’andamento crescente della silica amorfa.
La seconda parte di questa tesi discute l’idrodinamica del calore, cioè il regime in cui l’equazione del calore di Fourier (che descrive la conduzione come un fenomeno diffusivo) fallisce e la propagazione del calore diventa idrodinamica. Il regime idrodinamico del trasporto termico appare in cristalli caratterizzati da debole anarmonicità e celle primitive semplici, condizioni sotto le quali la formulazione di Wigner qui introdotta si riduce a quella di Peierls-Boltzmann. Queste condizioni permettono di utilizzare la descrizione del trasporto termico basata sulla teoria cinetica dei rilassoni (recentemente introdotta in Ref. [A. Cepellotti e N. Marzari, Phys. Rev. X 6, 041013 (2016)]), che permette di risolvere esattamente l’equazione di Peierls-Boltzmann e di scriverne la soluzione in forma chiusa come somma su rilassoni (cioè, eccitazioni foniche collettive, definite come autovettori dell’operatore di collisione che appare nell’equazione di Peierls-Boltzmann). I rilassoni hanno una parità ben definita, ed è stato mostrato nell’articolo [A. Cepellotti e N. Marzari, Phys. Rev. X 6, 041013 (2016)] che solo i rilassoni dispari contribuiscono alla conducibilità termica. Si dimostra che l’insieme complementare dei rilassoni pari determina un’altra quantità — la viscosità termica — che entra nella descrizione della conduzione del calore, ed è particolarmente rilevante nel regime idrodinamico, dove la dissipazione del momento cristallino attraverso lo scattering Umklapp diventa debole o trascurabile. Tale intuizione microscopica, basata sulla parità dei rilassoni, viene utilizzata per semplificare, tramite una procedura di coarse-graining, l’equazione microscopica integro-differenziale di Peierls-Boltzmann in due "equazioni del calore viscoso" mesoscopiche. Le equazioni del calore viscoso qui introdotte sono equazioni differenziali alle derivate parziali per i campi di temperatura e di velocità di deriva dei fononi, descrivono sia il limite della diffusione di Fourier che quello dell’idrodinamica del calore (che appaiono rispettivamente nel regime di forte o debole dissipazione del momento cristallino). Infine, viene introdotto un parametro (chiamato "Fourier Deviation Number") per predire le deviazioni dalla legge di Fourier dovute agli effetti idrodinamici. Questa teoria mesoscopica viene applicata a vari materiali, in particolare viene mostrata la capacità di questa teoria di predire in modo accurato l’emergenza del regime idrodinamico del trasporto termico in dispositivi fatti di grafite, ottenendo un notevole accordo con le recenti misure sperimentali di trasporto termico idrodinamico in questo materiale. Viene anche suggerito che il comportamento idrodinamico del calore può apparire in dispositivi fatti di nitruro di boro esagonale layered, e a temperature attorno a 75 K. Questa formulazione mesoscopica generalizza rigorosamente l’equazione del calore di Fourier, permettendo di descrivere non solo la conduzione del calore come fenomeno diffusivo ma anche l’emergenza di effetti idrodinamici.

Contents

Acknowledgements i

Abstract (English/Italian) iii

Introduction 1

I Thermal transport beyond Boltzmann 9

1 Quantum thermal transport in solids from Wigner's phase-space formalism 13

- 1.1 Abstract . . . 15
- 1.2 Introduction . . . 15
- 1.3 Quantum description of atomic vibrations . . . 17
  - 1.3.1 Second quantization for atomic vibrations . . . 17
  - 1.3.2 Evolution equation for the density matrix . . . 21
- 1.4 Phase-space formalism . . . 23
  - 1.4.1 Wigner transform . . . 24
  - 1.4.2 Wigner-Boltzmann transport equation . . . 25
- 1.5 Thermal conductivity . . . 29
  - 1.5.1 Vibrational energy field and flux . . . 29
  - 1.5.2 Steady-state solution of the WBTE . . . 31
- 1.6 Phase convention and size consistency . . . 34
- 1.7 Applications to materials science . . . 37
  - 1.7.1 Lanthanum zirconate . . . 37
  - 1.7.2 Halide perovskite $CsPbBr_3$ . . . 41
- 1.8 Conclusions . . . 42

Appendices 45

- 1.A Localization of the bosonic operators in direct space . . . 45
  - 1.A.1 Localization problems of the phonon-mode basis . . . 48
- 1.B Lindblad master equation . . . 49
  - 1.B.1 Evolution of the many-body density matrix . . . 49
  - 1.B.2 Evolution of the one-body density matrix . . . 53
- 1.C Collision superoperator for vibrations . . . 54
  - 1.C.1 Phonon collisions at the many-body level . . . 54

1.C.2 Linearized collision superoperator for the one-body density matrix . . . 56
1.C.3 Wigner transform of the collision superoperator 60
1.D Mathematical properties of the Wigner matrix 61
1.E Microscopic energy field & flux 67
1.F Details on the velocity operator 72
1.F.1 Velocity operators in terms of eigenvectors and eigenvalues of the dynamical matrix 73
1.G Effects of the phase convention on the thermal conductivity 74
1.H The limiting case of harmonic glasses 75
1.I Computational details 77
1.I.1 $La_2Zr_2O_7$ 77
1.I.2 $CsPbBr_3$ 78

2 Heat conduction in glasses and its application to vitreous silica 81
2.1 Abstract 83
2.2 Introduction 83
2.3 Wigner-Boltzmann formulation for thermal transport 84
2.4 Glasses in periodic boundary conditions 86
2.5 Thermal conductivity of vitreous silica 88
2.5.1 Anharmonic Thermal diffusivity 91
2.6 The phonon liquid picture 94
2.7 Conclusions 96

Appendices 99
2.A Accuracy of the SMA approximation in glasses 99
2.B Finite-size broadening of the Dirac delta and bulk limit within the Allen-Feldman framework 99
2.C Bulk limit within the WBTE formulation 102
2.C.1 WBTE regularization protocol 103
2.D Quantum harmonic specific heat 105
2.E Velocity operator as a function of frequency 106
2.F Mean free path calculations 107
2.G First-principles calculations 109

3 Transition from simple to complex crystal in silica polymorphs 115
3.1 Introduction 115
3.2 Effects of disorder on the vibrational properties 116
3.3 Thermal conductivity of meteoritic low tridymite 118
3.4 Conclusions 120

Appendices 121
3.A Computational details 121
3.A.1 First-principles calculations of force constants 121

3.A.2 Computation of the phonon linewidths 122
3.A.3 Computation of the thermal conductivity 122

II Thermal transport beyond Fourier **127**

4 Generalization of Fourier's Law into Viscous Heat Equations **131**
4.1 Abstract 133
4.2 Introduction 133
4.3 Thermal viscosity 136
4.4 Viscous heat equations 143
4.5 Second sound 146
4.6 Case study 148
4.7 Fourier Deviation Number 150
4.8 Conclusions 156

Appendices **159**
4.A Eigenvectors of the scattering matrix 159
4.A.1 Bose-Einstein eigenvector: local temperature 160
4.A.2 Drift eigenvectors: local drift velocity 161
4.A.3 Local equilibrium 162
4.B Thermal viscosity 162
4.B.1 Single-mode relaxation-time approximation 165
4.C Size effects on the thermal conductivity and viscosity 166
4.D Viscous heat equations 167
4.D.1 The projection of the LBTE on the 1st (Bose-Einstein) eigenvector: energy moment 168
4.D.2 The projection of the LBTE on the 2nd/3rd/4th eigenvectors: the momentum eigenspace 171
4.E Parameters entering the viscous heat equations. 174
4.F Second sound 177
4.F.1 Second sound from the viscous heat equations (bottom-up approach) . 177
4.F.2 Second sound from the viscous heat equations (top-down approach) . . 179
4.G Analytical 1D example 181
4.H Estimate of the characteristic drift velocity 182
4.I Hydrodynamic behavior in macroscopic diamond samples 185
4.J Computational details 185

5 Hydrodynamic heat transport in hBN **187**
5.1 Introduction 187
5.2 Transport coefficients of hBN 188
5.2.1 Thermal conductivity 188
5.2.2 Thermal viscosity 189
5.3 Heat hydrodynamics in hBN 191

5.3.1 Solution of the viscous heat equations in hBN 192
5.3.2 Hydrodynamic deviations from Fourier's law 195
5.4 Conclusions 195

Appendices **197**
5.A Computational details 197
5.B Parameters entering in the viscous heat equations for hBN 198

III Conclusions **201**

Conclusions **203**

Bibliography **207**

Curriculum Vitae **231**

Introduction

The phenomenon of heat flowing through a solid is of critical importance to many and diverse technological applications, including e.g. miniaturization and efficiency of electronic devices, waste-heat harvesting, design of thermal shields and thermal barrier coatings, and even in therapy against cancer. All these different applications aim to engineer heat flow via the chemical composition, the structure (crystalline or amorphous), or the shape of the material through which heat flows. As a result, the variety of conditions and materials in which this phenomenon is exploited is very wide. For example, current research efforts in electronics are aiming at finding materials with very high thermal conductivity, since building electronic devices using materials with conductivity higher than silicon would facilitate the removal of heat generated by Joule effect, and consequently allow to increase their efficiency and miniaturization [1, 2, 3]. Conversely, in the field of thermoelectric energy harvesting, increasing the efficiency of the conversion of waste heat into electricity requires finding electrically conductive materials with a thermal conductivity as low as possible [4]. Materials with ultralow thermal conductivity are relevant to the aerospace industry, since heat-insulating materials are employed to protect turbine blades from thermal stresses or to shield spaceships from extreme temperatures. Degradation of heat-insulating materials can lead to turbine's blade fatigue crack and consequent engine failure [5]; in 2018 an accident of this type caused an uncontained engine failure of a Boeing 737-700 with fatal consequences [6]. Finally, in medicine heat is employed in photothermal therapy [7, 8] against cancer, consisting in injecting nanoparticles into a tumor and then heating these with electromagnetic radiation up to a temperature that can destroy the cancer cells.

Heat transport can display very different behavior depending on the material in which it takes place and engineering such a phenomenon in everyday applications requires equations that allow e.g. to predict how the shape of a device affects its capability to exchange heat and thus its local temperature (which is a macroscopic, easily measurable quantity). This is particularly relevant in electronics, where integrated circuits have to be designed in ways that prevent the formation of hot spots, *i.e.* regions where the temperature reaches values that cause damage or melting of the device. On the other hand, innovating on current technologies that rely on heat transfer, or envisioning new applications, requires understanding heat transport from first principles — *i.e.*, in Aristoteles's words, understanding it in terms of *"the first basis from which a thing is known"* [9]. In practice, this corresponds to finding a microscopic theoretical description, here in the context of quantum physics.

Fourier's macroscopic equation and Peierls Boltzmann's microscopic equation

The first solution to the challenge of developing an equation capable of describing the macroscopic evolution of a temperature field $T(\boldsymbol{r},t)$ in space ($\boldsymbol{r}$) and time (t) during heat transfer was proposed by Fourier in 1822 [10], who introduced the celebrated "heat equation"

$$C\frac{\partial T(\boldsymbol{r},t)}{\partial t}-\sum_{i,j=1}^{3}\kappa^{ij}\frac{\partial^2 T(\boldsymbol{r},t)}{\partial r^i \partial r^j}=0\,, \tag{1}$$

where C is the specific heat and κ^{ij} the thermal conductivity tensor, both quantities that can be measured in experiments. Fourier's heat equation is widely used nowadays in any engineering practice involving macroscopic objects exchanging heat.

The first microscopic theory for thermal transport was developed by Peierls in 1929 [11], who formulated a semiclassical theory and rationalized heat conduction in crystals in terms of atomic vibrational waves (phonon wave packets) diffusing and colliding as if they were particles of a classical gas (*i.e.* evolving according to an equation analogous to that developed by Boltzmann for classical gases). The central quantity of this semiclassical formulation is the phonon wave-packet distribution $n(\boldsymbol{x},\boldsymbol{q},t)_s$, where $\boldsymbol{x}$ is the position of the wave packet in direct space, $\hbar\boldsymbol{q}$ is its quasimomentum (in a crystal, periodicity implies that the wavevector $\boldsymbol{q}$ can be restricted to the first Brillouin zone $\mathfrak{B}$), t is time, and s is a band index that specifies the energy of the wave packet [12, 13]. The evolution of such semiclassical distribution function is ruled by the phonon Boltzmann transport equation (BTE)

$$\frac{\partial n(\boldsymbol{x},\boldsymbol{q},t)_s}{\partial t}+\boldsymbol{v}(\boldsymbol{q})_s\cdot\nabla_{\boldsymbol{x}}n(\boldsymbol{x},\boldsymbol{q},t)_s=\frac{\partial n(\boldsymbol{x},\boldsymbol{q},t)_s}{\partial t}\bigg|_{\rm col}, \tag{2}$$

where $\boldsymbol{v}(\boldsymbol{q})_s$ is the group velocity of the wave packet with wavevector $\boldsymbol{q}$ and in band s, and $\frac{\partial n(\boldsymbol{x},\boldsymbol{q},t)_s}{\partial t}\big|_{\rm col}$ a collision operator that is computed using the Fermi golden rule [12, 14, 15]. The relevance of the Peierls-Boltzmann equation (2) is its capability to predict the thermal conductivity of a crystal from its microscopic vibrational properties (described by the distribution $n(\boldsymbol{x},\boldsymbol{q},t)_s$). In fact, Hardy [16] showed that the the heat flux $\boldsymbol{Q}$, which is by definition related to the conductivity κ and temperature gradient ∇T via $\boldsymbol{Q}=-\kappa\nabla T$, is determined by the microscopic solution of Eq. (2) in the steady-state and homogeneous regime:

$$\boldsymbol{Q}=\frac{1}{(2\pi)^3}\int_{\mathfrak{B}}\sum_s \hbar\omega(\boldsymbol{q})_s\boldsymbol{v}(\boldsymbol{q})_s n(\boldsymbol{q})_s, \tag{3}$$

where $\omega(\boldsymbol{q})_s$ is the frequency of the wave packet with wavevector $\boldsymbol{q}$ and in band s. Therefore, the solution liner in the temperature gradient of Eq. (2) in the steady-state and homogeneous regime, determines the heat flux (3) and thus the thermal conductivity of a material via $\kappa=-Q^x/\nabla_x T$ (here we have reported a simplified description that considers κ as a scalar and the heat flux collinear with a temperature gradient in direction x, the general case will be discussed later in this Thesis).

Failures of Fourier's law: hydrodynamic regime of thermal transport

Nowadays, Fourier's equation is still used to model heat transfer at scales larger than a millimeter and at room temperatures or higher, e.g. to design heating or refrigeration systems. Fourier's law fails in the so-called hydrodynamic regime of thermal transport, *i.e.* when the heat flow becomes similar to the flow of a fluid. Hydrodynamic heat transport was discovered in the sixties at cryogenic conditions (*i.e.* $T \lesssim 20K$), with signatures such as Poiseuille-like heat flow [17] and second sound [18]. The former effect manifests itself with a heat flow analogous to the flow of a fluid in a pipe (*i.e.* displaying a paraboliclike profile with a maximum in the center and minimum at the boundaries [19], due to viscous effects [20, 21]); the latter instead shows propagation of heat in the form of a coherent temperature wave, rather than in the usual diffusive form (Fig. 1).

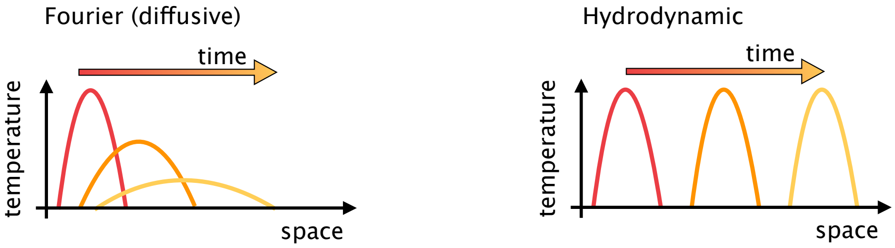

Figure 1 – **Qualitative difference between diffusive and hydrodynamic thermal transport.** Left, schematic representation of the temporal evolution of a temperature perturbation in the diffusive regime, where Fourier's equation is accurate. Right, schematic representation of heat propagation in the form of "second sound" in the hydrodynamic regime of thermal transport, where Fourier's equation fails. The color here is related to time, with red representing a time instant happened earlier than yellow (orange represents an intermediate time instant).

Several theoretical pioneering works focused on providing a quantitative description of heat hydrodynamics. Fundamental insights were obtained from the microscopic BTE, according to which these phenomena can appear when collisions between phonon wavepackets that conserve the crystal momentum ("normal processes") are much more frequent than momentum-dissipating collisions ("Umklapp processes") [21]. Under these conditions, the equilibrium distribution of phonon wave packets depends on two parameters, temperature T (which emerges from the conservation of energy in collision), and "drift-velocity" $\boldsymbol{u}$ (which is emerges from the conservation of momentum in the most frequent normal collision); T and $\boldsymbol{u}$ play a role analogous to pressure and velocity field in fluids, and from this it follows a prediction of a fluid-like (hydrodynamic) behavior for heat [21].

The complex integro-differential form of the microscopic BTE, unpractical for predicting the appearance and behavior of hydrodynamic heat transport phenomena, motivated research on a description at the mesoscopic level, *i.e.*, in terms of partial differential equations for temperature T and drift velocity $\boldsymbol{u}$ that are simpler than the microscopic integro-differential BTE. Starting from the linearized BTE (LBTE), several works derived mesoscopic equations for second sound or for Poiseuille heat flow assuming simplified phonon dispersion relations [19, 20, 21, 22], or neglecting momentum dissipation [23]. A more rigorous mesoscopic formulation for these hydrodynamic phenomena was introduced in Refs. [24, 25], albeit limited to low temperatures (*i.e.* not generalizable to the diffusive regime where Umklapp dissipation becomes strong). The turn of the century brought renewed interest in hydrodynamic transport phenomena. On the theoretical side, computational and algorithmic advances have allowed to solve exactly and from first principles the LBTE, and thus investigate its accuracy and that of the mesoscopic models derived from it. Also, recent research efforts in theory have been directed at extending the mesoscopic models developed in the sixties, to account for the effect of the boundaries on the heat flow [26, 27, 28, 29, 30]. On the experimental side, recent measurements [31, 32] have demonstrated the appearance of heat hydrodynamics in graphite at non cryogenic temperatures (around 100 K), thus paving the way for the exploitation of this phenomenon in technological applications.

Despite the substantial work done in the field, the challenge of developing mesoscopic partial differential equations that can describe accurately and on equal footing Fourier diffusion, hydrodynamic propagation, and all regimes in between, is still a matter of research, and this problem will be tackled in this thesis.

Failures of Peierls-Boltzmann equation: complex crystals

Despite the formulation of the BTE dating back to 1929, addressing it in real materials has become possible only recently, since modern algorithms allow to solve its linearized form either approximately (in the so-called single mode approximation (SMA) [33]) or exactly, using iterative [34, 35, 36], variational [37], or exact diagonalization [38, 39] methods; its accuracy, thanks to the predictive capabilities of first-principles methods [40, 41], has been highlighted in many studies [7, 33, 35, 42, 43]. Nevertheless, we understand now that these cases are characterized by having well-separated phonon bands, *i.e.* interband spacings much larger than the linewidths; we will refer to these in the following as "simple" crystals (Fig. 2**a-c**).

Already in 1963 Hardy noted that the thermal conductivity can be expressed in terms of the phonon velocity operator [16], whose diagonal elements are the phonon group velocities entering the Peierls' BTE and the missing off-diagonal terms are actually negligible in simple crystals [16]. In 1989 Allen and Feldman [44] envisioned that these off-diagonal elements, neglected so far, could become dominant in disordered systems, where Peierls' picture breaks down due to the impossibility of defining phonons and group velocities. As a consequence, a harmonic theory of thermal transport in glasses was introduced, where disorder limits thermal conductivity and heat is carried by the coupling of vibrational modes arising from the off-diagonal elements of the velocity operator. These considerations are thrown in sharp relief by the failure of the LBTE in describing "complex crystals" characterized by phonon interband spacings smaller that the linewidths; this regime appears in the presence of a large primitive cell or strong anharmonicity, conditions that also imply ultralow or glass-like thermal conductivity (see Fig. 2**d-e**) [45, 46, 47, 48, 49, 50]. Conversely, the harmonic theory of Allen and Feldman can be inadequate to describe some anharmonic glassy-and-disordered systems (*i.e.* amorphous composites) [51]; and crystal-like propagation mechanisms have been suggested (propagons [52]) — albeit without a formal justification — in order to explain the experimental results [52]. The study of such complex systems led also to the introduction of phenomenological models for heat conduction, based on the conjecture that glass- and crystal-like transport mechanisms coexist [47, 50, 53].

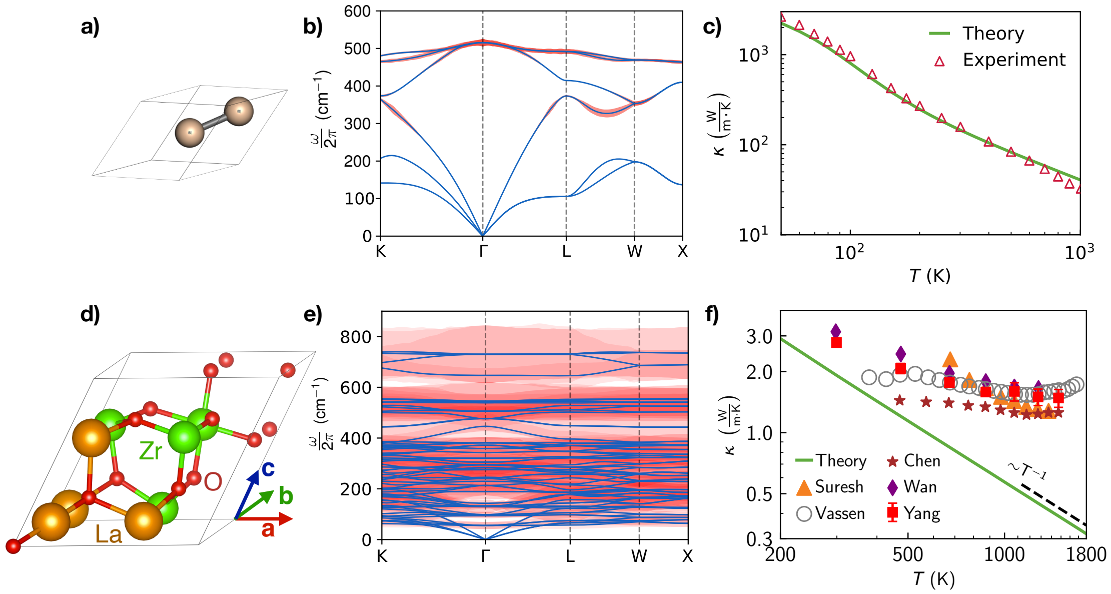

Figure 2 – **Predictive capabilities of the Peierls-Boltzmann equation: accuracy in simple crystals and failure in complex crystals.** "Simple crystals" such as silicon (panel **a**) are characterized by phonon interband spacings much larger than the linewidths (panel **b**, where the blue lines are the phonon bands and the shaded red areas are the linewidths at 300K, magnified by a factor of 10 for clarity). A sufficient condition for a material to behave as a simple crystal is to have a primitive cell containing a small number of atoms (this implies a small number of phonon bands) and to feature weak anharmonicity (this implies small linewidths). In the simple-crystal regime, the predictions of the thermal conductivity obtained from the Peierls-Boltzmann equation are in very good agreement with experiments [54] (panel **c**). In contrast, "complex crystals" such as lanthanum zirconate ($La_2Zr_2O_7$, panel **d**) are characterized by phonon interband spacings smaller than the linewidths (panel **e** shows phonon bands in blue and linewidths in red at 1800 K). A sufficient condition for a material to behave as a complex crystal is to have a primitive cell that contains many atoms (this implies many closely-spaced phonon bands) and to feature strong anharmonicity (this implies that the linewidths are large and thus allow the closely-spaced phonon bands to overlap). Panel **f** shows that in the complex-crystal regime, the conductivity predictions from the Peierls-Boltzmann equation (solid green) are in disagreement with the values observed in experiments (scatter points, representing measurements from Suresh *et al.* [55], Vassen *et al.* [56], Chen *et al.* [57], Wan *et al.* [58], Yang *et al.* [59]).

In summary, modern computational methods have allowed to solve the LBTE from first-principles and test its predictive capabilities. While accurate in simple crystals such as silicon, the LBTE fails to describe complex crystals such as perovskites [46], skutterudites [45], clathrates [49], zirconates [60], and many others complex materials [48, 50, 61, 62, 63] that display ultralow or glasslike thermal conductivity. This problem will be tackled in the first part of the thesis.

Structure of the thesis

This thesis addresses the aforementioned failures of Fourier's heat equation and of the microscopic Peierls-Boltzmann equation, and is divided in two parts. Since addressing the failures of the macroscopic Fourier's heat equation requires insights in the microscopic theory, the Wigner theory of thermal transport at the microscopic level will be presented first.

Part 1 is divided in three chapters, the first two are written in the form of a research article, and the third one discusses ongoing and future work. In particular:

- In Chapter 1 we address the shortcomings of the microscopic LBTE in describing complex crystals. We discuss how the Wigner's phase-space formulation of quantum mechanics [64, 65] allows to derive a microscopic unified heat-transport equation that describes on an equal footing heat conduction in crystals, glasses, and in the mixed regime of complex crystals. We shed light on formal aspects of the theory of thermal transport in solids, such as the microscopic definition of the heat flux and the derivation of an expression for the thermal conductivity. Relying on first-principles calculations, we show the capability of Wigner's formulation to predict correctly and in agreement with experiments the thermal conductivity of complex crystals used for thermal barrier coatings or thermoelectric applications.
- In Chapter 2 we demonstrate the capability of the newly-introduced microscopic unified theory to predict the opposite trends of thermal conductivity in crystals and in glasses. We analyze vitreous silica as a paradigmatic glass, discussing the negligible effects of anharmonicity in determining its thermal conductivity, and showing the emergence of a phonon liquid signature, corresponding to atomic vibrations having mean free paths that are mainly determined by the disorder length scale.
- In Chapter 3 we discuss preliminary results on meteoritic tridymite, a silica polymorph displaying thermal properties that are intermediate between those of crystalline quartz and amorphous silica.

Part 2 discusses thermal transport at the mesoscopic level, and focuses on simple crystals where the newly-introduced microscopic unified transport equation becomes equivalent to the LBTE. It is organized in two chapters:

- Chapter 4 is written in the form of a research article (already published in Ref. [66]).

First, we recall how the exact solution of the microscopic LBTE can be written as a linear combination of “relaxons” [39] (*i.e.* collective phonon excitations that are eigenvectors of the LBTE’s scattering matrix and have a well-defined mathematical parity), and such a solution determines a microscopic, closed-form expression for the thermal conductivity that receives contributions exclusively from odd relaxons. Then, we show that the complementary set of even relaxons determines another quantity, thermal viscosity, which becomes especially relevant in the hydrodynamic regime of thermal transport. We discuss how microscopic conservation laws can be exploited to coarse-grain the microscopic LBTE (which has a complex integro-differential form) into a set of mesoscopic “viscous heat equations”, partial differential equations that describe both heat diffusion and hydrodynamics at a much reduced complexity and more intuitively than the LBTE. We also introduce a descriptor, called "Fourier deviation number" (FDN), that captures all the physics needed to distinguish the hydrodynamic from the Fourier (diffusive) regime of heat transport. We show that this novel mesoscopic formulation, combined with first-principles calculations for its parameters, yields for graphite predictions of the temperatures and sizes at which hydrodynamic effects are largest in good agreement with very recent experimental findings [31].

- Chapter 5 discusses the emergence of hydrodynamic thermal transport in layered hexagonal boron nitride (hBN) relying on the viscous heat equations. In particular, it is discussed how the isotopic concentration of boron affects the magnitude of heat hydrodynamic effects.

Thermal transport beyond Boltzmann

Part I

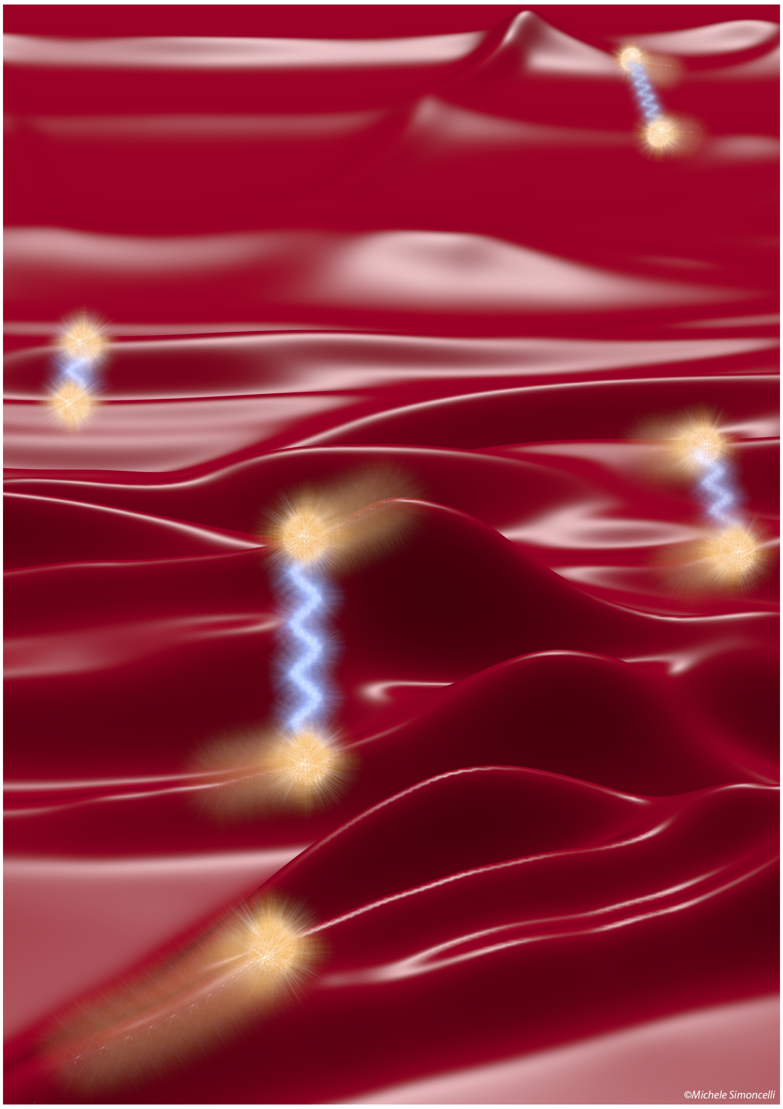

Figure 3 – Artistic representation of heat conduction in dielectric solids. The ridges represent the vibrational energy levels (*i.e.* the phonon spectrum) of the perovskite $CsPbBr_3$. Heat conduction originates from both vibrations' particle-like propagation (blurred spheres) and wave-like tunnelling between different energy levels (blue waves).

1 Quantum thermal transport in solids from Wigner's phase-space formalism

Crystals and glasses exhibit fundamentally different heat conduction mechanisms: the periodicity of crystals allows for the excitation of propagating vibrational waves that carry heat, as first discussed by Peierls, while in glasses the lack of periodicity breaks Peierls's picture and heat is mainly carried by the coupling of vibrational modes, often described by a harmonic theory introduced by Allen and Feldman. Anharmonicity or disorder are thus the limiting factors for thermal conductivity in crystals or glasses. In this chapter, we present the derivation of a unified transport equation, which describes thermal transport accounting for the interplay between anharmonicity, disorder, and the quantum Bose-Einstein statistics of atomic vibrations. The solution of such an equation yields a thermal conductivity formula that reduces to the Peierls and Allen–Feldman limits, respectively, in anharmonic crystals or harmonic glasses, while also covering the intermediate regimes where both effects are relevant. This approach also solves the long-standing problem of accurately predicting the thermal properties of crystals with ultralow or glass-like thermal conductivity.

This theoretical framework is especially relevant to applied research on thermally insulating and thermoelectric materials. In fact, materials for these applications have been hitherto identified and engineered combining challenging experiments, crystallography-driven intuitions, and computationally expensive molecular-dynamics simulations. The formulation discussed here allows to determine how changes in the chemical composition or in the structure of a material affect its capability to conduct heat, thus enables the computational high-throughput screening or the theory-driven optimization of materials for these applications.

This chapter discusses extensively the formal derivation of the *"Unified theory of thermal transport in crystals and glasses"*, whose salient features have been published in the journal Nature Physics [67]. This work has been done jointly with my PhD advisor, Prof. Nicola Marzari, and with Prof. Francesco Mauri (University of Rome "La Sapienza"). I contributed to this work as first author, specifically: (i) I raised some issues on the regime of applicability of the Peierls-Boltzmann equation; (ii) I did the calculations with inputs from Prof. Nicola Marzari and Prof. Francesco Mauri; (iii) I wrote the first draft of the manuscript.

Full bibliographic references:
Michele Simoncelli, Nicola Marzari, and Francesco Mauri
Unified theory of thermal transport in crystals and glasses. Nature Physics, 15 809 (2019)

DOI	https://doi.org/10.1038/s41567-019-0520-x
URL	https://www.nature.com/articles/s41567-019-0520-x
Copyright	2019 Springer Nature

Michele Simoncelli, Nicola Marzari, and Francesco Mauri
Quantum thermal transport in solids from Wigner's phase-space formalism.
To be submitted

Quantum thermal transport in solids from Wigner's phase-space formalism

Michele Simoncelli [1], Nicola Marzari[1], and Francesco Mauri[2]

1.1 Abstract

Two different heat-transport mechanisms are known in solids: in crystals the heat carriers (phonon wavepackets) propagate and scatter like particles, as described by the Peierls-Boltzmann equation; in glasses instead heat behaves wave-like, diffusing via a Zener-like tunneling between quasi-degenerate vibrational eigenstates, as exemplified by the Allen-Feldman equation. Recently it has been shown [Simoncelli, Marzari, Mauri, Nature Physics 15, 809 (2019)] that these two conduction mechanisms emerge as limiting cases from a unified quantum heat transport equation, which describes solids ranging from crystals (extremely ordered materials with small primitive cell) to glasses (disordered materials with infinitely large primitive cell); most importantly, in materials with intermediate disorder (e.g. complex materials used for thermal barriers or thermoelectrics) the two conduction mechanisms coexist, and it is crucial to account for both of them to perform accurate predictions. Here, we discuss the theoretical aspects needed to derive such transport equation from the Wigner phase-space formulation of quantum mechanics, elucidating how the interplay between disorder, anharmonicity, and the quantum Bose-Einstein statistics of atomic vibrations determines the thermal conductivity. We demonstrate the existence of a preferential phase convention for the Wigner distribution, which is the only one yielding a size-consistent conductivity, *i.e.* invariant with respect to the size of the (non-conventional) unit cell used to describe a crystal. Finally, we show that the present approach overcomes the failures of the Peierls-Boltzmann theory in materials with ultralow or glass-like thermal conductivity, showing applications to materials used for thermal barrier coatings or thermoelectric energy conversion.

1.2 Introduction

In 1929 Peierls [11] formulated the phonon Boltzmann transport equation (BTE) to explain heat conduction in crystalline solids, envisioning that in crystals the microscopic heat carriers are phonon wavepackets that diffuse and scatter as if they were particles of a gas. Recent computational advances have allowed to compute the parameters entering in the linearized form of the BTE (LBTE) from first principles [40, 41, 68, 69, 70], and to solve it either approximately, in the so-called single mode approximation [33], or exactly, using iterative [34, 35, 36], variational [37], or exact diagonalization [38, 39, 66, 70] methods. Several studies [7, 33, 35, 42, 43] have highlighted the accuracy of the LBTE in "simple crystals" characterized by phonon interband spacings much larger than the linewidths. A sufficient condition for a material to behave as a simple crystal is to have a primitive cell containing a small number of atoms (this implies a small number of phonon bands) and to have weak anharmonicity (this implies small linewidths).

---

[1] Theory and Simulation of Materials (THEOS) and National Centre for Computational Design and Discovery of Novel Materials (MARVEL), École Polytechnique Fédérale de Lausanne, Lausanne, Switzerland.

[2] Dipartimento di Fisica, Università di Roma La Sapienza, Piazzale Aldo Moro 5, I-00185 Roma, Italy

An attempt to explain the microscopic heat-conduction mechanism in glasses was made by Kittel in 1949 [71], who introduced a phenomenological model where atomic vibrations have a constant mean free path that is determined by the disorder length scale; however, this model lacks rigorous validation and has aroused some controversy [44, 52, 72, 73], since it describes nonperiodic glasses through Peierls' theory for periodic crystals. A key step forward was made by Allen and Feldman in 1989 [44]: they envisioned that in disordered systems heat diffuses in a wave-like fashion, specifically through a (Zener-like) tunneling between quasi-degenerate vibrational eigenstates (with a tunneling strength dependent on the off-diagonal elements of the velocity operator [16]).

Recent works have shown that the LBTE fails to describe materials with ultralow thermal conductivity [45, 46, 47, 48, 49, 50, 53], leading to the speculation that particle- and wave-like transport mechanisms coexist [47, 50, 53]. Conversely, the theory of Allen and Feldman for glasses does not account for anharmonicity; thus, it is supposed to be accurate only in the low-temperature (harmonic) regime [44, 73]; however, it has been shown that in complex amorphous composites with strong anharmonicity the harmonic Allen and Feldman theory is not accurate, even at low temperatures [51]. Most importantly, the presence of particle-like propagation mechanisms have been suggested to occur also in glasses (propagons) — albeit without a formal justification — in order to explain experimental results [52].

The Wigner-Boltzmann transport equation (WBTE) we recently introduced [67] has shown that, in addition to Peierls' particle-like heat propagation, a complementary wave-like heat-conduction mechanism emerges when the coherences between atomic vibrations (phonon wavepackets) allow tunneling. This WBTE provides a comprehensive approach to heat-transport phenomena in solids, ranging from crystals (where particle-like propagation dominates) to glasses (where wave-like tunneling dominates), and to all intermediate cases.

Here we discuss the theoretical aspects needed to derive such WBTE equation from the Wigner phase-space formulation of quantum mechanics. The paper is organized as follows: In Sec. 1.3 we discuss a second-quantization formalism for atomic vibrations in direct space that allows to define an out-of-equilibrium, space-dependent one-body density matrix, thus to describe a device to which a temperature gradient is applied (*i.e.* with a space-dependent temperature). We then discuss the conditions under which thermal transport can be treated as a Markovian irreversible process ruled by the Lindblad master equation.

In Sec. 1.4 we discuss the salient features of the Wigner phase-space formalism and show that is particularly convenient to describe transport phenomena in solids. We use such a formalism to derive an equation that describes heat transport accounting for the interplay between disorder, anharmonicity, and the quantum (Bose-Einstein) statistics of atomic vibrations. Then, we focus on the close-to-equilibrium regime, where a small temperature gradient perturbs the uniform equilibrium temperature, and we show how in such a regime the heat transport equation can be greatly simplified — provided a particular phase convention for the Wigner distribution is adopted. The resulting WBTE generalizes the Peierls-Boltzmann equation accounting not only for the particle-like propagation of phonon wavepackets but also for their wave-like tunneling between different bands.

In Sec. 1.5 we use this phase-space formulation to derive an expression for the microscopic harmonic energy field and the related microscopic harmonic heat flux. The expression of the Wigner microscopic harmonic heat flux differs from the well-known expression derived by Hardy [16]: we show in Appendix 1.E that Wigner's expression is uniquely defined by the transformation that maps matrix elements of operators into phase-space distributions, while Hardy's expression [16] depends on the choice of the microscopic harmonic energy field [74, 75] and is thus ill-defined. Finally, we solve the Wigner-Boltzmann heat transport equation at linear order in the temperature gradient, thus computing from such solution the microscopic heat flux and obtaining a generalized thermal conductivity expression that accounts for both particle- and wave-like conduction mechanisms. Such generalized conductivity turns out to be equivalent to the (particle-like) Peierls-Boltzmann conductivity in the case of a "simple" crystal, and to the (wave-like) Allen-Feldman conductivity in the case of a harmonic glass, but it is more general and covers all intermediate cases.

In Sec. 1.6 we show that it is necessary to adopt an appropriated ("Wallace" [76]) phase convention for the Wigner distribution in order to obtain a size-consistent conductivity.

Finally, in Sec. 1.7 we demonstrate that the present approach allows to predict the ultralow thermal conductivity of complex crystals used for thermal barrier coatings and thermoelectrics, showing applications to the zirconate $La_2Zr_2O_7$ and the perovskite $CsPbBr_3$ [67] as materials representative of these classes, respectively.

1.3 Quantum description of atomic vibrations

In this section we discuss a second-quantization formalism for atomic vibrations in direct space that is suitable to define the one-body density matrix of an out-of-equilibrium system, to which a temperature gradient is applied (*i.e.* with a space-dependent temperature, related to a space-dependent atomic vibrational energy). We then discuss the conditions under which thermal transport can be treated as a Markovian irreversible process, *i.e.* described by a one-body density matrix whose evolution is ruled by the Lindblad master equation.

1.3.1 Second quantization for atomic vibrations

We start by considering an electrically-insulating 3-dimensional bulk crystal, *i.e.* an infinite Bravais lattice with basis having: primitive vectors $\boldsymbol{a}_\alpha$ (α=1,...,3 is a Cartesian index) and sites $\boldsymbol{R} = n_\alpha \boldsymbol{a}_\alpha$ ($n_\alpha \in \mathbb{Z}\ \forall \alpha$, in this paper we employ the repeated-indexes summation convention);

primitive cell with volume $\mathcal{V}$ and containing $N_{\rm at}$ atoms at positions $\boldsymbol{\tau}_b \in \mathcal{V}$ (b=1,…,$N_{\rm at}$ is an atomic label). To describe the thermal transport in a non-metallic crystal, the starting point is the nuclear Hamiltonian obtained in the Born-Oppenheimer approximation:

$$\hat{H} = \sum_{\boldsymbol{R},b,\alpha} \frac{\hat{p}^2(\boldsymbol{R})_{b\alpha}}{2M_b} + \mathrm{V}\big(\{\hat{u}(\boldsymbol{R})_{b\alpha}\}\big); \tag{1.1}$$

where $\hat{p}(\boldsymbol{R})_{b\alpha}$ and $\hat{u}(\boldsymbol{R})_{b\alpha}$ are respectively the component along the direction α of the momentum and deviation from equilibrium position[1] operators of the atom b in the primitive cell at position $\boldsymbol{R}$; the usual canonical commutation relations are satisfied [14]:

$$[\hat{u}(\boldsymbol{R})_{b\alpha}, \hat{p}(\boldsymbol{R}')_{b'\alpha'}] = i\hbar\delta_{b,b'}\delta_{\alpha,\alpha'}\delta_{\boldsymbol{R},\boldsymbol{R}'}. \tag{1.2}$$

Moreover, M_b is the mass of the atom b and $V\big(\{\hat{u}(\boldsymbol{R})_{b\alpha}\}\big)$ is the Born-Oppenheimer lattice-periodic inter-nuclear potential, which depends on all the displacement operators. In practice, atoms oscillate around equilibrium positions, allowing to approximate the Born-Oppenheimer potential as n-th order Taylor series of the displacement operators $\{\hat{u}(\boldsymbol{R})_{b\alpha}\}$. For the first part of the present paper it is sufficient to consider the leading (second-order) term in such expansion:

$$\mathrm{V}\big(\{\hat{u}(\boldsymbol{R})_{b\alpha}\}\big) \simeq \frac{1}{2}\sum_{\boldsymbol{R},\boldsymbol{R}'} \frac{\partial^2 \hat{V}}{\partial\hat{u}(\boldsymbol{R})_{b\alpha}\partial\hat{u}(\boldsymbol{R}')_{b'\alpha'}}\bigg|_{\rm eq} \hat{u}(\boldsymbol{R})_{b\alpha}\hat{u}(\boldsymbol{R}')_{b'\alpha'} + \mathcal{O}(\hat{u}(\boldsymbol{R})_{b\alpha}\hat{u}(\boldsymbol{R}')_{b'\alpha'}\hat{u}(\boldsymbol{R}'')_{b''\alpha''}), \tag{1.3}$$

where zeroth order term can be taken as reference for the energy (*i.e.* equal to zero) without loss of generality, and the first-order term is not reported because it vanishes when evaluated at equilibrium [14]. Using the approximation (1.3), the nuclear Hamiltonian (1.1) can be written as $\hat{H} = \hat{H}^{\rm har} + \hat{H}^{\rm per}$, where $\hat{H}^{\rm har}$ is the leading second-order (harmonic) term and $\hat{H}^{\rm per}$ is a perturbation, due to the presence of anharmonicity (third- or higher-order terms in Eq. (1.3)) and of isotopic mass disorder. With the goal of using perturbation theory, we now focus on the description of the leading Hamiltonian $\hat{H}^{\rm har}$; the perturbative term that introduces transitions between the eigenstates of $\hat{H}^{\rm har}$ will be discussed later. It is useful to recast the harmonic coefficients in Eq. (1.3) in terms of the tensor commonly employed in the literature [76, 77],

$$G_{\boldsymbol{R}b\alpha,\boldsymbol{R}'b'\alpha'} = \frac{1}{\sqrt{M_b M_{b'}}} \frac{\partial^2 \hat{V}}{\partial\hat{u}(\boldsymbol{R})_{b\alpha}\partial\hat{u}(\boldsymbol{R}')_{b'\alpha'}}\bigg|_{\rm eq}, \tag{1.4}$$

which is symmetric and translational invariant:

$$G_{\boldsymbol{R}b\alpha,\boldsymbol{R}'b'\alpha'} = G_{\boldsymbol{R}'b'\alpha',\boldsymbol{R}b\alpha}, \tag{1.5}$$

$$G_{\boldsymbol{R}b\alpha,\boldsymbol{R}'b'\alpha'} = G_{(\boldsymbol{R}-\boldsymbol{R}')b\alpha,\boldsymbol{0}b'\alpha'} = G_{\boldsymbol{0}b\alpha,(\boldsymbol{R}'-\boldsymbol{R})b'\alpha'}. \tag{1.6}$$

---

[1] Formally, the deviation-from-equilibrium operator is $\hat{u}(\boldsymbol{R})_{b\alpha} = \hat{x}(\boldsymbol{R})_{b\alpha} - x^0_{\boldsymbol{R}b\alpha}\hat{\boldsymbol{1}}$, where $\hat{x}(\boldsymbol{R})_{b\alpha}$ is the α component of the position operator of the nuclei b in unit cell $\boldsymbol{R}$, and $x^0_{\boldsymbol{R}b\alpha}$ the corresponding constant equilibrium position.

The leading Hamiltonian $\hat{H}^{\text{har}}$ is quadratic in the momentum and displacement operators, and thus represents a many-body system of harmonic oscillators. With the goal of exploiting the second-quantization formalism to simplify the description of this many-body problem, we introduce the bosonic operator

$$\hat{a}(\boldsymbol{R})_{b\alpha}=\frac{1}{\sqrt{2\hbar}}\sum_{\boldsymbol{R'}}\left(\sqrt[4]{G^{-1}}_{\boldsymbol{R}b\alpha,\boldsymbol{R'}b'\alpha'}\frac{\hat{p}(\boldsymbol{R'})_{b'\alpha'}}{\sqrt{M_{b'}}}-i\sqrt{M_{b'}}\,\hat{u}(\boldsymbol{R'})_{b'\alpha'}\sqrt[4]{G}_{\boldsymbol{R'}b'\alpha',\boldsymbol{R}b\alpha}\right), \tag{1.7}$$

which annihilates a vibration centered around atom b in the unit cell $\boldsymbol{R}$ (the centering of such an operator is discussed in Appendix 1.A, where we investigate how the (power-law) decay of the tensor $G_{\boldsymbol{R}b\alpha,\boldsymbol{R'}b'\alpha'}$ for $|\boldsymbol{R}+\boldsymbol{\tau}_b-\boldsymbol{R'}-\boldsymbol{\tau}_{b'}|\to\infty$ determines the (power-law) decay of the related tensors $\sqrt[4]{G}_{\boldsymbol{R}b\alpha,\boldsymbol{R'}b'\alpha'}$, $\sqrt[4]{G^{-1}}_{\boldsymbol{R}b\alpha,\boldsymbol{R'}b'\alpha'}$ in the same limit). Eq. (1.7) defines a set of bosonic operators (labeled by $\boldsymbol{R}, b\alpha$) that have been devised so that they satisfy the usual bosonic commutation relation

$$[\hat{a}(\boldsymbol{R})_{b\alpha},\hat{a}^{\dagger}(\boldsymbol{R'})_{b'\alpha'}]=\delta_{b,b'}\delta_{\alpha,\alpha'}\delta_{\boldsymbol{R},\boldsymbol{R'}}, \tag{1.8}$$

and allow to write the leading harmonic Hamiltonian in the second-quantized form

$$\hat{H}^{\text{har}}=\hbar\sum_{\boldsymbol{R},\boldsymbol{R'}}\sqrt{G}_{\boldsymbol{R}b\alpha,\boldsymbol{R'}b'\alpha'}\left(\hat{a}^{\dagger}(\boldsymbol{R})_{b\alpha}\,\hat{a}(\boldsymbol{R'})_{b'\alpha'}+\frac{\delta_{\boldsymbol{R},\boldsymbol{R'}}\delta_{b,b'}\delta_{\alpha,\alpha'}}{2}\right). \tag{1.9}$$

It can be easily verified that the commutation relation (1.8) follows from the canonical commutation relation (1.2). From Eq. (1.9) we see that the harmonic vibrational energy is a one-body operator; therefore, to compute its expectation value the knowledge of the complex many-body density operator $\hat{\rho}$ is not needed, but it is sufficient to know the much simpler one-body density matrix

$$\varrho(\boldsymbol{R},\boldsymbol{R'},t)_{b\alpha,b'\alpha'}=\text{Tr}\Big(\hat{\rho}(t)\hat{a}^{\dagger}(\boldsymbol{R'})_{b'\alpha'}\hat{a}(\boldsymbol{R})_{b\alpha}\Big). \tag{1.10}$$

In fact, it is easy to verify that

$$\text{Tr}\big(\hat{\rho}(t)\hat{H}^{\text{har}}\big)=\hbar\sum_{\boldsymbol{R},\boldsymbol{R'}}\sqrt{G}_{\boldsymbol{R}b\alpha,\boldsymbol{R'}b'\alpha'}\varrho(\boldsymbol{R'},\boldsymbol{R},t)_{b'\alpha',b\alpha}+E_0, \tag{1.11}$$

where the additive constant $E_0=\frac{\hbar}{2}\sum_{\boldsymbol{R}}\sqrt{G}_{\boldsymbol{R}b\alpha,\boldsymbol{R}b'\alpha'}\delta_{b'\alpha',b\alpha}$ represents the vacuum energy. The time dependence of the expectation value in Eq. (1.11) is inherited from the temporal evolution of the density matrix, and this will be discussed later.

Up to now we have managed to reduce the complexity of the many-body problem by introducing the bosonic operator in direct space (1.7) and introducing the one-body density matrix. Now we will show that the formulation can be further simplified exploiting the invariance under translation of the force-constant matrix (1.6). We start by defining the Fourier transform of the bosonic operator (1.7)

$$\begin{aligned}\hat{a}(\boldsymbol{q})_{b\alpha}&=\sum_{\boldsymbol{R}}\hat{a}(\boldsymbol{R})_{b\alpha}e^{-i\boldsymbol{q}\cdot(\boldsymbol{R}+\boldsymbol{\tau}_b)}\\&=\frac{1}{\sqrt{2\hbar}}\Big[\sqrt[4]{D^{-1}(\boldsymbol{q})}_{b\alpha,b'\alpha'}\hat{P}(\boldsymbol{q})_{b'\alpha'}-i\sqrt[4]{D(\boldsymbol{q})}_{b\alpha,b'\alpha'}\hat{U}^{\dagger}(\boldsymbol{q})_{b'\alpha'}\Big],\end{aligned} \tag{1.12}$$

where

$$\hat{U}(\boldsymbol{q})_{b\alpha}=\sqrt{M_b}\sum_{\boldsymbol{R}}\hat{u}(\boldsymbol{R})_{b\alpha}e^{+i\boldsymbol{q}\cdot(\boldsymbol{R}+\boldsymbol{\tau}_b)} \tag{1.13}$$

and

$$\hat{P}(\boldsymbol{q})_{b\alpha}=\frac{1}{\sqrt{M_b}}\sum_{\boldsymbol{R}}\hat{p}(\boldsymbol{R})_{b\alpha}e^{-i\boldsymbol{q}\cdot(\boldsymbol{R}+\boldsymbol{\tau}_b)} \tag{1.14}$$

are the Fourier transforms of the displacement and momentum operators, respectively,

$$\sqrt[4]{D(\boldsymbol{q})}_{b\alpha,b'\alpha'}=\sum_{\boldsymbol{h}}\sqrt[4]{G}_{\boldsymbol{h}b\alpha,\boldsymbol{0}b'\alpha'}e^{-i\boldsymbol{q}\cdot(\boldsymbol{h}+\boldsymbol{\tau}_b-\boldsymbol{\tau}_{b'})} \tag{1.15}$$

and

$$\sqrt[4]{D^{-1}(\boldsymbol{q})}_{b\alpha,b'\alpha'}=\sum_{\boldsymbol{h}}\sqrt[4]{G^{-1}}_{\boldsymbol{h}b\alpha,\boldsymbol{0}b'\alpha'}e^{-i\boldsymbol{q}\cdot(\boldsymbol{h}+\boldsymbol{\tau}_b-\boldsymbol{\tau}_{b'})} \tag{1.16}$$

are the Fourier transforms of the fourth root of the harmonic force-constant matrix and of its inverse. Combining Eq. (1.8) and Eq. (1.12), it is easy to show that also the operators in Fourier space (1.12) satisfy the bosonic commutation relation

$$[\hat{a}(\boldsymbol{q})_{b\alpha},\hat{a}^{\dagger}(\boldsymbol{q'})_{b'\alpha'}]=\tfrac{(2\pi)^3}{\mathcal{V}}\delta(\boldsymbol{q}-\boldsymbol{q'})\delta_{b,b'}\delta_{\alpha,\alpha'}. \tag{1.17}$$

The physical action of the operator (1.12) is to annihilate a vibration with wavevector $\boldsymbol{q}$, centered on the the atom b, and in direction α. The usefulness of the bosonic operators in Fourier space (1.12) is to reduce to a simple block-diagonal form the representation of translation-invariant quantities such as the harmonic Hamiltonian (1.9):

$$\hat{H}^{\rm har}=\frac{\mathcal{V}}{(2\pi)^3}\int_{\mathfrak{B}}\hbar\sqrt{D(\boldsymbol{q})}_{b\alpha,b'\alpha'}\Big(\hat{a}^{\dagger}(\boldsymbol{q})_{b\alpha}\hat{a}(\boldsymbol{q})_{b'\alpha'}+\tfrac{\delta_{b,b'}\delta_{\alpha,\alpha'}}{2}\Big)d^3q, \tag{1.18}$$

where $\mathfrak{B}$ is a Brillouin zone and

$$\begin{aligned}\sqrt{D(\boldsymbol{q})}_{b\alpha,b'\alpha'}&=\sqrt[4]{D(\boldsymbol{q})}_{b\alpha,b''\alpha''}\sqrt[4]{D(\boldsymbol{q})}_{b''\alpha'',b'\alpha'}\\&=\sum_{\boldsymbol{h}}\sqrt{G}_{\boldsymbol{h}b\alpha,\boldsymbol{0}b'\alpha'}e^{-i\boldsymbol{q}\cdot(\boldsymbol{h}+\boldsymbol{\tau}_b-\boldsymbol{\tau}_{b'})}\end{aligned} \tag{1.19}$$

is the square root of the dynamical matrix of the solid, whose eigenvalues are the phonon frequencies $\omega(\boldsymbol{q})_s$ ($s=1,\ldots,3N_{\rm at}$ is the phonon-mode index that labels the different eigenvalues (phonon bands) at a given $\boldsymbol{q}$ point):

$$\mathcal{E}^{\star}(\boldsymbol{q})_{s,b\alpha}\sqrt{D(\boldsymbol{q})}_{b\alpha,b'\alpha'}\mathcal{E}(\boldsymbol{q})_{s',b'\alpha'}=\omega(\boldsymbol{q})_s\delta_{s,s'}. \tag{1.20}$$

To compute the expectation value of the harmonic vibrational energy from Eq. (1.18) it is sufficient to know the one-body density matrix in reciprocal space,

$$\varrho(\boldsymbol{q},\boldsymbol{q'},t)_{b\alpha,b'\alpha'}={\rm Tr}\big(\hat{\rho}(t)\hat{a}^{\dagger}(\boldsymbol{q'})_{b'\alpha'}\hat{a}(\boldsymbol{q})_{b\alpha}\big). \tag{1.21}$$

It follows from Eq. (1.12) that the one-body density in reciprocal space (1.21) can be obtained from the one-body density in direct space (1.10) (and vice-versa). To describe the close-to-equilibrium regime, in which a small temperature gradient is present in direct space, it is convenient to work in the center-of-mass variables in Fourier space,

$$\varrho\big(\boldsymbol{q}+\tfrac{\boldsymbol{q}''}{2},\boldsymbol{q}-\tfrac{\boldsymbol{q}''}{2},t\big)_{b\alpha,b'\alpha'}=\sum_{\boldsymbol{R},\boldsymbol{R}'}\varrho(\boldsymbol{R},\boldsymbol{R}',t)_{b\alpha,b'\alpha'}\,e^{-i\boldsymbol{q}\cdot(\boldsymbol{R}+\boldsymbol{\tau}_b-\boldsymbol{R}'-\boldsymbol{\tau}_{b'})}\,e^{-i\boldsymbol{q}''\cdot\frac{\boldsymbol{R}+\boldsymbol{\tau}_b+\boldsymbol{R}'+\boldsymbol{\tau}_{b'}}{2}}\,, \tag{1.22}$$

since we will show later that in such a regime the one-body density matrix $\varrho\big(\boldsymbol{q}+\frac{\boldsymbol{q}''}{2},\boldsymbol{q}-\frac{\boldsymbol{q}''}{2},t\big)_{b\alpha,b'\alpha'}$ is close to its equilibrium (diagonal) form, *i.e.* is sharply peaked and different from zero only for $\boldsymbol{q}''\to 0$. The transformation (1.22) reminds that the one-body density matrix in direct and reciprocal space contain the same informations. Quantum heat transport in solids is driven by a temperature gradient in direct space, thus the formulation in direct space is convenient to keep track of the vibration's locations and relate them to the space-dependent temperature driving transport. Conversely, we have seen that the formulation in reciprocal space simplifies the expression of the harmonic Hamiltonian, whose expectation value we are interested in.

We note in passing that the standard phonon annihilation (creation) operators ($\hat{a}(\boldsymbol{q})_s$, s being the phonon band index appearing in Eq. (1.20)) are in general not suitable to track where vibrations are centered, since in the transformation (1.20), which maps the atomic and Cartesian indexes $b\alpha$ into the mode index s, informations about vibrations' locations are lost due to the presence of a phase freedom; details are discussed in Appendix 1.A.1.

In summary, we have presented a second-quantization formalisms for atomic vibrations that is suitable to track vibration's locations, and in the next section we will discuss how this can be exploited to describe heat transport.

1.3.2 Evolution equation for the density matrix

The goal of the present work is to describe heat conduction, *i.e.* the energy transfer across a solid material when a temperature gradient is imposed at its boundaries. A physical model for this phenomenon is sketched in Fig. 1.1: two thermal baths W, C (having Hamiltonians $\hat{H}_W$ and $\hat{H}_C$ and kept at fixed temperatures $\bar{T}\pm\frac{\delta T}{2}$, respectively) are connected at the extremities of a solid subsystem S (having Hamiltonian $\hat{H}_S = \hat{H}^{\text{har}} + \hat{H}^{\text{per}}$ and length L), introducing a small temperature perturbation around the equilibrium temperature $\bar{T}$ ($\delta T \ll \bar{T}$). In addition, we focus on the regime in which the weak temperature perturbation is appreciable over the macroscopic length scale L, and $L \gg l \gg a$, with l being an intermediate length scale below which it is not possible to resolve temperature variations and a being the typical interatomic spacing.

Clearly, the quantum state of the full system belongs to the Hilbert space $\mathscr{H}_W \otimes \mathscr{H}_S \otimes \mathscr{H}_C$, where $\mathscr{H}_S$ is the Hilbert space of the solid subsystem S, $\mathscr{H}_W$ and $\mathscr{H}_C$ are the Hilbert spaces of the thermal baths W and C, and $\otimes$ denotes the direct product. In the following, the subscripts of the operators will denote the Hilbert space on which they act, and multiple subscripts will correspond to tensor products between Hilbert spaces. The bath Hamiltonians $\hat{H}_W$, $\hat{H}_C$ are assumed to have a number of degrees of freedom much larger than the solid subsystem S, so that their interactions with S, described by the Hamiltonians $\hat{H}_{W,S}$ and $\hat{H}_{C,S}$, have a negligible effect on their state. This is the basic condition for irreversibility [78] and corresponds to assuming that the external systems remain described by the corresponding equilibrium canonical density matrix: $\hat{\rho}^{eq}_W{=}e^{-\beta_W \hat{H}_W}/\mathrm{Tr}(e^{-\beta_W \hat{H}_W})$, with $\beta_W{=}(k_B(\bar{T}{+}\delta T/2))^{-1}$, and $\hat{\rho}^{eq}_C{=}e^{-\beta_C \hat{H}_C}/\mathrm{Tr}(e^{-\beta_C \hat{H}_C})$ with $\beta_C{=}(k_B(\bar{T}{-}\delta T/2))^{-1}$. The reservoirs-system couplings $\hat{H}_{W,S}$ and $\hat{H}_{C,S}$ are considered to be weak and localized (see Fig. 1.1), and they enforce a temperature gradient $\nabla T{\sim}\mathcal{O}(-\frac{\delta T}{L})$ across the system. These considerations allow one to consider

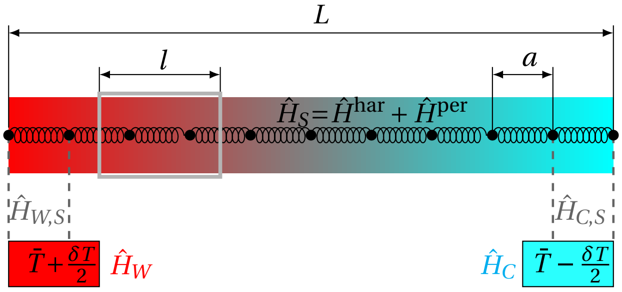
L
l
a
$\hat{H}_S{=}\hat{H}^{\mathrm{har}}+\hat{H}^{\mathrm{per}}$
$\hat{H}_{W,S}$
$\hat{H}_{C,S}$
$\bar{T}+\frac{\delta T}{2}$
$\hat{H}_W$
$\hat{H}_C$
$\bar{T}-\frac{\delta T}{2}$

Figure 1.1 – **Representative one-dimensional model for thermal transport.** A solid (rectangle of length L) is interacting with two thermal baths maintained at fixed temperatures $\bar{T}{\pm}\frac{\delta T}{2}$ (small red and blue rectangles). The black circles represent the atoms inside the solid, and the springs symbolize the interactions due to the interatomic potential appearing in Eq. (1.3). The dashed lines are the localized couplings with the external reservoirs, which enforce the temperature at the boundaries of the solid. The various relevant length scales are highlighted: $L{\gg}l{\gg}a$, where L is the length of the solid, l is an intermediate length scale over which temperature can be considered constant, and a is the interatomic spacing. Hamiltonian operators are denoted with an hat and are discussed in the text.

the density matrix of the full system to take the factorized form $\hat{\rho}_{\mathrm{tot}}(t){=}\hat{\rho}_S(t){\otimes}\hat{\rho}^{eq}_W{\otimes}\hat{\rho}^{eq}_C$ at any time $t{>}0$. Here we are interested in the irreversible evolution of the open quantum system S, whose continuous energy exchange with the heat baths can be accounted for by imposing proper boundary conditions [79, 80] (more on this later). Therefore, we do not aim to solve the full model but we focus on the subsystem of interest S, tracing out the degrees of freedom of the heat baths: $\hat{\rho}_S(t){=}\mathrm{Tr}_{W,C}[\hat{\rho}_{\mathrm{tot}}(t)]$. For this reason, we do not discuss here the details of the Hamiltonians $\hat{H}_W$, $\hat{H}_C$, $\hat{H}_{W,S}$, $\hat{H}_{C,S}$ and from now on we drop the subscript S from all the operators acting on the Hilbert space of the solid subsystem S.

The presence of the heat reservoirs ensures that the temporal correlation function of any excitation will decay after a time of the order of the transit time across the system [80]. In other words, the interaction with the heat baths makes the solid subsystem S lose memory of its state, yielding an irreversible evolution which can be modeled as Markovian and described by the Lindblad equation [81, 82]

$$\frac{\partial \hat{\rho}(t)}{\partial t} + \frac{i}{\hbar}\left[\hat{H}^{\text{har}}, \hat{\rho}(t)\right] = \frac{\partial \hat{\rho}(t)}{\partial t}\bigg|_{\hat{H}^{\text{per}}}; \tag{1.23}$$

where the collision superoperator $\frac{\partial \hat{\rho}(t)}{\partial t}\big|_{\hat{H}^{\text{per}}}$ is determined by the perturbative Hamiltonian $\hat{H}^{\text{per}}$ that accounts e.g. for the presence of anharmonic effects and isotopes (details are given in Appendix 1.B); as anticipated before, the presence of the heat baths will be considered through appropriate boundary conditions following the approach of Di Ventra [79].

Recalling Eq. (1.18), we have that $\hat{H}^{\text{har}}$ is a one-body operator; thus, applying the trace operation (1.21) to Eq. (1.23) gives us the evolution equation for the one-body density matrix (see Appendix 1.B.2 for details):

$$\begin{aligned}
&\frac{\partial \varrho\big(\boldsymbol{q}+\frac{\boldsymbol{q}''}{2}, \boldsymbol{q}-\frac{\boldsymbol{q}''}{2}, t\big)_{b\alpha,b'\alpha'}}{\partial t} \\
&+ i\left[\sqrt{D\big(\boldsymbol{q}+\tfrac{\boldsymbol{q}''}{2}\big)}_{b\alpha,b''\alpha''}\varrho\big(\boldsymbol{q}+\tfrac{\boldsymbol{q}''}{2}, \boldsymbol{q}-\tfrac{\boldsymbol{q}''}{2}, t\big)_{b''\alpha'',b'\alpha'} - \varrho\big(\boldsymbol{q}+\tfrac{\boldsymbol{q}''}{2}, \boldsymbol{q}-\tfrac{\boldsymbol{q}''}{2}, t\big)_{b\alpha,b''\alpha''}\sqrt{D\big(\boldsymbol{q}-\tfrac{\boldsymbol{q}''}{2}\big)}_{b''\alpha'',b'\alpha'}\right] \\
&= \frac{\partial \varrho\big(\boldsymbol{q}+\frac{\boldsymbol{q}''}{2}, \boldsymbol{q}-\frac{\boldsymbol{q}''}{2}, t\big)_{b\alpha,b'\alpha'}}{\partial t}\Bigg|_{\hat{H}^{\text{per}}};
\end{aligned} \tag{1.24}$$

where the one-body collision superoperator on the right-hand side is discussed in Appendix 1.C.2. At equilibrium, the system is homogeneous (translation-invariant) and thus from Eq. (1.22) it follows that the one-body density matrix is diagonal in $\boldsymbol{q}$, *i.e.* $\varrho\big(\boldsymbol{q}+\frac{\boldsymbol{q}''}{2}, \boldsymbol{q}-\frac{\boldsymbol{q}''}{2}, t\big)_{b\alpha,b'\alpha'} \propto \delta(\boldsymbol{q}'')$. Clearly, Eq. (1.24) yields a non-trivial evolution in the out-of-equilibrium regime, characterized by the presence of a non-homogeneity in direct space (*i.e.* a temperature gradient) and thus off-diagonal elements of the one-body density matrix. In the next section we will discuss a theoretical framework that makes the description of this non-homogeneous regime particularly simple and intuitive.

1.4 Phase-space formalism

The ideal framework to describe heat transport in solids should keep track of: (i) the equilibrium eigenstates towards which the system relaxes, which are labeled by the quasi-momentum $\hbar\boldsymbol{q}$; (ii) the spatial dependence of the perturbation driving transport, whose localization in direct space would be conveniently described by an Hilbert-space basis having as quantum number the Bravais lattice vector $\boldsymbol{R}$. However, the quasi-momentum and Bravais lattice operators ($\hbar\hat{\boldsymbol{q}}$ and $\hat{\boldsymbol{R}}$, respectively) are a pair of canonically conjugate operators [83], and thus their eigenvalues ($\hbar\boldsymbol{q}$ and $\boldsymbol{R}$, respectively) cannot be used to label simultaneously a quantum-mechanical representation within the usual Dirac formalism. The Wigner quantum phase-space formalism [64, 65, 84, 85, 86] allows to describe quantum mechanics in terms of distributions having as arguments eigenvalues of canonically conjugate operators, and in this section we discuss the application of such formalism to solids. We show that the central quantity appearing in this formulation generalizes the semiclassical distribution appearing in the Peierls-Boltzmann equation [12], describing not only intraband propagation of particle-like phonon wavepackets, but also wave-like interband (Zener) tunneling of phonons. This formalism is general and can be used to describe solids with any degree of disorder, ranging from ordered crystals with small primitive cell to disordered glasses (these treated as the limit of disordered crystals with infinitely-large primitive cells).

1.4.1 Wigner transform

As anticipated, the central objects of the Wigner formalism are phase-space distributions having as arguments eigenvalues of non-commuting operators. In order to show how such a framework allows to describe conveniently transport in non-homogeneous, out-of-equilibrium systems, it is useful to start from the Wigner transformation that maps the matrix elements of a one-body operator $O\big(\boldsymbol{q}+\frac{\boldsymbol{q}''}{2},\boldsymbol{q}-\frac{\boldsymbol{q}''}{2}\big)_{b\alpha,b'\alpha'}$ into a "phase-space" distribution that depends on a wavevector $\boldsymbol{q}$ (belonging to a Brillouin zone $\mathfrak{B}$) and a position $\boldsymbol{x}$ (see Refs. [65, 86, 87] and Appendix 1.D for details):

$$\mathscr{W}_{[O]}(\boldsymbol{x},\boldsymbol{q},t)_{b\alpha,b'\alpha'}=\frac{\mathcal{V}}{(2\pi)^3}\int\limits_{\mathfrak{B}} O\big(\boldsymbol{q}+\tfrac{\boldsymbol{q}''}{2},\boldsymbol{q}-\tfrac{\boldsymbol{q}''}{2},t\big)_{b\alpha,b'\alpha'}e^{i\boldsymbol{q}''\cdot\boldsymbol{x}}d^3q''. \tag{1.25}$$

When the Wigner transformation (1.25) is applied to the one-body density matrix, it becomes apparent that the Wigner distribution $W(\boldsymbol{x},\boldsymbol{q},t)_{b\alpha,b'\alpha'}=\mathscr{W}_{[\varrho]}(\boldsymbol{x},\boldsymbol{q},t)_{b\alpha,b'\alpha'}$ does not depend on space if the system is homogeneous (*i.e.* translation-invariant; this can be seen from Eq. (1.22), since for a translation-invariant system the one-body density matrix is nonzero only for $\boldsymbol{q}''=\boldsymbol{0}$). Conversely, for an out-of-equilibrium, non-homogeneous system the one-body density matrix is non-diagonal in $\boldsymbol{q}''$ and thus its Wigner representation depends on space.

In general, the position $\boldsymbol{x}$ appearing in Eq. (1.25) can be any (continuous) position in direct space. Nevertheless, restricting such a position to the discrete Bravais-lattice sites is sufficient to obtain a phase-space distribution that contains the same informations of the Dirac matrix element of the corresponding operator. In fact, knowing the phase-space distribution at the discrete Bravais sites ($\boldsymbol{x}$=$\boldsymbol{R}$) allows to determine the matrix element of the corresponding operator (proof in Appendix 1.D)

$$O\big(\boldsymbol{q}+\tfrac{\boldsymbol{q}''}{2},\boldsymbol{q}-\tfrac{\boldsymbol{q}''}{2},t\big)_{b\alpha,b'\alpha'}=\sum_{\boldsymbol{R}}\mathscr{W}_{[O]}\big(\boldsymbol{R},\tilde{\boldsymbol{q}},t\big)_{b\alpha,b'\alpha'}e^{-i\boldsymbol{q}''\cdot\boldsymbol{R}}\,. \tag{1.26}$$

Inserting Eq. (1.22) into Eq. (1.25), one obtains the transformation that relates matrix elements localized in direct space to the corresponding phase-space representation:

$$\mathscr{W}_{[O]}(\boldsymbol{x},\boldsymbol{q},t)_{b\alpha,b'\alpha'}=\sum_{\boldsymbol{R},\boldsymbol{R}'}O\big(\boldsymbol{R},\boldsymbol{R}',t\big)_{b\alpha,b'\alpha'}e^{-i\boldsymbol{q}\cdot(\boldsymbol{R}+\boldsymbol{\tau}_b-\boldsymbol{R}'-\boldsymbol{\tau}_{b'})}\frac{\mathcal{V}}{(2\pi)^3}\int_{\mathfrak{B}}e^{-i\boldsymbol{q}''\cdot\big(\frac{\boldsymbol{R}+\boldsymbol{\tau}_b+\boldsymbol{R}'+\boldsymbol{\tau}_{b'}}{2}-\boldsymbol{x}\big)}d^3q'', \tag{1.27}$$

where the integral over the Brillouin zone yields a function that is peaked around $\boldsymbol{x}=\frac{\boldsymbol{R}+\boldsymbol{\tau}_b+\boldsymbol{R}'+\boldsymbol{\tau}_{b'}}{2}$. Therefore, the closer is the average position of the localized matrix elements to the position $\boldsymbol{x}$, the more these contribute to the phase-space distribution at that position. We note in passing that the time dependence for O and $\mathscr{W}_{[O]}$ in Eqs. (1.25,1.26,1.27) has been reported for generality; in the present paper the only operator (distribution) that can depend on time is the density matrix (Wigner distribution $W(\boldsymbol{R},\boldsymbol{q},t)_{b\alpha,b'\alpha'}=\mathscr{W}_{[\varrho]}(\boldsymbol{R},\boldsymbol{q},t)_{b\alpha,b'\alpha'}$).

1.4.2 Wigner-Boltzmann transport equation

The equation describing the temporal evolution of the Wigner distribution at the Bravais site $\boldsymbol{R}$ and wavevector $\boldsymbol{q}$, $W(\boldsymbol{R},\boldsymbol{q},t)_{b\alpha,b'\alpha'}$, can be obtained by applying the transformation (1.25) to the evolution equation for the one-body density matrix (1.24). Here we are interested in the close-to-equilibrium regime characterized by weak non-homogeneities in direct space, *i.e.* in the regime where temperature varies slowly and causes spatial variations of the one-body density matrix to be appreciable only at "mesoscopic scales" l that are much larger than lengths a at which atomic positions can be resolved ($l \gg a$). We now present an intuitive derivation of a simplified evolution equation for the Wigner distribution in this close-to-equilibrium regime, and discuss how such an evolution equation generalizes the semiclassical Peierls-Boltzmann equation.

We start from Eq. (1.22), which shows that as the spatial variations of the one-body density matrix in direct space become smaller, the one-body density matrix in reciprocal space becomes closer to being diagonal in the arguments [2]. This implies that, in the close-to-equilibrium regime, the one-body density matrix $\varrho\big(\boldsymbol{q}-\frac{\boldsymbol{q}''}{2},\boldsymbol{q}+\frac{\boldsymbol{q}''}{2}\big)_{b\alpha,b'\alpha'}$ is sharply peaked around $\boldsymbol{q}$, and significantly different from zero only for $|\boldsymbol{q}''| \ll 2\pi/|\boldsymbol{a}_i|$. This property allows us to greatly simplify the evolution equation (1.24), performing a Taylor expansion for $|\boldsymbol{q}''|\to\boldsymbol{0}$ of the coefficients appearing in that equation:

$$\sqrt{D\big(\boldsymbol{q}\pm\tfrac{\boldsymbol{q}''}{2}\big)}_{b\alpha,b''\alpha''}\approx\sqrt{D(\boldsymbol{q})}_{b\alpha,b''\alpha''}\pm\nabla_{\boldsymbol{q}}\sqrt{D(\boldsymbol{q})}_{b\alpha,b''\alpha''}\cdot\frac{\boldsymbol{q}''}{2}. \tag{1.28}$$

Inserting such approximation into Eq. (1.24), one obtains the simplified evolution equation:

$$\begin{aligned}
&\frac{\partial\varrho\big(\boldsymbol{q}+\frac{\boldsymbol{q}''}{2},\boldsymbol{q}-\frac{\boldsymbol{q}''}{2},t\big)_{b\alpha,b'\alpha'}}{\partial t}\\
&+i\Big(\sqrt{D(\boldsymbol{q})}_{b\alpha,b''\alpha''}\varrho\big(\boldsymbol{q}+\tfrac{\boldsymbol{q}''}{2},\boldsymbol{q}-\tfrac{\boldsymbol{q}''}{2},t\big)_{b''\alpha'',b'\alpha'}-\varrho\big(\boldsymbol{q}+\tfrac{\boldsymbol{q}''}{2},\boldsymbol{q}-\tfrac{\boldsymbol{q}''}{2},t\big)_{b\alpha,b''\alpha''}\sqrt{D(\boldsymbol{q})}_{b''\alpha'',b'\alpha'}\Big)\\
&+\frac{1}{2}i\boldsymbol{q}''\Big(\Big(\nabla_{\boldsymbol{q}}\sqrt{D(\boldsymbol{q})}_{b\alpha,b''\alpha''}\Big)\varrho\big(\boldsymbol{q}+\tfrac{\boldsymbol{q}''}{2},\boldsymbol{q}-\tfrac{\boldsymbol{q}''}{2},t\big)_{b''\alpha'',b'\alpha'}+\varrho\big(\boldsymbol{q}+\tfrac{\boldsymbol{q}''}{2},\boldsymbol{q}-\tfrac{\boldsymbol{q}''}{2},t\big)_{b\alpha,b''\alpha''}\Big(\nabla_{\boldsymbol{q}}\sqrt{D(\boldsymbol{q})}_{b''\alpha'',b'\alpha'}\Big)\Big)\\
&=\frac{\partial\varrho\big(\boldsymbol{q}+\frac{\boldsymbol{q}''}{2},\boldsymbol{q}-\frac{\boldsymbol{q}''}{2},t\big)_{b\alpha,b'\alpha'}}{\partial t}\bigg|_{\hat{H}^{\rm per}}.
\end{aligned} \tag{1.29}$$

---

[2] given a one-body density matrix $\varrho(\boldsymbol{q}+\frac{\boldsymbol{q}''}{2},\boldsymbol{q}-\frac{\boldsymbol{q}''}{2})_{b\alpha,b'\alpha'}$, we say that it is diagonal in its two arguments ($\boldsymbol{q}+\frac{\boldsymbol{q}''}{2}$ and $\boldsymbol{q}-\frac{\boldsymbol{q}''}{2}$) if and only if it is nonzero only when the two arguments are equal (*i.e.* for $\boldsymbol{q}''=\boldsymbol{0}$).

Multiplying all terms in Eq. (1.29) by $\frac{\mathcal{V}}{(2\pi)^3}e^{i\boldsymbol{q}''\cdot\boldsymbol{R}}$ and integrating $\boldsymbol{q}''$ over the Brillouin zone yields a simplified evolution equation for the Wigner distribution

$$\begin{aligned}&\frac{\partial W(\boldsymbol{R},\boldsymbol{q},t)_{b\alpha,b'\alpha'}}{\partial t}+i\Big[\sqrt{D(\boldsymbol{q})},W(\boldsymbol{R},\boldsymbol{q},t)\Big]_{b\alpha,b'\alpha'}+\frac{1}{2}\Big\{\nabla_{\boldsymbol{q}}\sqrt{D(\boldsymbol{q})},\nabla_{\boldsymbol{R}}W(\boldsymbol{R},\boldsymbol{q},t)\Big\}_{b\alpha,b'\alpha'}\\&=\frac{\partial W(\boldsymbol{R},\boldsymbol{q},t)_{b\alpha,b'\alpha'}}{\partial t}\bigg|_{\hat{H}^{\rm per}},\end{aligned}\tag{1.30}$$

where we have introduced the notation $\Big[\sqrt{D(\boldsymbol{q})},W(\boldsymbol{R},\boldsymbol{q},t)\Big]_{b\alpha,b'\alpha'}$ to denote the matrix element of the commutator, *i.e.*, the quantity $\sqrt{D(\boldsymbol{q})}_{b\alpha,b''\alpha''}W(\boldsymbol{R},\boldsymbol{q},t)_{b''\alpha'',b'\alpha'}-W(\boldsymbol{R},\boldsymbol{q},t)_{b\alpha,b''\alpha''}\sqrt{D(\boldsymbol{q})}_{b''\alpha'',b'\alpha'}$; an analogous notation is employed for the anticommutator $\{,\}$. Moreover, we recall that the derivative of the Wigner distribution with respect to the position $\boldsymbol{R}$ is well defined, as explained in Sec. 1.4.1, and it has the following explicit form

$$\nabla_{\boldsymbol{R}}W(\boldsymbol{R},\boldsymbol{q},t)_{b\alpha,b'\alpha'}=i\frac{\mathcal{V}}{(2\pi)^3}\int_{\mathfrak{B}}\boldsymbol{q}''\varrho\big(\boldsymbol{q}+\tfrac{\boldsymbol{q}''}{2},\boldsymbol{q}-\tfrac{\boldsymbol{q}''}{2},t\big)_{b\alpha,b'\alpha'}e^{i\boldsymbol{q}''\cdot\boldsymbol{R}}d^3q''.\tag{1.31}$$

We stress that the approximation (1.28) implies the appearance of first-order derivatives with respect to position and wavevector in the simplified equation (1.30). These derivatives are sensitive to the phase convention adopted for the Fourier transform (1.12) and thus for the Wigner distribution (1.25); therefore, it is important to investigate if there is a preferential phase convention.

We recall that the Wigner transformations (1.25,1.27) are defined starting from matrix elements in the Cartesian basis (1.10) (or from its Fourier transform (Eqs. (1.12,1.22)), since matrix elements in this basis allow to keep track of the vibration's location in direct space (see Appendix 1.A.1). These transformations are affected by the freedom one has in choosing the phase convention for the Fourier transform. Specifically, we use the phase convention for the Fourier transform (Eqs. (1.12,1.22)) reported in the book of Wallace [76], *i.e.* the convention in which the phases ($e^{-i\boldsymbol{q}\cdot(\boldsymbol{R}+\boldsymbol{\tau}_b)}$) vary smoothly in direct space with the positions $\boldsymbol{R}+\boldsymbol{\tau}_b$ of a lattice with basis. In the context of Eq. (1.27), such a convention implies that a phase-space distribution at position $\boldsymbol{x}$, $\mathscr{W}_{[O]}(\boldsymbol{x},\boldsymbol{q},t)_{b\alpha,b'\alpha'}$, is mainly determined by localized matrix elements with average position close to $\boldsymbol{x}$ (see the bell-shaped function, resulting from the integral in Eq. (1.27), which weights localized matrix elements $O(\boldsymbol{R},\boldsymbol{R}',t)_{b\alpha,b'\alpha'}$ in a smooth way and depending on the distance between their average position $(\boldsymbol{R}+\boldsymbol{\tau}_b+\boldsymbol{R}'+\boldsymbol{\tau}_{b'})/2$ and the position $\boldsymbol{x}$). From an intuitive point of view, determining phase-space distributions weighing in a smooth and continuous way localized matrix elements in direct space is expected to yield smooth distributions that behave well with respect to differentiation. This intuitive reasoning is discussed further and validated quantitatively in Sec 1.6, where we demonstrate numerically that: (i) performing the approximation (1.28) employing the smooth phase convention of Wallace [76] (also called "C-type" convention [77, 88]) yields a size-consistent solution for the approximated evolution equation (1.30); (ii) performing the approximation (1.28) adopting the "step-like" phase convention of Ziman [14] (also called "D-type" convention [77, 88]), where the phases $e^{-i\boldsymbol{q}\cdot\boldsymbol{R}}$ do not depend on the atomic coordinate $\boldsymbol{\tau}_b$ in a lattice with a basis (thus they vary discontinuously from one Bravais-lattice cell to another) yields size-inconsistent results.

In Appendix 1.D we discuss an exact (*i.e.*, accurate also beyond the close-to-equilibrium regime) evolution equation for the Wigner distribution (Eq. (1.119)), which contains an infinite series of derivatives and allows a systematic analysis of quantum effects around the classical limit (with derivatives of increasingly higher order corresponding to decreasingly smaller quantum corrections). Importantly, Eq. (1.30) can be also obtained approximating to first order the series of derivatives appearing in the complex exact evolution equation (1.119), details are discussed in Appendix and results for the close-to-equilibrium regime are equivalent to those discussed here following a more intuitive procedure.

After having performed the first-order expansion, for which localization and differentiation properties are crucial, one can apply any unitary transformation to the simplified evolution equation (1.30), leaving the physics unchanged. Therefore, we can apply to Eq. (1.30) the unitary transformation (1.20) that diagonalizes the square root of the dynamical matrix, obtaining distributions that depend on position $\boldsymbol{R}$, wavevector $\boldsymbol{q}$, and phonon band indexes (s,s'), and thus can be compared directly with the distribution appearing in the Peierls-Boltzmann equation. Specifically, we introduce the quantities

$$N(\boldsymbol{R},\boldsymbol{q},t)_{s,s'}=\mathcal{E}^\star(\boldsymbol{q})_{s,b\alpha}W(\boldsymbol{R},\boldsymbol{q},t)_{b\alpha,b'\alpha'}\mathcal{E}(\boldsymbol{q})_{s',b'\alpha'}, \tag{1.32}$$

$$V^\beta(\boldsymbol{q})_{s,s'}=\mathcal{E}^\star(\boldsymbol{q})_{s,b\alpha}\nabla^\beta_{\boldsymbol{q}}\sqrt{D(\boldsymbol{q})}_{b\alpha,b'\alpha'}\mathcal{E}(\boldsymbol{q})_{s',b'\alpha'}, \tag{1.33}$$

which generalize the concepts of phonon distribution and group velocity appearing in the Peierls-Boltzmann equation [11, 39]. In fact, in the absence of degeneracies (*i.e.* for $s{\neq}s'$, $\omega(\boldsymbol{q})_s{\neq}\omega(\boldsymbol{q})_{s'}$) their diagonal elements ($s{=}s'$) coincide with the semiclassical phonon populations and group velocities, respectively, while their off-diagonal elements have a quantum origin related to the phase coherence between eigenstates s and s' [81, 89, 90, 91]. We note in passing that the velocity operator (1.33) has the following properties: it is Hermitian (since it is the incremental ratio of an Hermitian operator), its different Cartesian components do not commute $\big[\boldsymbol{V}^\alpha(\boldsymbol{q}),\boldsymbol{V}^\beta(\boldsymbol{q})\big]{\neq}0$ iff $\alpha{\neq}\beta$ (we have used the bold symbol $\boldsymbol{V}^\alpha(\boldsymbol{q})$ to denote a matrix having elements $V^\alpha(\boldsymbol{q})_{s,s'}$), and from the time-reversal symmetry of the dynamical matrix [77] it follows that $V^\beta(\boldsymbol{q})_{s,s'}=-V^\beta(-\boldsymbol{q})_{s',s}$.

From now on we will use the textbook nomenclature [92] and refer to the diagonal elements ($s{=}s'$) of the Wigner matrix distribution (1.32) as "populations" and to the off-diagonal ones ($s{\neq}s'$) as "coherences". We define the frequency matrix $\Omega(\boldsymbol{q})_{s,s'}{=}\omega(\boldsymbol{q})_s\delta_{s,s'}$, and represent with $\frac{\partial N(\boldsymbol{R},\boldsymbol{q},t)_{s,s'}}{\partial t}\Big|_{\hat{H}^{\rm per}}$ the collision superoperator in the basis of the phonon eigenmodes (which will be discussed later). Therefore, representing Eq. (1.30) in this phonon-mode basis we obtain the Wigner-Boltzmann transport equation

$$\frac{\partial N(\boldsymbol{R},\boldsymbol{q},t)_{s,s'}}{\partial t}+i\Big[\Omega(\boldsymbol{q}),N(\boldsymbol{R},\boldsymbol{q},t)\Big]_{s,s'}+\frac{1}{2}\Big\{\vec{V}(\boldsymbol{q}),\nabla_{\boldsymbol{R}}N(\boldsymbol{R},\boldsymbol{q},t)\Big\}_{s,s'}=\frac{\partial N(\boldsymbol{R},\boldsymbol{q},t)_{s,s'}}{\partial t}\bigg|_{\hat{H}^{\rm per}}; \quad (1.34)$$

where the commutator is reminiscent of the quantum evolution, the time derivative and the anticommutator involving the velocity operator generalize the diffusion term appearing in the Peierls-Boltzmann equation [11, 12]. Specifically, the populations terms in Eq. (1.34) describe the (intraband) particle-like propagation of phonon wavepackets exactly as in the semiclassical Peierls-Boltzmann transport equation [11, 12], while the coherences terms account for the (interband) wave-like tunneling of phonons from one band to another (see Fig. 1.2).

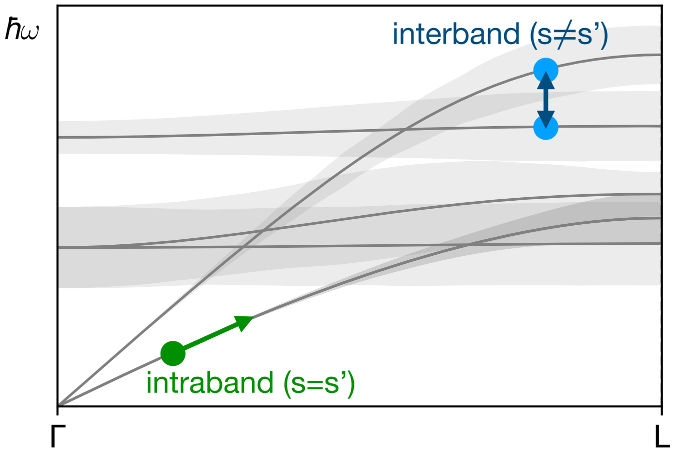

Figure 1.2 – **Particle-like (intraband) propagation versus wave-like (interband) tunneling.** Solid lines are the phonon bands of a representative solid and shaded areas the corresponding linewidths. The diagonal elements of the Wigner distribution ($s=s'$) describe the particle-like intraband propagation of phonon wavepackets (the green circle and arrow represent a phonon wavepacket propagating at its group velocity and remaining in its band). The off-diagonal elements ($s\neq s'$) describe the Zener-like interband tunneling of phonons between two different bands (blue circles represent phonons and the blue arrow their interband coupling via a Zener-like tunneling mechanism), and we will show later that interband tunneling becomes relevant whenever there is significant overlap between the linewidths of different bands.

The collision superoperator appearing in Eq. (1.34) is derived from the many-body collision superoperator appearing in Eq. (1.23), describing interactions between phonons at linear order in the deviation from equilibrium, as commonly done in the literature [37, 39]. The details are discussed in Appendix 1.C, and the result is

$$\begin{aligned}\frac{\partial N(\boldsymbol{R},\boldsymbol{q},t)_{s,s'}}{\partial t}\bigg|_{\hat{H}^{\rm per}}=&-(1-\delta_{s,s'})\frac{\Gamma(\boldsymbol{q})_s+\Gamma(\boldsymbol{q})_{s'}}{2}N(\boldsymbol{R},\boldsymbol{q},t)_{s,s'}\\&-\frac{\delta_{s,s'}}{(2\pi)^3}\sum_{s''}\int_{\mathfrak{B}}A(\boldsymbol{q},\boldsymbol{q}'')_{s,s''}\big[N(\boldsymbol{R},\boldsymbol{q}'',t)_{s'',s''}-\bar{N}^T(\boldsymbol{q}'')_{s''}\big]d^3q'',\end{aligned} \quad (1.35)$$

where $A(\boldsymbol{q},\boldsymbol{q}'')_{s,s''}$ is the usual phonon-phonon scattering operator (see Appendix 1.C), $\bar{N}(\boldsymbol{q}'')_{s''}{=}\left\{\exp\left[\hbar\omega(\boldsymbol{q}'')_{s''}/(k_B\bar{T})\right]-1\right\}^{-1}$ is the equilibrium Bose-Einstein distribution at the equilibrium temperature $\bar{T}$, and $\hbar\Gamma(\boldsymbol{q})_s{=}\hbar(2\pi)^{-3}A(\boldsymbol{q},\boldsymbol{q})_{s,s}$ is the phonon linewidth.

From Eq. (1.35) it is evident that populations scatter only with populations, and coherences scatter only with coherences. Importantly, Eq. (1.35) shows that scattering does not create but only destroys off-diagonal coherences ($s{\neq}s'$), while it can both create and destroy populations (*i.e.* it can redistribute phonons from a population $N(\boldsymbol{R},\boldsymbol{q},t)_{s,s}$ to another population $N(\boldsymbol{R},\boldsymbol{q},t)_{s',s'}$, increasing (decreasing) the population s and correspondingly decreasing (increasing) the other population s'). It follows that scattering drives the Wigner distribution towards the diagonal local-equilibrium distribution $\overline{N}(\boldsymbol{q})_s\delta_{s,s'}+\bar{n}(\boldsymbol{R},\boldsymbol{q})_s\delta_{s,s'}$ (*i.e.* the first two terms in Eq. (1.40)); in other words, the Wigner-Boltzmann transport equation (1.34) describes a relaxation towards to the same local-equilibrium state towards which the Peierls-Boltzmann transport equation evolves [93, 94].

1.5 Thermal conductivity

1.5.1 Vibrational energy field and flux

In the usual Dirac framework, a quantum mechanical observable is described by an operator $\hat{A}$, and its expectation value is determined from a trace operation $\langle\hat{A}\rangle{=}\mathrm{Tr}\big(\hat{\rho}(t)\hat{A}\big)$. Correspondingly, in the Wigner framework, observables are described by distributions in phase space (obtained applying the Wigner transform to the operators' matrix elements, as shown in Eq. (1.25)); it follows that in the Wigner framework the expectation value of an observable is computed as a phase-space-like integral of the product between the Wigner distribution and the phase-space distribution representing the observable (see Appendix 1.D and Ref. [86]):

$$\begin{aligned}\mathrm{Tr}\big(\hat{\rho}(t)\hat{A}\big) &= \frac{\mathcal{V}^2}{(2\pi)^6}\iint\limits_{\mathfrak{B}\mathfrak{B}}\varrho\big(\boldsymbol{q}{+}\tfrac{\boldsymbol{q}''}{2},\boldsymbol{q}{-}\tfrac{\boldsymbol{q}''}{2},t\big)_{b\alpha,b'\alpha'}A\big(\boldsymbol{q}{-}\tfrac{\boldsymbol{q}''}{2},\boldsymbol{q}{+}\tfrac{\boldsymbol{q}''}{2}\big)_{b'\alpha',b\alpha}d^3q\,d^3q'' \\ &= \frac{\mathcal{V}}{(2\pi)^3}\sum_{\boldsymbol{R}}\int_{\mathfrak{B}}\mathscr{W}_{[\varrho]}(\boldsymbol{R},\boldsymbol{q},t)_{b\alpha,b'\alpha'}\mathscr{W}_{[A]}(\boldsymbol{R},\boldsymbol{q})_{b'\alpha',b\alpha}d^3q.\end{aligned}\tag{1.36}$$

Eq. (1.36) allows to compute the expectation value of the harmonic vibrational energy of a crystal integrating a univocally defined, space-dependent “Wigner” energy field. To see this, we use Eq. (1.36) to compute the expectation value of the harmonic Hamiltonian (1.11), and a straightforward calculation shows that the Wigner transform (1.27) of the harmonic force-constant matrix $\sqrt{G}$ yields the square root of the dynamical matrix defined in Eq. (1.19):

$$\begin{aligned}\mathscr{W}_{[\sqrt{G}]}(\boldsymbol{R},\boldsymbol{q})_{b\alpha,b'\alpha'} &{=} \sum_{\boldsymbol{R}',\boldsymbol{R}''}\sqrt{G}_{\boldsymbol{R}'b\alpha,\boldsymbol{R}''b'\alpha'}e^{-i\boldsymbol{q}\cdot(\boldsymbol{R}'-\boldsymbol{R}''+\boldsymbol{\tau}_b-\boldsymbol{\tau}_{b'})}\left[\frac{\mathcal{V}}{(2\pi)^3}\int_{\mathfrak{B}}e^{-i\boldsymbol{q}'\cdot\left(\frac{\boldsymbol{R}'+\boldsymbol{R}''+\boldsymbol{\tau}_b+\boldsymbol{\tau}_{b'}}{2}-\boldsymbol{x}\right)}d^3q'\right] \\ &{=}\sqrt{D(\boldsymbol{q})}_{b\alpha,b'\alpha'}\,,\end{aligned}\tag{1.37}$$

where we highlight how the translational invariance of $\sqrt{G}$ (Eq. (1.6)) implies that its Wigner representation does not depend on position. Therefore, combining Eq. (1.36) with Eq. (1.37) allows to compute the expectation value of the harmonic vibrational energy as a spatial integration of an energy field [86], $\mathrm{Tr}(\hat{\rho}\hat{\mathrm{H}}^{\mathrm{har}})=\sum_{\boldsymbol{R}} E(\boldsymbol{R})+E_0$, where

$$\begin{aligned} E(\boldsymbol{R}) &= \frac{\mathcal{V}}{(2\pi)^3}\int_{\mathfrak{B}} \hbar\sqrt{D(\boldsymbol{q})}_{b\alpha,b'\alpha'} W(\boldsymbol{R},\boldsymbol{q})_{b'\alpha',b\alpha} d^3q \\ &= \frac{\mathcal{V}}{(2\pi)^3}\int_{\mathfrak{B}} \hbar\omega(\boldsymbol{q})_s \delta_{s,s'} N(\boldsymbol{R},\boldsymbol{q})_{s',s} d^3q, \end{aligned} \tag{1.38}$$

and E_0 is the vacuum energy (defined in Eq. (1.11)) that can be taken as reference energy and thus omitted, as it will be done in the following. We note that the Wigner microscopic energy field (1.38) differs from the microscopic energy field used by Hardy in Ref. [16]. In general, the harmonic (or two-body) energy field (which is the energy due to interactions between two atoms) is not uniquely defined at the microscopic level, because there are infinite ways of distributing the interaction energy between the two atoms interacting [74, 75]; however, within the Wigner framework, the microscopic energy field (1.38) is determined univocally by the property (1.11) [86].

The energy field (1.38) is normalized per number of primitive cells in the crystal, thus it has the units of energy and it is extensive with respect to the size of the primitive cell. Dividing Eq. (1.38) by the primitive-cell volume $\mathcal{V}$ yields the energy per unit volume of crystal, an intensive quantity whose time derivative can be related directly to the gradient of the intensive heat flux $\boldsymbol{Q}(\boldsymbol{R},t)$. Specifically, Using Eq. (1.34) to evaluate the time derivative of Eq. (1.38) (aptly normalized), one obtains a continuity equation that relates the time derivative of the energy field to the heat flux $\boldsymbol{Q}(\boldsymbol{R},t)$: $\frac{1}{\mathcal{V}}\frac{\partial}{\partial t}E(\boldsymbol{R},t) = -\nabla\cdot\boldsymbol{Q}(\boldsymbol{R},t)+\sigma(\boldsymbol{R},t)$, where

$$\boldsymbol{Q}(\boldsymbol{R},t) = \frac{\hbar}{(2\pi)^3}\int_{\mathfrak{B}} \frac{\omega(\boldsymbol{q})_s+\omega(\boldsymbol{q})_{s'}}{2}\vec{V}(\boldsymbol{q})_{s,s'} N(\boldsymbol{R},\boldsymbol{q},t)_{s',s} d^3q \tag{1.39}$$

is the heat flux (1.39) that originates from the leading harmonic Hamiltonian $\hat{H}^{\mathrm{har}}$ (Eq. (1.18)), while $\sigma(\boldsymbol{R},t)$ is a term due to the perturbation $\hat{H}^{\mathrm{per}}$ and of higher order in the perturbative treatment of anharmonicity with respect to the harmonic term, thus it will be neglected in the following. Importantly, the Wigner heat-flux expression (1.39) — which derives from the univocally-defined Wigner microscopic energy field (1.38) — differs from the well-known harmonic heat-flux expression derived by Hardy [16]. In Appendix 1.E we shed light on this difference, showing that using Hardy's approach it is possible to recover the results obtained here within Wigner's formalism. Specifically, we show that deriving the average heat flux using Hardy's approach [16] and choosing the microscopic energy field according to Wigner's prescription (1.38), one obtains exactly the spatial average of Eq. (1.39). This demonstrates that Hardy's heat flux expression [16] depends on the choice of the microscopic harmonic energy field and is thus ill-defined; in contrast, in the Wigner formalism the property (1.11) determines univocally the microscopic energy field (1.38), thus the Wigner heat-flux expression (1.39) that derives from it is also univocal, *i.e.* well defined.

1.5.2 Steady-state solution of the WBTE

The thermal conductivity is defined as the response tensor coefficient $\kappa^{\alpha\beta}$ that relates a temperature gradient to the heat flux generated in response to it: $Q^{\alpha}=-\kappa^{\alpha\beta}\nabla T^{\beta}$. Consequently, one can determine the thermal conductivity as follows: (i) fix a temperature gradient constant in time; (ii) solve Eq. (1.34) with boundary conditions corresponding to the temperature gradient fixed at point (i); (iii) determine the heat flux inserting the solution obtained at point (ii) into Eq. (1.39); (iv) determine the thermal conductivity as a tensor which relates the temperature gradient fixed at point (i) and the heat flux determined at point (iii). In this section we will determine the thermal conductivity from the solution of Eq. (1.34) following the protocol above.

We consider the system sketched in Fig. 1.1, where a steady and space-dependent temperature $T(\boldsymbol{x})\simeq\bar{T}+\nabla T\cdot\boldsymbol{x}$ is enforced along a certain direction by two thermal baths at temperatures $\bar{T}\pm\delta T/2$ (the approximated equality indicates that the temperature profile is to a good approximation linear, a condition that is realistic in regimes where ballistic effects can be neglected [95]). In addition, the temperature gradient is assumed to be small, *i.e.* in the case sketched in Fig. 1.1 one expects a temperature gradient $\nabla T\simeq-\frac{\delta T}{L}$, with $|\nabla T|\gg|\nabla^2 T|$ and $\bar{T}\gg\delta T$. Recalling the considerations made in Sec. 1.3.2 on the presence of the heat reservoirs at the boundaries, we have that the temperatures fixed to $\bar{T}\pm\delta T/2$ at the boundaries allow us to look for a solution as a perturbation of order ∇T on the local-equilibrium distribution corresponding to the local temperature $T(\boldsymbol{x})$ (see e.g. Ref. [96] for the mathematical details underlying this approximated solution method). Therefore, we look for a solution of the form

$$N(\boldsymbol{R},\boldsymbol{q})_{s,s'}=\overline{N}(\boldsymbol{q})_s\delta_{s,s'}+\bar{n}(\boldsymbol{R},\boldsymbol{q})_s\delta_{s,s'}+\vec{n}^{(1)}(\boldsymbol{q})_{s,s'}\cdot\nabla T, \tag{1.40}$$

where $\bar{N}(\boldsymbol{q})_s$ is the equilibrium Bose-Einstein distribution at temperature $\bar{T}$, $\bar{n}(\boldsymbol{R},\boldsymbol{q})_s\delta_{s,s'}=\frac{d\bar{N}(\boldsymbol{q})_s}{d\bar{T}}(T(\boldsymbol{R})-\bar{T})\delta_{s,s'}$ is the distribution that describes the local-equilibrium state corresponding to a local (space-dependent) temperature (such a local-equilibrium distribution has been discussed heuristically in Ref. [24], and relying on the quantum maximum entropy principle within the Wigner formalism in Refs. [97, 98]), and $\vec{n}^{(1)}(\boldsymbol{q})_{s,s'}\cdot\nabla T$ is in general non-diagonal in s, s' and contains the information concerning the deviation of the full solution from the local equilibrium solution (it is assumed to be of the order of the temperature gradient, as in previous work [37, 39]). We recall that, even though the phase-space distributions (1.25) are defined for all points in space, only the values of these distributions at the Bravais lattice sites appear in Eq. (1.34) and Eq. (1.40), since the knowledge of the Wigner distributions at these points is sufficient to fully describe the problem, as explained in Sec. 1.4.1.

Inserting the expansion (1.40) into the WBTE (1.34) at steady state, and considering only terms linear in the temperature gradient, we obtain a matrix equation that is decoupled in its diagonal and off-diagonal parts. The (diagonal) equation for the populations is the usual steady-state LBTE [37]:

$$\vec{V}(\boldsymbol{q})_{s,s}\cdot\left(\frac{\partial\bar{N}(\boldsymbol{q})_s}{\partial\bar{T}}\nabla T\right)=-\frac{1}{(2\pi)^3}\sum_{s''}\int_{\mathfrak{B}}A(\boldsymbol{q},\boldsymbol{q''})_{s,s''}\left[\vec{n}^{(1)}(\boldsymbol{q''})_{s'',s''}\cdot\nabla T\right]d^3q''; \tag{1.41}$$

where on the right-hand-side we have used the property that the local-equilibrium distribution $\bar{n}(\boldsymbol{R},\boldsymbol{q})_s\delta_{s,s'}$ is an eigenvector with zero eigenvalue of the collision superoperator [24, 66, 93]; thus, $\sum_{s''}\int_{\mathfrak{B}}A(\boldsymbol{q},\boldsymbol{q''})_{s,s''}\bar{n}(\boldsymbol{R},\boldsymbol{q''})_{s''}d^3q''{=}0$. Eq. (1.41) can be solved exactly using an iterative [36, 70, 99], variational [37] or exact diagonalization method [38, 39]. The off-diagonal equation for the coherences is ($s{\neq}s'$):

$$\frac{1}{2}\left(\frac{\partial\bar{N}(\boldsymbol{q})_s}{\partial\bar{T}}+\frac{\partial\bar{N}(\boldsymbol{q})_{s'}}{\partial\bar{T}}\right)\vec{V}(\boldsymbol{q})_{s,s'}\cdot\nabla T=-\left(i\big(\omega(\boldsymbol{q})_s-\omega(\boldsymbol{q})_{s'}\big)+\frac{\Gamma(\boldsymbol{q})_s+\Gamma(\boldsymbol{q})_{s'}}{2}\right)\vec{n}^{(1)}(\boldsymbol{q})_{s,s'}\cdot\nabla T, \tag{1.42}$$

and can be solved straightforwardly, yielding ($s\neq s'$):

$$n^{(1),\alpha}(\boldsymbol{q})_{s,s'}=-\frac{\hbar}{k_BT^2}V^\alpha(\boldsymbol{q})_{s,s'}\frac{\omega(\boldsymbol{q})_s\bar{N}(\boldsymbol{q})_s[\bar{N}(\boldsymbol{q})_s+1]+\omega(\boldsymbol{q})_{s'}\bar{N}(\boldsymbol{q})_{s'}[\bar{N}(\boldsymbol{q})_{s'}+1]}{2i[\omega(\boldsymbol{q})_s-\omega(\boldsymbol{q})_{s'}]+[\Gamma(\boldsymbol{q})_s+\Gamma(\boldsymbol{q})_{s'}]}. \tag{1.43}$$

We note that solving exactly the equation for the populations (1.41) requires accounting for all the interactions between populations (those described by the collision matrix $A(\boldsymbol{q},\boldsymbol{q''})_{s,s''}$); in contrast, the exact evolution equation for the coherences (1.42) contains only the coupling of a coherence $N(\boldsymbol{R},\boldsymbol{q})_{s,s'}$ (with $s{\neq}s'$) to itself. From a practical point of view, for materials with a primitive cell containing less than ~ 50 atoms, the computational cost for solving exactly the coherences' equation (1.42) is negligible compared to that for solving exactly the LBTE (*i.e.* the populations' equation (1.41))[3].

After having determined the solution of the WBTE (1.40) (*i.e.* the sum of the solutions of Eq. (1.41) and Eq. (1.42)), one can insert it into Eq. (1.39) and thus evaluate the heat flux. At this point it is straightforward to show that only the deviation-from-equilibrium part $\vec{n}^{(1)}(\boldsymbol{q})_{s,s'}\cdot\nabla T$ of the solution (1.40) gives a non-zero contribution to the heat flux, since the Bose-Einstein term ($\bar{N}(\boldsymbol{q})_s\delta_{s,s'}$) and the local-equilibrium term ($\bar{n}(\boldsymbol{R},\boldsymbol{q})_s\delta_{s,s'}$) are both even functions of the wavevector, and thus when multiplied by the diagonal elements of the velocity operator — which have odd parity in the wavevector — they yield an odd-parity function whose integral over the symmetric Brillouin zone yields zero [66]. Therefore, one obtains a linear relationship between heat flux and temperature gradient, $Q^\alpha{=}{-}\kappa^{\alpha\beta}\nabla^\beta T$, where the proportionality tensor is the thermal conductivity:

---

[3] Specifically, finding the exact solution of the populations' equation (1.41) requires applying iterative or variational algorithms to a matrix of size $(N_{\rm c}{\times}3{\times}N_{\rm at})^2$ (where $N_{\rm c}$ is the number of q-points used to sample the Brillouin zone in numerical calculations), while solving the equation for coherences requires just knowing the entries of a vector of size $N_{\rm c}\times(3\times N_{\rm at})^2$.

$$\begin{aligned}\kappa^{\alpha\beta}=\kappa_{\rm P}^{\alpha\beta}+\frac{1}{(2\pi)^3}\int_{\mathfrak{B}}\sum_{s\neq s'}\frac{\omega(\boldsymbol{q})_s+\omega(\boldsymbol{q})_{s'}}{4}\left[\frac{C(\boldsymbol{q})_s}{\omega(\boldsymbol{q})_s}+\frac{C(\boldsymbol{q})_{s'}}{\omega(\boldsymbol{q})_{s'}}\right]V^{\alpha}(\boldsymbol{q})_{s,s'}V^{\beta}(\boldsymbol{q})_{s',s}\\ \times\frac{\frac{1}{2}\left[\Gamma(\boldsymbol{q})_s+\Gamma(\boldsymbol{q})_{s'}\right]}{[\omega(\boldsymbol{q})_{s'}-\omega(\boldsymbol{q})_s]^2+\frac{1}{4}[\Gamma(\boldsymbol{q})_s+\Gamma(\boldsymbol{q})_{s'}]^2}d^3q;\end{aligned}\tag{1.44}$$

where $C(\boldsymbol{q})_s=\frac{\hbar^2\omega^2(\boldsymbol{q})_s}{k_B\bar{T}^2}\bar{N}(\boldsymbol{q})_s\big[\bar{N}(\boldsymbol{q})_s+1\big]$ is the specific heat of a phonon with wavevector $\boldsymbol{q}$ and mode s, $\kappa_{\rm P}^{\alpha\beta}$ is the “populations conductivity” obtained from the exact (*i.e.* iterative [34, 36], variational [37], or exact-diagonalization [38, 39, 70]) solution of the diagonal (population) part of the WBTE (1.41) — which is exactly the Peierls-Boltzmann equation for phonon wavepackets [12] — and the additional tensor derives from the equation for the coherences (1.42), thus it is called “coherences conductivity” ($\kappa_{\rm C}^{\alpha\beta}$). We also note that Eq. (1.44) can be directly implemented in computer programs by evaluating the integral over the Brillouin zone on a uniform mesh of wavevectors, *i.e.* replacing $\frac{1}{(2\pi)^3}\int_{\mathfrak{B}}d^3q\rightarrow\frac{1}{\mathcal{V}N_{\rm c}}\sum_{\boldsymbol{q}}$, where $N_{\rm c}$ is the number of q-points that sample the Brillouin zone and over which the sum runs, and $\mathcal{V}$ is the volume of the primitive cell [100].

We stress that the WBTE conductivity (1.44) derives from an exact solution of the WBTE (1.34) and thus is valid also in the hydrodynamic regime, where the collisions between phonons that conserve the crystal momentum (“normal processes”) dominate and yield a Peierls-Boltzmann thermal conductivity that is very high ($\kappa_P(300\ K)\gtrsim 10^3$ W/mK) and several order of magnitude larger than the coherences conductivity [66].

It is worth mentioning that in low-thermal-conductivity solids, where “Umklapp” collisions between phonon wavepackets that dissipate the crystal momentum are dominant, the collision superoperator for the populations can be simplified using the single-mode-relaxation time approximation (SMA) [37, 101]. In practice, such an approximation consists in discarding the off-diagonal elements of the linearized collision superoperator for the populations $A(\boldsymbol{q},\boldsymbol{q}')_{s,s'}$, *i.e.* in approximating it to its diagonal entries only: $(2\pi)^{-3}A(\boldsymbol{q},\boldsymbol{q}')_{s,s'}=\Gamma(\boldsymbol{q})_s\delta(\boldsymbol{q}-\boldsymbol{q}')\delta_{s,s'}$. This approximation results in the independent relaxation to equilibrium of different phonon populations, implying that the populations equation can be solved straightforwardly (and at a computational cost similar to that for solving exactly the equation for the coherences (1.42)), yielding

$$n^{(1),\alpha}_{\rm SMA}(\boldsymbol{q})_s=-\frac{\hbar}{k_B\bar{T}^2}V^{\alpha}(\boldsymbol{q})_{s,s}\frac{\omega(\boldsymbol{q})_s\bar{N}(\boldsymbol{q})_s[\bar{N}(\boldsymbol{q})_s+1]}{\Gamma(\boldsymbol{q})_s}.\tag{1.45}$$

When the approximated SMA solution for the populations (1.45) is inserted into the expression for the heat flux (1.39), the populations’ conductivity (term $\kappa_P^{\alpha\beta}$ in Eq. (1.44)) becomes exactly equal to the famous SMA expression for the Peierls-Boltzmann conductivity [100]:

$$\kappa^{\alpha\beta}_{\rm P,SMA}=\frac{1}{(2\pi)^3}\int_{\mathfrak{B}}\sum_{s}C(\boldsymbol{q})_sV^{\alpha}(\boldsymbol{q})_{s,s}V^{\beta}(\boldsymbol{q})_{s,s}\frac{1}{\Gamma(\boldsymbol{q})_s}d^3q.\tag{1.46}$$

Eq. (1.46) shows that the populations' conductivity can be interpreted in terms of particle-like phonon wavepackets labeled by $(\boldsymbol{q})_s$, which carry the specific heat $C(\boldsymbol{q})_s$ and propagate between collisions over a length $\Lambda^\alpha(\boldsymbol{q})_s{=}V^\alpha(\boldsymbol{q})_{ss}(\Gamma(\boldsymbol{q})_s)^{-1}$ (as mentioned before, $V^\alpha(\boldsymbol{q})_{ss}$ is the propagation (group) velocity in direction α and $[\Gamma(\boldsymbol{q})_s]^{-1}$ the typical inter-collision time). Importantly, we note that $\kappa_P^{\alpha\beta}$ can be interpreted in terms of microscopic carriers propagating particle-like without relying on the SMA approximation, since it has been shown that the conductivity deriving from the exact solution of the population's equation (1.32) can be determined exactly and in a closed form as a sum over relaxons [39, 66], *i.e.* particle-like collective phonon excitations that are the eigenvectors of the scattering matrix $A(\boldsymbol{q},\boldsymbol{q}'')_{s,s''}$ appearing in Eq. (1.32).

Concerning the other term $\kappa_{\rm C}$ appearing in the conductivity expression (1.44), it is determined by the wave-like tunnelling of phonons between different bands at the same wavevector $\boldsymbol{q}$, a mechanism that has some analogies with the Zener interband tunnelling of electrons discussed e.g. in Refs. [102, 103, 104, 105, 106] relying on the density-matrix formalism.

It has been shown in Ref. [66] that in "simple" crystals, *i.e.* those characterized by phonon interband spacings much larger that the linewidths (e.g. silicon, diamond), particle-like mechanisms dominate and thus $\kappa_{\rm P}^{\alpha\beta}{\gg}\kappa_{\rm C}^{\alpha\beta}$. We will discuss in Sec. 1.7 how in the "complex" crystal regime, characterized by phonon interband spacings smaller that the linewidths, particle-like and wave-like mechanisms coexist and are both relevant, implying $\kappa_{\rm P}^{\alpha\beta}{\lesssim}\kappa_{\rm C}^{\alpha\beta}$. Finally, we discuss in Appendix 1.H how for a harmonic glass — described as the limiting case of a disordered but periodic crystal with an increasingly larger unit cell ($N_{at}\to\infty$, *i.e.* $\mathcal{V}\to\infty$) and thus with the Brillouin zone reducing to the point $\boldsymbol{q}{=}\boldsymbol{0}$ only — the coherences conductivity dominates ($\kappa_{\rm C}^{\alpha\beta}{\gg}\kappa_{\rm P}^{\alpha\beta}$) and Eq. (1.44) becomes equivalent to the Allen-Feldman formula for the conductivity of glasses [44, 73].

1.6 Phase convention and size consistency

As anticipated in Sec. 1.4.2, the first-order Taylor expansion (1.28) yields a simplified evolution equation (1.34), whose dependence on the phase convention adopted has to be investigated. The choice of defining the Wigner distribution starting from the matrix elements in the Cartesian basis, either in direct or reciprocal space (Eqs. (1.10,1.22)), is dictated by the necessity to describe unambiguously localization properties (see Appendix 1.A.1). However, as discussed in Sec. 1.4.2, multiple phase conventions are possible for the Fourier transform (1.12), as can be seen from the lack of a standard choice in the literature, with Ziman [14] using a "step-like" phase $e^{-i\boldsymbol{q}\cdot\boldsymbol{R}}$ and Wallace [76] using a "smooth" phase $e^{-i\boldsymbol{q}\cdot(\boldsymbol{R}+\boldsymbol{\tau}_b)}$. While localization is well-defined with all these phase conventions, the "smooth" phase adopted by Wallace [76] seems to be convenient for differentiation (see the discussion reported in Sec. 1.4.2), and in order to shed light on such an intuitive claim, we compare here the predictions for the conductivity obtained using these two different phase conventions.

Up to now all the results have been formulated using the Wallace [76] phase convention.

Using the Ziman [14] phase convention, the Fourier transform (1.12) changes by a unitary transformation (quantities computed with the Ziman phase convention are underlined):

$$\underline{\hat{a}}(\boldsymbol{q})_{b\alpha}=\sum_{\boldsymbol{R}}\hat{a}(\boldsymbol{R})_{b\alpha}e^{-i\boldsymbol{q}\cdot\boldsymbol{R}}=\hat{a}(\boldsymbol{q})_{b\alpha}e^{i\boldsymbol{q}\cdot\boldsymbol{\tau}_b}. \tag{1.47}$$

It is straightforward to check that using the Ziman [14] phase convention implies removing all the atomic positions $\boldsymbol{\tau}_b, \boldsymbol{\tau}_{b'}$ from the complex exponentials in the derivations of Secs. 1.3,1.4; from Eq. (1.12) to Eq. (1.24) this produces no differences in the physical description. However, the phase convention adopted affects the transport equation (1.34), since the velocity operator appearing in Eq. (1.34) depends on the phase convention (it is straightforward to demonstrate that all other coefficients in Eq. (1.34), which are not obtained from a differentiation procedure, are unaffected by the phase convention). Specifically we show in Appendix 1.F.1 that using Ziman's step-like phase convention one obtains a velocity operator $\underline{V}^{\beta}(\boldsymbol{q})_{s,s'}$ related to that obtained using Wallace's phase convention ($V^{\beta}(\boldsymbol{q})_{s,s'}$, defined in Eq. (1.33)) as follows:

$$\underline{V}^{\beta}(\boldsymbol{q})_{s,s'}=V^{\beta}(\boldsymbol{q})_{s,s'}+i\big[\omega(\boldsymbol{q})_{s'}-\omega(\boldsymbol{q})_{s}\big]\sum_{b\alpha}\mathcal{E}^{\star}(\boldsymbol{q})_{s,b\alpha}\tau^{\beta}_{b}\mathcal{E}(\boldsymbol{q})_{s',b\alpha}. \tag{1.48}$$

From Eq. (1.48) it follows that velocity-operator elements $V^{\beta}(\boldsymbol{q})_{s,s'}$ on the diagonal ($s{=}s'$) or coupling degenerate vibrational modes (*i.e.* $s{\neq}s'$ with $\omega(\boldsymbol{q})_s{=}\omega(\boldsymbol{q})_{s'}$) do not depend on the phase convention. In contrast, off-diagonal elements of the velocity operator that couple non-degenerate vibrational modes depend on the phase convention. We note that in any subspace spanned by degenerate vibrational modes with wavevector $\boldsymbol{q}$ and with frequency[4] ω_d, one can exploit the freedom of rotating the degenerate eigenstates of the dynamical matrix (Eq. (1.20)) to render the representation of the velocity operator in direction β diagonal in the mode indexes. As mentioned in Sec. 1.4.2, the different Cartesian components of the velocity operator in general do not commute (not even in the degenerate subspaces), thus they can not be all diagonalized simultaneously (see e.g. Ref. [107] for a general discussion). Nevertheless, since one has the freedom to diagonalize in the degenerate subspace at least one Cartesian component of the velocity operator — thus to recover along such direction a populations' conductivity exactly equivalent to the Peierls-Boltzmann conductivity discussed in Ref. [37] — we consider the diagonal and degenerate velocity-operator elements as contributing exclusively to the Peierls-Boltzmann conductivity.

Therefore, we investigate numerically how the differences between the two velocity operators (1.48) affect the conductivity (1.44). We perform a test on size-consistency, computing the thermal conductivity of a crystal described in two mathematically different but physically equivalent ways: (i) repeating $N{\times}N{\times}N$ times a primitive cell with volume $\mathcal{V}$; (ii) repeating $\frac{N}{8}{\times}\frac{N}{8}{\times}N$ times a unit cell that is a supercell 8×8×1 of the primitive (see Fig. 1.3**a,b** for a schematic representation of these two cases when $N{=}8$, with panel **a)** representing case (i) and panel **b)** representing case (ii)).

---

[4] *i.e.* all the vibrational modes satisfying $\omega(\boldsymbol{q})_{s_d}=\omega_d\ \forall\ s_d\in\{i,\dots,j\}$, with $1\leq i<j\leq 3\cdot N_{at}$

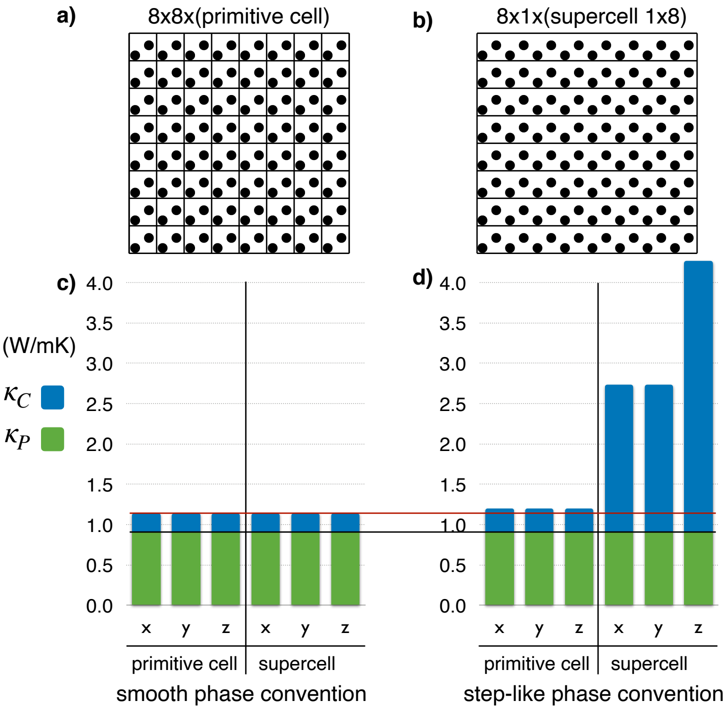

Figure 1.3 – **Size consistency of the WBTE conductivity adopting the smooth (Wallace) phase convention.** Size-consistency is tested computing the conductivity (1.44) of two equivalent representation of a silicon crystal at T=300 K and using a fictitious linewidth of $\hbar\Gamma(\boldsymbol{q})_s$=30 cm^{-1} $\forall\ \boldsymbol{q}, s$ (very large fictitious linewidth are used to enhance wave-like interband tunneling and render this mathematical test more informative). We sketch in panels **a,b)** two equivalent crystal representations: panel **a)** shows the representation obtained repeating the 2-atom primitive cell the same number of times along each Cartesian direction, while panel **b)** shows an equivalent representation obtained repeating a unit cell that is larger than the primitive. Panel **c)** shows that the smooth "Wallace"[76] phase convention (used in Eq. (1.12)) yields size-consistent numerical results, since the conductivity is unchanged when the silicon crystal with fictitious linewidths is modeled as: (i) a 16×16×16 repetition of the 2-atom primitive cell; (ii) a (physically equivalent) 2×2×16 repetition of a unit cell that is a supercell 8×8×1 of the primitive. Panel **d)** shows instead that the step-like "Ziman"[14] phase convention (used in Eq. (1.47)) is not size-consistent, since it yields different conductivities for the two physically equivalent representations of the crystal listed above. The black and red lines serve as a guide to the eye, to show that the Peierls-Boltzmann (populations) conductivity does not depend on the phase convention adopted (black), while the coherences conductivity depends on the phase convention adopted (red).

These two descriptions, which are equivalent from the physical point of view, result having the same thermal conductivity if the Wallace phase convention is adopted (Fig. 1.3**c**), while they absurdly result having different conductivities using Ziman's phase convention (Fig. 1.3**d**). This test demonstrates that the smooth phase of Wallace is the convention to be used, in agreement with the expectations based on intuitive arguments discussed in Sec. 1.4.

We note that the tests detailed in Fig. 1.3**c,d** have been performed using very large fictitious linewidths and very large unit cells, in order to enhance the importance the off-diagonal elements of the velocity operator in the conductivity formula (1.44); as such, the numerical values obtained from this test demonstrate mathematically the size-consistency of Eq. (1.44), but their absolute values have no physical meaning.

1.7 Applications to materials science

In this section we consider complex crystals, whose thermal conductivity is ultralow and not correctly described by the LBTE, as case studies for this more general Wigner-Boltzmann framework (Eq. (1.44)). In particular, we show applications to lanthanum zirconate ($La_2Zr_2O_7$) and to the halide perovskite $CsPbBr_3$, as examples of materials used for thermal barrier coatings or thermoelectric devices, respectively.

1.7.1 Lanthanum zirconate

$La_2Zr_2O_7$ is a material characterized by thermal stability and ultralow thermal conductivity, thus it is widely used for thermal barrier coatings applications [108]. This material is a good test case for the Wigner formulation discussed here, since at high temperature it is a complex crystal with many overlapping phonon bands and its temperature-conductivity curve is not correctly described by the LBTE. Here, we calculate the thermal conductivity as a function of temperature of $La_2Zr_2O_7$, computing from first principles the harmonic Hamiltonian and the collision superoperator (see Appendix 1.I.1 for computational details).

$La_2Zr_2O_7$ is characterized by a cubic structure (spacegroup: Fd-3m, number 227) and by an isotropic thermal conductivity tensor, thus in the following only the single independent component of the conductivity tensor will be reported ($\kappa{=}\kappa^{xx}{=}\kappa^{yy}{=}\kappa^{zz}$). Moreover, we rely on the SMA approximation to reduce the computational cost for solving populations' part of the WBTE (*i.e.* the LBTE, see Sec. 1.5.2), since it is known that for materials with ultralow conductivity the solution of the LBTE determined within the SMA approximation is practically indistinguishable from the exact solution of the LBTE [37, 60, 67, 101]. Therefore, the conductivity reported in the following is computed from Eq. (1.44) with the population's term evaluated in the SMA approximation (1.46).

Transport mechanisms: from simple to complex crystal

At low temperature (200 K) $La_2Zr_2O_7$ behaves as a simple crystal characterized by linewidths smaller than the phonon interband spacings (Fig. 1.4**a**(i)). As a consequence, the Peierls populations' conductivity ($\kappa_{\rm P}$, mainly determined by low-frequency phonon bands with large group velocities and weak anharmonicity, see Fig. 1.4**a**(ii)), is almost one order of magnitude larger than the coherences' conductivity ($\kappa_{\rm C}$, see Fig. 1.4**a**(iii)).

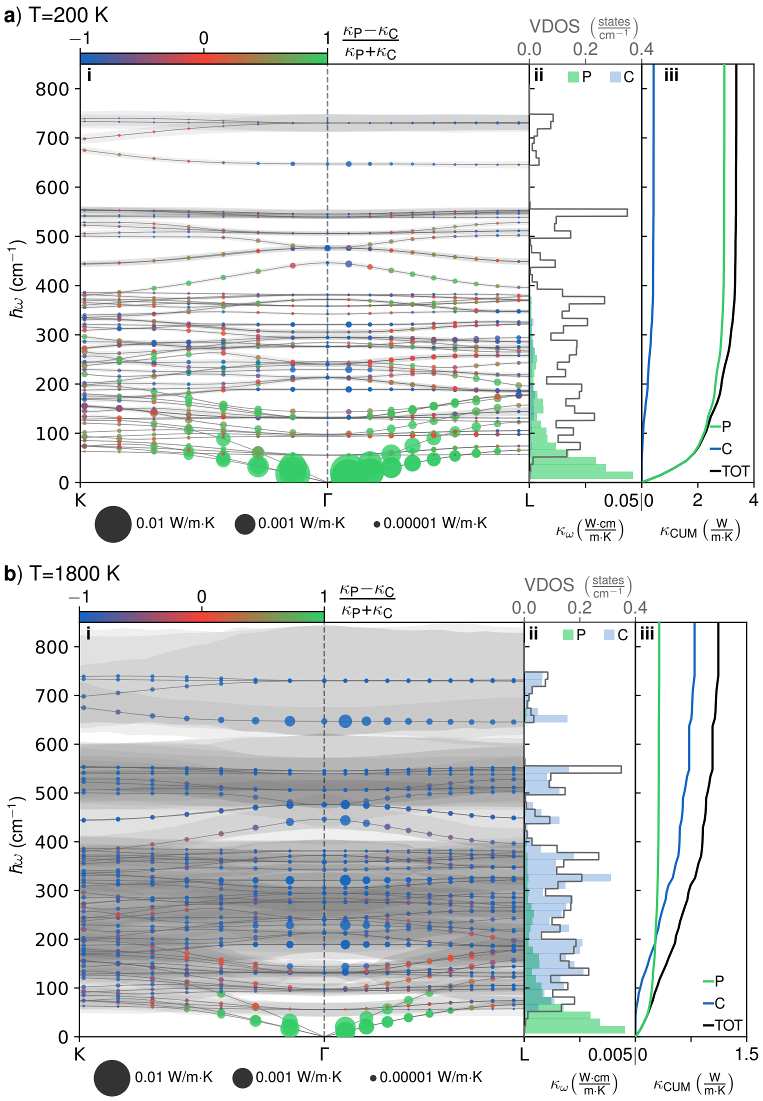

Figure 1.4 – **Vibrational properties and heat conduction mechanisms in La$_2$Zr$_2$O$_7$.** Panels **a**(i), **b**(i) show the phonon spectrum of La$_2$Zr$_2$O$_7$ (gray lines) with the phonon linewidths (the full amplitude of the shaded gray areas correspond to the full phonon linewidth or inverse lifetime $\Gamma(\boldsymbol{q})_s{=}[\tau(\boldsymbol{q})_s]^{-1}$) at 200 K and 1800 K, respectively. Colored circles represent the phonon eigenstates $(\boldsymbol{q})_s$ sampled in the calculation; the area of each circle is related to its contribution to κ (area $\propto \sqrt{\text{contribution to } \kappa}$ [109]) and the color identifies the origin of the contribution: green for populations' propagation and blue for coherences' anharmonic couplings (red corresponds to 50% of each). In the coherences' couplings between two modes $(\boldsymbol{q})_s$ and $(\boldsymbol{q})_{s'}$ the contribution of the single mode s is determined as $C(\boldsymbol{q})_s/[C(\boldsymbol{q})_s{+}C(\boldsymbol{q})_{s'}]$, where $C(\boldsymbol{q})_s{=}\frac{\hbar^2}{k_B T^2}\omega^2(\boldsymbol{q})_s \bar{N}^T(\boldsymbol{q})_s[\bar{N}^T(\boldsymbol{q})_s{+}1]$ is the specific heat of a given phonon. Panels **a**(ii), **b**(ii) show the thermal conductivity density of states κ_ω of populations ("P", green) and coherences ("C", blue) at 200 K and 1800 K, respectively. The gray line shows the vibrational density of states (VDOS). Panels **a**(iii), **b**(iii) show the cumulative total thermal conductivity (in black) as a sum of the populations' contribution ("P") in green and coherences' one ("C") in blue, at 200 K and 1800 K, respectively. At 200 K (panel **a**) La$_2$Zr$_2$O$_7$ is a simple crystal with interband spacings larger than the linewidths and $\kappa_P \gg k_C$, while at 1800 K it is a complex crystal with interband spacings smaller than the linewidths and $\kappa_P \lesssim k_C$.

At high temperature (1800 K) instead, $La_2Zr_2O_7$ behaves as a complex crystal characterized by interband spacings smaller than the linewidths (Fig. 1.4**b**(i)). In this regime the coherences conductivity receives significant contributions from highly anharmonic flat bands (Fig. 1.4**a**(ii)) and dominates over the populations' conductivity (Fig. 1.4**b**(iii)).

The density of states of the coherences' conductivity (blue histogram in Fig. 1.4**a,b**(ii)) can be also resolved in terms of the frequencies ω_1, ω_2 of the two modes coupled, as shown in Fig. 1.5. At 200 K, such a 2-dimensional density of states for the coherences' thermal conductivity ($\kappa_{C,\omega_1\omega_2}$, Fig. 1.5, left panel) shows couplings between quasi-degenerate vibrational modes, similarly to the case of harmonic glasses ($\Gamma(\boldsymbol{q})_s \to 0$). At 1800 K (Fig. 1.5, right panel) $\kappa_{C,\omega_1\omega_2}$ instead includes couplings between phonon modes having very different frequencies, driven by the large anharmonicity — therefore the corresponding heat conduction mechanism is intrinsically different from the one of harmonic glasses.

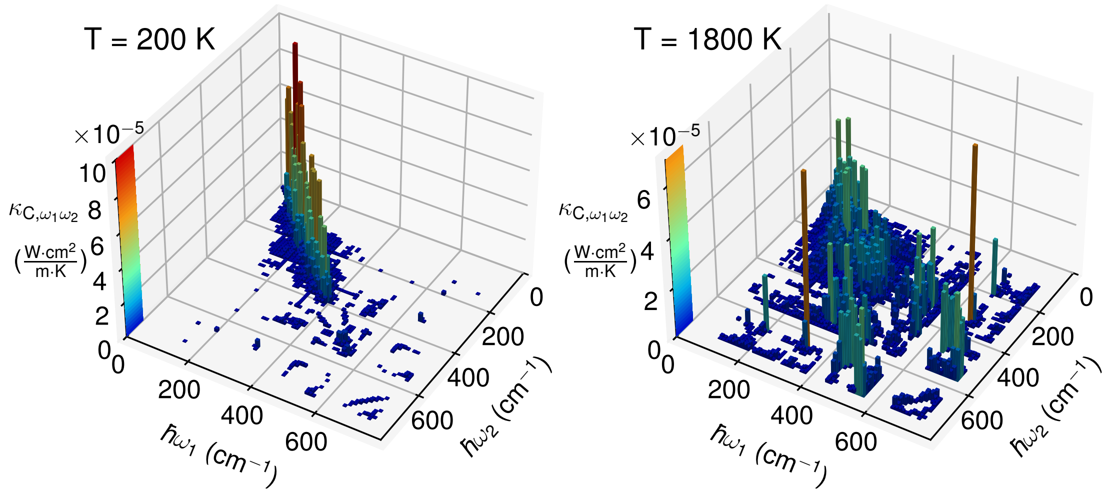

Figure 1.5 – **2-dimensional density of states for the thermal conductivity,** $\kappa_{C,\omega_1\omega_2}$, which resolves how much a Zener-like coupling between two vibrational modes having frequencies ω_1, ω_2 contributes to the coherences' conductivity. We show $\kappa_{C,\omega_1\omega_2}$ at 200 K (left panel) and at 1800 K (right panel). The points close to the diagonal $\omega_1 \sim \omega_2$ correspond to quasi-degenerate vibrational eigenstates; the Allen-Feldman framework considers couplings only between these.

Thermal conductivity

The conductivity as a function of temperature for $La_2Zr_2O_7$ is shown in Fig. 1.6.

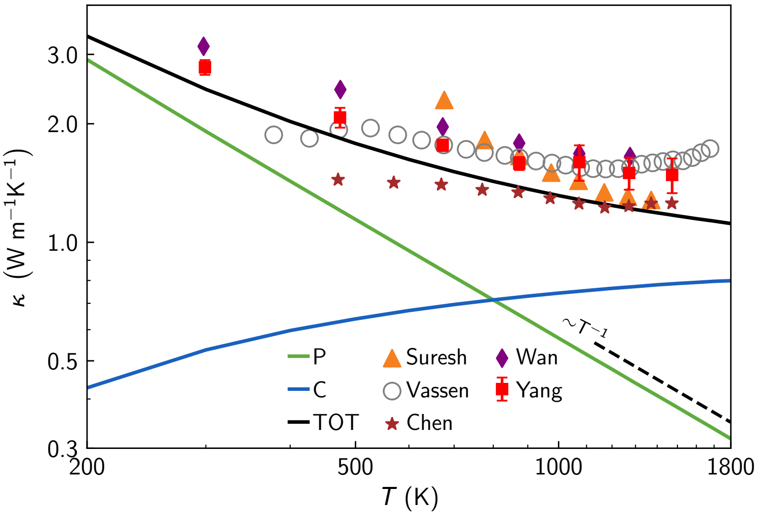

Figure 1.6 – **Bulk thermal conductivity of $La_2Zr_2O_7$.** Scatter points represent measurements from Suresh *et al.* [55], Vassen *et al.* [56], Chen *et al.* [57], Wan *et al.* [58], Yang *et al.* [59] (the experiment which best represents the bulk crystal studied here is that from Yang *et al.*, see text). Green, Peierls' LBTE conductivity ($\kappa_{\rm P}$), which displays the universal T^{-1} asymptotics (dashed line). Blue, coherences' conductivity ($\kappa_{\rm C}$). Black, total conductivity from equation (1.44): $\kappa_{\rm TOT}=\kappa_{\rm P}+\kappa_{\rm C}$ (we report the single independent component of the diagonal and isotropic conductivity tensor).

As anticipated, at low temperature $La_2Zr_2O_7$ behaves as a simple crystal, with the populations (Peierls-Boltzmann) conductivity $\kappa_{\rm P}$ dominating over the coherences conductivity $\kappa_{\rm C}$. Increasing temperature, the Peierls-Boltzmann conductivity decreases following the universal $1/T$ decay [14, 45, 49, 110] — a trend that is in broad disagreement with experiments [55, 56, 57, 58, 59]. The coherences conductivity instead increases with temperature, and becomes dominant at high temperature in the complex-crystal regime, where it offsets the incorrect $1/T$ decay of Peierls' conductivity, leading to a total conductivity ($\kappa_{\rm TOT}=\kappa_{\rm P}+\kappa_{\rm C}$) that is in much closer agreement with experiments. The experimental values of the thermal conductivity of $La_2Zr_2O_7$ reported in Fig. 1.6 can be considered as mainly determined by phonons (lattice thermal conductivity), *i.e.* radiative effects have negligible impact on these values. In particular, the data from Yang *et al.* [59] refer to experimental measurements of the lattice (phonon) contribution to the conductivity of bulk $La_2Zr_2O_7$. Importantly, Yang *et al.* [59] discuss how radiative effects are significantly reduced in sintered composites, and all the other experimental data reported in Fig. 1.6 (Refs. [55, 56, 57, 58]) refer to sintered samples for which radiative effects are suppressed.

Finally, we remark that the smooth phase convention of Wallace is the only one yielding a size-consistent conductivity — thus the convention to be used — and the results reported in Fig. 1.6 have been computed using the Wallace phase convention. For completeness, we discuss in Appendix 1.G how the conductivity changes if the size-inconsistent (wrong) Ziman phase convention is used, showing that the coherences' conductivity at high temperature is overestimated, while the populations' conductivity is not affected by the phase convention adopted (this is clear from Eq. 1.48, which shows that the diagonal elements of the velocity operator that enter in the populations' equation (1.41) are the same in both the Wallace and Ziman phase conventions).

1.7.2 Halide perovskite $CsPbBr_3$

The perovskite $CsPbBr_3$ belongs to a family of ultralow-thermal-conductivity materials promising for thermoelectric energy conversion [46, 111] and it has been used in Ref. [67] to showcase the predictive capabilities of the Wigner-Boltzmann formulation. The temperature-conductivity curve for $CsPbBr_3$ reported in our earlier work [67] was computed using the phase convention of Ziman, which has been shown in Sec. 1.6 to yield size-inconsistent results. Therefore, in this section we update the WBTE predictions for the temperature-conductivity curve of $CsPbBr_3$ using the correct size-consistent Wallace phase convention discussed before. We show in Fig. 1.7 a comparison between the conductivity predicted with the WBTE conductivity formula (1.44) in the smooth phase convention of Wallace and the experimental measurements [111], finding results which are not significantly different from those reported in Ref. [67] (see Appendix 1.G for a detailed analysis on how the x component of the conductivity tensor of $CsPbBr_3$ changes between the size-consistent smooth phase convention of Wallace and the size-inconsistent, step-like phase convention of Ziman). Specifically, Fig. 1.7 shows that at 300 K the populations conductivity contributes just $\sim \frac{1}{3}$ of the total conductivity, while the coherences' term provides an additional $\sim \frac{2}{3}$, leading to a much closer agreement with experiments that becomes even more relevant in the high-temperature asymptotics. Conversely, at low temperature the populations' conductivity becomes dominant, and at 50 K it provides $\sim \frac{3}{4}$ of the total conductivity. It can be seen that in the high-temperature limit $\kappa_{\rm P}^{xx} \propto T^{-1}$, as predicted by Peierls' theory [14, 45, 49, 110]; this in disagreement with experiments. Instead, the WBTE formulation predicts a decay of κ^{xx} much milder than T^{-1}, as shown here for $CsPbBr_3$, and as present in many other complex crystals [45, 47, 48, 49, 50, 112, 113].

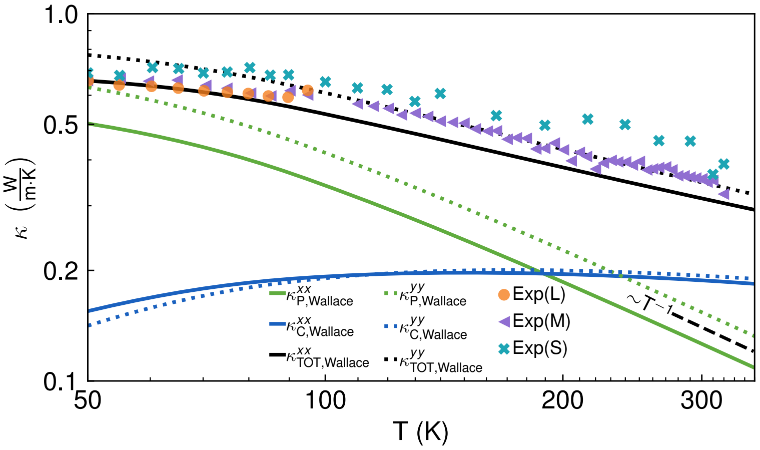

Figure 1.7 – **Bulk thermal conductivity of CsPbBr$_3$ in the smooth (Wallace) phase convention.** "Exp(L)", "Exp(M)" and "Exp(S)" refer to measurements [111] of κ^{xx} in nanowires having respectively sections of 800×380 nm^2, 320×390 nm^2 and 300×160 nm^2: their broad agreement supports the hypothesis of negligible finite-size boundary scattering [111]. Lines are theoretical predictions of the conductivity from equation (1.44) using the smooth phase convention of Wallace, with solid lines referring to the tensor component κ^{xx} (to be compared with experiments), and dotted lines referring to the component κ^{yy} (this last is reported here for completeness and is practically indistinguishable from the not-reported component κ^{zz}). Green, Peierls' LBTE conductivity ($\kappa_{\rm P}$), which displays the universal T^{-1} asymptotics (dashed line) [14, 45, 49, 110]. Blue, coherences' thermal conductivity ($\kappa_{\rm C}$). Black, total conductivity from equation (1.44): $\kappa_{\rm TOT} = \kappa_{\rm P} + \kappa_{\rm C}$.

1.8 Conclusions

In summary, we have derived from the Wigner phase space formulation of quantum mechanics a Wigner-Boltzmann transport equation (1.34) (WBTE) able to account rigorously and simultaneously for the interplay between the quantum Bose-Einstein statistics of atomic vibrations, anharmonicity, and disorder in determining the thermal properties of solids.

We have discussed how the Wigner phase-space framework allows to derive an expression for the microscopic harmonic energy field and the related microscopic harmonic heat flux; such an expression is uniquely defined by the Wigner transform that maps matrix elements of operators into phase-space distributions, and allows to determine the thermal conductivity from the solution of the WBTE. At leading order in the temperature gradient, the solution of the WBTE (1.34) yields a generalized WBTE thermal conductivity (1.44) that is the sum of two terms: a populations conductivity that describes the particle-like intraband propagation of phonons exactly as in the Peierls' LBTE, and a coherences conductivity describing the wave-like interband tunnelling of phonons. We note in passing that the coherences thermal conductivity has some analogies with the Zener interband electrical conductivity [15, 102, 105, 106, 114]; however, thermal transport is fundamentally different from electronic transport since the full phonon spectrum contributes to the heat flux, while only the bands close to the Fermi level contribute to the electronic Zener current. The WBTE conductivity (1.44) reduces to the LBTE conductivity in the limit of a simple crystal [66] (*i.e.* characterized by interband spacings much larger than the linewidths) and to the Allen–Feldman conductivity in the limit of a harmonic glass; most importantly, the WBTE conductivity (1.44) is more general and encompasses all intermediate cases, applying, for example, also to complex crystals and anharmonic glasses, which are characterized by interband spacings smaller than the linewidths.

We have discussed how the coefficients appearing in the WBTE (1.34), and in the WBTE conductivity (1.44) that follows from it, depend on the phase convention adopted, and we have demonstrated that Wallace's [76] smooth phase convention (1.12) yields a size-consistent thermal conductivity and thus is the convention to be used.

The LBTE approach, which accounts for populations only, greatly underestimates the thermal conductivity of the zirconate $La_2Zr_2O_7$ and of the perovskite $CsPbBr_3$, materials belonging to the family of complex crystals [45, 46, 47, 48, 49, 50] that display an ultralow and glass-like thermal conductivity at high-temperature. We have shown that the present approach predicts accurately the temperature-conductivity curves of these complex crystals, both displaying a decay much milder than the universal T^{-1} trend predicted by Peierls' theory (Figs. 1.6,1.7).

It is also worth mentioning that other approaches to describe thermal transport in both crystals and glasses have been proposed relying on the Green-Kubo theory of linear response [115, 116, 117].

We conclude by noting that this novel formulation is relevant for several technological applications, as it will potentially allow to predict the ultralow thermal conductivity of, for example, target materials for thermoelectric energy conversion [46, 113], porous materials for gas-storage technologies [118, 119], materials for thermal barrier coatings[55, 56, 57, 58, 108], and complex crystals used for high temperature piezoelectric transducers [120, 121] (see also Refs. [61, 62, 63, 122, 123] for recent applications of the present framework to materials science).

Appendix

1.A Localization of the bosonic operators in direct space

In this Appendix we investigate the localization of the vibrations created by the bosonic operator $\hat{a}^{\dagger}(\boldsymbol{R})_{b\alpha}$ defined in Eq. (1.7). In particular, we solve a toy model for several choices of the matrix $G_{\boldsymbol{R}b\alpha,\boldsymbol{R}'b'\alpha'}$ (*i.e.* with different decays in direct space). We study how the decay of the matrix $G_{\boldsymbol{R}b\alpha,\boldsymbol{R}'b'\alpha'}$ affects the decay of the matrices $\sqrt[4]{G}_{\boldsymbol{R}b\alpha,\boldsymbol{R}'b'\alpha'}$ and $\sqrt[4]{G^{-1}}_{\boldsymbol{R}b\alpha,\boldsymbol{R}'b'\alpha'}$, which determine the localization of the vibrations created by the operator (1.7).

We consider a one-dimensional chain with Born-von Karman periodic boundary conditions, which contains $N_{\rm c}$ atoms with mass M and spaced by a. The harmonic Hamiltonian of the system is

$$\hat{H}^{\rm har} = \sum_{R'} \frac{\hat{p}^2(R')}{2M} + \frac{M}{2} \sum_{R',R''} \hat{u}(R')\, G(\zeta)_{R',R''}\, \hat{u}(R''), \tag{1.49}$$

where the matrix $G(\zeta)_{R',R''}$ describes a second-order (harmonic) interaction, whose decay depends on the range parameter ζ:

$$G(\zeta)_{R,R'} = \begin{cases} \frac{g}{2} & \text{iff } R{=}R', \\ -\frac{g}{2N_0(\zeta)}\frac{1}{|R-R'|^{\zeta}} & \text{iff } R{\neq}R', \end{cases} \tag{1.50}$$

where $N_0(\zeta) = \frac{1}{N_{\rm c}} \sum_R \sum_{R'\neq R} \frac{1}{|R-R'|^{\zeta}}$ is a generalized Kac prescription [124, 125] that ensures the appropriate scaling of the interaction strength in the thermodynamic limit. For $\zeta = \infty$, Eq. (1.50) yields the case of nearest-neighbor interactions discussed e.g. in the book of Ziman [14]; for a generic ζ, Eq. (1.50) yields the rotor potential of Ref. [125] expanded at second order.

In order to see how the range parameter ζ affects the vibrational properties, we recast the Hamiltonian (1.49) in terms of the Fourier representation of the momentum ($\hat{P}(q) = \frac{1}{\sqrt{M}} \sum_{R''} \hat{p}(R'')e^{-iq\cdot R''}$) and displacement ($\hat{U}(q) = \sqrt{M} \sum_{R''} \hat{u}(R'')e^{+iq\cdot R''}$) operators, obtaining

$$\hat{H}^{\rm har} = \frac{1}{N_{\rm c}} \sum_q \left[\hat{P}^2(q) + \frac{1}{2}\hat{U}(q) D_{\zeta}(q) \hat{U}^{\dagger}(q)\right], \tag{1.51}$$

where $D_\zeta(q)$ is the dynamical matrix

$$D_\zeta(q) = \sum_h G(\zeta)_{h,0} e^{-iq\cdot h}, \tag{1.52}$$

whose square root is the phonon frequency at wavevector q. In figure (1.A.1) we show quantitatively how varying the range parameter ζ affects the decay of the matrix $G(\zeta)_{h,0}$ (which is a simplified model for Eq. (1.4)) in direct space, and the corresponding phonon dispersion relation, for a chain containing 10^4 atoms. A practical way to compute the fourth root of the matrix (1.50) is to take the fourth root of its Fourier transform (1.52) and then transform back to direct space:

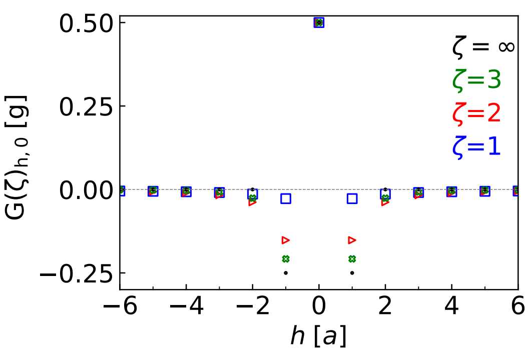

Figure 1.A.1 – **Interatomic force constants in direct space and phonon dispersion relation.** Left: matrix elements of the matrix $G(\zeta)_{h,0}$ as a function of h, for different range parameters ζ. Right: phonon dispersion relation of the Hamiltonian (1.49) for different range parameters ζ. These plots have been computed for a chain containing 10^4 atoms and are converged with respect of the length of the chain.

$$\sqrt[4]{G(\zeta)}_{R,R'} = \frac{1}{N_c}\sum_{q'} \sqrt[4]{D_\zeta(q')}e^{+iq'\cdot(R-R')}. \tag{1.53}$$

In an analogous way, the matrix $\sqrt[4]{G^{-1}(\zeta)}_{R,R'}$ is calculated taking the inverse Fourier transform of the inverse of the fourth root of the dynamical matrix

$$\sqrt[4]{G^{-1}(\zeta)}_{R,R'} = \frac{1}{N_c}\sum_{q'} \frac{1}{\sqrt[4]{D_\zeta(q')}} e^{+iq'\cdot h}, \tag{1.54}$$

where the mesh used for the discrete Fourier transform (1.54) contains an even number of points and is symmetric with respect to the origin (thus it does not contain the point $q=0$ where the frequencies of the dynamical matrix vanish). Therefore, the setup considered here allows to compute numerically the matrices $\sqrt[4]{G(\zeta)}_{R,R'}$, $\sqrt[4]{G^{-1}(\zeta)}_{R,R'}$ for chains having different sizes N_c and different range ζ; now we will proceed with analyzing the localization properties of these matrices as a function of the parameters N_c and ζ.

We plot in the top panel of Fig. 1.A.2 the trend of $\sqrt[4]{G(\zeta)}_{h,0}$ as a function of the distance h and of the range parameter ζ. Our numerical experiment shows that the stronger is the decay of the matrix $G(\zeta)_{h,0} \sim h^{-\zeta}$, the stronger is the decay of its square root $\sqrt[4]{G(\zeta)}_{h,0} \sim h^{-\xi}$. In the top panel of Fig. 1.A.3 we show that when the system's size N_c is increased, the decay exponent ξ tends to converge for all the systems considered, with a slower convergence for the system with $\xi = 1$.

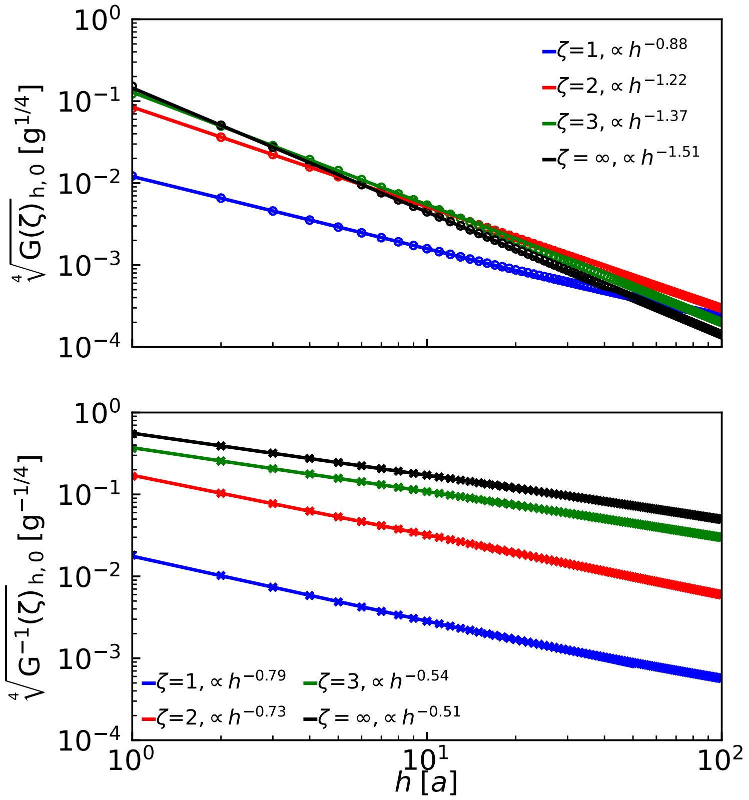

Figure 1.A.2 – **Decays of the matrix elements of $\sqrt[4]{G(\zeta)}_{h,0}$ and $\sqrt[4]{G^{-1}(\zeta)}_{h,0}$.** The slowest decay is found for $\sqrt[4]{G^{-1}(\zeta{=}\infty)}_{h,0}$, which displays a decay $\sim h^{-\frac{1}{2}}$. All these plots have been computed for a chain containing 10^4 atoms.

Concerning the fourth root of the inverse matrix $\sqrt[4]{G^{-1}(\zeta)}_{h,0}$, we plot its trend as a function of the distance h and of the range parameter ζ in the bottom panel of Fig. 1.A.2. In this case, we note that the stronger is the decay of $G(\zeta)_{h,0} \sim h^{-\zeta}$ (*i.e.* the larger is ζ), the slower is the decay of the $\sqrt[4]{G^{-1}(\zeta)}_{h,0} \sim h^{-\chi}$ (*i.e.* the lower is χ). We found that the slower decay occurs for $\zeta = \infty$, for which χ approaches 0.5 as the system's size N_c is increased (see bottom panel of Fig. 1.A.3).

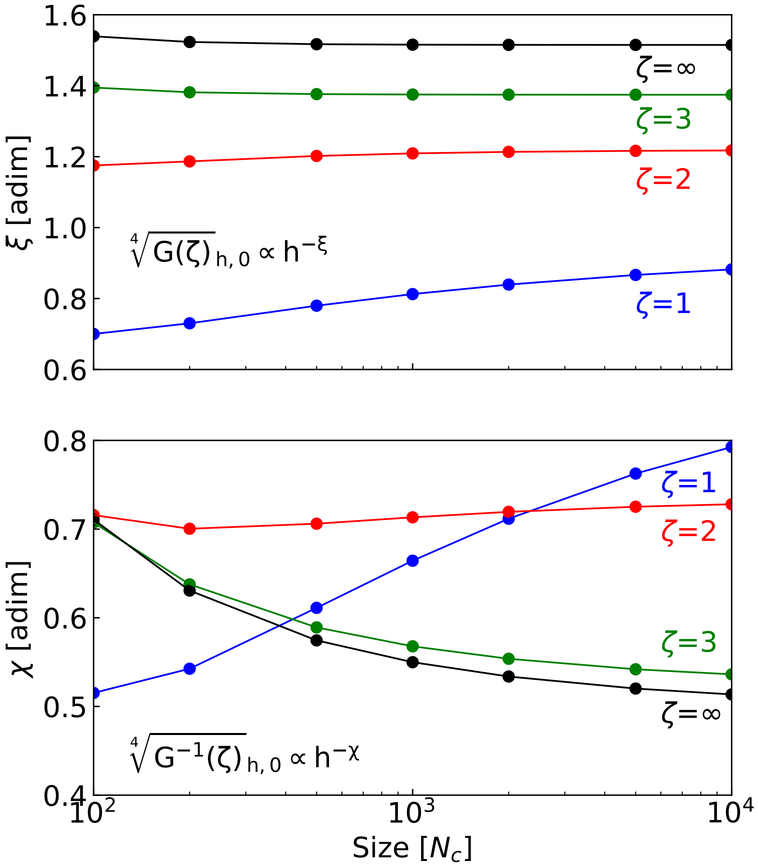

Figure 1.A.3 – **Dependence of the decay exponent on the system size.** Top panel: the stronger is the decay (ζ) of the force constant matrix $G(\zeta)_{h,0}$ (Eq. (1.50)), the stronger is the decay of its fourth root $\sqrt[4]{G(\zeta)}_{h,0}$ (Eq. (1.53)). Bottom panel: the decay of the inverse fourth root matrix $\sqrt[4]{G^{-1}(\zeta)}_{h,0}$ (Eq. (1.54)) is inversely related to the decay of $G(\zeta)_{h,0}$. All these plots have been computed for a chain containing 10^4 atoms.

In conclusion, the present numerical experiment has found that the matrices $\sqrt[4]{G(\zeta)}_{h,0}$, $\sqrt[4]{G^{-1}(\zeta)}_{h,0}$ display a power-law decay in direct space for force constant matrices of the form (1.50) with $\zeta \geq 1$. Therefore, the excitations created by the bosonic operator (1.7) can be considered centered around the position $\boldsymbol{R}+\boldsymbol{\tau}_b$. We also note that in polar insulators, dipole-dipole force constants decay as R^{-3} [126], and in the case of radial symmetry such 3-dimensional case has, due to the presence of the Jacobian R^2, a mathematical behavior analogous to the one-dimensional case with decay $\zeta = 1$.

1.A.1 Localization problems of the phonon-mode basis

In this section we show that the bosonic operators in the phonon-mode basis are not localized in direct space. Specifically, the bosonic operators in the basis of the phonon eigenmodes are obtained applying the unitary transformation that diagonalizes the dynamical matrix (see

Eq. (1.19)) to the Cartesian bosonic operator (1.12),

$$\hat{a}(\boldsymbol{q})_{s'} \quad = \mathscr{E}^{\star}(\boldsymbol{q})_{s',b'\alpha'}\hat{a}(\boldsymbol{q})_{b'\alpha'}. \tag{1.55}$$

The bosonic operator (1.55) does not allow to track the location of vibrations in direct space, due to the phase indeterminacy of the eigenstates $\mathscr{E}(\boldsymbol{q})_{s',b'\alpha'}$ of the dynamical matrix $D(\boldsymbol{q})_{b\alpha,b'\alpha'}$. This becomes apparent considering the following gauge transformation, allowed by the phase freedom on $\mathscr{E}(\boldsymbol{q})_{s',b'\alpha'}$ at each $\boldsymbol{q}$-point:

$$\hat{d}(\boldsymbol{q})_s = \hat{a}(\boldsymbol{q})_s e^{i\boldsymbol{q}\cdot\boldsymbol{R}_\Delta}; \tag{1.56}$$

where $\boldsymbol{R}_\Delta$ is a direct lattice vector. Despite $\hat{d}(\boldsymbol{q})_s$ and $\hat{a}(\boldsymbol{q})_s$ being equivalent for a description in Fourier space, their real space representations are shifted by $\boldsymbol{R}_\Delta$:

$$\begin{aligned} \hat{a}(\boldsymbol{R})_s &= \frac{\mathcal{V}}{(2\pi)^3}\int_{\mathfrak{B}} \hat{a}(\boldsymbol{q})_s e^{+i\boldsymbol{q}\cdot(\boldsymbol{R}+\boldsymbol{\tau}_b)} d^3q; \\ \hat{d}(\boldsymbol{R})_s &= \frac{\mathcal{V}}{(2\pi)^3}\int_{\mathfrak{B}} \hat{d}(\boldsymbol{q})_s e^{+i\boldsymbol{q}\cdot(\boldsymbol{R}+\boldsymbol{\tau}_b)} d^3q = \hat{a}(\boldsymbol{R}+\boldsymbol{R}_\Delta)_s. \end{aligned} \tag{1.57}$$

It is worth mentioning that this mirrors the electronic case, where the phase indeterminacy of the Bloch orbitals is reflected in the non-uniqueness of the transformation into Wannier functions [127]. In this work, the use of the Cartesian basis renders the real space description and hence the Wigner distribution (1.25,1.27) well-defined. We note in passing that Bamler [128] has highlighted similar localization problems that emerge when one attempts to define the Wigner distribution for electron using the Bloch basis (e.g. Refs. [129, 130, 131, 132]). Specifically, in the electronic case the phase freedom in the Bloch basis for electrons plays a role analogous to the phase freedom of the eigenstates of the dynamical matrix discussed in this appendix.

1.B Lindblad master equation

1.B.1 Evolution of the many-body density matrix

In this section we derive Eq. (1.23), which governs the evolution of the open system discussed in Sec. 1.3.2 and sketched in Fig. 1.1. We treat $\hat{H}^{\mathrm{per}}$ as a perturbation of $\hat{H}^{\mathrm{har}}$ (*i.e.*, $\mathrm{Tr}(\hat{\rho}\hat{H}^{\mathrm{har}}) \gg \mathrm{Tr}(\hat{\rho}\hat{H}^{\mathrm{per}})$), and we assume that the interactions between the solid subsystem S and the thermal reservoirs (which will be considered explicitly later imposing suitable boundary conditions) imply an irreversible evolution for S, with the temporal correlation function of any excitation in S decaying after a time of the order of the transit time across the system [33, 80].

Interaction picture

To decouple the different time scales in the problem, it is useful to work in the interaction picture [82]. Given the time-evolution operator of the leading Hamiltonian $\hat{H}^{\rm har}$, $\hat{\mathscr{U}}_0(t,t_0){=}e^{-\frac{i}{\hbar}\hat{H}^{\rm har}\cdot(t-t_0)}$, the interaction representation of an operator $\hat{A}$ is [133] $\hat{A}_I(t)=\hat{\mathscr{U}}_0^{\dagger}(t,t_0)\hat{A}(t)\hat{\mathscr{U}}_0(t,t_0)$. Applying this transformation to the evolution equation for the density matrix $\frac{{\rm d}\hat{\rho}}{{\rm d}t}{=}{-}\frac{i}{\hbar}\big[\hat{H}^{\rm har}{+}\hat{H}^{\rm per},\hat{\rho}\big]$, one obtains

$$\frac{{\rm d}\hat{\rho}_I(t)}{{\rm d}t}=-\frac{i}{\hbar}\Big[\hat{H}_I^{\rm per}(t),\hat{\rho}_I(t)\Big], \tag{1.58}$$

where $\hat{\rho}_I(t){=}\hat{\mathscr{U}}_0^{\dagger}(t,t_0)\hat{\rho}(t)\hat{\mathscr{U}}_0(t,t_0)$ and $\hat{H}_I^{\rm per}(t){=}\hat{\mathscr{U}}_0^{\dagger}(t,t_0)\hat{H}^{\rm per}\hat{\mathscr{U}}_0(t,t_0)$ are the interaction representations of the density matrix and perturbative Hamiltonian. Eq. (1.58) can be recast into the integro-differential form often used in the literature [82, 134] to expose the different time scales of the problem. Such an integro-differential evolution equation for the density matrix in the interaction picture is obtained first integrating Eq. (1.58) from t_0 to t,

$$\hat{\rho}_I(t)=\hat{\rho}_I(t_0)-\frac{i}{\hbar}\int_{t_0}^{t}\Big[\hat{H}_I^{\rm per}(t'),\hat{\rho}_I(t')\Big]dt', \tag{1.59}$$

and then inserting Eq. (1.59) into Eq. (1.58):

$$\frac{{\rm d}\hat{\rho}_I(t)}{{\rm d}t}=-\frac{1}{\hbar^2}\int_{t_0}^{t}\Big[\hat{H}_I^{\rm per}(t),\Big[\hat{H}_I^{\rm per}(t'),\hat{\rho}_I(t')\Big]\Big]dt'; \tag{1.60}$$

where the term $-\frac{i}{\hbar}\big[\hat{H}_I^{\rm per}(t),\hat{\rho}_I(t_0)\big]{=}0$ can be discarded under the assumption that the initial state of the system is a pure state of $\hat{H}^{\rm har}$ [82, 134]. Eq. (1.60) has the same physical content of Eq. (1.58), and we will show later that it has the advantage of exposing the different time scales of the problem, thus it is more convenient to perform approximations that simplify the formulation while capturing the relevant physics.

Different time scales of the problem

In the previous section we have seen that the evolution of the perturbation Hamiltonian in the interaction picture from time t_0 to time t ($\hat{H}_I^{\rm per}(t)$), is determined by the evolution operator $\hat{\mathscr{U}}_0(t,t_0)$, since the perturbation Hamiltonian in the Schrödinger picture $\hat{H}^{\rm per}$ does not depend on time. With the aim of comparing the evolution time scale of $\hat{H}_I^{\rm per}(t)$ with that of $\hat{\rho}_I(t)$, we look for the time-evolution operator $\hat{\mathscr{U}}'(t,t_0)$ that describes the time evolution of the density matrix in the interaction picture from time t_0 to time t, *i.e.* $\hat{\rho}_I(t){=}\hat{\mathscr{U}}'(t,t_0)\hat{\rho}_I(t_0)\hat{\mathscr{U}}'^{\dagger}(t,t_0)$ (we recall that $\hat{\rho}(t_0){=}\hat{\rho}_I(t_0)$). Substituting this expression into Eq. (1.58), we obtain the equation that determines $\hat{\mathscr{U}}'(t,t_0)$:

$$i\hbar\frac{\partial\hat{\mathscr{U}}'(t,t_0)}{\partial t}=\hat{H}_I^{\rm per}(t)\hat{\mathscr{U}}'(t,t_0). \tag{1.61}$$

Eq. (1.61) can be integrated on both sides yielding

$$\hat{\mathscr{U}}'(t,t_0) = \hat{1} - \frac{i}{\hbar}\int_{t_0}^{t} \hat{H}_I^{\text{per}}(t')\hat{\mathscr{U}}'(t',t_0)dt', \tag{1.62}$$

and then substituting equation (1.62) recursively into itself one obtains [134]:

$$\begin{aligned}\hat{\mathscr{U}}'(t,t_0)=\hat{1}-\frac{i}{\hbar}\int_{t_0}^{t}\hat{H}_I^{\text{per}}(t')dt'\\ -\frac{1}{\hbar^2}\int_{t_0}^{t}\hat{H}_I^{\text{per}}(t')\int_{t_0}^{t'}\hat{H}_I^{\text{per}}(t'')\hat{\mathscr{U}}(t'',t_0)dt''dt'+\ldots\end{aligned} \tag{1.63}$$

Now we notice that in the interaction picture, the evolution time scale of the density-matrix operator $\hat{\rho}_I(t)$ is much slower than that of the perturbation Hamiltonian $\hat{H}_I^{\text{per}}(t')$. In fact, $\hat{\rho}_I(t) = \hat{\mathscr{U}}'(t,t_0)\hat{\rho}_I(t_0)\hat{\mathscr{U}}'^{\dagger}(t,t_0)$, *i.e.* $\hat{\rho}_I(t)$ has oscillation frequencies that are set by the energy scale of the perturbative Hamiltonian; in contrast, $\hat{H}_I^{\text{per}}(t) = \hat{\mathscr{U}}_0^{\dagger}(t,t_0)\hat{H}^{\text{per}}\hat{\mathscr{U}}_0(t,t_0)$ has oscillation frequencies determined by the dominant Hamiltonian $\hat{H}^{\text{har}}$. Since the typical energy scale of the dominant Hamiltonian is larger than that of the perturbation, $\text{Tr}(\hat{\rho}\hat{H}^{\text{har}}) \gg \text{Tr}(\hat{\rho}\hat{H}^{\text{per}})$, the time scale $\mathscr{T}_\rho$ over which $\hat{\rho}_I(t)$ varies significantly is much slower than the time scale $\mathscr{T}_{\text{per}}$ over which $\hat{H}_I^{\text{per}}(t)$ varies significantly, $\mathscr{T}_\rho \gg \mathscr{T}_{\text{per}}$.

Markov approximation in Lindblad form

The different time scales of the problem discussed in Sec. 1.B.1 can be exploited to simplify Eq. (1.60). Following the procedure detailed in Refs. [81, 82, 92], we consider a time interval Δt such that $\mathscr{T}_{\text{per}} \ll \Delta t \ll \mathscr{T}_\rho$, *i.e.* that is much larger than the typical time scale of variation of $\hat{H}_I^{\text{per}}(t)$ and much smaller than the time scale of variation of $\hat{\rho}_I(t)$. Then, we compute the integral average of Eq. (1.60), integrating it on both sides over the time interval Δt and starting from a generic time $\tilde{t}$, obtaining

$$\frac{1}{\Delta t}\int_{\tilde{t}}^{\tilde{t}+\Delta t}\frac{d\hat{\rho}_I(t'')}{dt''}dt'' = \frac{\hat{\rho}_I(\tilde{t}+\Delta t)-\hat{\rho}_I(\tilde{t})}{\Delta t} = -\frac{1}{\Delta t}\int_{\tilde{t}}^{\tilde{t}+\Delta t}\frac{1}{\hbar^2}\int_{t_0}^{t''}\Big[\hat{H}_I^{\text{per}}(t''),\big[\hat{H}_I^{\text{per}}(t'),\hat{\rho}_I(t')\big]\Big]dt'dt''. \tag{1.64}$$

Now we can perform the center-of-mass change of variable, that is we recast Eq. (1.64) in terms of the average time $\bar{t} = \frac{t'+t''}{2}$, and of the displacement time $\breve{t}=t''-t'$:

$$\frac{\hat{\rho}_I(\tilde{t}+\Delta t)-\hat{\rho}_I(\tilde{t})}{\Delta t} = -\frac{1}{\Delta t}\int_{\frac{\tilde{t}+t_0}{2}}^{\tilde{t}+\Delta t}\frac{1}{\hbar^2}\int_{I(\bar{t})}\Big[\hat{H}_I^{\text{per}}(\bar{t}+\tfrac{\breve{t}}{2}),\big[\hat{H}_I^{\text{per}}(\bar{t}-\tfrac{\breve{t}}{2}),\hat{\rho}_I(\bar{t}-\tfrac{\breve{t}}{2})\big]\Big]d\breve{t}d\bar{t}, \tag{1.65}$$

where $I(\bar{t})$ is the integration domain for the displacement time $\breve{t}$ and depends on the average time $\bar{t}$ [82, 92]. The term on the left-hand-side of Eq. (1.65) is called “coarse-grained” rate of variation [92], since it is the integral average of the derivative $\frac{d\hat{\rho}_I}{dt''}$ over the interval Δt.

Eq. (1.65) has a form that allows us to perform on it the Markov approximation in Lindblad form [81, 92]. Specifically, this consists in: (i) approximating time variations of the integrand as originating exclusively from time variations of $\hat{H}_I^{\text{per}}(t)$ (as discussed in Sec. 1.B.1, these are much faster than those of $\hat{\rho}_I(t)$), *i.e.* approximating $\hat{\rho}_I(\bar{t}-\frac{\breve{t}}{2}) \approx \hat{\rho}_I(\bar{t})$ inside the integral in Eq. (1.65); (ii) approximating the coarse-grained derivative at the left member of Eq. (1.65) as not being sensitive to the time interval over which the average is performed, *i.e.* $\frac{\hat{\rho}_I(\tilde{t}+\Delta t)-\hat{\rho}_I(\tilde{t})}{\Delta t}=\frac{1}{\Delta t}\int_{\tilde{t}}^{\tilde{t}+\Delta t}\frac{d\hat{\rho}_I(\bar{t})}{d\bar{t}}d\bar{t} \approx \frac{1}{\Delta t}\int_{\frac{\tilde{t}+t_0}{2}}^{\tilde{t}+\Delta t}\frac{d\hat{\rho}_I(\bar{t})}{d\bar{t}}d\bar{t}$. Therefore, performing the Markov approximation in Lindblad form on Eq. (1.65) yields and equation in which the future state of the density matrix is completely determined by the present state of the density matrix [81]:

$$\frac{d\hat{\rho}_I(\bar{t})}{d\bar{t}}=-\frac{1}{\hbar^2}\int_{I(\bar{t})}\Big[\hat{H}_I^{\text{per}}(\bar{t}+\tfrac{\breve{t}}{2}),[\hat{H}_I^{\text{per}}(\bar{t}-\tfrac{\breve{t}}{2}),\hat{\rho}_I(\bar{t})]\Big]d\breve{t}. \tag{1.66}$$

Then, as explained in Ref. [81], the integration domain of Eq. (1.66) can be symmetrized and extended to infinity, provided one introduces in Eq. (1.66) a Gaussian correlation function $e^{-\breve{t}^2/(2\cdot\mathcal{T}_c^2)}$ whose width $\mathcal{T}_c$ might be regarded as a safe overestimation of the collision duration, which is typically shorter than the macroscopic evolution time scale ($\mathcal{T}_c \ll \Delta t \sim I(\bar{t})$):

$$\frac{d\hat{\rho}_I(\bar{t})}{d\bar{t}}=-\frac{1}{2\hbar^2}\int_{-\infty}^{\infty}e^{-\breve{t}^2/(2\cdot\mathcal{T}_c^2)}\Big[\hat{H}_I^{\text{per}}(\bar{t}+\tfrac{\breve{t}}{2}),[\hat{H}_I^{\text{per}}(\bar{t}-\tfrac{\breve{t}}{2}),\hat{\rho}_I(\bar{t})]\Big]d\breve{t}. \tag{1.67}$$

The final step to obtain a dynamical map of Lindblad type (*i.e.* which preserves the trace and the positive definiteness of the density matrix [81, 82]) consists in exploiting again the different time scales of the problem to symmetrize Eq. (1.67). Specifically, we perform a "temporal coarse graining" [81], *i.e.* a time average over a microscopic time scale over which $\hat{\rho}_I(\bar{t})$ can be considered constant (we note in passing that the approximation of averaging the rapidly oscillating terms in the master equation in order to obtain a Lindblad dynamical map is also known as "rotating wave approximation" [82]). In practice, such a temporal coarse graining is performed using a Gaussian distribution having variance $(\mathcal{T}_c/2)^2$ as follows [81]:

$$\frac{d\hat{\rho}_I(t)}{dt}=-\frac{1}{2\hbar^2}\frac{1}{\sqrt{2\pi}(\mathcal{T}_c/2)}\int_{-\infty}^{\infty}e^{-\frac{t''^2}{2(\mathcal{T}_c/2)^2}}\int_{-\infty}^{\infty}e^{-\frac{t'^2}{2\cdot\mathcal{T}_c^2}}\Big[\hat{H}_I^{\text{per}}(t+t''+\tfrac{t'}{2}),[\hat{H}_I^{\text{per}}(t+t''-\tfrac{t'}{2}),\hat{\rho}_I(t)]\Big]dt'dt'', \tag{1.68}$$

where we have simplified the notation renaming the variables $\bar{t} \to t$, $\breve{t} \to t'$ (and the integration over t'' is necessary to perform the temporal coarse-graining).

We now go back to the Schrödinger picture applying the transformation
$\hat{\rho}(t)=\hat{\mathcal{U}}_0(t,t_0)\hat{\rho}_I(t)\hat{\mathcal{U}}_0^{\dagger}(t,t_0)$ to Eq. (1.68), obtaining

$$\frac{\partial\hat{\rho}(t)}{\partial t}+\frac{i}{\hbar}\Big[\hat{H}^{\text{har}},\hat{\rho}(t)\Big]=-\frac{1}{2}\Big[\hat{\mathcal{L}},[\hat{\mathcal{L}},\hat{\rho}(t)]\Big], \tag{1.69}$$

where we have defined:

$$\hat{\mathscr{L}} = \frac{1}{\hbar}\sqrt[4]{\frac{2}{\pi \mathscr{T}_c^2}}\int_{-\infty}^{+\infty} e^{+\frac{i}{\hbar}\hat{H}^{\text{har}}\cdot t'}\,\hat{H}^{\text{per}}e^{-\frac{i}{\hbar}\hat{H}^{\text{har}}\cdot t'}\,e^{-t'^2/\mathscr{T}_c^2}\,dt'. \tag{1.70}$$

In conclusion, Eq. (1.69) is Eq. (1.23) of the main text, with $\frac{\partial \hat{\rho}(t)}{\partial t}\big|_{\hat{H}^{\text{per}}} = -\frac{1}{2}\big[\hat{\mathscr{L}},[\hat{\mathscr{L}},\hat{\rho}\,(t)]\big]$.

1.B.2 Evolution of the one-body density matrix

Eq. (1.24) can be derived straightforwardly from equation (1.23) by applying the operator $\hat{a}^\dagger(\boldsymbol{q}')_{b'\alpha'}\,\hat{a}(\boldsymbol{q})_{b\alpha}$ on both sides, exploiting the bosonic commutation relation and taking the trace. Alternatively, one can derive the same equation starting from direct space and then taking the Fourier transform (1.22), as we will show here.

As a first step we apply the operator $\hat{a}^\dagger(\boldsymbol{R}')_{b'\alpha'}\hat{a}(\boldsymbol{R})_{b\alpha}$ on equation (1.69), and then we take the trace. Such a procedure yields and equation for the one-body density matrix (1.10), where the time derivative of the many-body density matrix in Eq. (1.69) becomes the time derivative for the one-body density matrix, and the commutator in Eq. (1.69) becomes

$$\begin{aligned}
&\frac{i}{\hbar}\text{Tr}\big([\hat{H}^{\text{har}},\hat{\rho}]\,\hat{a}^\dagger(\boldsymbol{R}')_{b'\alpha'}\,\hat{a}(\boldsymbol{R})_{b\alpha}\big)\\
&= i\text{Tr}\sum_{\hat{\boldsymbol{R}},\tilde{\boldsymbol{R}}}\sqrt{G}_{\hat{\boldsymbol{R}}\hat{b}\hat{\alpha},\tilde{\boldsymbol{R}}\tilde{b}\tilde{\alpha}}\Big(\hat{a}^\dagger(\boldsymbol{R}')_{b'\alpha'}\,\hat{a}(\boldsymbol{R})_{b\alpha}\,\hat{a}^\dagger(\hat{\boldsymbol{R}})_{\hat{b}\hat{\alpha}}\,\hat{a}(\tilde{\boldsymbol{R}})_{\tilde{b}\tilde{\alpha}} - \hat{a}^\dagger(\hat{\boldsymbol{R}})_{\hat{b}\hat{\alpha}}\,\hat{a}(\tilde{\boldsymbol{R}})_{\tilde{b}\tilde{\alpha}}\,\hat{a}^\dagger(\boldsymbol{R}')_{b'\alpha'}\,\hat{a}(\boldsymbol{R})_{b\alpha}\Big)\hat{\rho},
\end{aligned} \tag{1.71}$$

where we have used the cyclic property of the trace. Exploiting the commutation relations (1.8), we obtain the evolution equation for the one-body density matrix

$$\begin{aligned}
&\frac{\partial}{\partial t}\varrho(\boldsymbol{R},\boldsymbol{R}')_{b\alpha,b'\alpha'} + i\sum_{\hat{\boldsymbol{R}}}\Big[\sqrt[2]{G}_{\boldsymbol{R}b\alpha,\hat{\boldsymbol{R}}\hat{b}\hat{\alpha}}\,\varrho(\hat{\boldsymbol{R}},\boldsymbol{R}')_{\hat{b}\hat{\alpha},b'\alpha'} - \varrho(\boldsymbol{R},\hat{\boldsymbol{R}})_{b\alpha,\hat{b}\hat{\alpha}}\sqrt[2]{G}_{\hat{\boldsymbol{R}}\hat{b}\hat{\alpha},\boldsymbol{R}'b'\alpha'}\Big]\\
&= -\text{Tr}\bigg(\frac{1}{2}\Big[\hat{\mathscr{L}},\big[\hat{\mathscr{L}},\hat{\rho}\,(t)\big]\Big]\,\hat{a}^\dagger(\boldsymbol{R}')_{b'\alpha'}\,\hat{a}(\boldsymbol{R})_{b\alpha}\bigg).
\end{aligned} \tag{1.72}$$

Recasting Eq. (1.72) using the Fourier transform (1.12), one obtains the evolution equation (1.24) for the one-body density matrix in reciprocal space, where the collision superoperator in Fourier space reads

$$\frac{\partial}{\partial t}\varrho\big(\boldsymbol{q}+\tfrac{\boldsymbol{q}''}{2},\boldsymbol{q}-\tfrac{\boldsymbol{q}''}{2}\big)_{b\alpha,b'\alpha'}\Big|_{\hat{H}^{\text{per}}} = -\frac{1}{2}\text{Tr}\Big(\Big[\hat{\mathscr{L}},\big[\hat{\mathscr{L}},\hat{\rho}\,(t)\big]\Big]\,\hat{a}^\dagger\big(\boldsymbol{q}-\tfrac{\boldsymbol{q}''}{2}\big)_{b'\alpha'}\,\hat{a}\big(\boldsymbol{q}+\tfrac{\boldsymbol{q}''}{2}\big)_{b\alpha}\Big), \tag{1.73}$$

and will be evaluated in the next section.

1.C Collision superoperator for vibrations

In this Appendix we discuss how to account for phonon scattering due to third-order anharmonicity or to the presence of isotopes on several levels. In Sec. 1.C.1, we discuss the key ideas underlying the derivation of the collision superoperator appearing in the many-body Lindblad equation (1.23). Then, in Sec. 1.C.2 we report the detailed calculations for the linearized collision superoperator for the one-body density matrix in the spatially-homogeneous regime. Finally, in Sec. 1.C.3 we rely on the reasoning detailed in Ref. [91] to extend the collision superoperator for the one-body density matrix in the spatially-homogeneous regime to the deviation from equilibrium (linear in the temperature gradient) of the Wigner distribution.

1.C.1 Phonon collisions at the many-body level

We start by discussing the form of the collision superoperator that appears in the equation for the many-body density matrix (1.23,1.68). Such an equation is exact at the Markovian level and invariant under change of basis (we recall that the preferential choice of the basis discussed in Sec. 1.4.2 is relevant only when approximations involving differentiation of matrix elements are performed); to discuss scattering it is useful to recast it in the Fock-space basis formed by the eigenstates of the Harmonic Hamiltonian (1.18). To this aim, we start by recasting the harmonic Hamiltonian (1.18) in terms of the bosonic operators (1.55) in the phonon-mode basis, obtaining:

$$\hat{H}^{\text{har}}=\frac{\mathcal{V}}{(2\pi)^3}\int_{\mathfrak{B}}\sum_{s}\hbar\omega(\boldsymbol{q})_s\big[\hat{a}^{\dagger}(\boldsymbol{q})_s\hat{a}(\boldsymbol{q})_s+\tfrac{1}{2}\big]d^3q, \tag{1.74}$$

The many-body eigenstates of the Hamiltonian (1.74) have the form

$$\big|\boldsymbol{\mu}\rangle=\big|n(\boldsymbol{\mu})_{\boldsymbol{q}_1s_1},n(\boldsymbol{\mu})_{\boldsymbol{q}_2s_2},\dots,n(\boldsymbol{\mu})_{\boldsymbol{q}_ms_m},\dots\rangle\,, \tag{1.75}$$

and $n(\boldsymbol{\mu})_{\boldsymbol{q}_1s_1}$ is the occupation number of the state having wavevector $\boldsymbol{q}_1$ and mode s_1. The many-body states (1.75) are generated starting from the vacuum state using the adjoint of the bosonic operators (1.55) as follows:

$$\hat{a}^{\dagger}(\boldsymbol{q})_s\big|\dots,n(\boldsymbol{\mu})_{\boldsymbol{q}s},\dots\rangle=\sqrt{\frac{(2\pi)^3}{\mathcal{V}}}\sqrt{n(\boldsymbol{\mu})_{\boldsymbol{q}s}+1}\big|\dots,n(\boldsymbol{\mu})_{\boldsymbol{q}s}+1,\dots\rangle. \tag{1.76}$$

where the prefactor $\sqrt{\frac{(2\pi)^3}{\mathcal{V}}}$ follows from the bosonic commutation relation (1.12).

The eigenvalue corresponding to the eigenstate (1.75) is denoted as follows

$$\begin{aligned}\hat{H}^{\text{har}}\big|\boldsymbol{\mu}\rangle&=\left[\frac{\mathcal{V}}{(2\pi)^3}\int_{\mathfrak{B}}\sum_{s}\hbar\omega(\boldsymbol{q})_s n(\boldsymbol{\mu})_{\boldsymbol{q}s}d^3q+E_0\right]\big|\boldsymbol{\mu}\rangle\\&=\big[\hbar\omega(\boldsymbol{\mu})+E_0\big]\big|\boldsymbol{\mu}\rangle\end{aligned} \tag{1.77}$$

where E_0 is the vacuum energy discussed below Eq. (1.11), and we have denoted with $\hbar\omega(\boldsymbol{\mu})$ the energy originating from the excitations in the eigenstate $|\boldsymbol{\mu}\rangle$.

Here we want to discuss the general form of the collision superoperator appearing in Eq. (1.68), the details which depend on the particular form of $\hat{H}^{\text{per}}$ will be discussed in the next section. We start by evaluating the operator (1.70) that appears in the collision superoperator of Eq. (1.69). Expanding the double commutator and computing the matrix elements with respect to the Fock basis (1.75), one obtains

$$\left.\frac{\partial \rho(t)_{\boldsymbol{\mu}\boldsymbol{\nu}}}{\partial t}\right|_{\hat{H}^{\text{per}}} = \sum_{\boldsymbol{\iota},\boldsymbol{\lambda}} \left(\mathscr{L}_{\boldsymbol{\mu}\boldsymbol{\iota}} \rho_{\boldsymbol{\iota}\boldsymbol{\lambda}} \mathscr{L}_{\boldsymbol{\lambda}\boldsymbol{\nu}} - \frac{\mathscr{L}_{\boldsymbol{\mu}\boldsymbol{\iota}} \mathscr{L}_{\boldsymbol{\iota}\boldsymbol{\lambda}} \rho_{\boldsymbol{\lambda}\boldsymbol{\nu}} + \rho_{\boldsymbol{\mu}\boldsymbol{\iota}} \mathscr{L}_{\boldsymbol{\iota}\boldsymbol{\lambda}} \mathscr{L}_{\boldsymbol{\lambda}\boldsymbol{\nu}}}{2} \right), \tag{1.78}$$

where the matrix elements $\mathscr{L}_{\boldsymbol{\mu}\boldsymbol{\iota}}$ are

$$\begin{aligned} \mathscr{L}_{\boldsymbol{\mu}\boldsymbol{\iota}} &= \frac{1}{\hbar} \sqrt[4]{\frac{2}{\pi \mathscr{T}_c^2}} \int_{-\infty}^{+\infty} e^{+i[\omega(\boldsymbol{\mu})-\omega(\boldsymbol{\iota})]\,t'} \langle \boldsymbol{\mu} | \hat{H}^{\text{per}} | \boldsymbol{\iota} \rangle e^{-t'^2/\mathscr{T}_c^2} \, dt' \\ &= \frac{1}{\hbar} \sqrt[4]{2\pi \mathscr{T}_c^2} \exp\left[-\frac{[\omega(\boldsymbol{\mu})-\omega(\boldsymbol{\iota})]^2}{2(\sqrt{2}/\mathscr{T}_c)^2} \right] \langle \boldsymbol{\mu} | \hat{H}^{\text{per}} | \boldsymbol{\iota} \rangle. \end{aligned} \tag{1.79}$$

From Eq. (1.79) it follows that:

$$\mathscr{L}_{\boldsymbol{\mu}\boldsymbol{\iota}} \mathscr{L}_{\boldsymbol{\lambda}\boldsymbol{\nu}} = \frac{2\pi}{\hbar} \langle \boldsymbol{\mu} | \hat{H}^{\text{per}} | \boldsymbol{\iota} \rangle \langle \boldsymbol{\lambda} | \hat{H}^{\text{per}} | \boldsymbol{\nu} \rangle \frac{1}{\sqrt{2\pi}\Delta_\epsilon} \exp\left[-\frac{1}{2\Delta_\epsilon^2} \frac{[\hbar\omega(\boldsymbol{\mu})-\hbar\omega(\boldsymbol{\iota})]^2 + [\hbar\omega(\boldsymbol{\lambda})-\hbar\omega(\boldsymbol{\nu})]^2}{2} \right], \tag{1.80}$$

where $\Delta_\epsilon = \hbar/\mathscr{T}_c$ is the energy uncertainty in the collision allowed by the temporal coarse-graining performed in Eq. (1.68). Here we consider the completed-collision limit $\Delta_\epsilon \to 0$, and assuming that $(\boldsymbol{\iota} \neq \boldsymbol{\lambda}, \boldsymbol{\mu} \neq \boldsymbol{\nu}) \Rightarrow |\omega(\boldsymbol{\mu})-\omega(\boldsymbol{\iota})| \neq |\omega(\boldsymbol{\lambda})-\omega(\boldsymbol{\nu})|$, we have that Eq. (1.80) yields the Fermi-golden-rule rate [81] $\mathscr{P}_{\boldsymbol{\iota}}^{\boldsymbol{\mu}} = \mathscr{P}_{\boldsymbol{\mu}}^{\boldsymbol{\iota}}$:

$$\begin{aligned} \mathscr{L}_{\boldsymbol{\mu}\boldsymbol{\iota}} \mathscr{L}_{\boldsymbol{\lambda}\boldsymbol{\nu}} &= \frac{2\pi}{\hbar} \left| \langle \boldsymbol{\mu} | \hat{H}^{\text{per}} | \boldsymbol{\iota} \rangle \right|^2 \delta\big(\hbar\omega(\boldsymbol{\mu})-\hbar\omega(\boldsymbol{\iota})\big) \delta_{\boldsymbol{\iota},\boldsymbol{\lambda}} \delta_{\boldsymbol{\mu},\boldsymbol{\nu}} \\ &= \mathscr{P}_{\boldsymbol{\iota}}^{\boldsymbol{\mu}} \delta_{\boldsymbol{\iota},\boldsymbol{\lambda}} \delta_{\boldsymbol{\mu},\boldsymbol{\nu}}. \end{aligned} \tag{1.81}$$

Inserting Eq. (1.81) into Eq. (1.78) yields

$$\left.\frac{\mathrm{d}\rho(t)_{\boldsymbol{\mu}\boldsymbol{\nu}}}{\mathrm{d}t}\right|_{\hat{H}^{\text{per}}} = +\,\delta_{\boldsymbol{\mu},\boldsymbol{\nu}} \sum_{\boldsymbol{\iota}} \mathscr{P}_{\boldsymbol{\iota}}^{\boldsymbol{\mu}} \rho_{\boldsymbol{\iota}\boldsymbol{\iota}} - \sum_{\boldsymbol{\iota}} \frac{\mathscr{P}_{\boldsymbol{\iota}}^{\boldsymbol{\mu}} + \mathscr{P}_{\boldsymbol{\iota}}^{\boldsymbol{\nu}}}{2} \rho_{\boldsymbol{\mu}\boldsymbol{\nu}}. \tag{1.82}$$

Eq. (1.82) shows that in the aforementioned “completed-collision limit” the scattering of populations ($\boldsymbol{\mu}=\boldsymbol{\nu}$) and coherences ($\boldsymbol{\mu}\neq\boldsymbol{\nu}$) are independent: populations scatter only with populations, and coherences scatter only with coherences. Then, since the rates (1.81) are non negative, one can identify in Eq. (1.78) two collision mechanisms: a pumping mechanism that increases (plus sign) the elements of the density matrix operator, and a depumping mechanism (minus sign) that decreases the elements of the density matrix operator. Importantly, in the completed-collision limit, coherences $\boldsymbol{\mu}\neq\boldsymbol{\nu}$ are characterized by depumping only. This demonstrates that collisions do not create but only destroy off-diagonal coherences, and thus drive the density matrix towards the diagonal equilibrium form (*i.e.* the diagonal Bose-Einstein density matrix that maximizes the entropy [135]). Such an evolution towards the equilibrium (maximum entropy) density matrix can be also related to the non-negative entropy production rate that characterizes the irreversible Markovian dynamics of the Lindblad equation (1.23) [82].

1.C.2 Linearized collision superoperator for the one-body density matrix

In this section we discuss how to derive a linear collision superoperator for the one-body density matrix, which accounts for third-order anharmonicity and isotopic scattering.

We are interested in the close-to-equilibrium regime where a homogeneous temperature gradient drives heat conduction. Since the temperature gradient ∇T is constant in space, the response to it is translation-invariant and thus local in $\boldsymbol{q}$, this in analogy with the response of electrons to an homogeneous electric field [91, 136]. In this regime, the many-body density matrix in the Fock basis (1.75) is close to the diagonal Bose-Einstein distribution $\overline{N}(\boldsymbol{q})_s$, and it can be expanded as follows:

$$\begin{aligned}\hat{\rho} =&\big|...,\overline{N}(\boldsymbol{q})_s,...\big\rangle\big\langle...,\overline{N}(\boldsymbol{q})_s,...\big|+\\ &\big|...,\bar{n}(\boldsymbol{q})_s,...\big\rangle\big\langle...,\bar{n}(\boldsymbol{q}')_s,...\big|+\\ &\big|...,\vec{n}^{(1)}(\boldsymbol{q})_s{\cdot}\nabla T,...\big\rangle\big\langle...,\vec{n}^{(1)}(\boldsymbol{q})_{s'}{\cdot}\nabla T,...\big|+\mathscr{O}(\mathrm{MB},\nabla T^2).\end{aligned} \tag{1.83}$$

The first term in Eq. (1.83) is the diagonal Bose-Einstein equilibrium distribution; the second term is non diagonal in the wavevectors and diagonal in the eigenmodes indexes, and accounts for the local-equilibrium (space-dependent) temperature [24]; the third term describes the response to a homogeneous temperature gradient (since the temperature gradient ∇T is constant in space, the response to it is translation-invariant and thus yields a many-body density matrix diagonal in $\boldsymbol{q}$); the remaining terms includes many-body correlations or perturbations of order higher-than-first in the small temperature gradient.

From the expansion (1.83) for the many-body density matrix, it follows that the one-body density matrix obtained from it is:

$$\begin{aligned}&\varrho\big(\boldsymbol{q}{+}\tfrac{\boldsymbol{q}''}{2},\boldsymbol{q}{-}\tfrac{\boldsymbol{q}''}{2}\big)_{s,s'}{=}\sum_{\boldsymbol{\mu}}\langle\boldsymbol{\mu}|\hat{\rho}\,\hat{a}^{\dagger}\big(\boldsymbol{q}{-}\tfrac{\boldsymbol{q}''}{2}\big)_{s'}\hat{a}\big(\boldsymbol{q}{+}\tfrac{\boldsymbol{q}''}{2}\big)_{s}|\boldsymbol{\mu}\rangle\\ &\quad{=}\overline{N}(\boldsymbol{q})_s\frac{(2\pi)^3}{\mathcal{V}}\delta(\boldsymbol{q}'')\delta_{s,s'}{+}\varrho^{\mathrm{loc}}\big(\boldsymbol{q}{+}\tfrac{\boldsymbol{q}''}{2},\boldsymbol{q}{-}\tfrac{\boldsymbol{q}''}{2}\big)_s\delta_{s,s'}{+}\vec{n}^{(1)}(\boldsymbol{q})_{s,s'}{\cdot}\nabla T\frac{(2\pi)^3}{\mathcal{V}}\delta(\boldsymbol{q}'')+\mathscr{O}(\nabla^2 T),\end{aligned} \tag{1.84}$$

where the three terms on the right-hand-side of Eq. (1.84) are obtained from the corresponding many-body density matrices in Eq. (1.83). The terms $\overline{N}(\boldsymbol{q})_s\frac{(2\pi)^3}{\mathcal{V}}\delta(\boldsymbol{q}'')\delta_{s,s'}{+}\varrho^{\mathrm{loc}}\big(\boldsymbol{q}{+}\frac{\boldsymbol{q}''}{2},\boldsymbol{q}{-}\frac{\boldsymbol{q}''}{2}\big)_s\delta_{s,s'}$ describe the local equilibrium [24, 97, 98] and are obtained from the first two terms on the right-hand-side of Eq. (1.83). It is possible to show that the term $\varrho^{\mathrm{loc}}\big(\boldsymbol{q}{+}\frac{\boldsymbol{q}''}{2},\boldsymbol{q}'{-}\frac{\boldsymbol{q}''}{2}\big)_s\delta_{s,s'}$, which accounts for the local-equilibrium temperature, is an eigenvector with zero eigenvalue of the linearized collision superoperator, and thus is left unchanged by scattering [24, 66, 93].

The term $\vec{n}^{(1)}(\boldsymbol{q})_{s,s'}\cdot\nabla T\frac{(2\pi)^3}{\mathcal{V}}\delta(\boldsymbol{q''})$ describes the one-body response to a temperature gradient ∇T constant in space; it is diagonal in $\boldsymbol{q}$ and thus has a translation-invariant Fourier transform — this mirrors the electronic case, where the one-body density matrix that describes the response to an homogeneous electric field is translation-invariant (diagonal in Fourier space) [91, 136]. We also note that the numerical prefactors $\frac{(2\pi)^3}{\mathcal{V}}$ in Eq. (1.84) follow from the normalization convention chose for the bosonic operator (1.76).

These considerations allow to obtain from Eq. (1.82) and Eqs. (1.83,1.84) a collision superoperator diagonal in $\boldsymbol{q}$, which describes scattering at the one-body level (*i.e.* in terms of occupation numbers, $N(\boldsymbol{q})_s \propto \varrho(\boldsymbol{q},\boldsymbol{q})_{s,s}$) in the close-to-equilibrium regime. Specifically, denoting with $N(\boldsymbol{q})_s{=}\overline{N}(\boldsymbol{q})_s{+}\vec{n}^{(1)}(\boldsymbol{q})_s\cdot\nabla T$ the occupation numbers close to the Bose-Einstein equilibrium value ($\overline{N}(\boldsymbol{q})_s \gg \vec{n}^{(1)}(\boldsymbol{q})_s\cdot\nabla T$), one has that the many-body state $|\boldsymbol{\mu}\rangle$ that appears in Eq. (1.81) and Eq. (1.82) has the form

$$|\boldsymbol{\mu}\rangle=|\ldots,N(\boldsymbol{q})_s,N(\boldsymbol{q'})_{s'},N(\boldsymbol{q''})_{s''},\ldots\rangle. \tag{1.85}$$

In order to compute the matrix elements appearing in Eq. (1.82), the specific form of the perturbative Hamiltonian must be known. As anticipated, here we consider a perturbation of the form $\hat{H}^{\text{per}}{=}\hat{H}^{\text{anh}}{+}\hat{H}^{\text{iso}}$, with $\hat{H}^{\text{anh}}$ accounting for anharmonic (third-order) terms in the expansion (1.3), and $\hat{H}^{\text{iso}}$ for the scattering due to isotopes. The Hamiltonian that accounts for third-order anharmonicity is [14]

$$\begin{aligned}\hat{H}^{\text{anh}}&=\frac{1}{3!}\sum_{\boldsymbol{R},\boldsymbol{R'},\boldsymbol{R''}}\frac{\partial^3\hat{V}}{\partial\hat{u}(\boldsymbol{R})_{b\alpha}\partial\hat{u}(\boldsymbol{R'})_{b'\alpha'}\partial\hat{u}(\boldsymbol{R''})_{b''\alpha''}}\Bigg|_{\text{eq}}\hat{u}(\boldsymbol{R})_{b\alpha}\,\hat{u}(\boldsymbol{R'})_{b'\alpha'}\,\hat{u}(\boldsymbol{R''})_{b''\alpha''}\\&=\frac{1}{3!}\iiint_{\mathfrak{B}^3}d^3q\,d^3q'\,d^3q''\,F(\boldsymbol{q},\boldsymbol{q'},\boldsymbol{q''})_{s,s',s''}\big[\hat{a}^\dagger(\boldsymbol{q})_s-\hat{a}(-\boldsymbol{q})_s\big]\big[\hat{a}^\dagger(\boldsymbol{q'})_{s'}-\hat{a}(-\boldsymbol{q'})_{s'}\big]\big[\hat{a}^\dagger(\boldsymbol{q''})_{s''}-\hat{a}(-\boldsymbol{q''})_{s''}\big],\end{aligned} \tag{1.86}$$

where the tensor $F(\boldsymbol{q},\boldsymbol{q'},\boldsymbol{q''})_{s,s',s''}$ is obtained performing the Fourier transform of the third derivative of the interatomic potential, then recasting the Fourier transform of the displacement operator in terms of the bosonic operator (1.12), and finally applying the unitary transformation (1.55) to recast the bosonic operators in the eigenmodes basis. The resulting expression is:

$$\begin{aligned}F(\boldsymbol{q},\boldsymbol{q'},\boldsymbol{q''})_{s,s',s''}&=i\frac{\mathcal{V}^2}{(2\pi)^6}\sum_{\boldsymbol{G}}\delta(\boldsymbol{q}+\boldsymbol{q'}+\boldsymbol{q''}-\boldsymbol{G})\mathscr{E}^\star(\boldsymbol{q})_{s,b\alpha}\mathscr{E}^\star(\boldsymbol{q'})_{s',b'\alpha'}\mathscr{E}^\star(\boldsymbol{q''})_{s'',b''\alpha''}\\&\times\sqrt{\frac{\hbar}{2M_b\omega(\boldsymbol{q})_s}}\sqrt{\frac{\hbar}{2M_{b'}\omega(\boldsymbol{q'})_{s'}}}\sqrt{\frac{\hbar}{2M_{b''}\omega(\boldsymbol{q''})_{s''}}}\sum_{\boldsymbol{h'},\boldsymbol{h''}}\frac{\partial^3\hat{V}}{\partial\hat{u}(\boldsymbol{0})_{b\alpha}\partial\hat{u}(\boldsymbol{h'})_{b'\alpha'}\partial\hat{u}(\boldsymbol{h''})_{b''\alpha''}}\Bigg|_{\text{eq}}\\&\times e^{-i\boldsymbol{q}\cdot\boldsymbol{\tau}_b}e^{-i\boldsymbol{q'}\cdot(\boldsymbol{h'}+\boldsymbol{\tau}_{b'})}e^{-i\boldsymbol{q''}\cdot(\boldsymbol{h''}+\boldsymbol{\tau}_{b''})},\end{aligned} \tag{1.87}$$

where $\boldsymbol{G}$ is a reciprocal lattice vector.

The Hamiltonian that accounts for scattering due to isotopic mass disorder is [137]

$$
\begin{aligned}
\hat{H}^{\rm iso} =& \sum_{\boldsymbol{R},b,\alpha}\left(\frac{m_{\boldsymbol{R}b}}{M_b}-1\right)\frac{\hat{p}^2(\boldsymbol{R})_{b\alpha}}{2M_b}\\
=&\frac{\hbar}{4}\sum_{b\alpha,s,s'}\frac{\mathcal{V}^2}{(2\pi)^6}\iiint_{\mathfrak{B}^3}\delta(\boldsymbol{q}+\boldsymbol{q'}+\boldsymbol{q''})\sqrt{\omega(\boldsymbol{q})_s\omega(\boldsymbol{q'})_{s'}}\Delta M_b(\boldsymbol{q''})\\
&\times\mathcal{E}(\boldsymbol{q})_{s,b\alpha}\mathcal{E}(\boldsymbol{q'})_{s',b\alpha}\big[\hat{a}(\boldsymbol{q})_s\hat{a}^\dagger(-\boldsymbol{q'})_{s'}+\hat{a}^\dagger(-\boldsymbol{q})_s\hat{a}(\boldsymbol{q'})_{s'}\big]d^3q''d^3qd^3q',
\end{aligned}
\tag{1.88}
$$

where $m_{\boldsymbol{R}b}$ is the exact mass of atom at position $\boldsymbol{R}+\boldsymbol{\tau}_b$, M_b the average mass of the atom at position $\boldsymbol{\tau}_b$ in the unit cell, $\Delta M_b(\boldsymbol{q''})=\sum_{\boldsymbol{R}}\frac{m_{\boldsymbol{R}b}-M_b}{M_b}e^{-i\boldsymbol{q''}\cdot(\boldsymbol{R}+\boldsymbol{\tau}_b)}$, and in Eq. (1.88) terms of the type $\hat{a}^\dagger(-\boldsymbol{q})_s\hat{a}^\dagger(-\boldsymbol{q'})_{s'}$ and $\hat{a}(\boldsymbol{q})_s\hat{a}(\boldsymbol{q'})_{s'}$ have been discarded since they do not conserve energy, and this implies a zero contribution to the transition rate computed with the Fermi golden rule (1.81). We note that in the present work Eq. (1.88) is implemented under the simplified assumption that the isotopic mass distribution depends only on the atomic index b and not on the direct lattice $\boldsymbol{R}$, implying that $\Delta M_b(\boldsymbol{q''})\propto\delta(\boldsymbol{q''})$ [37].

From the form of the Hamiltonians (1.86,1.88) and the action of the bosonic operators (1.76), it follows that matrix elements $\mathscr{P}_{\boldsymbol{\mu\iota}}$, with the state $|\boldsymbol{\mu}\rangle$ having the form shown in Eq. (1.85), are different from zero if and only if the occupation numbers of the state $|\boldsymbol{\iota}\rangle$ differ of at most one from those of $|\boldsymbol{\mu}\rangle$, *i.e.* $|\boldsymbol{\iota}\rangle=|...,N(\boldsymbol{q})_s\pm1,N(\boldsymbol{q'})_{s'}\pm1,N(\boldsymbol{q''})_{s''}\pm1,...\rangle$ (see e.g. Refs. [14, 37] for a detailed discussion).

Specifically, one can identify two types of three-body processes that originate from third-order anharmonicity:
(i) coalescence, in which two phonons $\boldsymbol{q}_s$ and $\boldsymbol{q'}_{s'}$ combine into a phonon $\boldsymbol{q''}_{s''}$, *i.e.* a process in which the initial state is $|\boldsymbol{\mu}\rangle=|...,N(\boldsymbol{q})_s,N(\boldsymbol{q'})_{s'},N(\boldsymbol{q''})_{s''},...\rangle$ and the final one is $|\boldsymbol{\iota}\rangle=|...,N(\boldsymbol{q})_s-1,N(\boldsymbol{q'})_{s'}-1,N(\boldsymbol{q''})_{s''}+1,...\rangle$. The rate for such a process is:

$$
\mathscr{P}^{\boldsymbol{\mu}}_{\boldsymbol{\iota}}=\mathscr{P}^{\boldsymbol{q''}s''}_{\boldsymbol{q}s,\boldsymbol{q'}s'}=N(\boldsymbol{q})_sN(\boldsymbol{q'})_{s'}[N(\boldsymbol{q''})_{s''}+1]\mathscr{R}^{\boldsymbol{q''}s''}_{\boldsymbol{q}s,\boldsymbol{q'}s'},
\tag{1.89}
$$

where

$$
\mathscr{R}^{\boldsymbol{q''}s''}_{\boldsymbol{q}s,\boldsymbol{q'}s'}=\frac{2\pi}{\hbar}|F(\boldsymbol{q},\boldsymbol{q'},\boldsymbol{q''})_{s,s',s''}|^2\left[\frac{(2\pi)^3}{\mathcal{V}}\right]^{3/2}\delta\big(\hbar\omega(\boldsymbol{q''})_{s''}-\hbar\omega(\boldsymbol{q})_s-\hbar\omega(\boldsymbol{q'})_{s'}\big).
\tag{1.90}
$$

(ii) decay, in which a phonon $\boldsymbol{q}_s$ decays into two phonons $\boldsymbol{q'}_{s'}$ and $\boldsymbol{q''}_{s''}$, *i.e.* a process in which the initial state is $|\boldsymbol{\mu}\rangle=|...,N(\boldsymbol{q})_s,N(\boldsymbol{q'})_{s'},N(\boldsymbol{q''})_{s''},...\rangle$ and the final one is $|\boldsymbol{\iota}\rangle=|...,N(\boldsymbol{q})_s-1,N(\boldsymbol{q'})_{s'}+1,N(\boldsymbol{q''})_{s''}+1,...\rangle$. The rate for such a process is:

$$
\mathscr{P}^{\boldsymbol{\mu}}_{\boldsymbol{\iota}}=\mathscr{P}^{\boldsymbol{q'}s',\boldsymbol{q''}s''}_{\boldsymbol{q}s}=N(\boldsymbol{q})_s[N(\boldsymbol{q'})_{s'}+1][N(\boldsymbol{q''})_{s''}+1]\mathscr{R}^{\boldsymbol{q'}s',\boldsymbol{q''}s''}_{\boldsymbol{q}s},
\tag{1.91}
$$

where

$$
\mathscr{R}^{\boldsymbol{q'}s',\boldsymbol{q''}s''}_{\boldsymbol{q}s}=\frac{2\pi}{\hbar}|F(\boldsymbol{q},\boldsymbol{q'},\boldsymbol{q''})_{s,s',s''}|^2\left[\frac{(2\pi)^3}{\mathcal{V}}\right]^{3/2}\delta\big(\hbar\omega(\boldsymbol{q''})_{s''}+\hbar\omega(\boldsymbol{q'})_{s'}-\hbar\omega(\boldsymbol{q})_s\big).
\tag{1.92}
$$

Isotopic scattering is instead a two-body process, characterized by the rates

$$\mathscr{P}^{\boldsymbol{\mu}}_{\boldsymbol{\iota}}=\mathscr{P}^{\boldsymbol{q}'s'}_{\boldsymbol{q}s}=N(\boldsymbol{q})_s[N(\boldsymbol{q}')_{s'}+1]\mathscr{R}^{\boldsymbol{q}'s'}_{\boldsymbol{q}s}, \tag{1.93}$$

where[5]

$$\mathscr{R}^{\boldsymbol{q}'s'}_{\boldsymbol{q}s}=\frac{\pi}{2}\omega(\boldsymbol{q})_s\omega(\boldsymbol{q}')_{s'}\delta\big(\omega(\boldsymbol{q})_s-\omega(\boldsymbol{q}')_{s'}\big)\frac{\mathcal{V}}{(2\pi)^3}\left|\sum_{b\alpha}\int_{\mathfrak{B}}\Delta M_b(\boldsymbol{q}'')\mathscr{E}(\boldsymbol{q})_{s,b\alpha}\mathscr{E}(\boldsymbol{q}')_{s',b\alpha}\delta(\boldsymbol{q}+\boldsymbol{q}'+\boldsymbol{q}'')d^3q''\right|^2. \tag{1.94}$$

Now we notice that, once the collision superoperator for the diagonal elements $\boldsymbol{\mu}=\boldsymbol{\nu}$ in Eq. (1.82) is known, the collision superoperator for the off-diagonal elements $\boldsymbol{\mu}\neq\boldsymbol{\nu}$ follows, since $\rho_{\boldsymbol{\mu\nu}}$ is affected by depumping only, and its depumping rate is the average of the depumping rates of the diagonal elements $\rho_{\boldsymbol{\mu\mu}}$ and $\rho_{\boldsymbol{\nu\nu}}$. Therefore, we focus on the collision superoperator for the diagonal elements, and the rates discussed before yield [14]

$$\begin{aligned}&\frac{\partial\varrho(\boldsymbol{q},\boldsymbol{q})_{ss}}{\partial t}\bigg|_{\hat{H}^{\text{anh}}}+\frac{\partial\varrho(\boldsymbol{q},\boldsymbol{q})_{ss}}{\partial t}\bigg|_{\hat{H}^{\text{iso}}}=\\&=\sum_{s',s''}\iint_{\mathfrak{B}\mathfrak{B}}\bigg\{\Big[[N(\boldsymbol{q})_s{+}1][N(\boldsymbol{q}')_{s'}{+}1]N(\boldsymbol{q}'')_{s''}-N(\boldsymbol{q})_sN(\boldsymbol{q}')_{s'}[N(\boldsymbol{q}'')_{s''}{+}1]\Big]\mathscr{R}^{\boldsymbol{q}''s''}_{\boldsymbol{q}s,\boldsymbol{q}'s'}\\&\quad+\frac{1}{2}\Big[[N(\boldsymbol{q})_s{+}1]N(\boldsymbol{q}')_{s'}N(\boldsymbol{q}'')_{s''}-N(\boldsymbol{q})_s[N(\boldsymbol{q}')_{s'}{+}1][N(\boldsymbol{q}'')_{s''}{+}1]\Big]\mathscr{R}^{\boldsymbol{q}'s',\boldsymbol{q}''s''}_{\boldsymbol{q}s}\bigg\}d^3q'd^3q''\\&\quad+\sum_{s'}\int_{\mathfrak{B}}\Big[[N(\boldsymbol{q})_s{+}1]N(\boldsymbol{q}')_{s'}{-}N(\boldsymbol{q})_s[N(\boldsymbol{q}')_{s'}{+}1]\Big]\mathscr{R}^{\boldsymbol{q}'s'}_{\boldsymbol{q}s}d^3q',\end{aligned} \tag{1.95}$$

where the factor 1/2 is needed in order to not to count the same process twice over.

Eq. (1.95) is nonlinear in the occupation numbers (*i.e.* diagonal one-body density matrix elements); in the close-to-equilibrium regime — characterized by occupation numbers close to the Bose-Einstein values — it can be linearized replacing $N(\boldsymbol{q})_s{=}\overline{N}(\boldsymbol{q})_s{+}\vec{n}^{(1)}(\boldsymbol{q})_s{\cdot}\nabla T$ and keeping only terms up to first order in ∇T. Performing such a procedure one obtains a linear collision superoperator [37, 39]:

$$\frac{\partial\varrho(\boldsymbol{q},\boldsymbol{q})_{ss}}{\partial t}\bigg|_{\hat{H}^{\text{per}}}=-\sum_{s''}\frac{1}{(2\pi)^3}\int_{\mathfrak{B}}A(\boldsymbol{q},\boldsymbol{q}'')_{s,s''}\frac{(2\pi)^3}{\mathcal{V}}\vec{n}^{(1)}(\boldsymbol{q}'')_{s''}{\cdot}\nabla T \tag{1.96}$$

---

[5] In Eq. (1.94), the factor $\frac{\mathcal{V}}{(2\pi)^3}$ comes from multiplying the factor $\frac{(2\pi)^3}{\mathcal{V}}$ (which originates from the action of the bosonic operators (1.76)) by the factor $\frac{\mathcal{V}^2}{(2\pi)^6}$ appearing in Eq. (1.88).

where the scattering matrix $A(\boldsymbol{q},\boldsymbol{q}'')_{s,s''}$ is [37, 39]:

$$
\begin{aligned}
&A(\boldsymbol{q},\boldsymbol{q}'')_{s,s''} = \\
&\frac{1}{\overline{N}(\boldsymbol{q}'')_{s''}\left[\overline{N}(\boldsymbol{q}'')_{s''}{+}1\right]}\frac{\mathcal{V}}{(2\pi)^3}\left[\sum_{\dot{s},\ddot{s}}\iint_{\mathfrak{B}^2}\left(\overline{\mathscr{P}}{}^{\dot{\boldsymbol{q}}\dot{s}}_{\boldsymbol{q}s,\ddot{\boldsymbol{q}}\ddot{s}}+\frac{1}{2}\overline{\mathscr{P}}{}^{\boldsymbol{q}s}_{\dot{\boldsymbol{q}}\dot{s},\ddot{\boldsymbol{q}}\ddot{s}}\right)d^3\dot{q}\,d^3\ddot{q}+\sum_{\dot{s}}\int_{\mathfrak{B}}\overline{\mathscr{P}}{}^{\dot{\boldsymbol{q}}\dot{s}}_{\boldsymbol{q}s}d^3\dot{q}\right]\delta_{s,s''}\delta(\boldsymbol{q}-\boldsymbol{q}'') \\
&-\frac{1}{\overline{N}(\boldsymbol{q}'')_{s''}\left[\overline{N}(\boldsymbol{q}'')_{s''}{+}1\right]}\frac{\mathcal{V}}{(2\pi)^3}\left[\sum_{\dot{s}}\int_{\mathfrak{B}}\left(\overline{\mathscr{P}}{}^{\boldsymbol{q}''s''}_{\boldsymbol{q}s,\dot{\boldsymbol{q}}\dot{s}}-\overline{\mathscr{P}}{}^{\dot{\boldsymbol{q}}\dot{s}}_{\boldsymbol{q}s,\boldsymbol{q}''s''}+\overline{\mathscr{P}}{}^{\boldsymbol{q}s}_{\boldsymbol{q}''s'',\dot{\boldsymbol{q}}\dot{s}}\right)d^3\dot{q}-\overline{\mathscr{P}}{}^{\boldsymbol{q}''s''}_{\boldsymbol{q}s}\right].
\end{aligned}
\tag{1.97}
$$

In Eq. (1.97) the transition rates with the bar above are computed from Eqs. (1.89,1.91,1.93) using the Bose-Einstein occupation numbers, and they are symmetric [37, 39]: $\overline{\mathscr{P}}{}^{\dot{\boldsymbol{q}}\dot{s}}_{\boldsymbol{q}s,\ddot{\boldsymbol{q}}\ddot{s}}=\overline{\mathscr{P}}{}^{\boldsymbol{q}s,\ddot{\boldsymbol{q}}\ddot{s}}_{\dot{\boldsymbol{q}}\dot{s}}$ and $\overline{\mathscr{P}}{}^{\boldsymbol{q}''s''}_{\boldsymbol{q}s}=\overline{\mathscr{P}}{}^{\boldsymbol{q}s}_{\boldsymbol{q}''s''}$. In the right member of Eq. (1.97), the first term describes depumping and defines the phonon linewidths $\Gamma(\boldsymbol{q})_s=\frac{1}{(2\pi)^3}A(\boldsymbol{q},\boldsymbol{q})_{s,s}$, while the second term describes the repumping due to the incoming scattered phonons [37].

Up to now we focused on the one-body collision superoperator for the populations (diagonal elements). From the considerations done above, it follows that the one-body collision superoperator for the off-diagonal coherences is the average depumping rate of the corresponding populations,

$$
\left.\frac{\partial\varrho(\boldsymbol{q},\boldsymbol{q})_{s,s'}}{\partial t}\right|_{\hat{H}^{\rm per}}=-\frac{\Gamma(\boldsymbol{q})_s+\Gamma(\boldsymbol{q})_{s'}}{2}\frac{(2\pi)^3}{\mathcal{V}}\vec{n}^{(1)}(\boldsymbol{q})_{s,s'}\cdot\nabla T. \tag{1.98}
$$

1.C.3 Wigner transform of the collision superoperator

The formal, mathematically rigorous description of dissipative effects due to scattering in the Wigner phase-space framework is an active research field [80, 91, 93, 138, 139, 140]. It is generally accepted that the collision superoperator appearing in the semiclassical Boltzmann equation, which is local in space, is an adequate approximation also for the Wigner distribution, provided the dwell time of carriers inside the device is sufficiently long (*i.e.* devices are sufficiently large) [140].

Various derivations, involving approximations of different levels of accuracy, have derived a collision superoperator for the Wigner distribution that is local in space. Vasko and Raichev [91] have discussed how the collision superoperator appearing in the equation for the one-body density matrix of a system homogeneous in space (translation-invariant) applies also to the Wigner distribution; specifically, such an operator is local in space and operates only on the quasimomentum (wavevector) variable of the Wigner distribution.

For the specific case of atomic vibrations, Spohn [93] has derived a collision superoperator for the one-atom, one-dimensional Wigner distribution (*i.e.* having a Wigner matrix that reduces to a scalar, thus accounts exclusively for the population term and misses the off-diagonal coherences terms); such a collision superoperator is local in space and coincides with the collision superoperator appearing in the Boltzmann equation for phonons.

Vasko and Raichev [91] have discussed how for electrons in an homogeneous field, the collision superoperator for the one-body electronic density matrix coincides with the collision superoperator for the Wigner distribution. Such a reasoning can be extended to the case of thermal transport in focus here. Specifically, in the close-to-equilibrium regime, the deviation from equilibrium $\vec{n}^{(1)}(\boldsymbol{q})_{s,s'}\cdot\nabla T$ is local in Fourier space and thus it is not affected by the Wigner transform; this can be checked straightforwardly, since then Wigner transform of Eq. (1.84) yields exactly the expansion (1.40). Therefore, in such a regime, the collision superoperator for the Wigner distribution coincides with that reported in Eqs. (1.96,1.98) for the one-body density matrix, and is reported in Eq. (1.35). We note that the collision superoperator obtained in such a way for the diagonal ($s{=}s'$) elements of the Wigner distribution coincides with the standard collision superoperator appearing in the Peierls-Boltzmann transport equation, this in agreement with the final result of Ref. [140].

We conclude by noting that the present description of scattering might be extended, accounting e.g. for a finite collision time in Eq. (1.79) and thus for the presence of a repumping mechanism also for coherences or energy-renormalization effects [81, 92].

1.D Mathematical properties of the Wigner matrix

Here we discuss the properties of the Wigner matrix defined in Eqs. (1.25,1.27). Specifically, the Wigner representation of a one-body operator $\hat{O}$ is a distribution that depends on a direct lattice vector $\boldsymbol{R}$ and a wavevector $\boldsymbol{q}$, it can depend on time t, and carries two matrix indexes $b\alpha, b'\alpha'$ that denote positions inside the primitive cell of the crystal; in this Appendix, such a distribution will be denoted with $\mathscr{W}_{[O]}(\boldsymbol{R},\boldsymbol{q})_{b\alpha,b'\alpha'}{=}O(\boldsymbol{R},\boldsymbol{q})_{b\alpha,b'\alpha'}$ (the time dependence will be reported only if needed). Despite this phase-space distribution is discussed for the particular case of vibrational excitations (phonons) here, its extension to other quasiparticles in a periodic potential is straightforward. Specifically, the one-body matrix element $O(\boldsymbol{q}{+}\frac{\boldsymbol{q}''}{2},\boldsymbol{q}{-}\frac{\boldsymbol{q}''}{2})_{b\alpha,b'\alpha'}$ appearing in Eq. (1.25) is a matrix element in the Zak basis [141, 142, 143], which has as quantum numbers eigenvalues of translation operators in direct and reciprocal spaces (that is a position inside a unit cell $\boldsymbol{\tau}$, which is a continuous position for electrons and the discrete atomic position for phonons, and a wavevector $\boldsymbol{q}$ belonging to a Brillouin zone). We also note that, in order to adapt the formulation discussed here to other quasiparticles, the phase convention for the Zak eigenfunctions has to be chosen according to the convention (1.12), *i.e.* it must yield a transformation that relates the matrix elements in the Zak basis to the matrix elements in the standard position basis analogous to Eq. (1.22).

We want now to discuss and demonstrate the mathematical properties satisfied by the direct and inverse Wigner transformations (Eq. (1.25) and Eq. (1.26)).

Proof of the inverse Wigner transform (1.26). To prove that the transformation (1.26) is the inverse of the transformation (1.25), it is sufficient to show that inserting the first into the second (or vice versa) one obtains the identity:

$$\begin{aligned} O(\boldsymbol{q}{+}\tfrac{\boldsymbol{q}''}{2},\boldsymbol{q}{-}\tfrac{\boldsymbol{q}''}{2})_{b\alpha,b'\alpha'} &= \int_{\mathfrak{B}} O(\boldsymbol{q}{+}\tfrac{\boldsymbol{q}'}{2},\boldsymbol{q}{-}\tfrac{\boldsymbol{q}'}{2})_{b\alpha,b'\alpha'} \frac{\mathcal{V}}{(2\pi)^3}\sum_{\boldsymbol{R}} e^{i(\boldsymbol{q}'-\boldsymbol{q}'')\cdot\boldsymbol{R}} d^3q' \\ &= \int_{\mathfrak{B}} O(\boldsymbol{q}{+}\tfrac{\boldsymbol{q}'}{2},\boldsymbol{q}{-}\tfrac{\boldsymbol{q}'}{2})_{b\alpha,b'\alpha'}\delta(\boldsymbol{q}'-\boldsymbol{q}'')d^3q'. \end{aligned} \tag{1.99}$$

The Wigner transform of a translation-invariant operator does not depend on space. Eq. (1.27) implies that the Wigner transform of an operator having matrix elements invariant under Bravais-lattice translations (e.g. the harmonic force-constant matrix of a solid defined in Eq. (1.4) and satisfying $G_{(\boldsymbol{R}+\boldsymbol{h})b\alpha,\boldsymbol{R}b'\alpha'}{=}G_{\boldsymbol{h}b\alpha,\boldsymbol{0}b'\alpha'}$) is independent from the spatial position $\boldsymbol{x}$. A direct computation shows this straightforwardly:

$$\begin{aligned} \mathcal{W}_{[G]}(\boldsymbol{R},\boldsymbol{q})_{b\alpha,b'\alpha'} &= \sum_{\boldsymbol{R}',\boldsymbol{R}''} G_{\boldsymbol{R}'b\alpha,\boldsymbol{R}''b'\alpha'} e^{-i\boldsymbol{q}\cdot(\boldsymbol{R}'-\boldsymbol{R}''+\boldsymbol{\tau}_b-\boldsymbol{\tau}_{b'})}\left[\frac{\mathcal{V}}{(2\pi)^3}\int_{\mathfrak{B}} e^{-i\boldsymbol{q}'\cdot\left(\frac{\boldsymbol{R}'+\boldsymbol{R}''+\boldsymbol{\tau}_b+\boldsymbol{\tau}_{b'}}{2}-\boldsymbol{x}\right)}d^3q'\right] \\ &= \sum_{\boldsymbol{h}} G_{\boldsymbol{h}b\alpha,\boldsymbol{0}b'\alpha'} e^{-i\boldsymbol{q}\cdot(\boldsymbol{h}+\boldsymbol{\tau}_b-\boldsymbol{\tau}_{b'})}\left[\int_{\mathfrak{B}}\left(\frac{\mathcal{V}}{(2\pi)^3}\sum_{\boldsymbol{R}''} e^{-i\boldsymbol{q}'\cdot\boldsymbol{R}''}\right) e^{-i\boldsymbol{q}'\cdot\left(\frac{\boldsymbol{h}+\boldsymbol{\tau}_{b'}+\boldsymbol{\tau}_b}{2}-\boldsymbol{x}\right)}d^3q'\right] \\ &= \sum_{\boldsymbol{h}} G_{\boldsymbol{h}b\alpha,\boldsymbol{0}b'\alpha'} e^{-i\boldsymbol{q}\cdot(\boldsymbol{h}+\boldsymbol{\tau}_b-\boldsymbol{\tau}_{b'})} = D(\boldsymbol{q})_{b\alpha,b'\alpha'}. \end{aligned} \tag{1.100}$$

where we have used $\frac{\mathcal{V}}{(2\pi)^3}\sum_{\boldsymbol{R}''} e^{-i\boldsymbol{q}'\cdot\boldsymbol{R}''} = \delta(\boldsymbol{q}')$. This property has been used in Eq. (1.37) in the main text.

Hermiticity. The standard Wigner distribution is real [87]. Here we are considering a generalized (matrix) Wigner distribution [130], for which the reality condition translates into the hermiticity condition $O(\boldsymbol{R},\boldsymbol{q})^*_{b\alpha,b'\alpha'} = O(\boldsymbol{R},\boldsymbol{q})_{b'\alpha',b\alpha}$. This hermiticity condition of the Wigner matrix can be easily proved from the hermiticity of a generic observable, $O(\boldsymbol{q},\boldsymbol{q}')_{b\alpha,b'\alpha'} = O^*(\boldsymbol{q}',\boldsymbol{q})_{b'\alpha',b\alpha}$, and from Eq. (1.25).

Marginal of the Wigner matrix distribution. Integrating the Wigner matrix distribution over all the direct-lattice vectors yields the diagonal elements of the one-body density matrix in reciprocal space:

$$\begin{aligned} \sum_{\boldsymbol{R}} W(\boldsymbol{R},\boldsymbol{q})_{b\alpha,b'\alpha'} &= \frac{\mathcal{V}}{(2\pi)^3}\int_{\mathfrak{B}} \varrho(\boldsymbol{q}{+}\tfrac{\boldsymbol{q}''}{2},\boldsymbol{q}{-}\tfrac{\boldsymbol{q}''}{2})_{b\alpha,b'\alpha'}\sum_{\boldsymbol{R}} e^{+i\boldsymbol{q}''\cdot\boldsymbol{R}}d^3q'' \\ &= \varrho(\boldsymbol{q},\boldsymbol{q})_{b\alpha,b'\alpha'}\,. \end{aligned} \tag{1.101}$$

Inner product. As discussed in Eq. (1.36) of the main text, the trace of the product of two one-body operators in the Dirac framework can be rewritten as phase-space integral involving the Wigner representations of these operators. Here we prove such a property, starting by recasting the first line of Eq. (1.36) using the properties of the Dirac delta:

$$\begin{aligned}
&\mathrm{Tr}\big(\hat{\rho}(t)\hat{A}\big)\\
&=\frac{\mathcal{V}^2}{(2\pi)^6}\iint\limits_{\mathfrak{B}\mathfrak{B}}\varrho\big(\boldsymbol{q}+\tfrac{\boldsymbol{q}''}{2},\boldsymbol{q}-\tfrac{\boldsymbol{q}''}{2},t\big)_{b\alpha,b'\alpha'}A\big(\boldsymbol{q}-\tfrac{\boldsymbol{q}''}{2},\boldsymbol{q}+\tfrac{\boldsymbol{q}''}{2}\big)_{b'\alpha',b\alpha}d^3q\,d^3q''\\
&=\frac{\mathcal{V}^2}{(2\pi)^6}\iiint\limits_{\mathfrak{B}\mathfrak{B}\mathfrak{B}}\varrho\big(\boldsymbol{q}+\tfrac{\boldsymbol{q}'}{2},\boldsymbol{q}-\tfrac{\boldsymbol{q}'}{2},t\big)_{b\alpha,b'\alpha'}\delta(\boldsymbol{q}'-\boldsymbol{q}'')\,A\big(\boldsymbol{q}-\tfrac{\boldsymbol{q}''}{2},\boldsymbol{q}+\tfrac{\boldsymbol{q}''}{2}\big)_{b'\alpha',b\alpha}d^3q\,d^3q'\,d^3q''.
\end{aligned}\tag{1.102}$$

Then we rewrite the Dirac delta introduced above using its exponential representation [144], $\delta(\boldsymbol{q}'-\boldsymbol{q}'')=\frac{\mathcal{V}}{(2\pi)^3}\sum_{\boldsymbol{R}}e^{i(\boldsymbol{q}'-\boldsymbol{q}'')\cdot\boldsymbol{R}}$, obtaining:

$$\mathrm{Tr}\big(\hat{\rho}(t)\hat{A}\big)=\frac{\mathcal{V}^3}{(2\pi)^9}\iiint\limits_{\mathfrak{B}\mathfrak{B}\mathfrak{B}}\varrho\big(\boldsymbol{q}+\tfrac{\boldsymbol{q}'}{2},\boldsymbol{q}-\tfrac{\boldsymbol{q}'}{2},t\big)_{b\alpha,b'\alpha'}\sum_{\boldsymbol{R}}e^{i(\boldsymbol{q}'-\boldsymbol{q}'')\cdot\boldsymbol{R}}A\big(\boldsymbol{q}-\tfrac{\boldsymbol{q}''}{2},\boldsymbol{q}+\tfrac{\boldsymbol{q}''}{2}\big)_{b'\alpha',b\alpha}d^3q\,d^3q'\,d^3q''.\tag{1.103}$$

Now we exchange the order of sum and integrals, and it is easy to recognize that the integrals over $\boldsymbol{q}'$ and $\boldsymbol{q}''$ yield the phase-space representation of the one-body density matrix and of the one-body operator $A(\boldsymbol{q},\boldsymbol{q}')_{b\alpha,b'\alpha'}$, *i.e.* Eq. (1.36). We also note that Eq. (1.36) can be written using the plane-wave (continuous) representation of the Dirac delta $\delta(\boldsymbol{q}'-\boldsymbol{q}'')=\frac{1}{(2\pi)^3}\int_{\mathbb{R}^3}e^{i(\boldsymbol{q}'-\boldsymbol{q}'')\cdot\boldsymbol{x}}d^3x$ and the values of the Wigner representations determined evaluating Eq. (1.25) at the continuous positions $\boldsymbol{x}$:

$$\mathrm{Tr}\big(\hat{\rho}(t)\hat{A}\big)=\frac{1}{(2\pi)^3}\iint\limits_{\mathbb{R}^3\mathfrak{B}}\mathscr{W}_{[\varrho]}(\boldsymbol{x},\boldsymbol{q},t)_{b\alpha,b'\alpha'}\mathscr{W}_{[A]}(\boldsymbol{x},\boldsymbol{q})_{b'\alpha',b\alpha}d^3q\,d^3x.\tag{1.104}$$

Moyal product. In the Dirac framework, the matrix product of two one-body operators $A(\boldsymbol{q},\boldsymbol{q}')_{b\alpha,b'\alpha'}$ and $B(\boldsymbol{q},\boldsymbol{q}')_{b\alpha,b'\alpha'}$ can be written as

$$C\big(\boldsymbol{q}+\tfrac{\boldsymbol{q}''}{2},\boldsymbol{q}-\tfrac{\boldsymbol{q}''}{2}\big)_{b\alpha,b'\alpha'}=\frac{\mathcal{V}}{(2\pi)^3}\int_{\mathfrak{b}}A\big(\boldsymbol{q}+\tfrac{\boldsymbol{q}''}{2},\boldsymbol{q}'\big)_{b\alpha,b''\alpha''}B\big(\boldsymbol{q}',\boldsymbol{q}-\tfrac{\boldsymbol{q}''}{2}\big)_{b''\alpha'',b'\alpha'}d^3q',\tag{1.105}$$

where $\mathfrak{b}$ can be any Brillouin zone.

Here we prove that the Wigner transform of the product $C(\boldsymbol{q}+\frac{\boldsymbol{q}''}{2},\boldsymbol{q}-\frac{\boldsymbol{q}''}{2})_{b\alpha,b'\alpha'}$ can be obtained from the Wigner transforms of the two operators multiplied using a generalized Moyal product formula, which is reminiscent of that used for the Wigner matrices in different contexts [132, 145]:

$$\begin{aligned}
\mathscr{W}_{[C]}(\boldsymbol{R},\boldsymbol{q})_{b\alpha,b'\alpha'}&=\mathscr{W}_{[A]}(\boldsymbol{R},\boldsymbol{q})_{b\alpha,b''\alpha''}e^{\frac{i}{2}\left[\frac{\overleftarrow{\partial}}{\partial\boldsymbol{R}}\frac{\overrightarrow{\partial}}{\partial\boldsymbol{q}}-\frac{\overleftarrow{\partial}}{\partial\boldsymbol{q}}\frac{\overrightarrow{\partial}}{\partial\boldsymbol{R}}\right]}\mathscr{W}_{[B]}(\boldsymbol{R},\boldsymbol{q})_{b''\alpha'',b\alpha}\\
&\simeq\mathscr{W}_{[A]}(\boldsymbol{R},\boldsymbol{q})_{b\alpha,b''\alpha''}\mathscr{W}_{[B]}(\boldsymbol{R},\boldsymbol{q})_{b''\alpha'',b\alpha}\\
&\quad+\frac{i}{2}\frac{\partial\mathscr{W}_{[A]}(\boldsymbol{R},\boldsymbol{q})_{b\alpha,b''\alpha''}}{\partial\boldsymbol{R}}\frac{\partial\mathscr{W}_{[B]}(\boldsymbol{R},\boldsymbol{q})_{b''\alpha'',b\alpha}}{\partial\boldsymbol{q}}-\frac{i}{2}\frac{\partial\mathscr{W}_{[A]}(\boldsymbol{R},\boldsymbol{q})_{b\alpha,b''\alpha''}}{\partial\boldsymbol{q}}\frac{\partial\mathscr{W}_{[B]}(\boldsymbol{R},\boldsymbol{q})_{b''\alpha'',b\alpha}}{\partial\boldsymbol{R}}+\mathscr{O}(\partial^2)\,,
\end{aligned}\tag{1.106}$$

where the approximated equality in Eq. (1.106) has been obtained expanding the exponential in Taylor series and considering derivatives up to first order. In addition, in Eq. (1.106) we have introduced the symbol $\frac{\partial}{\partial \boldsymbol{R}}$ to denote a spatial derivative evaluated at the Bravais-lattice site $\boldsymbol{R}$. We also note that $\hbar$ does not appear in Eq. (1.106), since derivatives are performed with respect to the wavevector $\boldsymbol{q}$. Recasting Eq. (1.106) in terms of the crystal momentum $\hbar\boldsymbol{q}$ yields and expansion in powers of $\hbar$, which allows a systematic analysis of quantum effects around the classical limit [132].

To prove Eq. (1.106), we start from the product of two one-body operators (1.105) and we apply to it the Wigner transform (1.25), obtaining:

$$C\big(\boldsymbol{R},\boldsymbol{q}\big)_{b\alpha,b'\alpha'} = \frac{\mathcal{V}^2}{(2\pi)^6}\iint\limits_{\mathfrak{B}\mathfrak{b}} A(\boldsymbol{q}+\tfrac{\boldsymbol{q}''}{2},\boldsymbol{q}')_{b\alpha,b''\alpha''} B(\boldsymbol{q}',\boldsymbol{q}-\tfrac{\boldsymbol{q}''}{2})_{b''\alpha'',b'\alpha'}\, e^{i\boldsymbol{q}''\cdot\boldsymbol{R}}\, d^3q'\, d^3q''. \tag{1.107}$$

Now we rewrite the matrix elements $A(\boldsymbol{q}+\frac{\boldsymbol{q}''}{2},\boldsymbol{q}')_{b\alpha,b''\alpha''}$ and $B(\boldsymbol{q}',\boldsymbol{q}-\frac{\boldsymbol{q}''}{2})_{b''\alpha'',b'\alpha'}$ appearing in Eq. (1.107) in terms of their inverse Wigner transform (1.26),

$$A(\boldsymbol{q}+\tfrac{\boldsymbol{q}''}{2},\boldsymbol{q}')_{b\alpha,b''\alpha''} = \sum_{\boldsymbol{R}'} A\big(\boldsymbol{R}',\tfrac{1}{2}\big[\boldsymbol{q}+\tfrac{\boldsymbol{q}''}{2}+\boldsymbol{q}'\big]\big)_{b\alpha,b''\alpha''} e^{-i(\boldsymbol{q}+\frac{\boldsymbol{q}''}{2}-\boldsymbol{q}')\cdot\boldsymbol{R}'} \tag{1.108}$$

$$= \frac{1}{\mathcal{V}}\int_{\mathbb{R}^3} A\big(\boldsymbol{x}',\tfrac{1}{2}\big[\boldsymbol{q}+\tfrac{\boldsymbol{q}''}{2}+\boldsymbol{q}'\big]\big)_{b\alpha,b''\alpha''} e^{-i(\boldsymbol{q}+\frac{\boldsymbol{q}''}{2}-\boldsymbol{q}')\cdot\boldsymbol{x}'} d^3x'. \tag{1.109}$$

Eq. (1.108) shows that the knowledge of the Wigner distribution at the discrete Bravais-lattice points is sufficient to have an invertible framework, while Eq. (1.109) — which can be proved straightforwardly using Eq. (1.25) — yields the same result using the continuous set of points in direct space. The advantage of using Eq. (1.109) instead of Eq. (1.108) is that Eq. (1.109) will allows us to exploit the properties of differential calculus to simplify the algebra. We note in passing that in Eq. (1.108) the quantity $\frac{1}{2}\big[\boldsymbol{q}+\frac{\boldsymbol{q}''}{2}+\boldsymbol{q}'\big]$ can belong to any Brillouin zone, since for a generic reciprocal lattice vector $\boldsymbol{G}$ we have $A\big(\boldsymbol{R}',\boldsymbol{q}+\boldsymbol{G}\big)_{b\alpha,b''\alpha''}=A\big(\boldsymbol{R}',\boldsymbol{q}\big)_{b\alpha,b''\alpha''}e^{-i\boldsymbol{G}\cdot(\boldsymbol{\tau}_b-\boldsymbol{\tau}_{b'})}$. Now we insert Eq. (1.109) (and the corresponding Eq. for B) into Eq. (1.107), obtaining

$$\begin{aligned} C\big(\boldsymbol{R},\boldsymbol{q}\big)_{b\alpha,b'\alpha'} = &\frac{1}{(2\pi)^6}\iint\limits_{\mathfrak{B}\mathfrak{b}}\int\limits_{\mathbb{R}^3} A\big(\boldsymbol{x}',\tfrac{1}{2}\big[\boldsymbol{q}+\tfrac{\boldsymbol{q}''}{2}+\boldsymbol{q}'\big]\big)_{b\alpha,b''\alpha''} e^{-i(\boldsymbol{q}+\frac{\boldsymbol{q}''}{2}-\boldsymbol{q}')\cdot\boldsymbol{x}'} d^3x' \\ &\times \int\limits_{\mathbb{R}^3} B\big(\boldsymbol{x}'',\tfrac{1}{2}\big[\boldsymbol{q}'+\boldsymbol{q}-\tfrac{\boldsymbol{q}''}{2}\big]\big)_{b''\alpha'',b'\alpha'} e^{-i(\boldsymbol{q}'-\boldsymbol{q}+\frac{\boldsymbol{q}''}{2})\cdot\boldsymbol{x}''} e^{i\boldsymbol{q}''\cdot\boldsymbol{R}} d^3x''\, d^3q'\, d^3q''. \end{aligned} \tag{1.110}$$

At this point we note that the wavevector $\boldsymbol{q}$ is kept fixed inside the integral on the right-hand-side of Eq. (1.110), thus we can write the Wigner distributions appearing in Eq. (1.110) as a Taylor expansion around $\boldsymbol{q}$. To do this we define the multindex $\gamma = (\gamma_1,\gamma_2,\gamma_3)$ whose modulus is $|\gamma| = \gamma_1+\gamma_2+\gamma_3$ and factorial is $\gamma! = (\gamma_1!)(\gamma_2!)(\gamma_3!)$. We have that $\boldsymbol{q}^\gamma = q_1^{\gamma_1} q_2^{\gamma_2} q_3^{\gamma_3}$ and $\frac{\partial^\gamma}{\partial \boldsymbol{q}^\gamma} f = \frac{\partial^{\gamma_1}}{\partial q_1^{\gamma_1}}\frac{\partial^{\gamma_2}}{\partial q_2^{\gamma_2}}\frac{\partial^{\gamma_3}}{\partial q_3^{\gamma_3}} f$. Thus, we write the Wigner distributions A and B as an infinite

Taylor series around $\boldsymbol{q}$:

$$A(\boldsymbol{x}',\tfrac{1}{2}[\boldsymbol{q}+\tfrac{\boldsymbol{q}''}{2}+\boldsymbol{q}'])_{b\alpha,b''\alpha''}=\sum_{|\gamma|=0}^{\infty}\frac{1}{\gamma!}\frac{\partial^{\gamma}A(\boldsymbol{x}',\bar{\boldsymbol{q}})_{b\alpha,b''\alpha''}}{\partial\bar{\boldsymbol{q}}^{\gamma}}\bigg|_{\bar{\boldsymbol{q}}=\boldsymbol{q}}\Big(\tfrac{1}{2}[\boldsymbol{q}+\tfrac{\boldsymbol{q}''}{2}+\boldsymbol{q}']-\boldsymbol{q}\Big)^{\gamma}. \tag{1.111}$$

We rewrite Eq. (1.110) in terms of Eq. (1.111),

$$\begin{aligned}C(\boldsymbol{R},\boldsymbol{q})_{b\alpha,b'\alpha'}=&\sum_{|\gamma|,|\gamma'|}\frac{1}{2^{\gamma+\gamma'}\gamma!\gamma'!}\frac{1}{(2\pi)^{6}}\iint_{\mathfrak{B}\mathfrak{b}}\iint_{\mathbb{R}^3\mathbb{R}^3}e^{i\boldsymbol{q}''\cdot\boldsymbol{R}}\frac{\partial^{\gamma}A(\boldsymbol{x}',\boldsymbol{q})_{b\alpha,b''\alpha''}}{\partial\boldsymbol{q}^{\gamma}}(\boldsymbol{q}'-\boldsymbol{q}+\tfrac{\boldsymbol{q}''}{2})^{\gamma}e^{-i(\boldsymbol{q}'-\boldsymbol{q}+\frac{\boldsymbol{q}''}{2})\cdot\boldsymbol{x}''}\\&\times\frac{\partial^{\gamma'}B(\boldsymbol{x}'',\boldsymbol{q})_{b''\alpha'',b'\alpha'}}{\partial\boldsymbol{q}^{\gamma'}}(\boldsymbol{q}'-\boldsymbol{q}-\tfrac{\boldsymbol{q}''}{2})^{\gamma'}e^{+i(\boldsymbol{q}'-\boldsymbol{q}-\frac{\boldsymbol{q}''}{2})\cdot\boldsymbol{x}'}d^3q'\,d^3q''\,d^3x'\,d^3x''.\end{aligned} \tag{1.112}$$

Now we recognize that in Eq. (1.112) we have terms that can be rewritten as

$$(\boldsymbol{q}'-\boldsymbol{q}+\tfrac{\boldsymbol{q}''}{2})^{\gamma}e^{-i(\boldsymbol{q}'-\boldsymbol{q}+\frac{\boldsymbol{q}''}{2})\cdot\boldsymbol{x}''}=i^{\gamma}\tfrac{\partial}{\partial\boldsymbol{x}''^{\gamma}}e^{-i(\boldsymbol{q}'-\boldsymbol{q}+\frac{\boldsymbol{q}''}{2})\cdot\boldsymbol{x}''}. \tag{1.113}$$

Therefore we obtain

$$\begin{aligned}C(\boldsymbol{R},\boldsymbol{q})_{b\alpha,b'\alpha'}=&\sum_{|\gamma|,|\gamma'|}\frac{(-1)^{\gamma}(-i)^{\gamma+\gamma'}}{\gamma!\gamma'!2^{\gamma+\gamma'}}\frac{1}{(2\pi)^{6}}\iint_{\mathfrak{B}\mathfrak{b}}\iint_{\mathbb{R}^3\mathbb{R}^3}e^{i\boldsymbol{q}''\cdot\boldsymbol{R}}\\&\frac{\partial^{\gamma}A(\boldsymbol{x}',\boldsymbol{q})_{b\alpha,b''\alpha''}}{\partial\boldsymbol{q}^{\gamma}}\Big[\frac{\partial^{\gamma}}{\partial\boldsymbol{x}''^{\gamma}}e^{-i(\boldsymbol{q}'-\boldsymbol{q}+\frac{\boldsymbol{q}''}{2})\cdot\boldsymbol{x}''}\Big]\\&\frac{\partial^{\gamma'}B(\boldsymbol{x}'',\boldsymbol{q})_{b''\alpha'',b'\alpha'}}{\partial\boldsymbol{q}^{\gamma'}}\Big[\frac{\partial^{\gamma'}}{\partial\boldsymbol{x}'^{\gamma'}}e^{+i(\boldsymbol{q}'-\boldsymbol{q}-\frac{\boldsymbol{q}''}{2})\cdot\boldsymbol{x}'}\Big]d^3x'\,d^3x''\,d^3q'\,d^3q''.\end{aligned} \tag{1.114}$$

Applying γ times the integration by part in $\boldsymbol{R}''$ and α times the integration by part in $\boldsymbol{x}'$ gives

$$\begin{aligned}C(\boldsymbol{R},\boldsymbol{q})_{b\alpha,b'\alpha'}=&\sum_{|\gamma|,|\gamma'|}\frac{(-1)^{\gamma'}(-i)^{\gamma+\gamma'}}{\gamma!\gamma'!2^{\gamma+\gamma'}}\frac{1}{\mathcal{V}^2}\iint_{\mathbb{R}^6}\frac{\partial^{\gamma+\gamma'}A(\boldsymbol{x}',\boldsymbol{q})_{b\alpha,b''\alpha''}}{\partial\boldsymbol{q}^{\gamma}\partial\boldsymbol{x}'^{\gamma'}}\frac{\partial^{\gamma+\gamma'}B(\boldsymbol{x}'',\boldsymbol{q})_{b''\alpha'',b'\alpha'}}{\partial\boldsymbol{x}''^{\gamma}\partial\boldsymbol{q}^{\gamma'}}\\&\Big[e^{i\boldsymbol{q}\cdot(\boldsymbol{x}''-\boldsymbol{x}')}\frac{\mathcal{V}^2}{(2\pi)^6}\iint_{\mathfrak{B}\mathfrak{b}}e^{i\boldsymbol{q}'\cdot(\boldsymbol{x}'-\boldsymbol{x}'')}e^{-i\boldsymbol{q}''\cdot(\frac{\boldsymbol{x}'+\boldsymbol{x}''}{2}-\boldsymbol{R})}d^3q'\,d^3q''\Big]d^3x'\,d^3x'',\end{aligned} \tag{1.115}$$

where the prefactor $(-1)^{\gamma'}$ emerges from the product $(-1)^{\gamma}(-1)^{\gamma}(-1)^{\gamma'}$, the boundary term resulting from the integration by part is not reported because it vanishes at infinity, since the function in square bracket is sharply peaked around $\boldsymbol{R}$. Now we use the equivalence between Eq. (1.108) and Eq. (1.109) to replace the double integral in direct space with a double discrete sum:

$$\begin{aligned} C(\boldsymbol{R},\boldsymbol{q})_{b\alpha,b'\alpha'} = &\sum_{|\gamma|,|\gamma'|} \frac{(-1)^{\gamma'}(-i)^{\gamma+\gamma'}}{\gamma!\gamma'!2^{\gamma+\gamma'}} \sum_{\boldsymbol{R'}\boldsymbol{R''}} \\ &\frac{\partial^{\gamma+\gamma'} A(\boldsymbol{R'},\boldsymbol{q})_{b\alpha,b''\alpha''}}{\partial \boldsymbol{q}^{\gamma}\partial \boldsymbol{R}'^{\gamma'}} \frac{\partial^{\gamma+\gamma'} B(\boldsymbol{R''},\boldsymbol{q})_{b''\alpha'',b'\alpha'}}{\partial \boldsymbol{R}''^{\gamma}\partial \boldsymbol{q}^{\gamma'}} \\ &\left[e^{i\boldsymbol{q}\cdot(\boldsymbol{R''}-\boldsymbol{R'})} \frac{\mathcal{V}^2}{(2\pi)^6} \iint_{\mathfrak{Bb}} e^{+i\boldsymbol{q'}\cdot(\boldsymbol{R'}-\boldsymbol{R''})} e^{-i\boldsymbol{q''}\cdot(\frac{\boldsymbol{R'}+\boldsymbol{R''}}{2}-\boldsymbol{R})} d^3q' d^3q'' \right]. \end{aligned} \tag{1.116}$$

Now we can further simplify Eq. (1.116), since the term in square brackets gives $\delta_{\boldsymbol{R'},\boldsymbol{R''}}\delta_{\boldsymbol{R'},\boldsymbol{R}}$, and therefore it follows that

$$C(\boldsymbol{R},\boldsymbol{q})_{b\alpha,b'\alpha'} = \sum_{|\gamma|,|\gamma'|} \frac{(-1)^{\gamma} i^{\gamma+\gamma'}}{\gamma!\gamma'!2^{\gamma+\gamma'}} \frac{\partial^{\gamma+\gamma'} A(\boldsymbol{R},\boldsymbol{q})_{b\alpha,b''\alpha''}}{\partial \boldsymbol{q}^{\gamma}\partial \boldsymbol{R}^{\gamma'}} \frac{\partial^{\gamma+\gamma'} B(\boldsymbol{R},\boldsymbol{q})_{b''\alpha'',b'\alpha'}}{\partial \boldsymbol{R}^{\gamma}\partial \boldsymbol{q}^{\gamma'}}. \tag{1.117}$$

Eq. (1.117) is mathematically equivalent to Eq. (7.5) and Eq (D6) by Blount [129], although the proof reported here does not require to have matrix elements of operators computed in a basis periodic in reciprocal space. The compact Moyal-like multiplication rule reported in Eq. (1.106) can be obtained rearranging Eq. (1.117) as follows:

$$\begin{aligned} C(\boldsymbol{R},\boldsymbol{q})_{b\alpha,b'\alpha'} &= \sum_{|\gamma|,|\gamma'|} \frac{1}{\gamma!\gamma'!} \frac{i^{\gamma+\gamma'}}{2^{\gamma+\gamma'}} A(\boldsymbol{R},\boldsymbol{q})_{b\alpha,b''\alpha''} (-1)^{\gamma} \frac{\overleftarrow{\partial^{\gamma}}}{\partial \boldsymbol{q}^{\gamma}} \frac{\overrightarrow{\partial^{\gamma}}}{\partial \boldsymbol{R}^{\gamma}} \frac{\overleftarrow{\partial^{\gamma'}}}{\partial \boldsymbol{R}^{\gamma'}} \frac{\overrightarrow{\partial^{\gamma'}}}{\partial \boldsymbol{q}^{\gamma'}} B(\boldsymbol{R},\boldsymbol{q})_{b''\alpha'',b'\alpha'} \\ &= A(\boldsymbol{R},\boldsymbol{q})_{b\alpha,b''\alpha''} \left[\sum_{|\gamma'|} \frac{1}{\gamma'!} \frac{i^{\gamma'}}{2^{\gamma'}} \frac{\overleftarrow{\partial^{\gamma'}}}{\partial \boldsymbol{R}^{\gamma'}} \frac{\overrightarrow{\partial^{\gamma'}}}{\partial \boldsymbol{q}^{\gamma'}} \right] \left[\sum_{|\gamma|} \frac{1}{\gamma!} \frac{(-i)^{\gamma}}{2^{\gamma}} \frac{\overleftarrow{\partial^{\gamma}}}{\partial \boldsymbol{q}^{\gamma}} \frac{\overrightarrow{\partial^{\gamma}}}{\partial \boldsymbol{R}^{\gamma}} \right] B(\boldsymbol{R},\boldsymbol{q})_{b''\alpha'',b'\alpha'} \\ &= A(\boldsymbol{R},\boldsymbol{q})_{b\alpha,b''\alpha''} e^{\frac{i}{2}\left(\frac{\overleftarrow{\partial}}{\partial \boldsymbol{R}} \frac{\overrightarrow{\partial}}{\partial \boldsymbol{q}} - \frac{\overleftarrow{\partial}}{\partial \boldsymbol{q}} \frac{\overrightarrow{\partial}}{\partial \boldsymbol{R}} \right)} B(\boldsymbol{R},\boldsymbol{q})_{b''\alpha'',b'\alpha'}, \end{aligned} \tag{1.118}$$

where we have used the arrow to indicate on which distribution a differential operators acts. We conclude by noting that Eq. (1.118) can be regarded as a matrix extension of Eq. (2.56) in Ref. [145].

Exact evolution equation for the Wigner distribution in differential form. The equation describing the temporal evolution of the Wigner distribution $W(\boldsymbol{R},\boldsymbol{q},t)_{b\alpha,b'\alpha'}$ can be obtained applying the transformation (1.25) to the evolution equation for the one-body density matrix (1.24), and using Eq. (1.106) for transforming the product of one-body matrices. The resulting exact evolution equation is:

$$\begin{aligned}
&\frac{\partial W(\boldsymbol{R},\boldsymbol{q},t)_{b\alpha,b'\alpha'}}{\partial t}\\
&+i\sqrt{D(\boldsymbol{q})}_{b\alpha,b''\alpha''}e^{\frac{i}{2}\left[\frac{\overleftarrow{\partial}}{\partial \boldsymbol{R}}\frac{\overrightarrow{\partial}}{\partial \boldsymbol{q}}-\frac{\overleftarrow{\partial}}{\partial \boldsymbol{q}}\frac{\overrightarrow{\partial}}{\partial \boldsymbol{R}}\right]}W(\boldsymbol{R},\boldsymbol{q},t)_{b''\alpha'',b'\alpha'}\\
&-iW(\boldsymbol{R},\boldsymbol{q},t)_{b\alpha,b''\alpha''}e^{\frac{i}{2}\left[\frac{\overleftarrow{\partial}}{\partial \boldsymbol{R}}\frac{\overrightarrow{\partial}}{\partial \boldsymbol{q}}-\frac{\overleftarrow{\partial}}{\partial \boldsymbol{q}}\frac{\overrightarrow{\partial}}{\partial \boldsymbol{R}}\right]}\sqrt{D(\boldsymbol{q})}_{b''\alpha'',b'\alpha'}\\
&=\frac{\partial W(\boldsymbol{R},\boldsymbol{q},t)_{b\alpha,b'\alpha'}}{\partial t}\Big|_{\hat{H}^{\mathrm{per}}},
\end{aligned}\tag{1.119}$$

where we have exploited the property (1.100), which implies that the Wigner transform of the square root of the dynamical matrix is exactly itself, and as such it does not depend on the position $\boldsymbol{R}$ (this follows from Eq. (1.37)). We conclude by noting that performing the first-order expansion of the Moyal product (see Eq. (1.106)) in the exact equation (1.119) yields the simplified evolution equation (1.30).

1.E Microscopic energy field & flux

In this Appendix we investigate the difference between the heat flux expression derived by Hardy [16], and the expression obtained from the Wigner framework (1.39). We show that these differences originate from a different expression for the microscopic energy field used as starting point for the computation of the heat flux in the Hardy approach.

Within the microscopic Wigner framework, the thermal conductivity is directly related to the heat flux (see Sec. 1.5.2), as in the density-matrix-based approach developed by Hardy [16]. We recall that in the Wigner framework, the microscopic harmonic energy field (1.38) is determined univocally by the property (1.11) [86], and consequently an univocal expressions for the Wigner energy flux (Eq. (1.39)) and for the WBTE thermal conductivity (Eq. (1.44)) follow. In contrast, in the density-matrix approach developed by Hardy [16] to compute the heat flux, multiple choices for the microscopic energy field are possible, and the resulting heat flux — and thus thermal conductivity — are not invariant under different choices for the microscopic energy field (details will be discussed later).

We note that the freedom in choosing the microscopic energy field is present also in the Kubo correlation function formalism, where the harmonic interaction energy between two atoms can be partitioned in infinite ways between the two atoms interacting [74, 75]. Notably, Ref. [75] has recently demonstrated that such a freedom does not affect the thermal conductivity computed within the Kubo correlation function formalism, since there exists a "gauge invariance" principle that implies the thermal conductivity computed from the Kubo formalism to be invariant under different choices of the microscopic heat flux. Such a gauge invariance principle for the Kubo conductivity relies on the factorization of the correlation function of two observables at large time lags, and at present it is not clear if it can be applied to the density-matrix (Hardy) formalism (where heat flux and conductivity depend on the microscopic energy field) — future work will aim at understanding this. In this Appendix we show that the Hardy approach yields an heat flux compatible with the (univocal) heat flux obtained from the Wigner framework if a particular microscopic energy field is used as starting point. In particular, we show that starting from the uniquely-defined Wigner harmonic energy field (1.38) and computing the expectation value of the heat flux operator computed following the Hardy approach [16], one obtains exactly the same result of the Wigner framework (specifically, the spatial average of the univocally-defined Wigner heat flux (1.39)).

The basic idea of the approach developed by Hardy [16] to derive the (harmonic) energy flux operator is to define a microscopic (harmonic) energy density operator, $\hat{h}(\boldsymbol{x})$, such that its integral in space gives the harmonic Hamiltonian (1.9) (or equivalently, Eq. (1.18)). The choice of such microscopic energy field operator is, in general, not unique[74, 75].

In the Wigner phase-space framework, the microscopic energy field is univocally defined by Eqs. (1.36,1.25) and is:

$$\begin{aligned} E(\boldsymbol{R}) &= \frac{\hbar\mathcal{V}}{(2\pi)^3}\int_{\mathfrak{B}}\sqrt{D(\boldsymbol{q})}_{b\alpha,b'\alpha'}W(\boldsymbol{R},\boldsymbol{q})_{b'\alpha',b\alpha}d^3q \\ &= \frac{\hbar\mathcal{V}^2}{(2\pi)^6}\iint\limits_{\mathfrak{B}\mathfrak{B}}\sqrt{D(\boldsymbol{q})}_{b\alpha,b'\alpha'}\varrho(\boldsymbol{q}+\tfrac{\boldsymbol{q}''}{2},\boldsymbol{q}-\tfrac{\boldsymbol{q}''}{2})_{b'\alpha',b\alpha}e^{i\boldsymbol{q}''\cdot\boldsymbol{R}}d^3q\,d^3q''. \end{aligned} \tag{1.120}$$

The microscopic energy field (1.120) can be interpreted as expectation value of an energy field operator (in the Hardy sense) $\hat{e}(\boldsymbol{R})$, *i.e.* $E(\boldsymbol{R}) = \mathrm{Tr}(\hat{e}(\boldsymbol{R})\hat{\rho})$, where the expression of such an operator follows from combining Eq. (1.21) with Eq. (1.120):

$$\hat{e}(\boldsymbol{R})=\frac{\hbar\mathcal{V}^2}{(2\pi)^6}\iint\limits_{\mathfrak{B}\mathfrak{B}}\sqrt{D(\boldsymbol{q})}_{b\alpha,b'\alpha'}\hat{a}^\dagger(\boldsymbol{q}-\tfrac{\boldsymbol{q}''}{2})_{b\alpha}\hat{a}(\boldsymbol{q}+\tfrac{\boldsymbol{q}''}{2})_{b'\alpha'}e^{i\boldsymbol{q}''\cdot\boldsymbol{R}}d^3q\,d^3q'', \tag{1.121}$$

and clearly $\sum_{\boldsymbol{R}}\hat{e}(\boldsymbol{R})=\hat{H}^{\mathrm{har}}$ (Eq. (1.18)). The approach of Hardy [16] employs a continuous energy field, that here is obtained convolving the discrete operator (1.121) with a continuous normalized distribution, $\Delta_l(\boldsymbol{x}-\boldsymbol{R})=\frac{1}{(\pi^3 l^3)^{3/2}}\exp\left[-\frac{(\boldsymbol{x}-\boldsymbol{R})^2}{l^2}\right]$: $\hat{h}(\boldsymbol{x})=\sum_{\boldsymbol{R}}\hat{e}(\boldsymbol{R})\Delta_l(\boldsymbol{x}-\boldsymbol{R})$, where l is a length much larger than the interatomic spacing over which temperature can be considered constant (see Fig. 1.1). It is easy to show that the continuous energy field satisfies $\int\hat{h}(\boldsymbol{x})d^3x = \hat{H}^{\mathrm{har}}$.

Hardy [16] computes the heat flux operator $\hat{\boldsymbol{j}}(\boldsymbol{x})$ from the time derivative of the local energy field and requiring the continuity equation to be satisfied, *i.e.* $\frac{d\hat{h}(\boldsymbol{x})}{dt}=-\nabla\cdot\hat{\boldsymbol{j}}(\boldsymbol{x})$. The time derivative of the energy field is readily computed as

$$-\nabla\cdot\hat{\boldsymbol{j}}(\boldsymbol{x}) = \frac{d\hat{h}(\boldsymbol{x})}{dt} = -\frac{i}{\hbar}\left[\hat{h}(\boldsymbol{x}),\hat{H}^{\mathrm{har}}\right], \tag{1.122}$$

implying that the divergence of the energy flux operator can be computed from the commutator

$$\nabla\cdot\hat{\boldsymbol{j}}(\boldsymbol{x}) = \frac{i}{\hbar}\sum_{\boldsymbol{R},\boldsymbol{R}'}\Big[\Delta_l(\boldsymbol{x}-\boldsymbol{R}) - \Delta_l(\boldsymbol{x}-\boldsymbol{R}')\Big]\hat{e}(\boldsymbol{R})\hat{e}(\boldsymbol{R}'). \tag{1.123}$$

Now the quantity in square bracket can be written in terms of the Taylor series of the distributions Δ_l around the point $\boldsymbol{x}$:

$$\begin{aligned}\Delta_l(\boldsymbol{x}{-}\boldsymbol{R}) - \Delta_l(\boldsymbol{x}{-}\boldsymbol{R}') &= \sum_{|\gamma|}\tfrac{1}{\gamma!}\Big[\tfrac{\partial^\gamma}{\partial\boldsymbol{y}^\gamma}\Delta_l(\boldsymbol{y})\big|_{\boldsymbol{y}=\boldsymbol{x}}\Big](\boldsymbol{x}{-}\boldsymbol{R})^\gamma - \sum_{|\gamma|}\tfrac{1}{\gamma!}\Big[\tfrac{\partial^\gamma}{\partial\boldsymbol{y}^\gamma}\Delta_l(\boldsymbol{y})\big|_{\boldsymbol{y}=\boldsymbol{x}}\Big](\boldsymbol{x}{-}\boldsymbol{R}')^\gamma\\ &= \sum_{|\gamma|\geq 1}\tfrac{1}{\gamma!}[(\boldsymbol{x}-\boldsymbol{R})^\gamma - (\boldsymbol{x}-\boldsymbol{R}')^\gamma]\tfrac{\partial^\gamma\Delta_l(\boldsymbol{x})}{\partial\boldsymbol{x}^\gamma},\end{aligned} \tag{1.124}$$

where γ is the multiindex used for multi-dimensional Taylor expansions (see in the Appendix 1.D), and clearly the zeroth order term of the resulting series is zero. It follows that Eq. (1.123) can be recast as

$$\nabla\cdot\hat{\boldsymbol{j}}(\boldsymbol{x}) {=} \frac{i}{\hbar}\sum_{\boldsymbol{R},\boldsymbol{R}'}\hat{e}(\boldsymbol{R})\hat{e}(\boldsymbol{R}')\sum_{|\gamma|\geq 1}\tfrac{1}{\gamma!}[(\boldsymbol{x}{-}\boldsymbol{R})^\gamma{-}(\boldsymbol{x}{-}\boldsymbol{R}')^\gamma]\tfrac{\partial^\gamma\Delta_l(\boldsymbol{x})}{\partial\boldsymbol{x}^\gamma}, \tag{1.125}$$

implying that the local heat flux operator reads

$$\hat{\boldsymbol{j}}(\boldsymbol{x}) {=} \frac{i}{\hbar}\sum_{\boldsymbol{R},\boldsymbol{R}'}\hat{e}(\boldsymbol{R})\hat{e}(\boldsymbol{R}')\Big\{(\boldsymbol{R}'-\boldsymbol{R})\Delta_l(\boldsymbol{x}) + \sum_{|\gamma|\geq 2}\tfrac{1}{\gamma!}[(\boldsymbol{x}{-}\boldsymbol{R})^\gamma{-}(\boldsymbol{x}{-}\boldsymbol{R}')^\gamma]\tfrac{\partial^{\gamma-1}\Delta_l(\boldsymbol{x})}{\partial\boldsymbol{x}^{\gamma-1}}\Big\}. \tag{1.126}$$

For the computation of the thermal conductivity one needs the average heat flux over the total volume of the crystal [16] ($V_{\text{tot}} = \mathcal{V}N_{\text{c}}$, where $\mathcal{V}$ is the primitive cell volume and N_{c} the number of primitive cells in the crystal), obtained as

$$\hat{\boldsymbol{Q}}_a = \frac{1}{\mathcal{V}N_{\text{c}}}\int_{V_{\text{tot}}}\hat{\boldsymbol{j}}(\boldsymbol{x})d^3x. \tag{1.127}$$

When integrating the local heat flux (1.126) over the volume, one has that $\Delta_l(\boldsymbol{x})$ is non-zero only over a small region of space, so the volume integral of the derivatives can be neglected and one obtains the expression for the average heat flux:

$$\hat{\boldsymbol{Q}}_a {=} \frac{i}{\hbar\mathcal{V}N_{\text{c}}}\sum_{\boldsymbol{R},\boldsymbol{R}'}(\boldsymbol{R}'-\boldsymbol{R})\hat{e}(\boldsymbol{R})\hat{e}(\boldsymbol{R}'). \tag{1.128}$$

Eq. (1.128) can be easily evaluated in terms of the bosonic operators using Eq. (1.121):

$$\begin{aligned}\hat{\boldsymbol{Q}}_a = \frac{i}{\hbar\mathcal{V}N_{\text{c}}}\sum_{\boldsymbol{R},\boldsymbol{R}'}(\boldsymbol{R}'{-}\boldsymbol{R})&\frac{\hbar\mathcal{V}^2}{(2\pi)^6}\iint\limits_{\mathfrak{B}\mathfrak{B}}\sqrt{D(\tilde{\boldsymbol{q}})}_{b\alpha,b'\alpha'}\hat{a}^\dagger(\tilde{\boldsymbol{q}}{-}\tfrac{\tilde{\boldsymbol{q}}''}{2})_{b\alpha}\hat{a}(\tilde{\boldsymbol{q}}{+}\tfrac{\tilde{\boldsymbol{q}}''}{2})_{b'\alpha'}e^{i\tilde{\boldsymbol{q}}''\cdot\boldsymbol{R}}d^3\tilde{q}d^3\tilde{q}''\\ \times&\frac{\hbar\mathcal{V}^2}{(2\pi)^6}\iint\limits_{\mathfrak{B}\mathfrak{B}}\sqrt{D(\bar{\boldsymbol{q}})}_{\dot{b}\dot{\alpha},\ddot{b}\ddot{\alpha}}\hat{a}^\dagger(\bar{\boldsymbol{q}}{-}\tfrac{\bar{\boldsymbol{q}}''}{2})_{\dot{b}\dot{\alpha}}\hat{a}(\bar{\boldsymbol{q}}{+}\tfrac{\bar{\boldsymbol{q}}''}{2})_{\ddot{b}\ddot{\alpha}}e^{i\bar{\boldsymbol{q}}''\cdot\boldsymbol{R}'}d^3\bar{q}d^3\bar{q}''.\end{aligned} \tag{1.129}$$

In order to ease the algebra in the next part of this section, we rewrite Eq. (1.129) performing the inverse center of mass change of variable $\boldsymbol{q}''{=}\tilde{\boldsymbol{q}}{-}\frac{\tilde{\boldsymbol{q}}''}{2}$, $\boldsymbol{q}{=}\tilde{\boldsymbol{q}}{+}\frac{\tilde{\boldsymbol{q}}''}{2}$, and $\ddot{\boldsymbol{q}}{=}\bar{\boldsymbol{q}}{-}\frac{\bar{\boldsymbol{q}}''}{2}$, $\dot{\boldsymbol{q}}{=}\bar{\boldsymbol{q}}{+}\frac{\bar{\boldsymbol{q}}''}{2}$, which also requires changing the integration domain from the Cartesian product of two Brillouin zone $\mathfrak{B}\times\mathfrak{B}$ to a different domain $\mathfrak{I}_2$ (see Fig. 1.E.1 for a representative case that applies to one-dimensional wavevectors); nevertheless, we will see later that only the diagonal of such domain will be used at the end of our calculation.

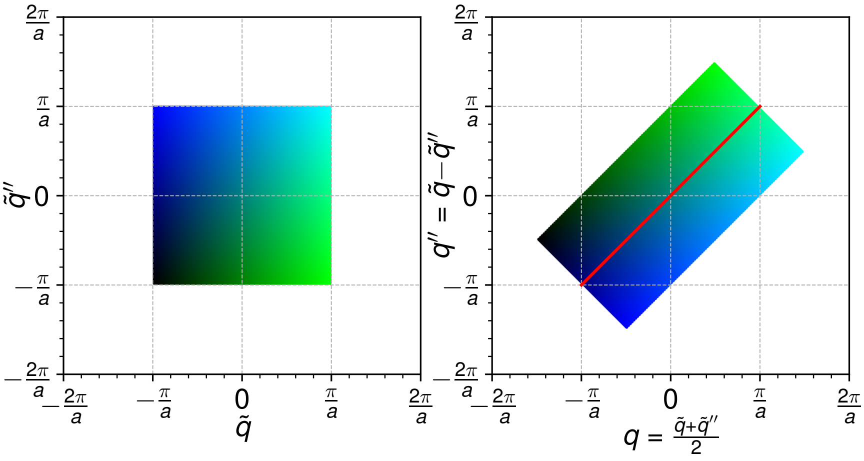

Figure 1.E.1 – **Center of mass change of variable.** The colors show how for one-dimensional wavevectors the points in the center-of-mass frame ($\mathfrak{B}{\times}\mathfrak{B}$, square in the left panel, with coordinates $\tilde{q}, \tilde{q}''$) are mapped into the points in the Cartesian frame ($\mathfrak{I}_2$, rectangle in the right panel, with coordinates $q{=}\frac{\tilde{q}+\tilde{q}''}{2}$, $q''{=}\tilde{q}{-}\tilde{q}''$). The red line in the right panel shows the points which will be used in our final calculation for the average heat flux.

After having performed this change of variable, we obtain

$$\hat{\boldsymbol{Q}}_a = \frac{i\hbar}{\mathcal{V}N_{\mathrm{c}}}\sum_{\boldsymbol{R},\boldsymbol{R}'}(\boldsymbol{R}'{-}\boldsymbol{R})\frac{\mathcal{V}^4}{(2\pi)^{12}}\iint_{\mathfrak{I}_2}\iint_{\mathfrak{I}_2}\sqrt{D(\tfrac{\boldsymbol{q}+\boldsymbol{q}''}{2})}_{b\alpha,b'\alpha'}\sqrt{D(\tfrac{\dot{\boldsymbol{q}}+\ddot{\boldsymbol{q}}}{2})}_{\dot{b}\dot{\alpha},\ddot{b}\ddot{\alpha}}$$
$$\times\hat{a}^\dagger(\boldsymbol{q}'')_{b\alpha}\hat{a}(\boldsymbol{q})_{b'\alpha'}\hat{a}^\dagger(\ddot{\boldsymbol{q}})_{\dot{b}\dot{\alpha}}\hat{a}(\dot{\boldsymbol{q}})_{\ddot{b}\ddot{\alpha}}e^{i(\boldsymbol{q}-\boldsymbol{q}'')\cdot\boldsymbol{R}}e^{i(\dot{\boldsymbol{q}}-\ddot{\boldsymbol{q}})\cdot\boldsymbol{R}'}d^3q\,d^3q''d^3\dot{q}\,d^3\ddot{q}. \tag{1.130}$$

Using the bosonic commutation relation (see Sec. 1.3), we rewrite the operators in normal-ordered form

$$\hat{a}^\dagger(\boldsymbol{q}'')_{b\alpha}\hat{a}(\boldsymbol{q})_{b'\alpha'}\hat{a}^\dagger(\ddot{\boldsymbol{q}})_{\dot{b}\dot{\alpha}}\hat{a}(\dot{\boldsymbol{q}})_{\ddot{b}\ddot{\alpha}} = \hat{a}^\dagger(\boldsymbol{q}'')_{b\alpha}\hat{a}^\dagger(\ddot{\boldsymbol{q}})_{\dot{b}\dot{\alpha}}\hat{a}(\boldsymbol{q})_{b'\alpha'}\hat{a}(\dot{\boldsymbol{q}})_{\ddot{b}\ddot{\alpha}}$$
$$+\hat{a}^\dagger(\boldsymbol{q}'')_{b\alpha}\hat{a}(\dot{\boldsymbol{q}})_{\ddot{b}\ddot{\alpha}}\frac{(2\pi)^3}{\mathcal{V}}\delta(\ddot{\boldsymbol{q}}{-}\boldsymbol{q})\delta_{b'\dot{b}}\delta_{\alpha',\dot{\alpha}}. \tag{1.131}$$

Inserting Eq. (1.131) into Eq. (1.130), it becomes apparent that the term containing four bosonic operators yields a total contribution equal to zero. Therefore, we are left with the term containing two bosonic operators only, and using the properties of the Dirac delta, we have:

$$\begin{aligned}\hat{\boldsymbol{Q}}_a=&\frac{i\hbar}{\mathcal{V}N_{\mathrm{c}}}\sum_{\boldsymbol{R},\boldsymbol{R}'}(\boldsymbol{R}'-\boldsymbol{R})\frac{\mathcal{V}^3}{(2\pi)^9}\iint_{\mathfrak{I}_2}\iint_{\mathfrak{I}_2}\sqrt{D(\tfrac{\boldsymbol{q}+\boldsymbol{q}''}{2})}_{b\alpha,b'\alpha'}\sqrt{D(\tfrac{\dot{\boldsymbol{q}}+\boldsymbol{q}}{2})}_{b'\alpha',\ddot{b}\ddot{\alpha}}\\&\hat{a}^{\dagger}(\boldsymbol{q}'')_{b\alpha}\hat{a}(\dot{\boldsymbol{q}})_{\ddot{b}\ddot{\alpha}}\delta(\ddot{\boldsymbol{q}}-\boldsymbol{q})e^{i(\boldsymbol{q}-\boldsymbol{q}'')\cdot\boldsymbol{R}}e^{i(\dot{\boldsymbol{q}}-\boldsymbol{q})\cdot\boldsymbol{R}'}d^3q\,d^3q''\,d^3\dot{q}\,d^3\ddot{q}.\end{aligned}\tag{1.132}$$

Now we note that we can rewrite Eq. (1.132) using the properties of the exponential

$$i(\boldsymbol{R}'-\boldsymbol{R})e^{i(\boldsymbol{q}-\boldsymbol{q}'')\cdot\boldsymbol{R}}e^{i(\dot{\boldsymbol{q}}-\boldsymbol{q})\cdot\boldsymbol{R}'}=-\nabla_{\boldsymbol{q}}e^{i(\boldsymbol{q}-\boldsymbol{q}'')\cdot\boldsymbol{R}}e^{i(\dot{\boldsymbol{q}}-\boldsymbol{q})\cdot\boldsymbol{R}'},\tag{1.133}$$

obtaining

$$\begin{aligned}\hat{\boldsymbol{Q}}_a=&-\frac{\hbar}{(2\pi)^3N_{\mathrm{c}}}\iint_{\mathfrak{I}_2}\iint_{\mathfrak{I}_2}\sqrt{D(\tfrac{\boldsymbol{q}+\boldsymbol{q}''}{2})}_{b\alpha,b'\alpha'}\sqrt{D(\tfrac{\dot{\boldsymbol{q}}+\boldsymbol{q}}{2})}_{b'\alpha',\ddot{b}\ddot{\alpha}}\\&\times\hat{a}^{\dagger}(\boldsymbol{q}'')_{b\alpha}\hat{a}(\dot{\boldsymbol{q}})_{\ddot{b}\ddot{\alpha}}\delta(\ddot{\boldsymbol{q}}-\boldsymbol{q})\nabla_{\boldsymbol{q}}\left[\frac{\mathcal{V}^2}{(2\pi)^6}\sum_{\boldsymbol{R},\boldsymbol{R}'}e^{i(\boldsymbol{q}-\boldsymbol{q}'')\cdot\boldsymbol{R}}e^{i(\dot{\boldsymbol{q}}-\boldsymbol{q})\cdot\boldsymbol{R}'}\right]d^3q\,d^3q''\,d^3\dot{q}\,d^3\ddot{q}.\end{aligned}\tag{1.134}$$

At this point it is evident that the term in square bracket can be rewritten as:

$$\begin{aligned}\sum_{\boldsymbol{R},\boldsymbol{R}'}e^{i(\boldsymbol{q}-\boldsymbol{q}'')\cdot\boldsymbol{R}}e^{i(\dot{\boldsymbol{q}}-\boldsymbol{q})\cdot\boldsymbol{R}'}&=\sum_{\boldsymbol{R},\boldsymbol{h}}e^{i(\dot{\boldsymbol{q}}-\boldsymbol{q}'')\cdot\boldsymbol{R}}e^{i(\dot{\boldsymbol{q}}-\boldsymbol{q})\cdot\boldsymbol{h}}\\&=\frac{(2\pi)^6}{\mathcal{V}^2}\delta(\dot{\boldsymbol{q}}-\boldsymbol{q}'')\delta(\dot{\boldsymbol{q}}-\boldsymbol{q}).\end{aligned}\tag{1.135}$$

Inserting Eq. (1.135) into Eq. (1.134) and integrating with respect to $\dot{\boldsymbol{q}}$ and $\ddot{\boldsymbol{q}}$, we obtain:

$$\begin{aligned}\hat{\boldsymbol{Q}}_a=&-\frac{\hbar}{(2\pi)^3N_{\mathrm{c}}}\iint_{\mathfrak{I}_2}\sqrt{D(\tfrac{\boldsymbol{q}+\boldsymbol{q}''}{2})}_{b\alpha,b'\alpha'}\sqrt{D(\tfrac{\boldsymbol{q}''+\boldsymbol{q}}{2})}_{b'\alpha',\ddot{b}\ddot{\alpha}}\\&\times\hat{a}^{\dagger}(\boldsymbol{q}'')_{b\alpha}\hat{a}(\boldsymbol{q}'')_{\ddot{b}\ddot{\alpha}}\nabla_{\boldsymbol{q}}\delta(\boldsymbol{q}''-\boldsymbol{q})d^3q\,d^3q''.\end{aligned}\tag{1.136}$$

In order to further simplify Eq. (1.136), we recast the coefficients inside the integral as follows,

$$\begin{aligned}&\sqrt{D(\tfrac{\boldsymbol{q}+\boldsymbol{q}''}{2})}_{b\alpha,b'\alpha'}\sqrt{D(\tfrac{\boldsymbol{q}''+\boldsymbol{q}}{2})}_{b'\alpha',\ddot{b}\ddot{\alpha}}\nabla_{\boldsymbol{q}}\delta(\boldsymbol{q}''-\boldsymbol{q})=\\&=\nabla_{\boldsymbol{q}}\left[\sqrt{D(\tfrac{\boldsymbol{q}+\boldsymbol{q}''}{2})}_{b\alpha,b'\alpha'}\sqrt{D(\tfrac{\boldsymbol{q}''+\boldsymbol{q}}{2})}_{b'\alpha',\ddot{b}\ddot{\alpha}}\delta(\boldsymbol{q}''-\boldsymbol{q})\right]-\left[\nabla_{\boldsymbol{q}}\left(\sqrt{D(\tfrac{\boldsymbol{q}+\boldsymbol{q}''}{2})}_{b\alpha,b'\alpha'}\sqrt{D(\tfrac{\boldsymbol{q}''+\boldsymbol{q}}{2})}_{b'\alpha',\ddot{b}\ddot{\alpha}}\right)\right]\delta(\boldsymbol{q}''-\boldsymbol{q}),\end{aligned}\tag{1.137}$$

and we notice that: (i) the integration domain selected by the Dirac delta is symmetric (the diagonal of the domain $\mathfrak{I}$, see red line in the representative case of Fig. 1.E.1); (ii) the function appearing in the curly bracket is even in $\boldsymbol{q}$, so its derivative is odd; (iii) the product of the operators $\hat{a}^{\dagger}(\boldsymbol{q}'')_{b\alpha}\hat{a}(\boldsymbol{q}'')_{\ddot{b}\ddot{\alpha}}$ is even in $\boldsymbol{q}$ for $\boldsymbol{q}''=\boldsymbol{q}$. From these considerations it follows that the term in curly brackets gives zero when integrated, and thus we are left with the term in square bracket in Eq. (1.137), which can be written as:

$$
\begin{aligned}
\hat{\boldsymbol{Q}}_a = & \frac{\hbar}{(2\pi)^3 N_{\rm c}} \int\limits_{\mathfrak{B}} \tfrac{1}{2}\Big[\nabla_{\boldsymbol{q}} \sqrt{D(\boldsymbol{q})}_{b\alpha,b'\alpha'}\Big] \sqrt{D(\boldsymbol{q})}_{b'\alpha',\ddot{b}\ddot{\alpha}}\, \hat{a}^{\dagger}(\boldsymbol{q})_{b\alpha} \hat{a}(\boldsymbol{q})_{\ddot{b}\ddot{\alpha}} d^3q \\
& + \frac{\hbar}{(2\pi)^3 N_{\rm c}} \int\limits_{\mathfrak{B}} \sqrt{D(\boldsymbol{q})}_{b\alpha,b'\alpha'} \tfrac{1}{2}\Big[\nabla_{\boldsymbol{q}} \sqrt{D(\boldsymbol{q})}_{b'\alpha',\ddot{b}\ddot{\alpha}}\Big] \hat{a}^{\dagger}(\boldsymbol{q})_{b\alpha} \hat{a}(\boldsymbol{q})_{\ddot{b}\ddot{\alpha}} d^3q .
\end{aligned}
\tag{1.138}
$$

Eq. (1.138) can be recast in the eigenmodes basis using the transformation of Eq. (1.33), yielding

$$
\hat{\boldsymbol{Q}}_a = \frac{\hbar}{(2\pi)^3 N_{\rm c}} \int_{\mathfrak{B}} \frac{\omega(\boldsymbol{q})_s + \omega(\boldsymbol{q})_{s'}}{2} \vec{V}(\boldsymbol{q})_{s,s'} \hat{a}^{\dagger}(\boldsymbol{q})_s \hat{a}(\boldsymbol{q})_{s'} d^3q . \tag{1.139}
$$

For the computation of the thermal conductivity, the heat flux operator (1.139) obtained with the Hardy approach yielding results equivalent to those obtained using the heat flux (1.39) obtained from the Wigner formalism. In fact, the expectation value $\mathrm{Tr}(\hat{\boldsymbol{Q}}_a \hat{\rho})$ is the spatial average of the Wigner heat flux (1.39), $\langle \boldsymbol{Q}(\boldsymbol{R},t)\rangle = \frac{1}{N_{\rm c}} \sum_{\boldsymbol{R}} \boldsymbol{Q}(\boldsymbol{R},t)$, as shown by the following direct calculation (which relies on Eq. (1.32), Eq. (1.101), Eq. (1.21), and Eq. (1.55)):

$$
\begin{aligned}
\frac{1}{N_{\rm c}} \sum_{\boldsymbol{R}} \boldsymbol{Q}(\boldsymbol{R},t) &= \frac{\hbar}{(2\pi)^3} \int_{\mathfrak{B}} \frac{\omega(\boldsymbol{q})_s + \omega(\boldsymbol{q})_{s'}}{2} \vec{V}(\boldsymbol{q})_{s,s'} \mathcal{E}^{\star}(\boldsymbol{q})_{s',b'\alpha'} \frac{1}{N_{\rm c}} \sum_{\boldsymbol{R}} W(\boldsymbol{R},\boldsymbol{q},t)_{b'\alpha',b\alpha} \mathcal{E}(\boldsymbol{q})_{s,b\alpha} d^3q \\
&= \frac{\hbar}{(2\pi)^3 N_{\rm c}} \int_{\mathfrak{B}} \frac{\omega(\boldsymbol{q})_s + \omega(\boldsymbol{q})_{s'}}{2} \vec{V}(\boldsymbol{q})_{s,s'} \mathcal{E}^{\star}(\boldsymbol{q})_{s',b'\alpha'} \varrho(\boldsymbol{q},\boldsymbol{q},t)_{b'\alpha',b\alpha} \mathcal{E}(\boldsymbol{q})_{s,b\alpha} d^3q \\
&= \mathrm{Tr}\left[\hat{\rho}(t) \left(\frac{\hbar}{(2\pi)^3 N_{\rm c}} \int_{\mathfrak{B}} \frac{\omega(\boldsymbol{q})_s + \omega(\boldsymbol{q})_{s'}}{2} \vec{V}(\boldsymbol{q})_{s,s'} \hat{a}^{\dagger}(\boldsymbol{q})_s \hat{a}(\boldsymbol{q})_{s'} d^3q \right)\right] \\
&= \mathrm{Tr}\big[\hat{\rho}(t) \hat{\boldsymbol{Q}}_a\big] .
\end{aligned}
\tag{1.140}
$$

In summary, we have proved that a suitable (Wigner) choice for the microscopic energy field operator in Hardy's formulation [16] yields an heat flux operator whose expectation value is equivalent to the average heat flux obtained from the Wigner framework. Therefore, the conductivity obtained from these two heat fluxes using the formula $Q^{\alpha} = -\kappa^{\alpha\beta} \nabla^{\beta} T$ is the same.

1.F Details on the velocity operator

In this Appendix we report details about the numerical computation of the velocity operator (1.33). The square root of the dynamical matrix (1.19) can be evaluated numerically from the eigenvectors and eigenvalues of the dynamical matrix (see Eq. (1.20)):

$$
\begin{aligned}
\sqrt{D(\boldsymbol{q})}_{b\alpha,b'\alpha'} &= \mathcal{E}(\boldsymbol{q})_{s,b\alpha} \sqrt{\mathcal{E}^{\star}(\boldsymbol{q})_{s,c\beta} D(\boldsymbol{q})_{c\beta,c'\beta'} \mathcal{E}(\boldsymbol{q})_{s',c'\beta'}} \mathcal{E}^{\star}(\boldsymbol{q})_{s',b'\alpha'} \\
&= \mathcal{E}(\boldsymbol{q})_{s,b\alpha} \omega(\boldsymbol{q})_s \delta_{s,s'} \mathcal{E}^{\star}(\boldsymbol{q})_{s',b'\alpha'} .
\end{aligned}
\tag{1.141}
$$

From Eq. (1.141), it follows that the velocity operator (1.33) can be computed numerically as:

$$\begin{aligned} V^{\beta}(\boldsymbol{q})_{s,s'} &= \mathscr{E}^{\star}(\boldsymbol{q})_{s,b\alpha}\frac{\partial\sqrt{D(\boldsymbol{q})}_{b\alpha,b'\alpha'}}{\partial q^{\beta}}\mathscr{E}(\boldsymbol{q})_{s',b'\alpha'} \\ &= \lim_{\delta q^{\beta}\to 0}\mathscr{E}^{\star}(\boldsymbol{q})_{s,b\alpha}\frac{\sqrt{D(\boldsymbol{q}+\delta q^{\beta})}_{b\alpha,b'\alpha'}-\sqrt{D(\boldsymbol{q}-\delta q^{\beta})}_{b\alpha,b'\alpha'}}{2\delta q^{\beta}}\mathscr{E}(\boldsymbol{q})_{s',b'\alpha'}, \end{aligned} \tag{1.142}$$

where δq^{β} is a discretization step to be used in the numerical calculation of the derivative with the finite-difference method.

1.F.1 Velocity operators in terms of eigenvectors and eigenvalues of the dynamical matrix

Here we report a useful identity that relates the velocity operator to the eigenvectors and eigenvalues of the dynamical matrix. From the properties of the derivative, it follows that:

$$\begin{aligned} \nabla_{\boldsymbol{q}}\Big[\sqrt{D(\boldsymbol{q})}_{b\alpha,b'\alpha'}\mathscr{E}(\boldsymbol{q})_{s',b'\alpha'}\Big] &= \Big[\nabla_{\boldsymbol{q}}\sqrt{D(\boldsymbol{q})}_{b\alpha,b'\alpha'}\Big]\mathscr{E}(\boldsymbol{q})_{s',b'\alpha'}+\sqrt{D(\boldsymbol{q})}_{b\alpha,b'\alpha'}\Big[\nabla_{\boldsymbol{q}}\mathscr{E}(\boldsymbol{q})_{s',b'\alpha'}\Big] \\ &= \big[\nabla_{\boldsymbol{q}}\omega(\boldsymbol{q})_{s'}\big]\mathscr{E}(\boldsymbol{q})_{s',b\alpha}+\omega(\boldsymbol{q})_{s'}\big[\nabla_{\boldsymbol{q}}\mathscr{E}(\boldsymbol{q})_{s',b\alpha}\big]. \end{aligned} \tag{1.143}$$

Taking the scalar product of Eq. (1.143) with $\mathscr{E}(\boldsymbol{q})_{s,b\alpha}$ yields an expression that relates the velocity operator to the eigenvalues and the eigenvectors of the dynamical matrix (see Eq. (1.20)):

$$\vec{V}(\boldsymbol{q})_{s,s'}=\big[\nabla_{\boldsymbol{q}}\omega(\boldsymbol{q})_{s}\big]\delta_{s,s'}+\big[\omega(\boldsymbol{q})_{s'}-\omega(\boldsymbol{q})_{s}\big]\sum_{b\alpha}\mathscr{E}^{\star}(\boldsymbol{q})_{s,b\alpha}\big[\nabla_{\boldsymbol{q}}\mathscr{E}(\boldsymbol{q})_{s',b\alpha}\big]. \tag{1.144}$$

The identity (1.144) can be used to prove the relationship between the velocity operators computed using the Ziman (step-like) or Wallace (smooth) phase conventions reported in Eq. (1.48). In fact, Eq. (1.47) implies that Ziman's step-like phase convention yields a dynamical matrix that is related to that reported in Eq. (1.19) (obtained with Wallace's smooth phase convention) as:

$$\underline{\sqrt{D(\boldsymbol{q})}}_{b\alpha,b'\alpha'}=\sqrt{D(\boldsymbol{q})}_{b\alpha,b'\alpha'}e^{i\boldsymbol{q}\cdot(\boldsymbol{\tau}_{b}-\boldsymbol{\tau}_{b'})}, \tag{1.145}$$

and it is straightforward to see that the transformation (1.145) leaves the eigenvalues unchanged, while it modifies the eigenvectors as [77]:

$$\underline{\mathscr{E}(\boldsymbol{q})}_{s,b\alpha}=\mathscr{E}(\boldsymbol{q})_{s,b\alpha}e^{i\boldsymbol{q}\cdot\boldsymbol{\tau}_{b}}. \tag{1.146}$$

Eq. (1.48) can thus be proved straightforwardly combining Eqs. (1.143,1.144,1.146).

1.G Effects of the phase convention on the thermal conductivity

In this section we discuss the effects of the phase convention adopted for the Wigner distribution on the thermal conductivity. We remark that the smooth phase convention of Wallace is the only one yielding a size-consistent conductivity — thus the convention to be used — and the results reported in Fig. 1.6 and Fig. 1.7 have been computed using the phase convention of Wallace.

We show in Fig. 1.G.1 and Fig. 1.G.2 how the predictions of the conductivity of $La_2Zr_2O_7$ and $CsPbBr_3$, respectively, change if the wrong (size-inconsistent) Ziman phase convention is used in place of correct (size-consistent) Wallace phase convention.

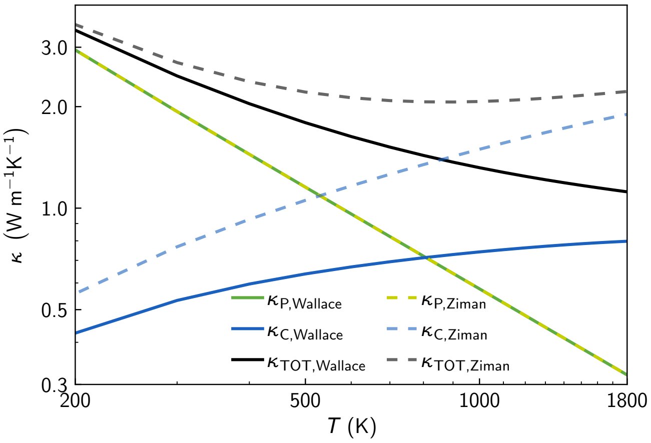

Figure 1.G.1 – **Effect of the phase convention on the thermal conductivity of $La_2Zr_2O_7$.** Solid lines are the conductivities computed using the correct size-consistent Wallace smooth phase convention, dashed lines are the conductivities computed using the size-inconsistent Ziman phase convention. The populations' conductivities are green (κ_P), and they are equal in the two phase conventions (see text). The coherences' conductivities (κ_C) are blue. The total conductivity (black) is given by the sum $\kappa_{TOT} = \kappa_P + \kappa_C$. Ziman's step-like phase convention yields a total conductivity larger than that obtained using the smooth phase convention of Wallace. We recall that the populations and coherences conductivity tensors of $La_2Zr_2O_7$ are proportional to the identity (see Sec 1.7.1), thus populations and coherences conductivities are represented as scalars in this plot.

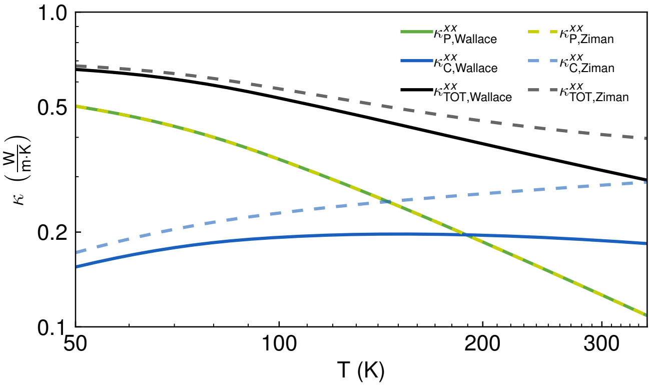

Figure 1.G.2 – **Effect of the phase convention on the thermal conductivity of CsPbBr$_3$.** Solid lines are the conductivities computed using the correct size-consistent Wallace smooth phase convention, dashed lines are the conductivities computed using the size-inconsistent Ziman phase convention (also reported in Fig. 1 of Ref. [67]). The populations' conductivities are green (κ^{xx}_{P}), and they are equal in the two phase conventions (see text). The coherences' conductivities (κ^{xx}_{C}) are blue. The total conductivity (black) is given by the sum $\kappa^{xx}_{\mathrm{TOT}} = \kappa^{xx}_{\mathrm{P}} + \kappa^{xx}_{\mathrm{C}}$. Ziman's step-like phase convention yields a total conductivity larger than that obtained using the smooth phase convention of Wallace.

Clearly, the populations' terms of the conductivity κ_{P} is not affected by the phase convention adopted, since the diagonal elements of the velocity operator do not depend on the phase convention (see Eq. (1.48)); the differences in the conductivity are especially relevant at very high temperature and arise exclusively from the coherences' conductivity κ_{C}, with the Ziman's phase convention yielding a larger κ_{C}.

1.H The limiting case of harmonic glasses

As discusses in Sec. 1.5.2, a glass can be described as the limiting case of a disordered but periodic crystal with an increasingly larger unit cell ($N_{at} \to \infty$, *i.e.* $\mathcal{V} \to \infty$), and thus with the Brillouin zone reducing to the point $\boldsymbol{q}$=$\mathbf{0}$ only. In this ideal bulk limit the particle-like conductivity in Eq. (1.44) vanishes ($\kappa_P^{\alpha\beta}$=0), since at $\boldsymbol{q}$=$\mathbf{0}$ acoustic vibrations have zero specific heat, and the time-reversal symmetry of the dynamical matrix [77] implies that the group velocities for optical vibrations are zero. Consequently, these vibrations are called "nonpropagating"; it is the wave-like contribution ($\kappa_C^{\alpha\beta}$ in Eq. (1.44)) that determines a nonzero total conductivity, provided some off-diagonal velocity-operator elements are nonzero (a condition that is verified when vibrations are nonpropagating and "extended", *i.e.* not Anderson-localized [52, 73]). In this Appendix we show that in the limiting case of harmonic glasses, the coherence contribution to the thermal conductivity κ_C reduces to the Allen-Feldman formula [44, 73]:

$$\kappa_A = \frac{1}{\mathcal{V}} \sum_i C_i(T) D_i(T); \tag{1.147}$$

where i=1,...,3$\cdot N_{\rm at}$ denotes a vibrational mode of the non-periodic glass (and thus has wavevector $\boldsymbol{q}$=$\mathbf{0}$, omitted here for the sake of the conciseness). In Eq. (1.147), $C_i(T)$=$\big(\frac{\hbar\omega_i^2}{\mathcal{V}T}\big)\big(-\frac{\partial\bar{N}_i}{\partial\omega_i}\big)$ is the specific heat of a vibrational mode with energy $\hbar\omega_i$ ($\bar{N}_i=\big(\exp\left[\hbar\omega_i/(k_B T)\right]-1\big)^{-1}$ is the Bose-Einstein distribution) and $D_i(T)$ is the diffusivity [73] of the vibrational mode i:

$$D_i(T)=\frac{\pi}{3\omega_i^2}\sum_{j\neq i}\left|\vec{V}^{\rm A}_{i,j}\frac{\omega_i+\omega_j}{2}\right|^2\delta(\omega_i-\omega_j). \tag{1.148}$$

$\vec{V}^{\rm A}_{s,s'}$ is the velocity operator derived by Auerbach and Allen [146] following the approach developed by Hardy [16]; it is evaluated at $\boldsymbol{q}$=$\mathbf{0}$ and it is different from the velocity operator discussed in this work:

$$\vec{V}^{\rm A}(\boldsymbol{q})_{s,s'}=\frac{\omega(\boldsymbol{q})_s+\omega(\boldsymbol{q})_{s'}}{2\sqrt{\omega(\boldsymbol{q})_s\omega(\boldsymbol{q})_{s'}}}\vec{V}(\boldsymbol{q})_{s,s'}. \tag{1.149}$$

Importantly, such differences are irrelevant for the computation of the harmonic mode diffusivity (1.148), since the Dirac delta in Eq. (1.148) selects only the elements corresponding to (quasi) degenerate eigenstates, and these are equivalent for the two velocity operators in equation (1.149).

We now want to show that in the harmonic disordered limit the normalized trace of the coherence conductivity ($\frac{1}{3}\kappa_C^{\alpha\alpha}$) is equivalent to the Allen-Feldman formula (1.147). To this aim, we discretize the coherences term in Eq. (1.44), replacing [144] $\frac{1}{(2\pi)^3}\sum_s\int_{\mathfrak{B}}d^3q\to\frac{1}{\mathcal{V}N_{\rm c}}\sum_s\sum_{\boldsymbol{q}}$ ($N_{\rm c}$ is the number of $\boldsymbol{q}$-points appearing in the summation), and then we consider the amorphous limit in which $N_{\rm c}$=1 and $\boldsymbol{q}$=$\mathbf{0}$ (thus from now on the dependence on $\boldsymbol{q}$ will be omitted). Then, we recast the resulting expression in terms of quantities appearing in Eq. (1.147), $\frac{\hbar^2}{k_B T^2}\omega_s\bar{N}_s[\bar{N}_s{+}1]{=}{-}\frac{\partial\bar{N}_s}{\partial\omega_s}\frac{\hbar\omega_s}{T}$, and we consider the following ordered limits: first, we take the limit $\Gamma_s{\to}\eta\ \forall\ s$; then we consider $\eta{\to}0$. As a result, we obtain

$$\kappa^{\alpha\beta}_{\rm dis}{=}{-}\sum_{s\neq s'}\frac{\hbar\omega_s^2}{\mathcal{V}T}\frac{\partial\bar{N}_s}{\partial\omega_s}\frac{\pi}{\omega_s}\delta(\omega_{s'}{-}\omega_s)\frac{\omega_s{+}\omega_{s'}}{2}V^{\alpha}{}_{s,s'}V^{\beta}_{s',s}; \tag{1.150}$$

where we have obtained the delta distribution as the limit of a Lorentzian for $\Gamma_s{\to}\eta{\to}0$. Computing the normalized trace of the conductivity $\kappa_A{=}\kappa^{\alpha\alpha}_{\rm dis}/3$, we recover the Allen-Feldman formula with $\vec{V}^{\rm A}_{s,s'}$ (Eq. (1.149)) replaced by the velocity operator defined in equation (1.33) computed at the Brillouin zone center ($\omega_s{=}\omega(\boldsymbol{q}{=}\mathbf{0})_s$, $\bar{N}_s{=}\bar{N}(\boldsymbol{q}{=}\mathbf{0})_s$ and $\vec{V}_{s,s'}{=}\vec{V}(\boldsymbol{q}{=}\mathbf{0})_{s,s'}$):

$$\kappa_A{=}\frac{1}{3}\sum_{s'\neq s}-\frac{\hbar\omega_s^2}{\mathcal{V}T}\frac{\partial\bar{N}_s}{\partial\omega_s}\frac{\pi}{\omega_s^2}\delta(\omega_{s'}-\omega_s)\left(\frac{\omega_s+\omega_{s'}}{2}\right)^2V^{\alpha}_{s,s'}V^{\alpha}_{s',s}. \tag{1.151}$$

1.I Computational details

1.I.1 $La_2Zr_2O_7$

The crystal structure of $La_2Zr_2O_7$ is cubic with spacegroup Fd$\bar{3}$m [227] and has been taken from the materials project database [147] (id = mp-4974 [148]). The equilibrium crystal structure has been computed performing a "vc-relax" calculation with Quantum ESPRESSO [149] and testing the functionals LDA (with ultrasoft pseudopotentials from the psilibrary [150]), PBEsol (with GBRV [151] pseudopotentials), and PBE with Grimme D2 correction [152] (with pseudopotentials from the SSSP precision library [153, 154]). A summary of the computational parameters and equilibrium lattice parameter is reported in Table 1.I.1.

Table 1.I.1 – Lattice parameters of $La_2Zr_2O_7$ (cubic) obtained by first-principles simulations or experiments [155]. A 4×4×4 mesh of k-points with a (1×1×1) shift is used.

functional	cutoff [Ry] (dual)	lattice parameter [Å]
LDA	80 (8)	10.6594462
PBE+D2	50 (8)	10.6591719
PBEsol	50 (8)	10.7391572
Experiment [155]		10.805

The PBEsol functional has been selected on the basis of the best agreement between first-principles and experimental lattice parameters [155] (see table (1.I.1)). Second-order force constants have been computed on a 4×4×4 mesh using density-functional perturbation theory [40] and accounting for the non-analytic term correction due to the dielectric tensor and Born effective charges. Third-order force constants have been computed using the finite-difference method implemented in ShengBTE [68], on a 2×2×2 supercell, integrating the Brillouin zone with a 2×2×2 Monkhorst-Pack mesh, and considering interactions up to 7.8 Å. Then, harmonic force constants have been converted from Quantum ESPRESSO format to `hdf5` format using PHONOPY [156], and third order force constants have been converted to `hdf5` format using HIPHIVE [69]. The WBTE conductivity formula (1.44) has been implemented in the PHONO3PY software [70] (such an implementation will be made publicly available in a next release). Results reported in Fig. 1.6 have been computed using a mesh 19×19×19, and evaluating the collision operator accounting for natural-abundance isotopic scattering [33, 137] and third-order anharmonicity [36, 37, 41, 70, 99, 157]. The conductivity has been computed using the single-mode relaxation time approximation (SMA), since for this system the exact Peierls-Boltzmann thermal conductivity is known to be practically indistinguishable from the SMA value [60] (in agreement with expectations for materials with ultralow thermal conductivity [37, 101]). The tetrahedron method has been used for the computation of the phonon linewidths. The data shown in Fig. 1.6 for κ_P are compatible with the Peierls-Boltzmann conductivity presented in Ref. [60].

1.I.2 $CsPbBr_3$

The crystal structure of orthorhombic $CsPbBr_3$ has been taken from Ref. [158] (Crystallographic Open Database [159] id 4510745) and converted to *Pnmb* spacegroup using VESTA [160]. The equilibrium crystal structure has been obtained performing a "vc-relax" calculation with Quantum ESPRESSO [149], employing the PBEsol exchange-correlation functional and GBRV [151] pseudopotentials. The PBEsol functional is selected on the basis of its good agreement between first-principles and experimental lattice parameters [46, 158] (see table (1.I.2)) and its capability to accurately describe the vibrational properties of inorganic halide perovskites [46]. Kinetic energy cutoffs of 50 and 400 Ry have been used for the wave functions and the charge density; the Brillouin zone has been integrated with a Monkhorst-Pack mesh of 5×5×4 points, with a (1,1,1) shift, and second-order force constants have been computed on a 4×4×4 mesh using density-functional perturbation theory [40] and accounting for the non-analytic term correction due to the dielectric tensor and Born effective charges. Third-order force constants have been computed using the finite-difference method implemented in ShengBTE [68], on a 2×2×2 supercell, integrating the Brillouin zone with a 2×2×2 Monkhorst-Pack mesh, and considering interactions up to 6 Å. Then, anharmonic force constants have been converted from SHENGBTE format to `mat3R` format using the conversion software `d3_import_shengbte.x` provided with the D3Q package [41, 161], including interactions up to the third neighbouring cell for the re-centering of the third-order force constants (parameter NFAR=3). Thermal conductivity calculations have been performed with the software D3Q, using a mesh 8×7×5. The collision operator has been computed using a Gaussian smearing of 2 cm^{-1}, considering third-order anharmonicity [37, 41] and scattering due to isotopes at natural abundance [33, 137]. The conductivity is computed using the single-mode relaxation time approximation (SMA), since for this system the exact thermal conductivity is practically indistinguishable from the SMA value (in agreement with expectations for materials with ultralow thermal conductivity [37, 101]). The data shown in Fig. 1.7 for $\kappa_P^{\alpha\beta}$ are compatible with the theoretical results presented in Ref. [46] and related Supplementary Material. In particular, the direction xx in this work corresponds to the [010] direction in Ref. [46]. Experimental data from Ref. [46] do not allow to evaluate the effect of boundary scattering, as they refer to nanowires having roughly the same size, and are smaller than all the nanowires used in Ref. [111]. Therefore, we compared the bulk thermal conductivity predictions of equation (1.44) with the experimental data from Ref. [111]. The results reported in Fig. 1.7 have been reproduced using the software PHONO3PY [70] and the tetrahedron method (the softwares PHONOPY [156] and HIPHIVE [69] have been used to convert force constants from Quantum ESPRESSO or ShengBTE format to the `hdf5` format used by PHONO3PY).

An implementation of Eq. (1.44) will be made available as an update for the packages PHONO3PY [70] and D3Q [37, 41, 161].

Table 1.I.2 – Lattice parameters of orthorhombic $CsPbBr_3$, obtained by first-principles simulations or experiments [46, 162]. The directions $\hat{x}$, $\hat{y}$ and $\hat{z}$ discussed e.g. in figure (1.7) refer respectively to lattice vectors $\boldsymbol{a}_1$, $\boldsymbol{a}_2$ and $\boldsymbol{a}_3$.

	a_1 [Å]	a_2 [Å]	a_3 [Å]
Present (th)	7.963	8.389	11.632
Ref. [46] (th)	7.990	8.416	11.674
Ref. [158] (exp)	8.198	8.244	11.735
Ref. [162] (exp)	8.223	8.243	11.761

2 Heat conduction in glasses and its application to vitreous silica

The trend of the temperature-conductivity curve of crystals is opposite to that of glasses (Fig. 2.0.1). As discussed in Chapter 1, the behavior of crystals was addressed by Peierls, who explained how crystals behave as “phonon gases”, since phonons (atomic vibrations) have a mean free path determined by anharmonicity and thus dependent on temperature and phonon energy. The opposite behavior of glasses was addressed by Kittel in 1949 [71] introducing the phenomenological model of a phonon liquid, based on the speculation that atomic vibrations have a mean free path that is determined by the disorder length scale, and is thus independent from temperature and energy of the vibration.

Kittel’s phenomenological model has aroused some controversy [44, 72], since it relies on Peierls’ theory for periodic crystals to describe non-periodic glasses. A major step forward in this field was made by Allen and Feldman in 1989, who introduced the harmonic theory for the conductivity of disordered solids and used it to resolve the microscopic mechanisms underlying heat conduction in glasses in terms of a “vibrational-mode diffusivity”. The Allen-Feldman theory focuses on the (low-temperature) regime where anharmonicity is negligible and disorder is the dominant limiting factor for the conductivity [73], and in such a regime it has successfully explained the increasing trend of the temperature-conductivity curve of several amorphous solids [44, 52, 163].

In this chapter we rely on the unified theory of thermal transport introduced in Chapter 1 to explore the role of anharmonicity in determining the thermal conductivity of glasses, analyzing vitreous silica as a paradigmatic case. We also introduce an “anharmonic thermal diffusivity”, a quantity that allows to interpret heat conduction in glasses microscopically and accounting for anharmonicity, disorder, and the quantum Bose-Einstein statistics of atomic vibrations. We show that in the low-temperature limit, where anharmonicity phases out, the anharmonic thermal diffusivity introduced here reduces to the harmonic thermal diffusivity defined by Allen and Feldman. Finally, we use the anharmonic thermal diffusivity to estimate the mean free path of vibrational excitations in glasses and shed light on Kittel’s phonon-liquid phenomenological model for glasses.

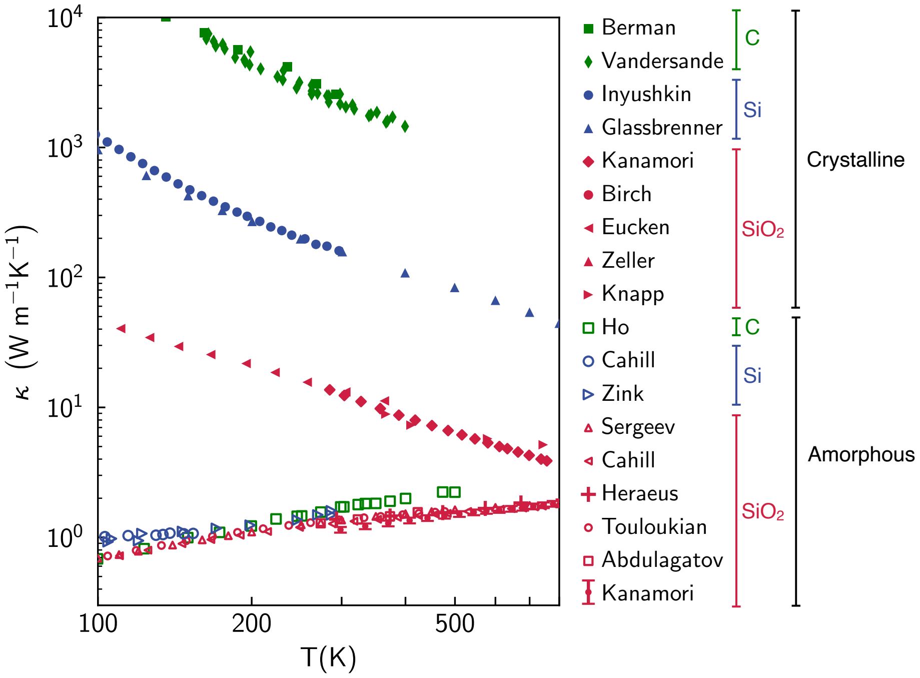

Figure 2.0.1 – **Thermal conductivities of bulk crystals and glasses.** Bulk crystals display a thermal conductivity that decreases with temperature, while glasses display the opposite trend. The thermal conductivity of crystals is strongly influenced by the chemical composition, while the conductivity of glasses is not. Crystalline materials have a much larger conductivity compared to their amorphous allotropes. For carbon, the conductivity of the crystalline phase (diamond) has been taken from the experimental work of Vandersande *et al.* [164] and Berman *et al.* [165], while the experimental data for amorphous carbon have been taken from the review by Ho *et al.* [166]. For silicon, experimental measurements of the conductivity of the amorphous structure have been taken from Zink *et al.* [167], and Cahill *et al.* [168], while experimental data for the crystalline structure have been taken from Glassbrenner *et al.* [54] and Inyushkin *et al.* [169]. For SiO_2, the experimental values of the conductivity of the crystalline structure (α-quartz, along direction c) have been taken from Eucken [170], Birch *et al.* [171], Knapp [172], Zeller *et al.* [173] and Kanamori *et al.* [174]; the data for the amorphous structure have been taken from the experimental works of Wray *et al.* [175], Kanamori *et al.* [174], Touloukian *et al.* [176], Sergeev *et al.* [177], Cahill [178], Abdulagatov *et al.* [179], Yang *et al.* [180] and Heraeus [181].

This chapter is written in the form of a research article. The work presented here has been done jointly with my PhD advisor, Prof. Nicola Marzari, and with Prof. Francesco Mauri (University of Rome “La Sapienza”). I contributed to this work as first author, specifically I did the analytical and numerical calculations with inputs from Prof. Nicola Marzari and Prof. Francesco Mauri, and I wrote the first draft of the manuscript.

Full bibliographic reference:
Michele Simoncelli, Francesco Mauri, Nicola Marzari,
Heat conduction in glasses and its application to vitreous silica. To be submitted.

Heat conduction in glasses and its application to vitreous silica

Michele Simoncelli [1], Francesco Mauri[2], Nicola Marzari[1]

2.1 Abstract

Predicting the thermal conductivity of glasses has hitherto been a prohibitively complex problem for first-principles techniques. Therefore, the conductivity of glasses has often been predicted combining the Allen-Feldman theory with classical potentials, or more recently using molecular dynamics in the Green-Kubo formulation, with the former being an harmonic quantum theory accurate in the low-temperature regime, and the latter being an approach accounting for anharmonicity but having an underlying classical Maxwell-Boltzmann statistics, thus accurate in the high-temperature regime only. Recently, a generalized Wigner-Boltzmann transport equation has been introduced [M. Simoncelli, N. Marzari, and F. Mauri, *Nat. Phys.* **15**, 809 (2019)], allowing to describe thermal transport in glasses over the entire temperature range, accounting for both the quantum statistics of atomic vibrations and anharmonicity. Here, we discuss how the interplay between the quantum statistics of atomic vibrations, disorder, and anharmonicity determines the thermal properties of amorphous solids, and we provide a general protocol to perform first-principles calculations of thermal conductivity in glasses. We also show the emergence of a phonon liquid signature in vitreous silica, corresponding to atomic vibrations having mean free paths that are mainly determined by the disorder length scale.

2.2 Introduction

In glasses, thermal conductivity increases with increasing temperature [173, 178]; bulk crystals exhibit instead the opposite trend, where conductivity decreases with increasing temperature [11, 35, 37]. For crystals, Peierls' theory [11] showed already in 1929 how heat is carried by phonon wavepackets that propagate and scatter as if they were particles of a gas, since they have mean free paths much larger than the lattice spacing. These mean free paths depend on both phonon energy and temperature. The behavior of glasses was addressed by Kittel in 1949 [71] introducing the phenomenological model of a phonon liquid, based on the speculation that atomic vibrations have a mean free path that is determined by the disorder length scale, and is thus a constant, *i.e.* independent from temperature and energy. However, this model lacks rigorous validation and has aroused some controversy [44, 52, 72, 73], since it describes nonperiodic glasses through Peierls' theory for periodic crystals.

A key step forward was made by Allen and Feldman in 1989, who envisioned that in disordered systems heat is carried by the couplings between vibrational modes that arise from the off-diagonal elements of the velocity operator [44]. Thus, they formulated an harmonic theory—

---

[1] Theory and Simulation of Materials (THEOS) and National Centre for Computational Design and Discovery of Novel Materials (MARVEL), École Polytechnique Fédérale de Lausanne, Lausanne, Switzerland.

[2] Dipartimento di Fisica, Università di Roma La Sapienza, Piazzale Aldo Moro 5, I-00185 Roma, Italy

valid at temperatures low enough that disorder is the dominant limiting factor [73]—which predicts a thermal conductivity that mirrors the specific heat, *i.e.* increases with temperature up to a saturation value. The role of anharmonicity on heat transport in glasses—missing from the Allen-Feldman harmonic formulation (AF)—was first investigated in the 1980s with the fracton model, based on the conjecture that glasses (which do not have a fractal structure) have vibrational excitations that behave analogously to those of materials characterized by a fractal structure (e.g. porous or granular solids) [182, 183]; still, such conjecture lacks proof or experimental evidence [184]. A number of studies have instead investigated thermal transport using molecular dynamics in the Green-Kubo (GKMD) formulation (either relying on classical [51, 53, 185, 186] or first-principles [74, 187, 188] simulations) or in a non-equilibrium setup (NEMD) [51, 189, 190]. GKMD or NEMD account rigorously for anharmonicity, while missing quantum effects on vibrations, since the statistic underlying these simulations is that of Maxwell-Boltzmann distinguishable particles; therefore, additional phenomenological corrections are often adopted [186]. Even in the high-temperature regime, where the Bose-Einstein statistics can be approximated to the Maxwell-Boltzmann one, these approaches require models containing hundreds to thousands of atoms and simulations of the order of tens to hundreds of picoseconds, with computational costs that have until recently [191] hindered their application.

The recently-introduced Wigner-Boltzmann transport equation (WBTE) [67, 192] (Chapter 1) has shown that, in addition to Peierls' particle-like heat propagation, a complementary wave-like heat-conduction mechanism emerges when the phase coherences between atomic vibrations allows tunnelling, offering a comprehensive approach to heat-transport phenomena in solids, that encompass both crystals (where particle-like propagation dominates) and amorphous systems and glasses (where wave-like tunnelling dominates). Here we show that the thermal properties of glasses are mainly determined by disorder and, at low temperatures, by the quantum Bose-Einstein statistics of vibrations, since accounting for anharmonicity using the WBTE yields results that are practically indistinguishable from those obtained from the harmonic Allen-Feldman approach. We showcase these findings with first-principles calculations of the thermal properties of vitreous silica, as a paradigmatic model for a glass. Finally, we investigate heat conduction at the microscopic level, introducing the notion of anharmonic thermal diffusivity, and using this quantity to define the mean free paths of vibrational excitations in glasses. The numerical results support Kittel's speculation that glasses behave indeed as phonon liquids, with mean free paths independent from vibrations' energies and limited by the disorder length scale.

2.3 Wigner-Boltzmann formulation for thermal transport

From the WBTE formulation [67, 192] it rigorously emerges that heat conduction in dielectric solids is mediated by two coexisting mechanisms: particle-like propagation of vibrational eigenstates, and wave-like tunnelling between pairs of vibrational eigenstates. The WBTE formalism is general and can be used to describe solids with any degree of disorder, ranging from ordered crystals with small primitive cell and thus large Brillouin zone, to disordered glasses with infinitely-large primitive cell and thus the Brillouin zone reducing to the point $\boldsymbol{q}=\boldsymbol{0}$ only. In practice, in numerical simulations non-periodic glasses are approximately described as crystals with extremely large but finite primitive cell, thus having an extremely small but finite Brillouin zone where wavevectors different from $\boldsymbol{q}=\boldsymbol{0}$ can be defined. We will discuss in the next section the details on how to simulate accurately non-periodic glasses using finite-size models, after having introduced here the salient features of the WBTE formulation in the general case where vibrations can have a wavevector different from $\boldsymbol{q}=\boldsymbol{0}$.

For low-thermal-conductivity solids, which are the focus of this work, the WBTE can be solved accurately within the so-called single-mode relaxation-time approximation (SMA, see Appendix 2.A for details), which allows to write the conductivity in the following compact form:

$$\kappa = \frac{1}{\mathcal{V} N_{\mathrm{c}}}\sum_{\boldsymbol{q},s,s'} \frac{\omega(\boldsymbol{q})_s+\omega(\boldsymbol{q})_{s'}}{4}\left(\frac{C(\boldsymbol{q})_s}{\omega(\boldsymbol{q})_s}+\frac{C(\boldsymbol{q})_{s'}}{\omega(\boldsymbol{q})_{s'}}\right)\frac{\|\boldsymbol{V}(\boldsymbol{q})_{s,s'}\|^2}{3}\pi\mathscr{F}_{[\Gamma(\boldsymbol{q})_s+\Gamma(\boldsymbol{q})_{s'}]}(\omega(\boldsymbol{q})_s-\omega(\boldsymbol{q})_{s'})\,, \quad (2.1)$$

where the wavevector $\boldsymbol{q}$ and the mode index s label a vibrational eigenstate having energy $\hbar\omega(\boldsymbol{q})_s$, anharmonic linewidth $\hbar\Gamma(\boldsymbol{q})_s$, and specific heat

$$C(\boldsymbol{q})_s=C(\omega(\boldsymbol{q})_s,T)=\frac{\hbar^2\omega^2(\boldsymbol{q})_s}{k_{\mathrm{B}}T^2}\bar{N}(\boldsymbol{q})_s\big(\bar{N}(\boldsymbol{q})_s+1\big) \quad (2.2)$$

($\bar{N}(\boldsymbol{q})_s=[\exp(\hbar\omega(\boldsymbol{q})_s/k_{\mathrm{B}}T)-1]^{-1}$ is the Bose-Einstein distribution at temperature T). The quantity

$$\|\boldsymbol{V}(\boldsymbol{q})_{s,s'}\|^2=\sum_{\alpha=1}^{3} V^{\alpha}(\boldsymbol{q})_{s,s'}V^{\alpha}(\boldsymbol{q})_{s',s} \quad (2.3)$$

denotes the square modulus of the velocity operator [192] between eigenstates s and s' at the same wavevector $\boldsymbol{q}$ (α denotes a Cartesian direction, and since vitreous solids are in general isotropic, the scalar conductivity (2.1) is computed as the average trace of the tensor $\kappa^{\alpha\beta}$ given by Eq. (1.44); N_{c} is the number of $\boldsymbol{q}$-points entering in such a summation and $\mathcal{V}$ is the primitive-cell volume. Finally, $\mathscr{F}$ is a Lorentzian distribution having a full width at half maximum (FWHM) equal to $\Gamma(\boldsymbol{q})_s+\Gamma(\boldsymbol{q})_{s'}$:

$$\mathscr{F}_{[\Gamma(\boldsymbol{q})_s+\Gamma(\boldsymbol{q})_{s'}]}\big(\omega(\boldsymbol{q})_s-\omega(\boldsymbol{q})_{s'}\big)=\frac{1}{\pi}\frac{\frac{1}{2}\big(\Gamma(\boldsymbol{q})_s+\Gamma(\boldsymbol{q})_{s'}\big)}{\big(\omega(\boldsymbol{q})_s-\omega(\boldsymbol{q})_{s'}\big)^2+\frac{1}{4}\big(\Gamma(\boldsymbol{q})_s+\Gamma(\boldsymbol{q})_{s'}\big)^2}\,. \quad (2.4)$$

Particle-like heat-conduction determines the diagonal terms ($s=s'$) of the summation in the conductivity (2.1), since these can be written as $\kappa_{\mathrm{P}}=\frac{1}{3\mathcal{V}N_{\mathrm{c}}}\sum_{\boldsymbol{q}s}C(\boldsymbol{q})_s\boldsymbol{V}(\boldsymbol{q})_{s,s}\cdot\boldsymbol{\Lambda}(\boldsymbol{q})_s$, *i.e.* as particle-like vibrations having specific heat $C(\boldsymbol{q})_s$ and propagating between collisions over a length $\boldsymbol{\Lambda}(\boldsymbol{q})_s=\boldsymbol{V}(\boldsymbol{q})_{s,s}(\Gamma(\boldsymbol{q})_s)^{-1}$ (here $\boldsymbol{V}(\boldsymbol{q})_{s,s}$ is the propagation (group) velocity and $(\Gamma(\boldsymbol{q})_s)^{-1}$ the typical inter-collision time). Conversely, the thermal-energy transfer via wave-like tunnelling between two different vibrational eigenstates ($s\neq s'$) yields the summation's off-diagonal terms, and the conductivity contribution originating from these off-diagonal elements is denoted with $\kappa_{\rm C}$ [67, 192]; such wave-like tunnelling conductivity $\kappa_{\rm C}$ draws its name from the analogies with the electronic conductivity originating from Zener interband tunnelling [104]. It has been shown in refs. [67, 192] that in "simple" crystals, *i.e.* those characterized by phonon interbranch spacings much larger than their linewidths, particle-like mechanisms dominate and thus $\kappa_{\rm P} \gg \kappa_{\rm C}$, while in "complex" crystals characterized by interbranch spacings smaller than the linewidths both these mechanisms are relevant, implying $\kappa_{\rm P} \lesssim \kappa_{\rm C}$.

2.4 Glasses in periodic boundary conditions

A glass can be described as the limiting case of a disordered but periodic crystal with an increasingly larger primitive cell ($N_{\rm at} \to \infty$, *i.e.* $\mathcal{V} \to \infty$), and thus with the Brillouin zone (BZ) reducing to the point $\boldsymbol{q}=\mathbf{0}$ only. If we start already from this ideal bulk limit we obtain $\kappa_{\rm P}=0$ (since at $\boldsymbol{q}=\mathbf{0}$ acoustic vibrations have zero specific heat, and the time-reversal symmetry of the dynamical matrix [77] implies that the group velocities for optical vibrations are zero; consequently, these vibrations are called "nonpropagating"); it is the wave-like contribution $\kappa_{\rm C}$ that determines a nonzero total conductivity, provided some off-diagonal velocity-operator elements are nonzero (a condition that is verified when vibrations are nonpropagating but "extended", *i.e.* not Anderson-localized [52, 73]). Nevertheless, in actual calculations the bulk limit $\mathcal{V} \to \infty$ can not be reached by brute force, and a technique is needed to extrapolate the behavior of the ideal infinite system from a finite-size model of a disordered or glassy system. Here, we model vitreous silica using a large finite-size model with periodic boundary conditions, *i.e.* we treat vitreous silica as a crystal having a large primitive cell. The finite size of the model in use here implies that its Brillouin zone does not reduce to the point $\boldsymbol{q} = \mathbf{0}$ but has a finite volume; therefore, the thermal conductivity (2.1) must be evaluated sampling such a Brillouin zone with a $\boldsymbol{q}$-point mesh. Of course, the size of the $\boldsymbol{q}$-point mesh must be large enough to ensure that computational convergence is reached. We note that evaluating the thermal conductivity (2.1) on a $n \times n \times n$ $\boldsymbol{q}$-point mesh corresponds to computing the conductivity of a crystal made up of $n \times n \times n$ repetitions of the primitive cell, thus increasing the size of the $\boldsymbol{q}$-point mesh simulates a larger system. However, in this procedure the disorder length scale remains limited by the size of the primitive cell, thus it is necessary to check that the finite-size primitive cell employed is large enough to simulate disorder in a realistic way. To this aim, we evaluate the conductivity (2.1) in the $\boldsymbol{q}$-point sampling limit[1] for models of vitreous silica having larger and larger primitive cells. We show in Appendix 2.C that increasing the size of the primitive cell from 108 to 216 atoms does not yield significant variations of the temperature-conductivity curve, suggesting that these finite-size structures are large enough to simulate disorder in a realistic way.

Lowering the temperature yields decreasingly smaller linewidths, and in the combined limit of vanishing linewidths and infinite volume the WBTE allows thermal-energy transfer only between eigenstates that are degenerate in energy. This is apparent from the distribution (2.4) in such ordered limit, that to be well-defined requires first the volume $\mathcal{V}$ to go to infinity, and then each linewidth to vanish towards the same infinitesimal broadening $\hbar\eta$ ($\hbar\Gamma(\boldsymbol{q})_s \to \hbar\eta \to 0 \; \forall \; \boldsymbol{q}, s$, see refs. [44, 67, 73, 192] for details):

---

[1] With "sampling limit" we mean the limit in which the $\boldsymbol{q}$-point mesh is large enough to ensure computational convergence, *i.e.* increasing the size of mesh does not yield significant variations of the computational results.

$$\lim_{\eta\to 0}\left(\lim_{\mathcal{V}\to\infty} \mathscr{F}_{[2\eta]}(\omega(\boldsymbol{q})_s - \omega(\boldsymbol{q})_{s'})\right) = \delta\left(\omega(\boldsymbol{q})_s - \omega(\boldsymbol{q})_{s'}\right). \tag{2.5}$$

Eq. (2.5) implies that the $\kappa_{\rm C}$ term of the WBTE conductivity in the low-temperature bulk limit is equivalent to the harmonic Allen-Feldman expression [44, 73].

The finite size of the periodic model determines a lower bound on the temperature range over which the WBTE is accurate. In fact, for a $N_{\rm at}$-atom model having maximum vibrational energy $\hbar\omega_{\rm max}$, the average spacing between the vibrational energy levels is

$$\Delta\omega_{\rm L} = \frac{\omega_{\rm max}}{3N_{\rm at}}. \tag{2.6}$$

Decreasing the temperature, the linewidths $\hbar\Gamma(\boldsymbol{q})_s$ eventually become smaller than $\hbar\Delta\omega_{\rm L}$, progressively suppressing tunnelling in the distribution (2.4) between neighboring eigenstates (*i.e.* eigenstates that have energy differences of the order of $\hbar\Delta\omega_{\rm L}$ and that would be degenerate in the limit $N_{\rm at}\to\infty$). This would lead to the finite-size model $\kappa_{\rm C}$ failing to represent the harmonic conduction described by the distribution (2.5) and accurate for an ideal glass in the low-temperature limit. Within the aforementioned bulk-limit extrapolation procedure, at low temperature the particle-like conductivity $\kappa_{\rm P}$ becomes larger than the wave-like conductivity $\kappa_{\rm C}$, implying an unphysical, crystal-like conductivity (*i.e.* divergent at very low temperatures) for the periodic model of glass. This lower-bound temperature can be lowered using larger models (larger $N_{\rm at}$ and thus smaller $\Delta\omega_{\rm L}$; see Appendix 2.C); however, increasing computational costs impose limitations to such approach.

This limitation can be overcome exploiting the known analytical low-temperature limit (2.5). In fact, Allen and Feldman [44] showed that the harmonic contribution to the thermal conductivity of an infinite disordered solid can be accurately evaluated using finite-size models by replacing the Dirac δ in Eq. (2.5) with a distribution having a broadening η of the order of $\Delta\omega_{\rm L}$, in order to retain the physical property that heat tunnelling between neighboring eigenstates can occur. Details about this procedure are reported Appendix 2.C, showing that the optimal approach to preserve the low-temperature limit is to use a Voigt profile [193]—a two-parameter distribution $\mathscr{F}_{[\Gamma(\boldsymbol{q})_s+\Gamma(\boldsymbol{q})_{s'},\eta]}$ obtained as a convolution between a Lorentzian with FWHM $\Gamma(\boldsymbol{q})_s+\Gamma(\boldsymbol{q})_{s'}$ and a Gaussian with variance $\eta^2\pi/2$—in place of the one-parameter distribution $\mathscr{F}_{[\Gamma(\boldsymbol{q})_s+\Gamma(\boldsymbol{q})_{s'}]}$ appearing in Eq. (2.1). By doing so Eq. (2.1) reduces to the Allen-Feldman harmonic limit at low temperatures (where $\Delta\omega_{\rm L}\sim\eta\gg\frac{1}{2}(\Gamma(\boldsymbol{q})_s+\Gamma(\boldsymbol{q})_{s'})$), and to the anharmonic WBTE at intermediate and high temperatures (where $\Delta\omega_{\rm L}\sim\eta\ll\frac{1}{2}(\Gamma(\boldsymbol{q})_s+\Gamma(\boldsymbol{q})_{s'})$).

2.5 Thermal conductivity of vitreous silica

Vitreous silica (v-SiO$_2$) is often considered a paradigmatic model for a glass, and has been extensively studied because of its technological relevance in many fields, including e.g. the microelectronic, telecommunication, pharmaceutical and automotive industries [194, 195, 196, 197]. The thermal conductivity of v-SiO$_2$ has been measured in several experiments [174, 175, 176, 177, 178, 179, 180, 181], and results are in general in good agreement between each other. Theoretical predictions for the thermal conductivity of v-SiO$_2$ have been performed combining the Allen-Feldman theory with empirical [198] or semi-empirical [51] potentials. Alternatively, other works have investigated the conductivity of v-SiO$_2$ relying on classical molecular dynamics [51, 186, 189, 190]. Finally, it is worth mentioning that an important step forward in the field has recently been made by Ercole *et al.* [199], who have predicted the thermal conductivity of vitreous silica combining the Green-Kubo method with first-principles molecular dynamics, albeit missing quantum effects such as the Bose-Einstein statistics of atomic vibrations, since first-principles molecular dynamics simulations are characterized by an underlying classical Maxwell-Boltzmann statistics. In summary, simulating the thermal properties of amorphous systems from first first-principles and accounting rigorously for the Bose-Einstein statistics of atomic vibrations and for anharmonicity is a task which has hitherto not been accomplished, and the rest of this Article will discuss how to perform a simulation that fulfills these requirements relying on the WBTE framework.

We show in Fig. 2.5.1 the thermal conductivity of v-SiO$_2$ regularized with the Voigt distribution (rWBTE, solid green line), the Allen-Feldman theory [44] (dashed red, accurate at very low temperatures where anharmonicity phases out) and the standard WBTE [192] (dashed blue, accurate at intermediate and high temperatures where finite-size effects are negligible), and results from first-principles GKMD by Ercole *et al.* [199] (orange scatter points, accurate at high temperature where the quantum Bose-Einstein statistics reduces to the classical Maxwell-Boltzmann statistics underlying the GKMD simulation). It is apparent that at high temperatures, where the anharmonic linewidths are largest (see Fig. 2.C.2), the standard WBTE yields results very close to those obtained from first-principles molecular dynamics by Ercole *et al.* [199], as well as to the harmonic theory of Allen and Feldman. At low temperatures, where anharmonicity phases out (Fig. 2.C.2), the harmonic Allen-Feldman theory predicts correctly the trend of the temperature-conductivity curve observed in experiments; in contrast, first-principles GKMD yields a conductivity far from experiments, this because the physical quantum Bose-Einstein statistics of vibrations deviates significantly from the Maxwell-Boltzmann statistics of GKMD simulations [186]. We also note that in such a low-temperature regime, the regularized WBTE smoothly converges to the harmonic limit.

We highlight how the harmonic Allen-Feldman theory yields a temperature-conductivity curve that is practically indistinguishable from the anharmonic rWBTE, and the saturating trend displayed by these curves appears to be in agreement with the high-temperature conductivity obtained from first-principles GKMD. We recall that the Allen-Feldman theory does not account for anharmonicity, the rWBTE accounts for anharmonicity only at the third lowest order,

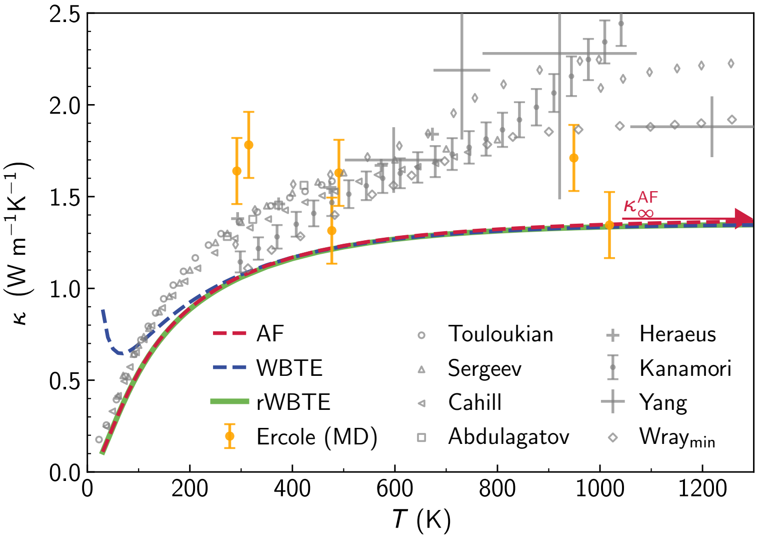

Figure 2.5.1 – **Thermal conductivity of vitreous silica.** Results for a periodic, 144-atom vitreous silica model: red is the Allen-Feldman expression (AF), blue is the standard Wigner-Boltzmann formulation (WBTE) and green is the regularized WBTE (rWBTE). The red arrow on the right indicates the saturation value for the AF conductivity (infinite-temperature or classical limit, see main text). Scatter points are conductivities measured in experiments from Wray *et al.* [175], Kanamori *et al.* [174], Touloukian *et al.* [176], Sergeev *et al.* [177], Cahill [178], Abdulagatov *et al.* [179], Yang *et al.* [180] and Heraeus [181].

and GKMD accounts for anharmonicity exactly (at all orders): the agreement between these approaches at high temperatures, where anharmonic effects are maximized, suggests that the thermal properties of glasses are mainly determined by disorder and not strongly influenced by anharmonicity.

Clearly, all these theoretical approaches fail to describe the increasing trend of the conductivity observed in experiments at high temperatures. Such an increasing trend is attributed in some experimental works to radiative energy transfer [175, 200, 201], which is not taken into account in the theoretical approaches employed here. Investigating if radiative energy transfer can explain the discrepancy between theory and experiments at high temperatures will be subject of future theoretical work.

All the quantities needed to evaluate the conductivity have been computed from density-functional theory using a 144-atom model of vitreous silica [202] (see Appendix 2.G for details). We have limited the calculations to a minimum temperature of 30 K because below this temperature the thermal properties are affected by universal features of glasses [72] (the boson peak in the vibrational density of states (vDOS) [203] and the "tunnelling two-level systems" [204]) that require models of v-SiO$_2$ larger than those used in this work in order to be reproduced [205]. Calculations analogous to those of Fig. 2.5.1 have been performed also for two additional, independently-generated v-SiO$_2$ models of 108 [206] and 216 [207] atoms each, and verifying that the results are converged in the size of the periodic model (see Appendix 2.C). We highlight how in the high-temperature limit the AF conductivity inherits the saturating trend from the quantum specific heat (Fig. 2.D.1); the saturation value ($\kappa^{\rm AF}_{\infty}$) can be obtained considering the temperature-independent classical specific heat: $\lim_{T\to\infty} C(\boldsymbol{q})_s = k_B \ \forall \ \boldsymbol{q}, s$.

In order to understand how anharmonicity affects the thermal conductivity of glasses at high temperature, we highlight from the WBTE conductivity (Eqs. (2.1) and (2.4)) that the contribution of the coherences to heat conduction originates from couplings between different vibrational eigenstates, and the strengths of those couplings are given by the average square modulus of the velocity-operator elements $\frac{1}{3}\|\boldsymbol{V}(\boldsymbol{q})_{s,s'}\|^2$. In the high-temperature limit, *i.e.* when the specific heat is close to the classical limit and thus can be considered independent from temperature (see Fig. 2.5.3**b)**), the rWBTE conductivity (2.1) can be seen as a Lorentzian weighted average of velocity-operator elements. The weights in such average depend on the energy difference between the eigenstates coupled, and the temperature-dependent anharmonic linewidths are the scale parameters (FWHM) of the Lorentzian distributions (2.4). Increasing temperature yields larger linewidths (Fig. 2.C.2), resulting in a broader Lorentzian distribution (2.4) that gives more weight to velocity-operator elements with larger energy differences when determining the conductivity. Therefore, the variation of the elements of the velocity operator with respect to the energy differences $\hbar\omega_{\rm d}=\hbar(\omega(\boldsymbol{q})_s-\omega(\boldsymbol{q})_{s'})$ determines how the conductivity varies with increasing temperature[2]: matrix elements increasing (decreasing) with ω_d imply a conductivity increasing (decreasing) with temperature. From this reasoning and from the saturating trend of the temperature-conductivity curve for vitreous silica shown in Fig. 2.5.1, we expect the velocity-operator elements for v-SiO$_2$ to be approximately constant with respect to with ω_d. To verify this prediction, we plot in Fig. 2.5.2 the velocity-operator elements for v-SiO$_2$ as a function of the energy difference $\hbar\omega_{\rm d}=\hbar(\omega(\boldsymbol{q})_s-\omega(\boldsymbol{q})_{s'})$ and of the energy average $\hbar\omega_{\rm a}=\hbar(\omega(\boldsymbol{q})_s+\omega(\boldsymbol{q})_{s'})/2$:

$$\langle |V^{\rm avg}_{\omega_{\rm a}\omega_{\rm d}}|^2\rangle = [\mathscr{G}(\omega_{\rm a},\omega_{\rm d})]^{-1}\frac{1}{\mathcal{V}N_{\rm c}}\sum_{\boldsymbol{q},s,s'}\frac{\|\boldsymbol{V}(\boldsymbol{q})_{s,s'}\|^2}{3}\delta\left(\omega_{\rm d}-(\omega(\boldsymbol{q})_s-\omega(\boldsymbol{q})_{s'})\right)\delta\left(\omega_{\rm a}-\frac{\omega(\boldsymbol{q})_s+\omega(\boldsymbol{q})_{s'}}{2}\right); \tag{2.7}$$

$\mathscr{G}(\omega_{\rm a},\omega_{\rm d})$ is a density of states that serves as normalization (see Appendix 2.E for details). The one-dimensional projections in the top panels of Fig. 2.5.2 show that these velocity-operator elements are almost constant at varying $\hbar\omega_{\rm d}$ for all values of $\hbar\omega_{\rm a}$. These findings validate the reasoning above: the variation of the velocity-operator elements $\frac{1}{3}\|\boldsymbol{V}(\boldsymbol{q})_{s,s'}\|^2$ with respect to the energy differences $\hbar\omega_{\rm d}=\hbar(\omega(\boldsymbol{q})_s-\omega(\boldsymbol{q})_{s'})$ determines how the conductivity varies with increasing temperature, implying that a saturating temperature-conductivity curve is obtained when most of the velocity-operator elements do not vary with $\hbar\omega_{\rm d}$.

---

[2] In this work the velocity operator is considered independent from anharmonicity and temperature, since we employ the standard approximation of considering the force constants to be independent from anharmonicity and temperature (for vitreous silica this approximation is realistic, as discussed in Appendix 2.D).

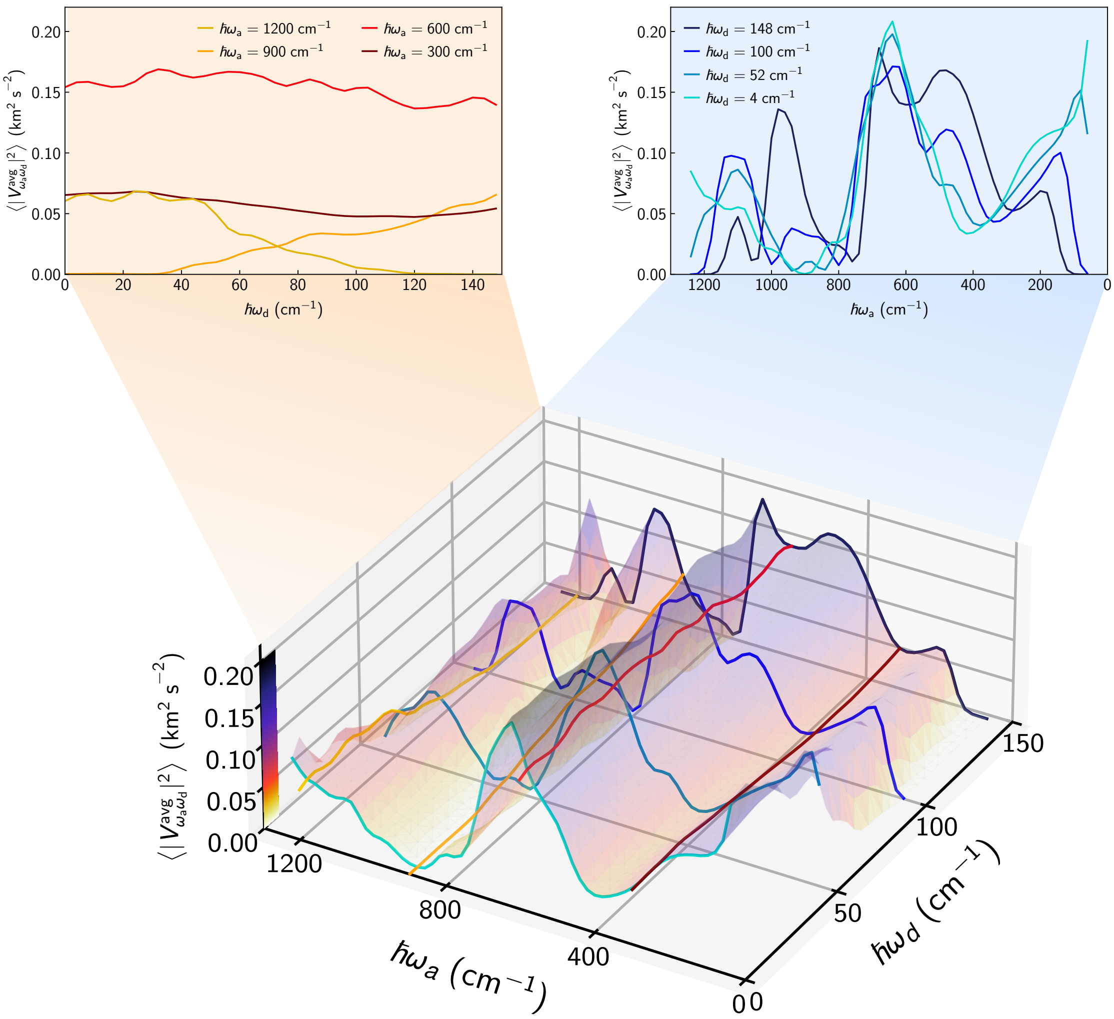

Figure 2.5.2 – **Velocity operator and conductivity saturation with temperature.** Average square modulus of the velocity-operator elements $\langle|V^{\mathrm{avg}}_{\omega_a\omega_d}|^2\rangle$ as a function of the energy differences ($\hbar\omega_{\mathrm{d}}{=}\hbar(\omega(\boldsymbol{q})_s{-}\omega(\boldsymbol{q})_{s'})$) and averages ($\hbar\omega_{\mathrm{a}}{=}\hbar\frac{\omega(\boldsymbol{q})_s+\omega(\boldsymbol{q})_{s'}}{2}$) of the two coupled eigenstates (having wavevector $\boldsymbol{q}$ and modes s, s'; see text for details). The one-dimensional projections in the top panels show that the elements $\langle|V^{\mathrm{avg}}_{\omega_a\omega_d}|^2\rangle$ are almost constant for increasingly different energies. For increasingly larger temperatures, these almost-constant elements drive the saturation the WBTE conductivity (Eqs. (2.1,2.4)), yielding results equal to the Allen-Feldman conductivity curve (Fig. 2.5.1).

2.5.1 Anharmonic Thermal diffusivity

In order to gain insight on the microscopic mechanisms underlying conduction it is useful to resolve how each vibrational mode contributes to transport, *i.e.* the quantity of heat that it carries and the rate at which it diffuses. In simple crystals the populations (particle-like) conductivity is several orders of magnitude larger than the coherences conductivity ($\kappa_{\mathrm{P}} \gg \kappa_{\mathrm{C}}$). Therefore, in simple crystals it is possible to consider only κ_{P}, and thus use Peierls' kinetic theory to resolve κ_{P} microscopically in terms of contributions from particle-like heat carriers. Rigorously speaking, the microscopic heat carriers in simple crystals are relaxons, *i.e.* collective excitations of phonons that are eigenvectors of the scattering matrix appearing in the LBTE [39, 66]. However, for the materials analyzed in this work the SMA approximation is accurate (*i.e.*, it yields results practically indistinguishable from the exact solution, see Appendix 2.F); therefore, here one can rely on the SMA and related simplified microscopic interpretation of thermal transport that considers phonons as the heat carriers [39].

For complex crystals or glasses wave-like conduction mechanisms emerge from the phase coherence between pairs of vibrational modes, as apparent from the off-diagonal terms ($s{\neq}s'$) of the double summation appearing in Eq. (2.1). It is possible to extract the contribution of a single vibration to such pairwise transport mechanism by factorizing the single-vibration specific heat $C(\boldsymbol{q})_s$ in the regularized WBTE conductivity (2.1), *i.e.* recasting it as $\kappa = \frac{1}{\mathcal{V}N_{\mathrm{c}}}\sum_{\boldsymbol{q}s} C(\boldsymbol{q})_s D(\boldsymbol{q})_s$, with the expression for the "anharmonic thermal diffusivity" $D(\boldsymbol{q})_s$ dictated by such factorization:

$$D(\boldsymbol{q})_s = \sum_{s'} \frac{\omega(\boldsymbol{q})_s+\omega(\boldsymbol{q})_{s'}}{4C(\boldsymbol{q})_s}\left(\frac{C(\boldsymbol{q})_s}{\omega(\boldsymbol{q})_s}+\frac{C(\boldsymbol{q})_{s'}}{\omega(\boldsymbol{q})_{s'}}\right)\frac{\|\boldsymbol{V}(\boldsymbol{q})_{s,s'}\|^2}{3}\pi\mathcal{F}_{[\Gamma(\boldsymbol{q})_s+\Gamma(\boldsymbol{q})_{s'},\eta]}(\omega(\boldsymbol{q})_s-\omega(\boldsymbol{q})_{s'})\,. \tag{2.8}$$

The goal of this decomposition is to resolve the rate at which the heat carried by a vibration with wavevector $\boldsymbol{q}$ and mode s diffuses, while also identifying Anderson-localized vibrations, since these have zero diffusivity [44, 52, 208]. We note that Eq. (2.8) accounts for the effects of anharmonicity on vibrations' diffusion by means of the linewidths, depends on temperature through both the specific heat and the linewidths, and applies to both glasses and crystals (in these latter, such an expression is accurate if and only if the SMA is accurate). In the very-low-temperature and infinite-primitive-cell limit, Eq. (2.8) reduces to the temperature-independent harmonic diffusivity introduced by Allen and Feldman [44] (this follows from the properties of the Voigt distribution $\mathcal{F}_{[\Gamma(\boldsymbol{q})_s+\Gamma(\boldsymbol{q})_{s'},\eta]}$ discussed before); in the following the dependence from temperature will be shown explicitly for the sake of clarity. Since the specific heat of a vibration depends only on its frequency ω and on temperature ($C(\boldsymbol{q})_s{=}C(\omega(\boldsymbol{q})_s,T)$ as shown before), it is convenient to represent also the temperature-dependent anharmonic thermal diffusivity as a function of frequency with $D(\omega,T){=}[g(\omega)\mathcal{V}N_{\mathrm{c}}]^{-1}\sum_{\boldsymbol{q},s}D(\boldsymbol{q})_s\delta(\omega{-}\omega(\boldsymbol{q})_s)$ (here $g(\omega){=}(\mathcal{V}N_{\mathrm{c}})^{-1}\sum_{\boldsymbol{q},s}\delta(\omega{-}\omega(\boldsymbol{q})_s)$ is the vDOS, which can be considered independent from temperature, as also shown in Appendix 2.D). In this frequency-dependent representation the conductivity reads

$$\kappa(T) = \int_0^{\infty} g(\omega)C(\omega,T)D(\omega,T)d\omega\,, \tag{2.9}$$

and intuitively allows to resolve the contribution of vibrations with frequency ω to heat transport through their density of states $g(\omega)$, the heat carried $C(\omega,T)$, and the diffusion rate $D(\omega,T)$. In order to rationalize the temperature-conductivity trend of v-SiO$_2$ in terms of the diffusivity introduced, we report in Fig. 2.5.3 all these quantities. In panel a) we show the vDOS for the 144-atom v-SiO$_2$ model studied, with peaks that are reminiscent of those of crystalline α-cristobalite; this similarity will be further discussed later in connection with the

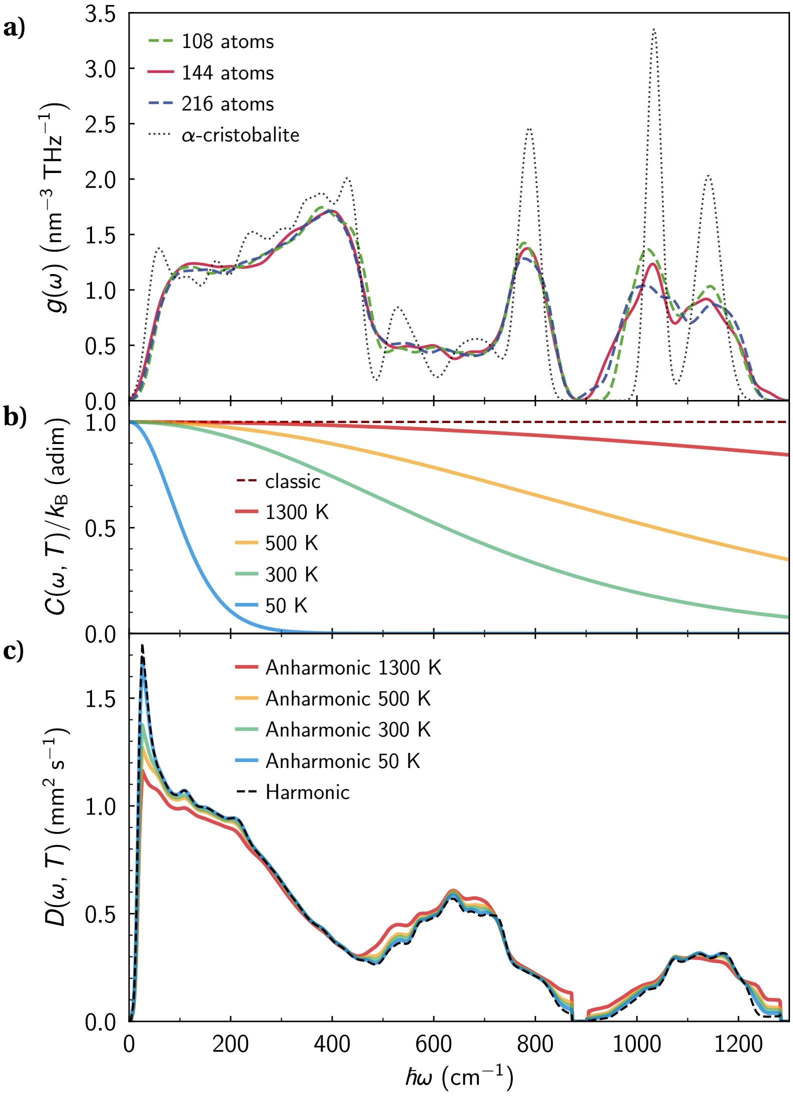

Figure 2.5.3 – **Vibrational DOS, diffusivity and specific heat of vitreous silica.** a) Vibrational density of states of vitreous silica (the dashed green line corresponds to a 108-atom model [206], solid red to a 144-atom model [202] and dashed blue to a 216-atom model [207]). The phonon density of states of α-cristobalite (dotted black line) is also reported for comparison. b) Quantum harmonic specific heat as a function of frequency. Solid lines are obtained evaluating the expression (2.2) as a function of frequency and for different temperatures. We highlight how increasing temperature populates vibrational modes with increasingly larger frequency that consequently contribute to heat conduction. The dashed line represents the classical specific heat (obtained from the quantum specific heat in the infinite-temperature limit), which is independent from frequency. c) Anharmonic thermal diffusivity computed from equation (2.8) using the 144-atom model at different temperatures (solid lines); the harmonic Allen-Feldman diffusivity, independent from temperature, is also reported (dashed line, see text for details).

microscopic length scale of thermal transport. We also show the vDOS of the two additional, independent 108- and 216-atom ν-SiO$_2$ models discussed in Appendix 2.C, very similar to the reference 144-atom model, whose capability to describe realistically vitreous silica has been extensively validated [202]. In panel b) we report the quantum harmonic specific heat as a function of frequency, showing how increasing temperature populates vibrational modes of increasingly larger frequency that consequently contribute to transport. We highlight how, for all the temperatures considered, the quantum specific heat differs from the constant classical limit (obtained letting $T{\to}\infty$ in Eq. (2.2)); this demonstrates the importance of properly accounting for the quantum statistics of vibrations. The solid lines in Panel c) show that the anharmonic thermal diffusivity of ν-SiO$_2$ changes very little with temperature, with visible changes happening mostly at very low frequencies, where the vibrational modes of glasses become similar to those of crystals [52] (this is also supported by the very similar speed of sound found in vitreous silica and in its crystalline counterpart α-cristobalite [209, 210]). We will discuss later how in simple crystals with dominant particle-like conduction mechanisms the diffusivity can be interpreted as $D(\boldsymbol{q})_s = V(\boldsymbol{q})_s\Lambda(\boldsymbol{q})_s$, where $V(\boldsymbol{q})_s$ is the free-propagation velocity of the particle-like vibration (a phonon wavepacket) and $\Lambda(\boldsymbol{q})_s$ its mean free path. In crystals increasing temperature (and thus the anharmonic linewidths) reduces the diffusivity of phonon wavepackets; the reduction of the diffusivity with temperature shown for the low-frequency vibrations of ν-SiO$_2$ in Fig. 2.5.3c) suggests that these are crystal-like, in agreement with the interpretation by Allen and Feldman [52]. The Allen-Feldman diffusivity (dashed line, obtained using Eq. (2.8) and the distribution (2.5) with the constant broadening discussed in Appendix 2.B) is instead independent from temperature.

2.6 The phonon liquid picture

We use the previously-defined anharmonic thermal diffusivity to characterize the microscopic length scale of heat transport in glasses, and compare it with the established case of simple crystals. In particular, we contrast vitreous silica with its crystalline polymorph having the closest density and vibrational properties, *i.e.* α-cristobalite [209, 210]. We show in Appendix 2.F that α-cristobalite is a simple crystal, for which solving the WBTE exactly or employing the SMA approximation gives practically indistinguishable results (Fig. 2.F.1). This, and the aforementioned accuracy of the SMA for amorphous systems with very low conductivity, motivates using the SMA for both α-cristobalite and vitreous silica.

We recall that in the framework of a particle theory, the diffusivity of a particle-like excitation with root-mean-square (RMS) free-propagation velocity $V(\boldsymbol{q})_s$ and inelastic inter-collision time $\tau(\boldsymbol{q})_s$ is $D(\boldsymbol{q})_s{=}V^2(\boldsymbol{q})_s\tau(\boldsymbol{q})_s$ [211], and therefore the RMS mean free path (MFP) of such particle is related to the diffusivity as $\Lambda(\boldsymbol{q})_s{=}D(\boldsymbol{q})_s/V(\boldsymbol{q})_s$. In a simple crystal vibrations behave particle-like and as such have a well-defined free-propagation velocity (the phonon group velocity), which can be represented as a function of the frequency ω as $V(\omega){=}\frac{1}{g(\omega)\mathcal{V}N_c}\sum_{\boldsymbol{q},s}\frac{\|\boldsymbol{V}(\boldsymbol{q})_{s,s}\|}{\sqrt{3}}\delta(\omega{-}\omega(\boldsymbol{q})_s)$. It follows that in the frequency representation, which allows to compare vibrations of α-cristobalite with those of ν-SiO$_2$ as shown in Fig. 2.5.3a, the

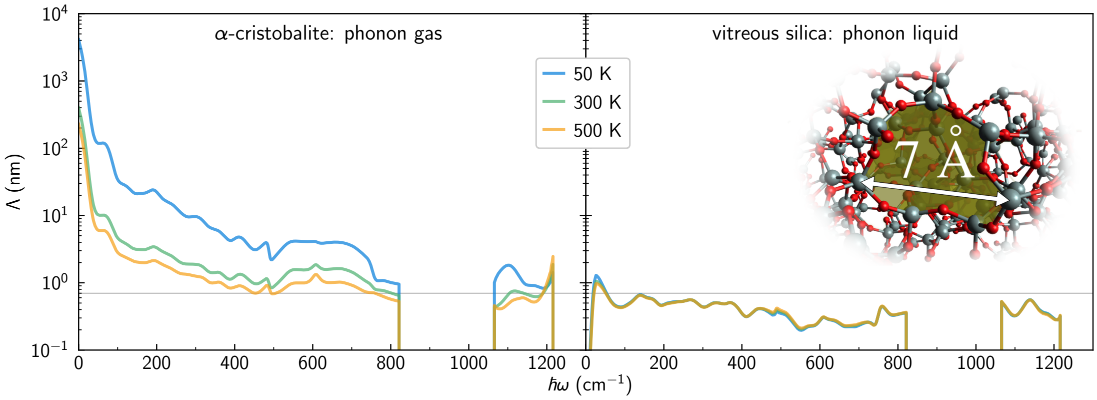

Figure 2.6.1 – **Phonon gas versus phonon liquid.** Mean free paths of α-cristobalite (left) and of vitreous silica (right), both computed according to Eq. (2.10). The MFPs of α-cristobalite are characteristic of a phonon gas: they vary with the vibrational energy and temperature, in analogy with the MFPs of the particles of a classical gas (however, we note that in a classical gas MFPs increase with kinetic energy and temperature [212], while here MFPs of phonons in a simple crystal decrease with energy and temperature). In contrast, vitreous silica can be classified as a "phonon liquid", since the MFPs of the vibrational excitations are determined by the disorder length scale and do not strongly depend on the vibrational energy, in analogy with the MFPs of particles in a classical liquid. The inset and the horizontal line represent the typical size of a ring in vitreous silica.

MFPs of vibrations can be estimated as (see Appendix 2.F for details):

$$\Lambda(\omega, T) = \frac{D(\omega, T)}{V(\omega)}. \tag{2.10}$$

We show in the left panel of Fig. 2.6.1 that for α-cristobalite Eq. (2.10) yields MFPs decreasingly smaller for increasingly larger frequencies; increasing temperature causes a shift of the MFP curve towards smaller values (the three temperatures reported are chosen to cover the range in which α-cristobalite is stable).

In glasses, instead, the diffusivity of a vibration originates from its wave-like tunnelling with other vibrations, and it is not possible to write it as a function of an experimentally-measurable free-propagation velocity $V(\boldsymbol{q})_s$. However, Eq. (2.8) provides an operational definition of a vibration's diffusivity that allows to interpret transport within an effective-particle picture. This can be done with the ansatz below on the free-propagation velocity, and then using Eq. (2.10) to extract the transport length scale from the diffusivity, in analogy with the case of crystals (in such effective-particle picture, we will refer to MFPs for these lengths). For vitreous silica, the vDOS (Fig. 2.5.3a), sound velocities, and other vibrational properties are all very similar to those of α-cristobalite [209, 210]; we thus assume as ansatz that the free-propagation velocity in v-SiO$_2$ is the same as in α-cristobalite. Therefore, we estimate the MFPs of vibrations in v-SiO$_2$ using Eq. (2.10) with the anharmonic thermal diffusivity of vitreous silica (Fig. 2.5.3c) and the velocity of free propagation determined from α-cristobalite (Fig. 2.F.2). Results are reported in the right panel of Fig. 2.6.1, and show that in this picture the MFPs in v-SiO$_2$ are approximately independent from their vibrational energy, and their numerical values are of the order of the disorder length scale ($\sim$ 7 Å, *i.e.* the typical ring size in v-SiO$_2$, also called medium-range order) and thus larger than the interatomic spacing (the average Si-O distance is ~1.63 Å in v-SiO$_2$).

These results reiterate the notion that simple crystals act as "phonon gases", and support quantitatively Kittel's intuition [71] that glasses are "phonon liquids", where vibrations' MFPs are mainly determined by the disorder length scale and thus independent from vibrational energy.

2.7 Conclusions

We have predicted from first-principles the thermal conductivity of a paradigmatic glass such as vitreous silica, accounting for the interplay between the quantum statistics of atomic vibrations, disorder, and anharmonicity relying on the recently introduced Wigner-Boltzmann transport equation [67, 192]. We have investigated at the quantum-mechanical level the trend of the temperature-conductivity curve of glasses. At low temperatures, anharmonicity phases out and the Bose-Einstein statistics determines the conductivity, which features a rapid increase with temperature akin to that of the quantum specific heat, and this trend is correctly captured by the harmonic Allen-Feldman theory and by the regularized WBTE. Increasing temperature (and thus the anharmonic linewidths), the harmonic Allen-Feldman theory and the anharmonic WBTE yield compatible predictions for the conductivity, which display a trend that saturates with temperature. This shows that anharmonicity, which is neglected in the Allen-Feldman theory and considered in the WBTE, does not play an important role in determining the trend at high temperature of the temperature-conductivity curve in paradigmatic glass such as silica. We note in passing that the conductivity obtained from the anharmonic WBTE, which accounts for anharmonicity at the lowest (third) order in the Taylor expansion of the Born-Oppenheimer interatomic potential [192], is, at high temperature, compatible with the conductivity obtained from Green-Kubo first-principles molecular dynamics simulations [199], which fully account for anharmonicity (although these latter consider the statistics of atomic vibrations to be that of Maxwell-Boltzmann classical particles). We have shed light on the negligible effect that anharmonicity has on the conductivity at high temperature, showing that it derives from off-diagonal velocity operator elements — which couple pairs of vibrational eigenstates allowing tunnelling between them — that are constant with respect to the energy difference between the eigenstates coupled.

The theoretical predictions reported here are in agreement with experiments at low temperatures, but fail to describe the increasing trend of the conductivity observed in experiments at high temperatures. Such a discrepancy at high temperatures might be due to not accounting for radiative energy transfer in the WBTE formulation employed here, and the investigation of such an effect will be subject of future theoretical work.

Also, thermal properties in the cryogenic temperature range (below ≈ 30 K) have not been studied here, because these require models of v-SiO_2 larger than those used in this work in order to be reproduced [205], and thus with a prohibitively large computational cost for a first-principles description. Fittingly, recent works have demonstrated the possibility to describe accurately — and at a computational cost much reduced compared to first-principles methods — glassy systems such as amorphous silicon[213, 214, 215]. Combining these advances with the methodology discussed here will potentially enable to study the thermal conductivity of glasses at cryogenic temperatures[167, 203, 205, 216, 217].

We have interpreted heat conduction in terms of frequency-resolved anharmonic thermal diffusivities for vibrations, and used these quantities to characterize the microscopic length scale of heat transport in vitreous silica; results highlight the signature of a phonon liquid, with vibrations' mean free paths determined by the disorder length scale and thus independent from temperature and energy, supporting quantitatively Kittel's conjecture [71].

Appendix

2.A Accuracy of the SMA approximation in glasses

Glasses feature a low thermal conductivity, and this is associated to strong scattering due to anharmonicity or disorder that quickly relaxes vibrational excitations to equilibrium. Furthermore, glasses can be modeled with large primitive cells, ideally containing a number of atoms $N_{\mathrm{at}}\to\infty$, so the $(3N_{\mathrm{at}})^2-3N_{\mathrm{at}}$ off-diagonal Wigner-distribution elements dominate in number over the $3N_{\mathrm{at}}$ diagonal Wigner-distribution elements. These two conditions imply that the role of repopulation (*i.e.* scattering events that yield an increase of the $3N_{\mathrm{at}}$ diagonal Wigner distribution elements) [192] is negligible in glasses, and consequently the SMA—which neglects repopulation—is accurate. In addition, it is known that the SMA works well in low-thermal-conductivity bulk crystalline materials that are characterized by the predominance of momentum-dissipating (Umklapp) over momentum-conserving (normal) phonon collisions [66, 68, 101]. For all the systems analyzed in this work, we have confirmed that solving the WBTE in full or employing the SMA approximation yields conductivities practically indistinguishable (see Fig. 2.F.1).

2.B Finite-size broadening of the Dirac delta and bulk limit within the Allen-Feldman framework

We report in Fig. 2.B.1 the conductivity computed with the Allen-Feldman formula (Eqs. (2.1) and (2.5)) as a function of the computational broadening used to approximate the Dirac distribution (2.5).

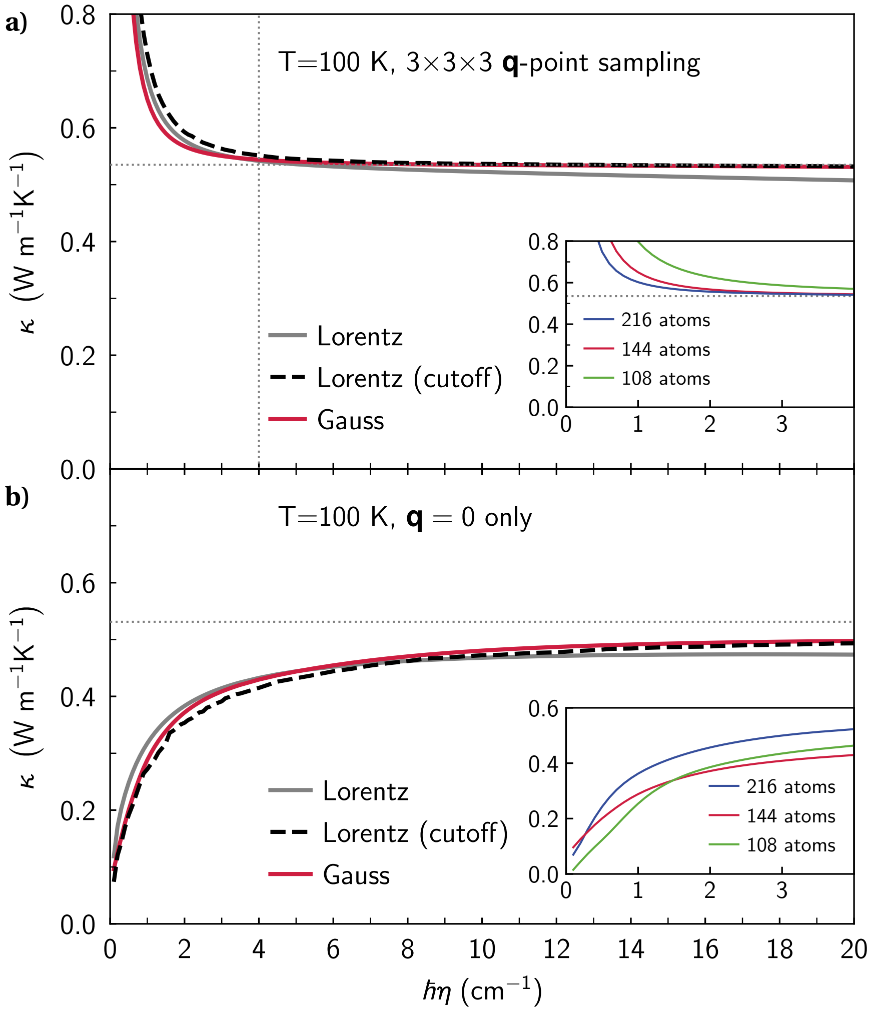

Figure 2.B.1 – **Convergence of broadening η in the harmonic framework.** Harmonic thermal conductivity at 100 K for the 144-atom model of vitreous silica as a function of the computational broadening η used for the Dirac delta appearing in the Allen-Feldman formula (Eqs. (2.1) and (2.5)), computed considering a 3×3×3 sampling of the BZ (panel a)) or considering the point $\boldsymbol{q}$=$\mathbf{0}$ only (panel b)). Different lines refer to different computational broadenings for the Dirac delta: "Lorentz" is a Lorentzian with FWHM 2η; "Lorentz (cutoff)" refers to a Lorentzian with a cutoff at distance 3η from its center (see text for details); "Gauss" is a Gaussian with variance $\eta^2\pi/2$ (*i.e.* the same maximum $(\pi\eta)^{-1}$ of the Lorentzian with FWHM 2η). The vertical dotted line in panel a) shows the value $\hbar\eta = 4$ cm^{-1}; for broadenings larger than this value the Allen-Feldman conductivity is independent from η (*i.e.* very close to the horizontal dotted line). Inset of panel a): increasing the size of the model extends the domain of convergence for the Gaussian broadening to smaller values of η. Panel b): poor convergence of the harmonic theory when sampled at the point $\boldsymbol{q}$=$\mathbf{0}$ only. Inset of panel b): for calculations at the point $\boldsymbol{q}$=$\mathbf{0}$ only, the Gaussian broadenings in the 108- and 216-atom models show the same qualitative behavior as the 144-atom model.

In panel a) we report the AF conductivity computed using different (fat-tailed or light-tailed) broadenings and employing the aforementioned $\boldsymbol{q}$-interpolation technique to determine the bulk limit (we report results obtained with a $3\times3\times3$ $\boldsymbol{q}$-mesh, it has been checked numerically that using larger $5\times5\times5$ and $7\times7\times7$ meshes yields practically unchanged results). In particular, the gray line is a fat-tailed Lorentzian having FWHM 2η, the red line is a light-tailed Gaussian with variance $\eta^2\pi/2$ (*i.e.* the same maximum $(\pi\eta)^{-1}$ of the Lorentzian with FWHM 2η), and the dashed-black line is a light-tailed Lorentzian with cutoff (*i.e.* a Lorentzian up to a distance 3η from the distribution's center and 0 otherwise, such a distribution is aptly normalized). Clearly, light-tailed broadenings yield a wide range of values for η over which the conductivity is not sensitive to the value of η—henceforth this will be referred to as "convergence plateau"—while the fat-tailed Lorentzian broadening yields, when the sampling of the Brillouin zone is considered, a conductivity that slightly decreases when the broadening is increased. Therefore, we choose the light-tailed Gaussian broadening to compute the Allen-Feldman conductivity reported in Fig. 2.5.1; we note this choice mirrors that performed in density-functional-theory calculations for metals, where light-tailed representations of the Dirac delta (e.g. Gaussian [218] or more refined [219, 220]) have been introduced as mathematical tool to improve convergence with respect to Brillouin-zone sampling, and are preferred to the fat-tailed Fermi-Dirac thermal broadening because of superior computational performance [221]. The vertical line in panel a) shows $\hbar\eta$=4 cm^{-1}, a converged value for the parameter η (*i.e.* broadening from which the convergence plateau starts), and the horizontal dotted line is the AF conductivity computed using this value for the Gaussian broadening. Results in Fig. 2.B.1 refer to 100 K; it has been verified numerically that analogous calculations at different temperatures show a similar convergence plateau. More precisely, the converged value $\hbar\eta$=4 cm^{-1} is independent from temperature, and we highlight that for the model of v-SiO$_2$ with 144 atoms (and thus 144·3 vibrational levels) and maximum vibrational energy $\hbar\omega_{\max}$~1300 cm^{-1} (see Fig. 2.5.3a) such a converged value is close to the average spacing between vibrational energy levels, *i.e.* $4\ \text{cm}^{-1} = \hbar\eta \sim \hbar\Delta\omega_{\text{L}} = 1300\ \text{cm}^{-1}/(144{\cdot}3) \simeq 3\ \text{cm}^{-1}$. The inset of Fig. 2.B.1a shows that employing larger models extends AF's convergence plateau to smaller values of η, *i.e.* larger models allow for more accurate approximations of the Dirac distribution. In panel b) we show that the evaluation of the AF conductivity at the point $\boldsymbol{q}$=$\mathbf{0}$ only converges poorly with respect to η. Most importantly, the inset of panel b) demonstrates that the AF conductivity at the point $\boldsymbol{q}$=$\mathbf{0}$ only — where the particle-like conductivity vanishes because of the time-reversal symmetry of the dynamical matrix (see main text) and only the coherences' conductivity is nonzero — depends on the model considered. These considerations motivate computing the harmonic bulk limit of the conductivity with the $\boldsymbol{q}$-interpolation.

The Allen-Feldman temperature-conductivity curves obtained using the $\boldsymbol{q}$-interpolation procedure for the 108-, 144-, and 216-atom models are reported in Fig. 2.C.1 (dashed lines), and together with the inset of Fig. 2.B.1a, these show that the converged value for the harmonic conductivity is compatible between models having different sizes at all the temperatures considered.

2.C Bulk limit within the WBTE formulation

In this section we discuss the computation of the bulk limit of the anharmonic WBTE conductivity (Eqs. (2.1) and (2.4)) using the aforementioned $\boldsymbol{q}$-interpolation technique. The WBTE framework accounts for anharmonicity through the linewidths; these are even functions of $\boldsymbol{q}$ (*i.e.* $\Gamma(\boldsymbol{q})_s = \Gamma(-\boldsymbol{q})_s$) [66]. For systems characterized by a very large primitive cell, the $\boldsymbol{q}$-interpolation procedure has negligible effect on smooth-and-even functions of $\boldsymbol{q}$, because their variations over the very small BZ result in values very similar to those at the point $\boldsymbol{q}$=$\mathbf{0}$; this can be verified e.g. looking at the vibrational energies (which are also even functions of $\boldsymbol{q}$), in particular we checked numerically that the vDOS computed at the point $\boldsymbol{q}$=$\mathbf{0}$ only is in perfect agreement with the vDOS computed interpolating energies over the BZ. In contrast, odd functions of $\boldsymbol{q}$ (e.g. the phonon group velocities $\boldsymbol{V}(\boldsymbol{q})_{ss} = -\boldsymbol{V}(-\boldsymbol{q})_{ss}$ [66]) are constrained to be zero at the point $\boldsymbol{q}$=$\mathbf{0}$, and therefore the $\boldsymbol{q}$-interpolation procedure can have relevant effect on these odd functions (e.g. in Fig. 2.B.1 the difference between the harmonic conductivity computed interpolating over the $\boldsymbol{q}$-mesh or at the point $\boldsymbol{q}$=$\mathbf{0}$ only arises from the diagonal velocity-operator elements). Keeping this in mind, and given that the computational cost for interpolating the anharmonic linewidths is much larger than that for interpolating the vibrational energies or velocity operators (since the linewidths require third-order force constants), when $\boldsymbol{q}$-interpolations are performed over the very small Brillouin zones of glass models we approximate the linewidths to their values at $\boldsymbol{q}$=$\mathbf{0}$. We note that such approximation implies that the acoustic modes, which have zero frequency and zero linewidth at the point $\boldsymbol{q}$=$\mathbf{0}$, are not taken into account in the present framework. An estimate of the effect of these acoustic modes on the thermal conductivity of the 108-atom model is discussed later in Fig. 2.G.1. Accounting for the effect of these acoustic modes on thermal transport requires computing their linewidths at $\boldsymbol{q}$≠$\mathbf{0}$, this problem is computationally very challenging and will be tackled in a future work.

We report in Fig. 2.C.1 a comparison between the conductivity predicted using the WBTE framework with the $\boldsymbol{q}$-interpolation (solid lines) and sampling $\boldsymbol{q}$=$\mathbf{0}$ only (dotted lines). At high temperatures, calculations performed with the $\boldsymbol{q}$-interpolation or considering $\boldsymbol{q}$=$\mathbf{0}$ only give very similar results. At very low temperatures ($T \lesssim 100$ K), the WBTE conductivity computed with the $\boldsymbol{q}$-interpolation diverges; this is a finite-size effect arising from the periodic boundary conditions (a reminiscence of the divergence at low temperature of the conductivity of bulk crystals, as explained in the main text), and indeed for increasingly larger models of vitreous systems it appears at decreasingly lower temperatures.

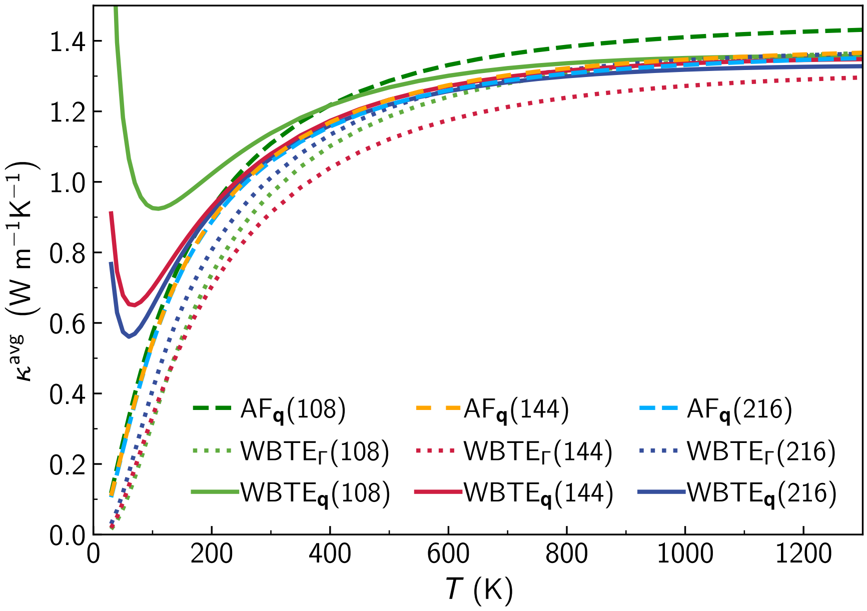

Figure 2.C.1 – **Size effects on conductivity.** Solid lines are the conductivities predicted by the WBTE framework using $\boldsymbol{q}$-interpolation to determine the bulk limit from finite-size glass models containing 108 (green), 144 (red), or 216 (blue) atoms. Dotted lines are the WBTE conductivities computed considering the point $\boldsymbol{q}$=$\mathbf{0}$ only, and dashed lines are predictions from the AF with the $\boldsymbol{q}$-interpolation ($\hbar\eta$=4 cm^{-1} for all the models) to extrapolate the bulk limit (AF calculations at $\boldsymbol{q}$=$\mathbf{0}$ only are not reported because they converge poorly with respect to the broadening η, as shown in Fig. 2.B.1b). It is clear that the anharmonic WBTE$_{\boldsymbol{q}}$ is very close to the harmonic AF$_{\boldsymbol{q}}$ at high temperatures, and then lowering temperature it diverges due to finite-size effects; the divergence of the WBTE$_{\boldsymbol{q}}$ conductivity shifts to decreasingly lower temperatures for increasingly larger models.

2.C.1 WBTE regularization protocol

We recall that the WBTE conductivity in the analytical low-temperature bulk-glass limit (Eqs. (2.1) and (2.5)) describes thermal-energy transfer only between degenerate eigenstates. In practice, when the WBTE conductivity is evaluated numerically using finite-size models, a proper procedure is required to describe such analytical low-temperature bulk-glass limit. In fact, when evaluated using a finite-size model, the WBTE conductivity (2.1,2.4) is accurate up to a lower-bound temperature T_L (defined as the temperature at which the WBTE temperature-conductivity curve changes concavity, see dashed-blue line in Fig. 2.5.1); below T_L, the finite-size effects discussed in the main text lead to a failure in describing the low-temperature regime, giving rise to a crystal-like divergence. One can approach the low-temperature limit by employing larger finite-size models (thus lowering T_L) as shown by the solid lines in Fig. 2.C.1. However this direct technique has practical limitations, since it requires increasingly larger models to predict the conductivity at decreasingly lower temperatures, and the computational cost of calculations increases with the size of the model.

A more convenient approach is the regularization protocol introduced in the main text. This protocol uses the numerical broadening technique proposed by Allen and Feldman [44, 73] to accurately estimate the analytical low-temperature bulk limit for the conductivity (Eqs. (2.1,2.5)) from a finite-size glass model, and then smoothly connects this Allen-Feldman conductivity—accurate at very low temperatures also in finite-size models—to the WBTE conductivity that for finite-size models can be applied at any temperature higher than T_L. This combination allows to predict the thermal conductivity of glasses over the entire non-cryogenic temperature range (*i.e.* above 30K, as explained in the main text) using finite-size models that can be solved from first-principles and accounting for anharmonicity. In addition to being analytically justified in the low-temperature limit as discussed before, this procedure is also validated numerically (Fig. 2.C.1). In practice, within the regularization protocol this is achieved using a Voigt profile as a distribution $\mathscr{F}$ appearing in the conductivity formula (2.1). We adopt the convention that defines the Voigt profile as the convolution between a Lorentzian with FWHM $\Gamma(\boldsymbol{q})_s+\Gamma(\boldsymbol{q})_{s'}$ and a Gaussian with variance $\eta^2\pi/2$, and we denote such two-parameter distribution with $\mathscr{F}_{[\Gamma(\boldsymbol{q})_s+\Gamma(\boldsymbol{q})_{s'},\eta]}$. The mathematical details of the Voigt profile can be found e.g. in ref. [193]. For the scope of this section it is sufficient to recall that for $\eta \ll \frac{1}{2}(\Gamma(\boldsymbol{q})_s+\Gamma(\boldsymbol{q})_{s'})$ the Voigt profile reduces to a Lorentzian with FWHM $\Gamma(\boldsymbol{q})_s+\Gamma(\boldsymbol{q})_{s'}$, while in the opposite limit of $\eta \gg \frac{1}{2}(\Gamma(\boldsymbol{q})_s+\Gamma(\boldsymbol{q})_{s'})$ the Voigt profile reduces to a Gaussian with variance $\eta^2\pi/2$; the transition between these two limiting distributions is smooth and occurs for $\eta \sim \frac{1}{2}(\Gamma(\boldsymbol{q})_s+\Gamma(\boldsymbol{q})_{s'})$. As anticipated in the main text, these considerations imply that Eq. (2.1) with the Voigt distribution $\mathscr{F}_{[\Gamma(\boldsymbol{q})_s+\Gamma(\boldsymbol{q})_{s'},\eta]}$ reduces to the AF with the Gaussian broadening η at very low temperatures (where anharmonicity phases out and thus $\frac{1}{2}(\Gamma(\boldsymbol{q})_s+\Gamma(\boldsymbol{q})_{s'}) \ll \eta$), and to the anharmonic WBTE at intermediate and high temperatures (where the large linewidths imply $\frac{1}{2}(\Gamma(\boldsymbol{q})_s+\Gamma(\boldsymbol{q})_{s'}) \gg \eta$).

In order to make these considerations quantitative, we compare in Fig. 2.C.2a the linewidths of vitreous silica (computed at $\boldsymbol{q}=\boldsymbol{0}$ using the 144-atom model and accounting for third-order anharmonicity [41, 68] and isotopic scattering [137]) with the broadening value $\hbar\eta$=4 cm^{-1} used in the AF formulation (horizontal dashed line, obtained as a central value of the convergence plateau reported in Fig. 2.B.1). It is clear that at 50 K most of the linewidths are smaller than $\hbar\eta$=4 cm^{-1}, implying that the Voigt profile is practically equivalent to the Gaussian with variance $\eta^2\pi/2$ used in the AF framework (dashed-red in Fig. 2.5.1); in contrast, at 300 K most of the linewidths are larger than $\hbar\eta$=4 cm^{-1}, implying that the Voigt profile is practically equivalent to the Lorentzian (2.4) used in the WBTE framework (dashed-blue in Fig. 2.5.1). In the intermediate temperature range from 100 to 300 K, where the linewidths are comparable to the constant broadening η, the Voigt profile (solid-green in Fig. 2.5.1) connects smoothly the low-temperature conductivity obtained with the AF to the intermediate-and-high-temperature conductivity obtained from the WBTE.

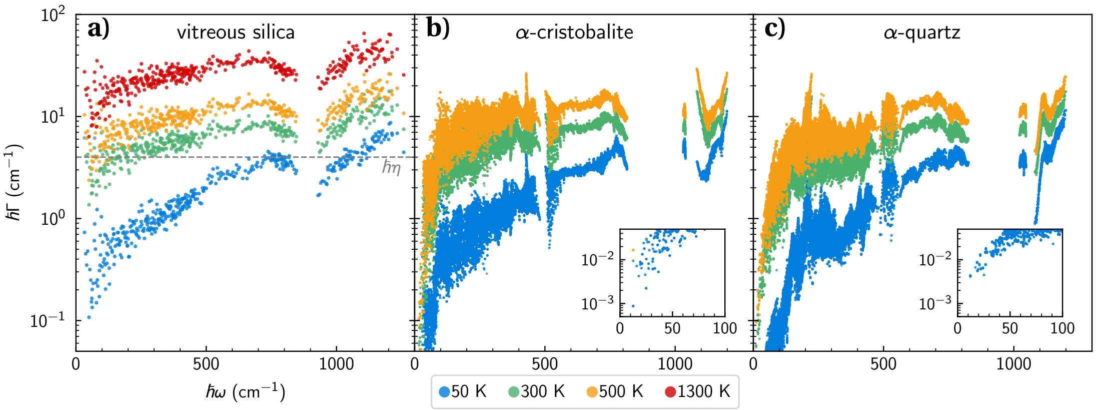

Figure 2.C.2 – **Increase of linewidths with temperature.** Increasing temperature yields an increase of the linewidths that account for third-order anharmonicity [41, 68] and isotopic scattering [137] in both vitreous and crystalline materials: panel a) shows a 144-atom vitreous-silica model, panel b) α-cristobalite, and panel c) α-quartz. The temperatures of 50, 300, and 500 K at which the linewidths distributions are reported are chosen to span the temperature range over which all these materials are stable. The 1300 K distribution shows the behavior at high temperature, and is reported only for vitreous silica since α-cristobalite and α-quartz are not stable at this temperature. The insets in panel b) and c) show the linewidths at low vibrational energies for α-cristobalite and α-quartz, respectively. The horizontal dashed line in panel a) represents the fixed broadening $\hbar\eta$=4 cm^{-1} used in the Allen-Feldman framework.

2.D Quantum harmonic specific heat

We show in Fig. 2.D.1 that the theoretical quantum harmonic specific heat at constant volume ($C_V^{\mathrm{Th}}(T) = \frac{1}{\rho \mathcal{V} N_c} \sum_{\boldsymbol{q},s} C(\boldsymbol{q})_s$, where ρ is the density) is in close agreement with the experimental specific heat at constant pressure [222]. This suggests that the renormalization of vibrational energies due to anharmonicity and temperature [62, 63, 223, 224] are negligibly small for v-SiO$_2$ in the temperature range considered [225], and as such these effects are not considered in this work.

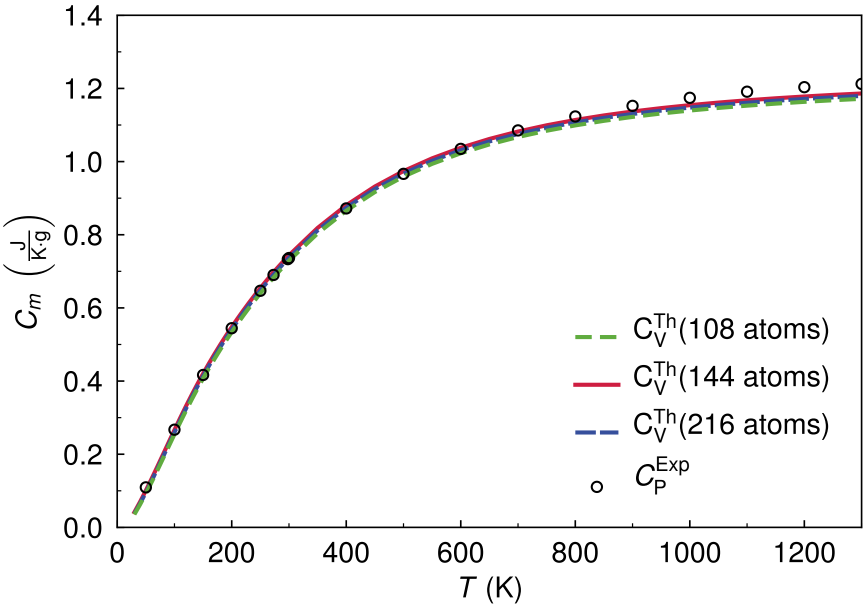

Figure 2.D.1 – **Specific heat of vitreous silica.** Lines are the quantum harmonic specific heat at constant volume and as a function of temperature computed in this work for vitreous-silica models containing 108 (dashed-green), 144 (solid-red), and 216 (dashed-blue) atoms. Circles are measurements [222] of the specific heat at constant pressure and different temperatures.

2.E Velocity operator as a function of frequency

In this section we provide all the details on the plot reported in Fig. 2.5.2. In order to gain insights into the increasing, non-saturating trend of the conductivity with temperature (Fig. 2.5.1), we recast the conductivity formula (2.1) as a function of $\omega_\mathrm{a}{=}(\omega(\boldsymbol{q})_s{+}\omega(\boldsymbol{q})_{s'})/2$ and $\omega_\mathrm{d}{=}\omega(\boldsymbol{q})_s{-}\omega(\boldsymbol{q})_{s'}$:

$$\begin{aligned}\kappa = \int_{0}^{\omega_\mathrm{max}} d\omega_\mathrm{a} \int_{-\omega_\mathrm{max}}^{\omega_\mathrm{max}} d\omega_\mathrm{d} \Bigg[\frac{1}{\mathcal{V} N_\mathrm{c}} \sum_{\boldsymbol{q},s,s'} \delta_{\sigma_\mathrm{a}}\!\left(\frac{\omega(\boldsymbol{q})_s+\omega(\boldsymbol{q})_{s'}}{2} - \omega_\mathrm{a} \right) \delta_{\sigma_\mathrm{d}}\!\big((\omega(\boldsymbol{q})_s-\omega(\boldsymbol{q})_{s'}) - \omega_\mathrm{d} \big) \\ \times \frac{\omega(\boldsymbol{q})_s+\omega(\boldsymbol{q})_{s'}}{4} \frac{\|\boldsymbol{V}(\boldsymbol{q})_{s,s'}\|^2}{3} \left(\frac{C(\boldsymbol{q})_s}{\omega(\boldsymbol{q})_s} + \frac{C(\boldsymbol{q})_{s'}}{\omega(\boldsymbol{q})_{s'}} \right) \pi \mathscr{F}_{[\Gamma(\boldsymbol{q})_s+\Gamma(\boldsymbol{q})_{s'},\eta]}(\omega(\boldsymbol{q})_s-\omega(\boldsymbol{q})_{s'}) \Bigg]\end{aligned} \tag{2.11}$$

where the distributions δ_σ are Gaussian broadenings of the Dirac delta:

$$\delta_\sigma(\Omega-\omega) = \frac{1}{\sqrt{2\pi}\sigma} \exp\left[-\frac{1}{2\sigma^2} (\Omega-\omega)^2 \right]. \tag{2.12}$$

In order to achieve our goal to recast Eq. (2.11) in terms of physically-insightful frequency-dependent functions, we approximate the linewidths as single-valued function of frequency, *i.e.* $\Gamma(\boldsymbol{q})_s = \mathscr{L}(\omega(\boldsymbol{q})_s)$; using this approximation allows to recast Eq. (2.11) as follows:

$$\kappa = \int_0^{\omega_{\rm max}} d\omega_{\rm a} \int_{-\omega_{\rm max}}^{\omega_{\rm max}} d\omega_{\rm d} \mathscr{G}(\omega_{\rm a},\omega_{\rm d}) \mathscr{C}(\omega_{\rm a},\omega_{\rm d}) \langle |V^{\rm avg}_{\omega_{\rm a},\omega_{\rm d}}|^2\rangle \pi \mathscr{F}_{[\mathscr{L}(\omega_{\rm a}+\frac{\omega_{\rm d}}{2})+\mathscr{L}(\omega_{\rm a}-\frac{\omega_{\rm d}}{2}),\eta]}(\omega_{\rm d}), \tag{2.13}$$

where $\mathscr{G}(\omega_{\rm a},\omega_{\rm d})$ is a density of states

$$\mathscr{G}(\omega_{\rm a},\omega_{\rm d}) = \frac{1}{N_{\rm at}} \frac{1}{\mathcal{V} N_{\rm c}} \sum_{\boldsymbol{q},s,s'} \delta_{\sigma_{\rm a}}\left(\frac{\omega(\boldsymbol{q})_s + \omega(\boldsymbol{q})_{s'}}{2} - \omega_{\rm a}\right) \delta_{\sigma_{\rm d}}\big((\omega(\boldsymbol{q})_s - \omega(\boldsymbol{q})_{s'}) - \omega_{\rm d}\big), \tag{2.14}$$

$\mathscr{C}(\omega_{\rm a},\omega_{\rm d})$ is a specific heat

$$\mathscr{C}(\omega_{\rm a},\omega_{\rm d}) = \frac{\omega_{\rm a}}{2}\left(\frac{C(\omega_{\rm a}+\frac{\omega_{\rm d}}{2})}{\omega_{\rm a}+\frac{\omega_{\rm d}}{2}} + \frac{C(\omega_{\rm a}-\frac{\omega_{\rm d}}{2})}{\omega_{\rm a}-\frac{\omega_{\rm d}}{2}}\right), \tag{2.15}$$

and $\langle |V^{\rm avg}_{\omega_{\rm a},\omega_{\rm d}}|^2\rangle$ is the average square modulus of the velocity operator defined in Eq. (2.7) (whose Dirac delta must be broadened with the Gaussian δ_σ discussed here) and plotted in Fig. 2.5.2. Eq. (2.13), together with Fig. 2.5.2 and Fig. 2.C.2, sheds light on the saturating trend of the conductivity with temperature (Fig. 2.5.1). In fact, among the various quantities entering in Eq. (2.13), the density of states (2.14) and the specific heat (2.15) have a trivial temperature dependence (the former is temperature-independent, the latter saturates with increasing temperature). The change of variable performed in Eq. (2.11) shows that the temperature-conductivity trend is determined by how the average square velocity-operator elements vary with the vibrational frequency difference $\omega_{\rm d}$, because the increase of the linewidths with temperature (Fig. 2.C.2a) results in a broader Lorentzian distribution (2.4) that encloses velocity-operator elements corresponding to increasingly larger frequency differences $\omega_{\rm d}$. In particular, for vitreous silica, the average square velocity-operator elements are almost independent from $\omega_{\rm d}$ for all values of $\omega_{\rm a}$ (Fig. 2.5.2). It follows that the saturating trend of the conductivity at high temperature reported in Fig. 2.5.1 is inherited from the saturating trend of the specific heat.

Fig. 2.5.2 is computed using a 3×3×3 $\boldsymbol{q}$-point mesh, $\hbar\sigma_{\rm a} = 20\ {\rm cm}^{-1}$ and $\hbar\sigma_{\rm d} = 4\ {\rm cm}^{-1}$. Increasing the $\boldsymbol{q}$-point mesh to 5×5×5 or multiplying $\sigma_{\rm a}$ and $\sigma_{\rm d}$ by a factor of 2 does not produce significant changes.

2.F Mean free path calculations

Here we discuss the details of the vibrations' MFP, in particular the "simple-crystal" behavior of α-cristobalite and the mathematical subtleties underlying Eq. (2.10) used to compute the MFP of vibrational excitations in α-cristobalite and vitreous silica (Fig. 2.6.1).

We show in Fig. 2.F.1a that α-cristobalite is a simple crystal, since its conductivity tensor com-

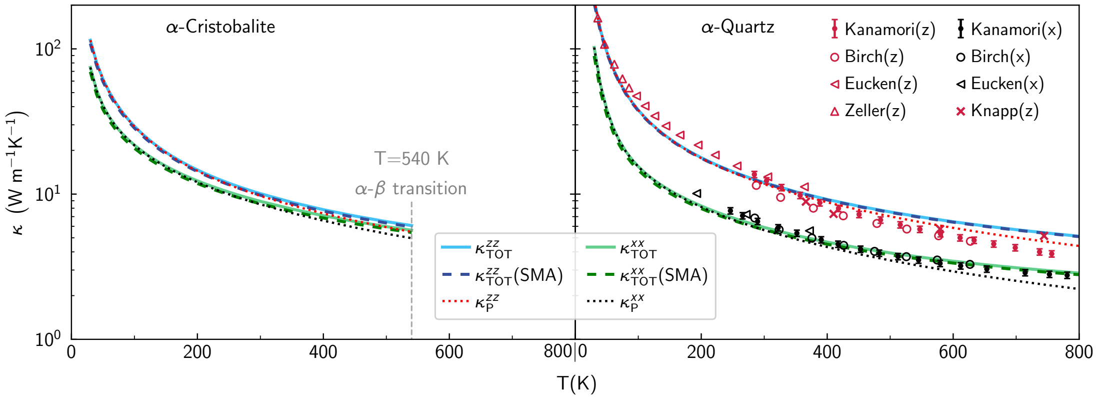

Figure 2.F.1 – **Thermal conductivity of α-cristobalite and α-quartz.** For these materials the total bulk conductivity resulting from the full solution of the WBTE (solid lines) is practically indistinguishable from the bulk conductivity computed relying on the SMA approximation (dashed lines). The α-β transition temperature for cristobalite is around 540 K [226], below this temperature both α-cristobalite and α-quartz are to a good approximation simple crystals, since their total conductivity is predominantly determined by the particle-like contribution ($\kappa_{\rm P}$, dotted lines). Scatter points are experiments by Eucken [170], Birch *et al.* [171], Knapp [172], Zeller *et al.* [173] and Kanamori *et al.* [174].

ponents (solid lines) are predominantly determined by the particle-like contribution (dotted lines), *i.e.* $\kappa^{\alpha\beta}_{\rm TOT} = \kappa^{\alpha\beta}_{\rm P} + \kappa^{\alpha\beta}_{\rm C} \approx \kappa^{\alpha\beta}_{\rm P}$. In addition, Fig. 2.F.1a shows that the SMA approximation is accurate in α-cristobalite, since the conductivities obtained from solving the WBTE exactly (solid lines) or employing the SMA approximation (dashed lines) are in very good agreement, and thus we will rely on the SMA approximation in the following. To the best of our knowledge, the thermal conductivity of α-cristobalite has been measured only in a powder sample and exclusively at room temperature [227]; no measurements are available in the literature to validate the theoretical temperature-conductivity curve for a bulk single crystal reported in Fig. 2.F.1a. Therefore, in order to validate the accuracy of the present first-principles approach also in crystalline silica polymorphs, we show in Fig. 2.F.1b that first-principles thermal conductivity calculations for α-quartz—performed with the same methodology used for α-cristobalite (see the Appendix 2.C for details)—yield conductivities in close agreement with experimental measurements.

Within the SMA approximation, for a simple crystal the RMS of the MFP of a phonon reads $\Lambda(\boldsymbol{q})_s{=}V(\boldsymbol{q})_s\tau(\boldsymbol{q})_s{=}D(\boldsymbol{q})_s/V(\boldsymbol{q})_s$, where $V(\boldsymbol{q})_s$ is the RMS of the phonon group velocity, $\tau(\boldsymbol{q})_s{=}(\Gamma(\boldsymbol{q})_s)^{-1}$ is the phonon lifetime and $D(\boldsymbol{q})_s{=}(V(\boldsymbol{q})_s)^2\tau(\boldsymbol{q})_s$ the normalized trace of the phonon diffusivity tensor. Such a MFP can be recast in terms of the frequency ω as follows:

$$\Lambda(\omega) = \frac{1}{g(\omega)\mathcal{V}N_{\rm c}}\sum_{\boldsymbol{q},s} V(\boldsymbol{q})_s\tau(\boldsymbol{q})_s\delta(\omega-\omega(\boldsymbol{q})_s)\,. \tag{2.16}$$

Eq. (2.16) is equivalent to Eq. (2.10) if the free-propagation velocity and lifetime are both single-valued functions of the frequency, *i.e.* $V(\boldsymbol{q})_s{=}V(\omega(\boldsymbol{q})_s)$ and $\tau(\boldsymbol{q})_s{=}\tau(\omega(\boldsymbol{q})_s)$. It has

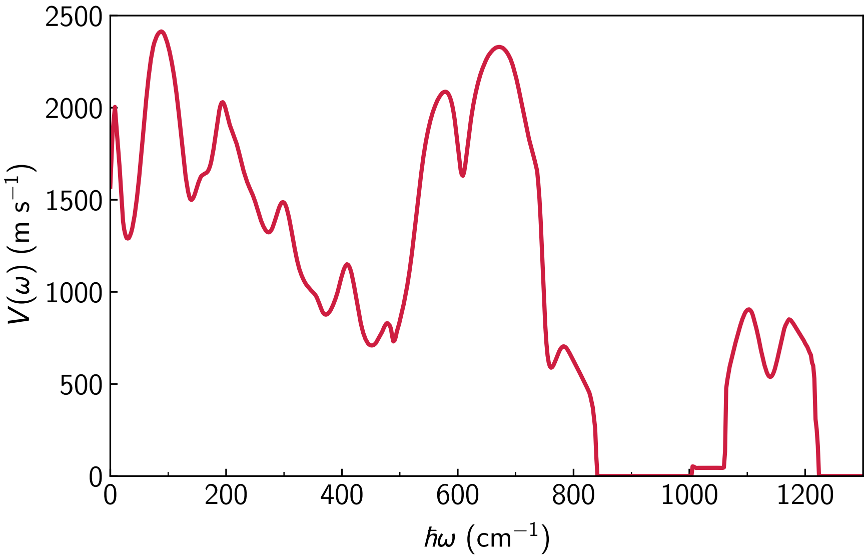

Figure 2.F.2 – **Vibration's free-propagation velocity in α-cristobalite.** Root mean square phonon group velocity in α-cristobalite as a function of phonon energy, computed as detailed in the main text and using a Gaussian broadening of $\hbar\sigma = 2$ cm^{-1} for the Dirac delta.

been checked numerically that for α-cristobalite Eq. (2.10) and Eq. (2.16) yield practically unchanged results.

Finally, recalling that in simple crystals vibrations (phonons) predominantly behave particle-like and as such have a well-defined free-propagation velocity (given by the phonon group velocity), we report in Fig. 2.F.2 the RMS phonon group velocity for α-cristobalite computed as a function of vibrational energy as detailed in the main text.

2.G First-principles calculations

All the density-functional theory (DFT) calculations have been performed with the Quantum ESPRESSO distribution [149] using the PBE functional with semiempirical Grimme-D2 corrections (PBE+D2) [152]. This choice is motivated by the benchmarks given in ref. [228] and accounting for the capability of Quantum ESPRESSO to compute phonons using density-functional perturbation theory (DFPT) [40] with the PBE+D2 functional. This choice is validated by the agreement between theoretical and experimental densities reported in table 2.G.1 and also by the capability of this functional to accurately describe the thermal properties of α-quartz (Fig. 2.F.1). We have used pseudopotentials from the SSSP efficiency library [153, 154] with a cutoff of 50 Ry and a dual of 8. In the following we report the details for all the three different systems studied: vitreous silica, α-cristobalite, and α-quartz.

Vitreus silica. The 144-atom structure of vitreous silica discussed in this work is taken from ref. [202] (and is available in the Materials Cloud Archive [234]). This structure is used as a reference model in this article since it reproduces accurately the experimental effective neutron density of states [235, 236] and other experimentally-measured quantities for vitreous silica [202]. For this structure, cell parameters and atomic positions are relaxed with DFT using Γ-point ($\boldsymbol{q}=\mathbf{0}$) sampling, a threshold of 10^{-4} Ry/Bohr for the atomic forces (*i.e.* a structure is considered relaxed if all the Cartesian components of the forces acting on atoms are smaller than this threshold), and a threshold of 0.1 kBar for pressure. Second-order force constant are computed in the primitive cell using Phonopy [156]. Third-order force constants are also in the primitive cell using ShengBTE [68], and with a cutoff of 0.32 nm (corresponding to the 6^{th} nearest-neighbor). The linewidths are computed at the point $\boldsymbol{q}=\mathbf{0}$ using Gaussian smearing $\hbar\sigma = 2\,\text{cm}^{-1}$ for the Dirac delta appearing in the collision operator. Thermal conductivity calculations are performed using a $\boldsymbol{q}$-interpolation mesh equal to 3×3×3; the convergence of this mesh is checked by verifying that using denser meshes (5×5×5 or 7×7×7) yields compatible results. The Voigt profile, used to combine the AF and the WBTE conductivities as detailed before, has been numerically implemented following the prescriptions reported in ref. [193].

The 108- and 216-atom structures are taken from ref. [206] and ref. [207], respectively. In particular, among the different structures reported in these references, we have selected the “SiO2.1586” model from ref. [206] and the model number 2 from ref. [207] (which has a cubic cell with a =14.835 Å) using the selection criterion based on the similarity between theoretical and experimental density [181, 229]. For both these structures, first-principles calculations of second- and third-order force constants are performed using the same parameters reported above for the 144-atom structure.

An analysis of the coordination numbers using the procedure based on the minimum of the radial distribution function as implemented in the R.I.N.G.S. software [237] or that based on the position of the Wannier centers discussed in ref. [238] have revealed in both cases that all the vitreous structures considered in this work do not have coordination defects or lone pairs

Table 2.G.1 – **Densities of silica polymorphs.** Comparison between theoretical (DFT-relaxed) and experimental densities ρ for the various silica polymorphs analyzed.

Structure	ρ (kg/m^3)
v-SiO_2, 216 atoms (num. 2 [207]), PBE+D2	2203.4
v-SiO_2, 144 atoms [202], PBE+D2	2220.6
v-SiO_2, 108 atoms (SiO2.1586 [206]), PBE+D2	2243.9
v-SiO_2, Experiment [229]	2203 ± 3
v-SiO_2, Experiment [181]	2200 ± 10
α-cristobalite [230], PBE+D2	2383.5
α-cristobalite, Experiment [231]	2326±12
α-quartz [232], PBE+D2	2641.9
α-quartz, Experiment [233]	2650

(both before and after the DFT relaxation).

Finally, it is worth mentioning that for all the structures of vitreous silica analyzed, the vibrational energies at the point $\boldsymbol{q}$=$\mathbf{0}$ are non-negative (only the 3 acoustic modes have zero energy, all the others have energy greater than 25 cm^{-1}), confirming an accurate structural relaxation of the primitive cell. When performing the $\boldsymbol{q}$-interpolation to compute with Eq. (2.1) the bulk thermal conductivities reported in Fig. 2.C.1, for the 108- and 216-atom structures few vibrational energies resulted negative at $\boldsymbol{q}$-points different from $\boldsymbol{q} = \mathbf{0}$. Negative vibrational energies at $\boldsymbol{q} \neq \mathbf{0}$ are often related to structural instabilities or numerical inaccuracies, and computing the conductivities for the 108- and 216-atom models with the $\boldsymbol{q}$-interpolation (solid blue and solid green in Fig. 2.C.1) required to discard from the thermal-conductivity expression 6 vibrational modes for the 108-atom structure (which has in total 108*3=324 modes), and 8 modes (out of 648) for the 216-atom structure. For the 108-atom model, we have checked that these vibrational modes with negative energies at $\boldsymbol{q} \neq \mathbf{0}$ disappear computing second-order interatomic force constants more precisely with DFPT. Specifically, computing the vibrational energies using DFPT on a 2×2×2 $\boldsymbol{q}$-point mesh and accounting for the non-analytic term correction due to the dielectric tensor and Born effective charges, yields non-negative vibrational energies (the 3 acoustic mode at $\boldsymbol{q} = \mathbf{0}$ have zero energy, all the other vibrational modes have positive energy). We show in Fig. 2.G.1 that computing the thermal conductivity of the 108-atom model using these more precise harmonic force constants yields results that are very similar to those obtained using the harmonic force constants computed in the primitive cell using phonopy and discarding the 6 vibrational modes with negative energy. We also recall that the approximation discussed in Sec. 2.C, which consists in assigning to a vibrational mode $\boldsymbol{q}, s$ a linewidth equal to $\Gamma(\boldsymbol{q} = \mathbf{0})_s$ (*i.e.* independent from the wavevector), implies that the 3 acoustic modes having zero linewidth at $\boldsymbol{q} = \mathbf{0}$ are not taken into account in the present framework. In order to estimate the effect of such approximation, we show in Fig 2.G.1 how much the conductivity, at a given temperature T and for the 108-atom model, changes if the acoustic modes are taken into account approximatively by assigning them the minimum positive linewidth obtained at temperature T and at the point $\boldsymbol{q}$=$\mathbf{0}$. We highlight how the conductivity obtained considering the heat carried by the acoustic modes via this approximated procedure (black line in Fig. 2.G.1) does not differ significantly from the conductivity obtained neglecting the acoustic modes (gray line in Fig. 2.G.1). Computing the linewidths of these acoustic vibrational modes at $\boldsymbol{q}$≠$\mathbf{0}$ is a problem that is computationally too expensive to be solved with the code used for this work; such a computational problem will be tackled in future.

In summary, Fig. 2.C.1 shows that the conductivities of the 108-, 144-, and 216-atom vitreous silica models studied here are very similar. These conductivities have been computed using second-order force constants obtained via the finite-difference method. We note that the calculation of the force constants with the finite-difference method is computationally much less expensive than the calculation of the force constants with DFPT[3], but it is less precise. In fact, when the $\boldsymbol{q}$-interpolation of the vibrational properties obtained from the force constants is performed, force constants computed using DFPT yield always-positive vibrational frequencies, while force constants computed using the finite-difference method yield few vibrational modes with negative frequencies that need to be discarded. In practice, the less accurate finite-difference method can be used in place of DFPT when the computational cost needs to be minimized, since Fig. 2.G.1 shows that the conductivity computed using precise harmonic force constants from DFPT does not change significantly from the conductivity computed using harmonic force constants obtained from the finite-difference method and discarding the small number of vibrational modes with negative frequencies.

---

[3] On 77 cores and for the 108-atom structure, the computation of the harmonic force constants took about 180 hours with DFPT, while about 12 hours with the finite differences.

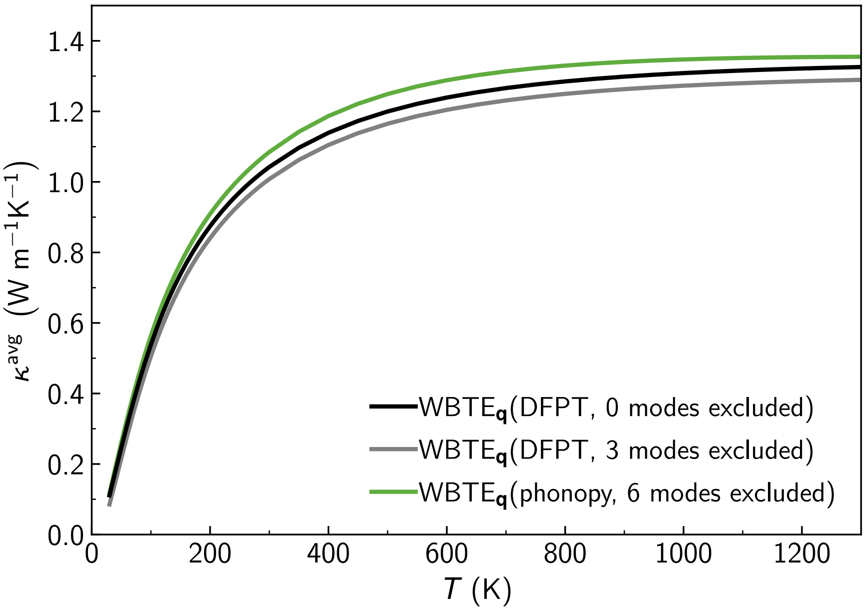

Figure 2.G.1 – **rWBTE conductivity of the 108-atom model of vitreous silica with harmonic force constants obtained from DFPT or finite differences.** All the lines in the plot are computed evaluating the expression (2.1) on a 3×3×3 $\boldsymbol{q}$-point mesh (to extrapolate the bulk limit, see text), different colors indicate results obtained using harmonic (second-order) force constants calculated in different ways. Grey, rWBTE conductivity computed using harmonic force constants obtained from DFPT on a 2×2×2 $\boldsymbol{q}$-point mesh and excluding the 3 acoustic modes for which the anharmonic linewidths can not be determined with the present approach, due to prohibitively large computational cost (further details are reported in the text). Black, rWBTE conductivity computed using harmonic force constants obtained from DFPT on a 2×2×2 $\boldsymbol{q}$-point mesh and accounting for all the vibrational modes, the linewidths of the three acoustic modes are set equal to the minimum positive linewidth obtained at the point $\boldsymbol{q}=\mathbf{0}$ (this approximation is performed to give an estimate about how much the conductivity can change by taking into account the acoustic modes at $\boldsymbol{q}\neq\mathbf{0}$, computing the linewidths of these acoustic modes is a computationally challenging problem that will be tackled in a future work). Green, rWBTE conductivity computed from harmonic force constants obtained in the primitive cell using the finite difference method implemented in phonopy; in this last case we have discarded the negative vibrational frequencies that emerge for the first 6 modes at $\boldsymbol{q}\neq\mathbf{0}$.

α-cristobalite. The crystal structure of α-cristobalite is taken from ref. [230] (ICSD collection code 47219). In first-principles calculations, the Brillouin zone is integrated with a Monkhorst–Pack mesh of $5\times5\times4$ points, with a (1, 1, 1) shift. Second-order force constants are computed using DFPT on a $5\times5\times4$ $\boldsymbol{q}$-point mesh, accounting also for the non-analytic term correction due to the dielectric tensor and Born effective charges. To obtain the third-order force constants the finite-difference method implemented in ShengBTE [68] is used, together with the interconversion software from ShengBTE to Quantum ESPRESSO, available in the D3Q package [37, 161]. In these third-order force constants calculations, a $2\times2\times2$ supercell with a $2\times2\times2$ k-point sampling is used, and interactions up to the 6th nearest neighbor (corresponding to ~ 0.39 nm) are considered. The linewidths (Fig. 2.C.2b) and thermal conductivity (Fig. 2.F.1a) are computed using a $17\times17\times13$ $\boldsymbol{q}$-point mesh and a Gaussian smearing $\hbar\sigma = 4\,\text{cm}^{-1}$.

α-quartz. The crystal structure of α-quartz is taken from ref. [232] (Crystallographic Open Database id 1526860). In first-principles calculations, the Brillouin zone is integrated with a Monkhorst–Pack mesh of $6\times6\times5$ points, with a (1, 1, 1) shift. Second-order force constants are computed using DFPT on a $4\times4\times4$ $\boldsymbol{q}$-point mesh, accounting also for the non-analytic term correction due to the dielectric tensor and Born effective charges. Third-order force constants are computed using the finite difference methods as implemented in ShengBTE [68], using a $3\times3\times2$ supercell with a Γ-only k-point sampling, and a cutoff for atomic interactions of 0.9 nm. The linewidths (Fig. 2.C.2c) and thermal conductivity (Fig. 2.F.1b) are computed using a $19\times19\times15$ $\boldsymbol{q}$-point mesh and a Gaussian smearing $\hbar\sigma = 4\,\text{cm}^{-1}$. Results are compatible to those reported in ref. [239].

We conclude by noting that in Fig. 2.5.3 the vDOS for all materials are computed using the same meshes used for the thermal conductivity calculations detailed above, and a Gaussian smearing of $15\,\text{cm}^{-1}$ for the vibrational energies. For all the structures of vitreous silica considered the vDOS computed at the point $\boldsymbol{q}=\mathbf{0}$ only is practically unchanged from the vDOS computed on a $3\times3\times3$ $\boldsymbol{q}$-point mesh.

Data availability. Raw data were generated using the SCITAS High Performance Computing facility at the École Polytechnique Fédérale de Lausanne. Derived data supporting the findings of this study will be made available on the Materials Cloud Archive.

Code availability. Quantum ESPRESSO is available at www.quantum-espresso.org; the scripts related to the computation of the third order force constants using the finite-difference method are available at bitbucket.org/sousaw/thirdorder; the D3Q package for Quantum ESPRESSO is available at sourceforge.net/projects/d3q/. The custom code developed in this work will be made available in a next release of the D3Q package.

3 Transition from simple to complex crystal in silica polymorphs

3.1 Introduction

In the previous chapters we have investigated how the interplay between the quantum Bose-Einstein statistics of atomic vibrations, disorder, and anharmonicity affects the thermal conductivity of solids. We have found that in complex crystals such as $La_2Zr_2O_7$ anharmonicity drives the increase of the coherences' conductivity at high temperature (see Fig. 1.6), while in a paradigmatic glass such as silica anharmonicity has minor effects even at high temperature (see Fig. 2.5.1, where the anharmonic Wigner-Boltzmann theory yields a conductivity practically indistinguishable from that predicted by the harmonic Allen-Feldman theory).

The findings discussed up to now have given a broad overview of the conditions under which the coherences interband conductivity becomes relevant or dominant, motivating the introduction of the term "complex crystal", *i.e.* a crystal characterized by phonon interband spacings smaller than the linewidths and displaying coherences' conductivity that is comparable or larger than Peierls' populations conductivity. We have discussed how such a regime depends on temperature (since increasing temperature yields larger linewidths and thus favors the overlap between phonon bands (see Fig. 1.4)), and on disorder (since the higher is the disorder in a solid, the larger is the size of the primitive cell needed to explicitly describe it; consequently, the larger is the number of phonon bands, and thus the more reduced are the spacings between them).

Silica forms many polymorphs [228, 240, 241] and in addition to the limiting cases of the completely ordered simple crystal (α-quartz) and the completely disordered glass (vitreous silica) studied before, it crystallizes also in structures with intermediate degree of disorder such as meteoritic low tridymite (which is a crystal with a large, 72-atom primitive cell [241]). The opposite trend of the temperature-conductivity curve found in the limiting cases of α-quartz and amorphous silica (Fig. 2.5.1 and Fig. 2.F.1) motivates us to study also the intermediate regime of meteoritic low tridymite.

In this chapter we discuss preliminary results obtained computing from first-principles the

Wigner-Boltzmann conductivity (Eq. (1.44)) of meteoritic tridymite. We show that meteoritic low tridymite features a temperature-conductivity curve with a trend intermediate between that of α-quartz (a simple crystal) and that of silica glass.

3.2 Effects of disorder on the vibrational properties

Meteoritic low tridymite is a silica crystalline polymorph that occurs naturally in several meteorites and is stable under 380 K [241]. It is characterized by a primitive cell containing 72 atoms and a monoclinic structure with space group Cc, thus it is more disordered than α-quartz (whose primitive cell contains 9 atoms), and less disordered than the finite-size models of amorphous silica analyzed in Chapter 2 (with primitive cells containing 108, 144, or 216 atoms).

We start by analyzing how disorder affects the harmonic vibrational properties of silica polymorphs. We show in Fig. 3.2.1 that the vibrational density of states (vDOS) of α-quartz, meteoritic low tridymite, and vitreous silica span a similar energy range. The peaks in the

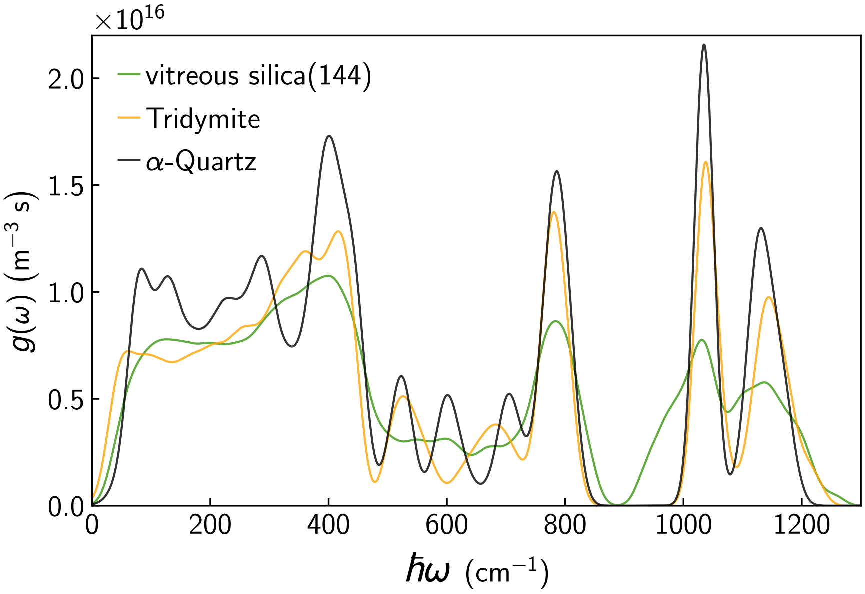

Figure 3.2.1 – **Vibrational density of states of silica polymorphs.** The vibrational density of states (vDOS) of α-quartz (black), meteoritic low tridymite (orange), and vitreous silica (green) span a similar energy range. The peaks in the vDOS become less pronounced as disorder increases: α-quartz is the most ordered structure (with a primitive cell containing 9 atoms) and its vDOS features peaks that are more pronounced than those of meteoritic low tridymite (whose primitive cell contains 72 atoms), and meteoritic low tridymite has peaks more pronounced than vitreous silica (which has the most disordered structure, here we show the finite-size model of vitreous silica discussed in Chapter 2 and containing 144 atoms in the primitive cell).

vDOS become decreasingly less pronounced as disorder increases (*i.e.* as the number of atoms in the primitive cell increases): α-quartz is the most ordered structure (9 atoms per primitive cell) and has the sharpest peaks, then in meteoritic low tridymite (72 atoms per primitive cell) and vitreous silica (here approximated with a finite-size model containing 144 atoms, see Chapter 2) have decreasingly less pronounced peaks.

In order to obtain more precise insights on how disorder affects the harmonic vibrational properties, we compare the phonon dispersion for α-quartz and meteoritic low tridymite, showing in Fig. 3.2.2 that increasing the size of the primitive cell (*i.e.* the number of atoms contained in it) yields a decrease of the phonon interband spacings.

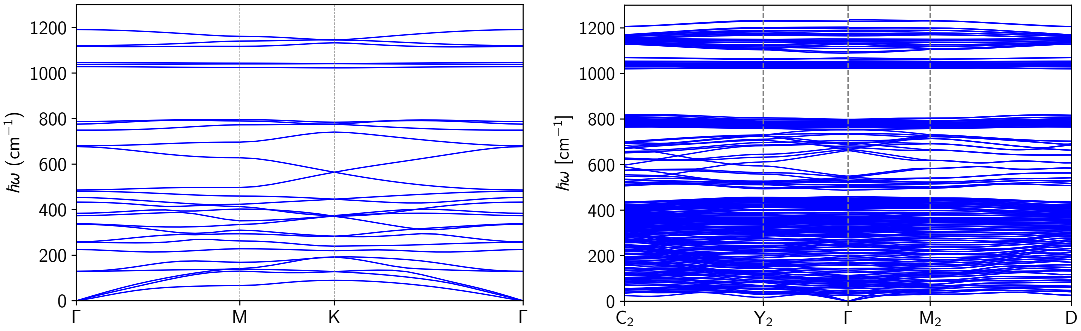

Figure 3.2.2 – **Effect of disorder on the phonon dispersion of silica polymorphs.** Increasing disorder in a crystal yields a reduction of the phonon interband spacings. Left, phonon dispersion relation of α-quartz, which is characterized by a primitive cell containing 9 atoms and thus has 27 phonon bands. Right, phonon dispersion relation of meteoritic low tridymite, a crystal which is more disordered than α-quartz since it has a larger primitive cell (containing 72 atoms, thus having 216 phonon bands).

Fig. 3.2.2 shows that the emergence of the complex crystal regime is favored by disorder, since increasing disorder yields a decrease of the average phonon interband spacing. We now focus on the other condition necessary for the emergence of the complex crystal regime, that is the presence of anharmonic linewidths that are larger than the phonon interband spacings. We show in Fig. 3.2.3 the linewidths of vitreous silica, meteoritic low tridymite, and α-quartz as a function of frequency and temperature. In general, all these materials are characterized by linewidths that are mainly increasing with frequency, and (trivially) with temperature. Disorder seems to affect mainly the linewidths of the low-frequency vibrational modes, with more disordered systems having larger minimum linewidth. Therefore, from Fig. 3.2.2 and Fig. 3.2.3 we deduce that disorder favors the emergence of the complex crystal regime by reducing the average interband spacing, and also slightly increasing the linewidths of the low-frequency vibrational modes.

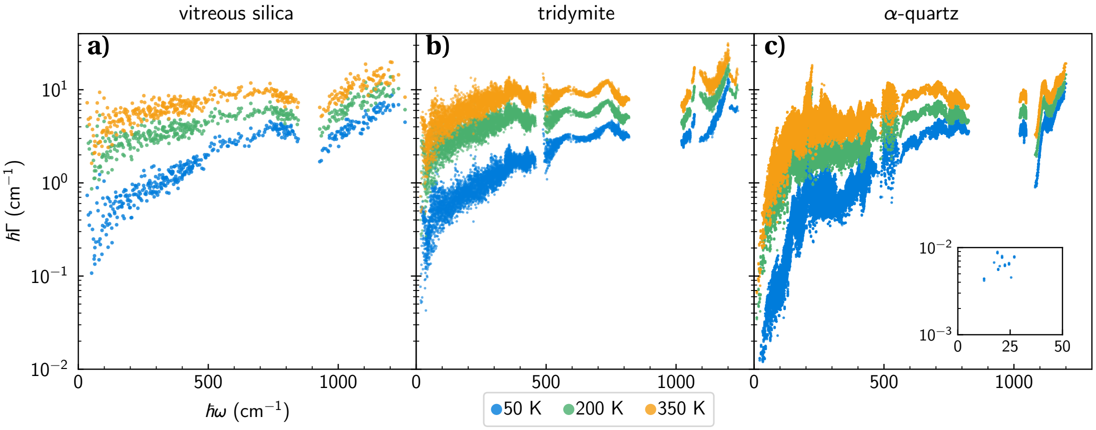

Figure 3.2.3 – **Linewidths as a function of frequency and temperature of silica polymorphs.** Increasing temperature yields an increase of the linewidths that account for third-order anharmonicity [41, 68] and isotopic scattering [137] in both vitreous and crystalline materials: panel a) shows a 144-atom vitreous-silica model, panel b) meteoritic low tridymite, and panel c) α-quartz. The temperatures of 50, 200, and 350 K at which the linewidth distributions are reported are chosen to span the temperature range over which all these materials are stable. The inset in panel c) shows the linewidths of the low-energy vibrational modes in α-quartz.

3.3 Thermal conductivity of meteoritic low tridymite

In the previous chapters we have mentioned that the single-mode relaxation-time approximation (SMA) for the collision operator appearing in the WBTE becomes increasingly more accurate in systems with decreasingly lower conductivity, where Umklapp collisions between phonons become dominant [37, 101].

In Chapter 2 we have demonstrated that the SMA is accurate for α-quartz, and since Fig. 3.2.3 shows that the anharmonic linewidths in meteoritic low tridymite are larger than those of α-quartz (*i.e.* anharmonicity, which limits heat conduction, is stronger in meteoritic low tridymite than in α-quartz), we employ here the SMA approximation for meteoritic low tridymite. Therefore, we use the generalized WBTE conductivity formula (1.44) in the SMA approximation to calculate the temperature-conductivity curve of meteoritic low tridymite, computing all the parameters entering in such expression from first-principles (see Appendix 3.A for computational details). The results are reported in Fig. 3.3.1, and show that meteoritic low tridymite behaves as a simple crystal at low temperature, with a Peierls' populations conductivity that dominates over the coherences' conductivity. Increasing temperature, meteoritic low tridymite becomes a complex crystal with a coherences' conductivity larger than the populations' conductivity.

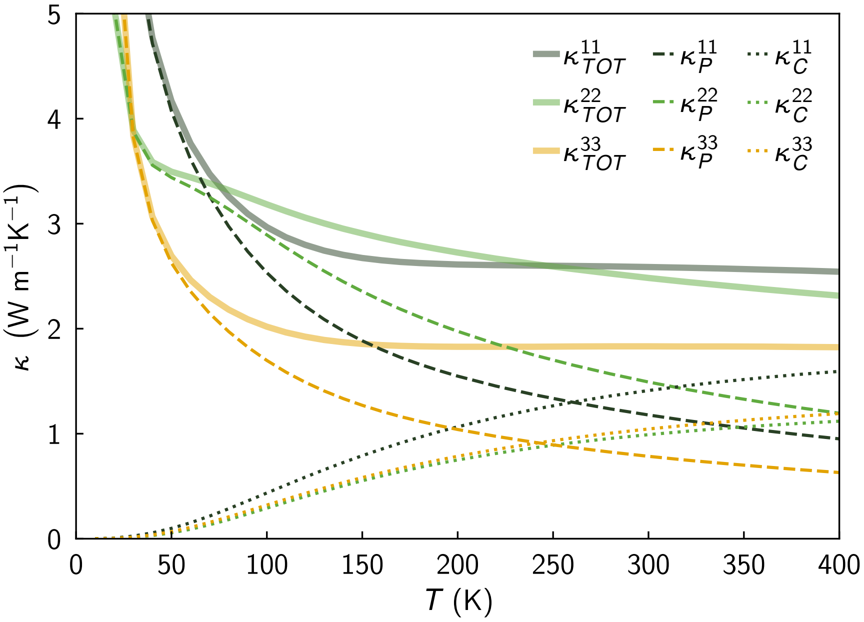

Figure 3.3.1 – **Thermal conductivity of meteoritic low tridymite.** We report the three eigenvalues of the total conductivity tensor (1.44) (solid lines), computed as sum of the eigenvalues of the populations'conductivity tensor (dashed lines) and eigenvalues of the coherences' conductivity tensor (dotted lines). The directions of the corresponding eigenvectors depend on temperature, with the exception of the eigenvector indexed by 2 that is always aligned with the lattice vector **b** of meteoritic low tridymite [241] (see also Fig. 3.3.2). At low temperature, meteoritic low tridymite behaves as a simple crystal with the populations' conductivity tensor dominating over the coherences' conductivity tensor. At high temperature instead, meteoritic low tridymite behaves as a complex crystal with a coherences' conductivity larger than the populations' conductivity, and a decay of the conductivity with temperature that is milder than the T^{-1} trend predicted by Peierls' theory along eigenvector 2 (approximately proportional to $T^{-1/4}$) or even absent along eigenvectors 1 and 3. Above 100 K, the results presented here have been obtained from Eq. (1.44) using a 7×7×3 **q**-point mesh and a Gaussian smearing of 2 cm^{-1} for the computation of the linewidths. Below 100 K, the results have been obtained evaluating Eq. (1.44) on a 15×15×11 **q**-point mesh and employing an approximated interpolation of the linewidths to reach computational convergence, see Appendix 3.A for details.

In order to compare the conductivity of tridymite computed here with the results for α-quartz and vitreous silica discussed in Chapter 2, we plot in Fig. 3.3.2 the temperature-conductivity curve for all these silica polymorphs. Results show that the temperature-conductivity curve of meteoritic low tridymite displays a trend which is intermediate between that of crystalline α-quartz and that of silica glass.

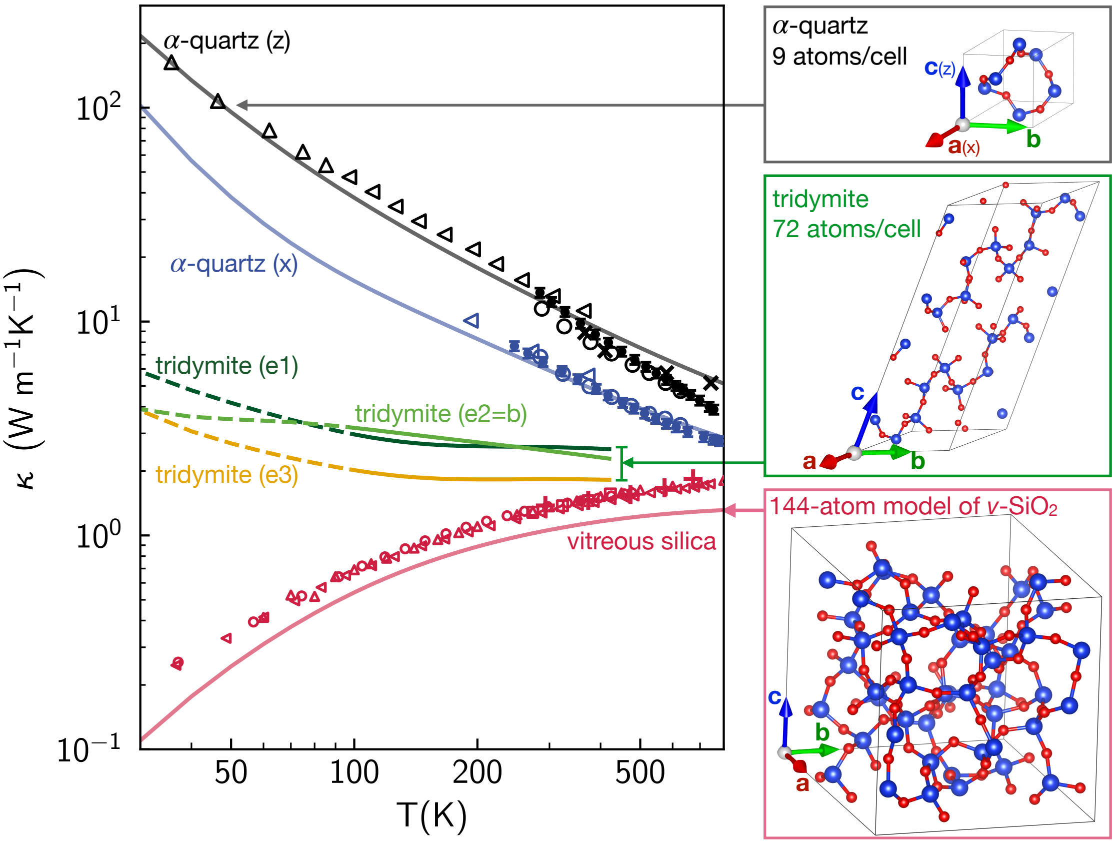

Figure 3.3.2 – **Thermal conductivity of silica polymorphs.** The Wigner-Boltzmann generalized conductivity formula (1.44) predicts a conductivity that is in reasonable agreement with experiments for α-quartz (black and blue lines and scatter points, with black and blue referring to directions z and x, respectively; lines are theory and scatter points are experiments from Refs. [170, 171, 172, 173, 174]), and for vitreous silica (red line is the Wigner-Boltzmann conductivity regularized with the Voigt protocol discussed in Chapter 2, and red scatter points are experiments [174, 175, 176, 177, 178, 179, 180, 181]. Finally, intermediate orange, dark- and light-green lines are theoretical predictions for tridymite. The conductivity of tridymite below 100 K (dashed line) has been computed employing an approximate interpolation for the linewidths to reach computational convergence, see Appendix 3.A for details.

3.4 Conclusions

We have predicted the temperature-conductivity curve of meteoritic low tridymite to display a trend intermediate between the decreasing trend of the crystalline polymorph α-quartz and the increasing trend of the glassy polymorph vitreous silica. This prediction awaits experimental confirmation, and suggests future studies on the possibility to engineer the trend of the temperature-conductivity curve in materials by varying their structural disorder (*i.e.* the size of their primitive cell).

Appendix

3.A Computational details

In this Appendix we discuss the computational techniques employed to calculate the conductivity reported in Fig. 3.3.1 and in Fig. 3.3.2.

3.A.1 First-principles calculations of force constants

All the density-functional theory (DFT) calculations have been performed with the Quantum ESPRESSO distribution [149] using the PBE functional with semiempirical Grimme-D2 corrections (PBE+D2) [152]. This choice is motivated by the benchmarks given in Ref. [228] and accounting for the capability of Quantum ESPRESSO to compute phonons using density-functional perturbation theory (DFPT) [40] with the PBE+D2 functional. This choice is validated by the agreement between theoretical and experimental densities reported in table 2.G.1 for several silica polymorphs, as well as the capability of the PBE+D2 functional to describe accurately the thermal properties of α-quartz (see Fig. 3.3.2 and Chapter 2). Specifically for the case of meteoritic low tridymite discussed here, we found a density of 2.28080 g/cm^3, in reasonable agreement with the experimental value of 2.254(5) g/cm^3 reported in Refs. [241, 242]. We have used pseudopotentials from the SSSP efficiency library [153, 154] with a cutoff of 50 Ry and a dual of 8.

The crystal structure of meteoritic low tridymite is taken from ref. [241]. In first-principles calculations, the Brillouin zone is integrated with a Monkhorst–Pack mesh of 3×3×2 points. Second-order force constants are computed using DFPT on a 3×3×2 $\boldsymbol{q}$-point mesh, accounting also for the non-analytic term correction due to the dielectric tensor and Born effective charges. Third-order force constants are computed using the finite difference methods as implemented in ShengBTE [68], using a 2×2×1 supercell with a Γ-only k-point sampling, and a cutoff for atomic interactions of 0.31 nm (corresponding to the 6^{th} nearest neighbor). Then, harmonic force constants are converted from Quantum ESPRESSO format to `hdf5` (phono3py) format using PHONOPY [156], and third order force constants are converted to `hdf5` (phono3py) format using HIPHIVE [69].

3.A.2 Computation of the phonon linewidths

The phonon linewidths are computed with phono3py [70], and we show in Fig. 3.A.1 that the linewidth distribution computed using a $\boldsymbol{q}$-point mesh equal to 4×4×2 is practically equal to the linewidth distribution obtained using a 7×7×3 $\boldsymbol{q}$-point mesh. The linewidths reported in Fig. 3.A.1 are computed using the tetrahedron method, using a Gaussian smearing of 0.06 THz (=2 cm^{-1}) and a cutoff at five standard deviations yielded practically unchanged results.

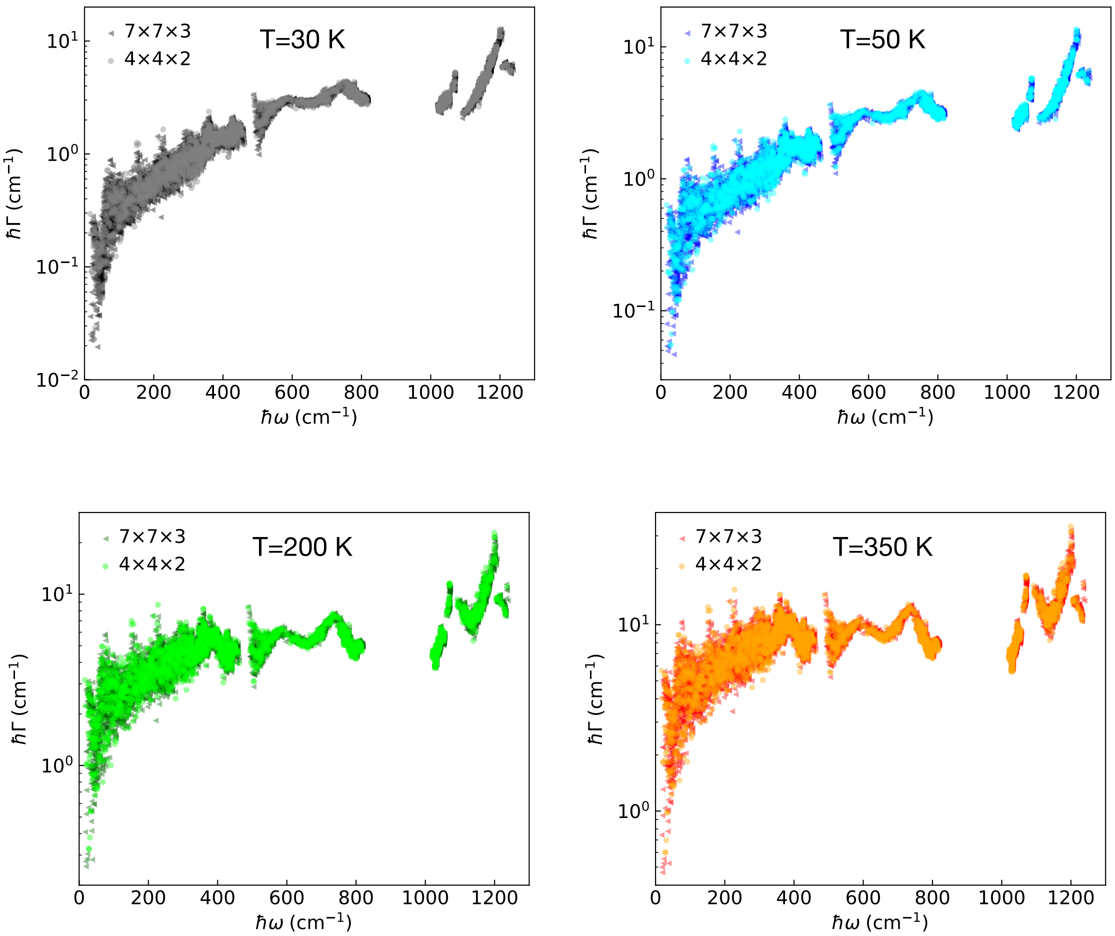

Figure 3.A.1 – **Convergence of the phonon linewidths with the q-point mesh.** Phonon linewidths as a function of frequency computed employing a 4×4×2 (circles) or 7×7×3 (triangles) $\boldsymbol{q}$-point mesh at 30 K (top left), 50 K (top right), 200 K (bottom left), 350 K (bottom right). The linewidth distributions computed with different meshed are practically indistinguishable, demonstrating that computational convergence has been reached.

3.A.3 Computation of the thermal conductivity

Results reported in Fig. 3.A.1 show that a 7×7×3 $\boldsymbol{q}$-point mesh yields computationally converged linewidths, thus we computed the thermal conductivity of meteoritic low tridymite using a 7×7×3 $\boldsymbol{q}$-point mesh with Eq. (1.44) in the SMA approximation (which is accurate in silica polymorphs, as discussed before in Chapter 2 and in Sec. 3.3). The results of such computation are reported in Fig. 3.A.2 (dashed lines), and show that along the direction of eigenvector 2 the conductivity of tridymite features a minimum around 30 K. We thus investigate the origin of such a minimum. In particular, the parameters entering in the WBTE thermal conductivity expression (1.44) have, in general, different speed of convergence.

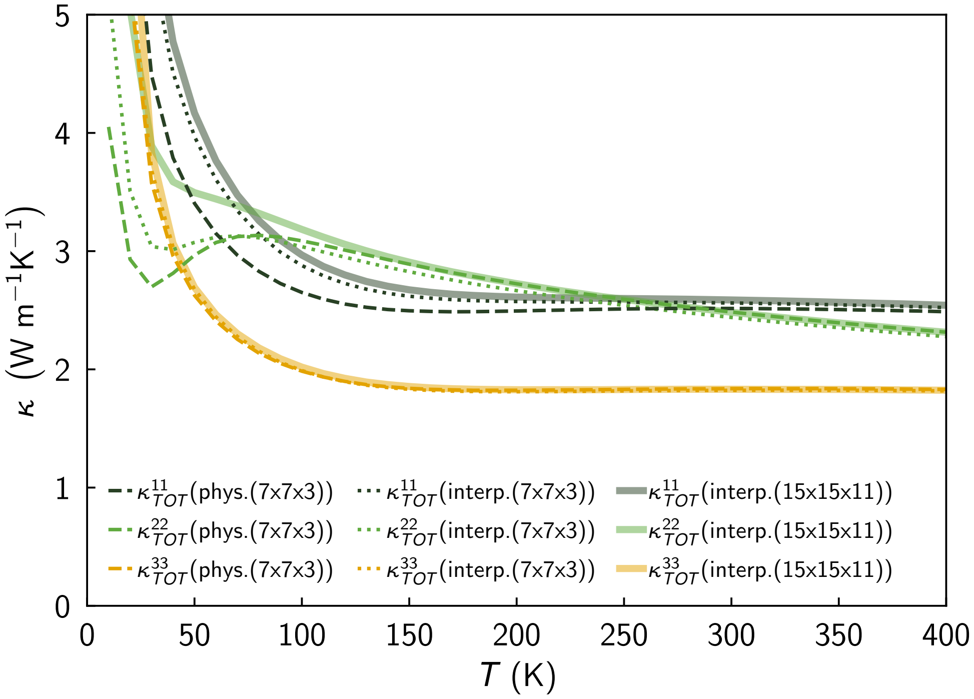

Figure 3.A.2 – **Thermal conductivity of tridymite: calculation with physical linewidths versus approximated interpolation.** We report the three eigenvalues of the total conductivity tensor of meteoritic low tridymite, computed evaluating the expression (1.44) in the SMA approximation on different $\boldsymbol{q}$-point meshes and with the linewidths computed in different ways: (i) on a $\boldsymbol{q}$-point mesh equal to 7×7×3 and with linewidths computed from first principles (dashed lines); (ii) on a $\boldsymbol{q}$-point mesh equal to 7×7×3 and with linewidths interpolated as a function of frequency (see text, dotted lines); (iii) on a $\boldsymbol{q}$-point mesh equal to 15×15×11 and with linewidths interpolated as a function of frequency (see text and Fig. 3.A.3, solid lines). A comparison between the dashed and dotted lines shows that the approximation of interpolating the linewidths as a function of frequency yields results that are very similar to these obtained using the linewidths computed from first principles. A comparison between the dashed and solid lines reveals that the minimum observed in the dashed-green temperature-conductivity curve around 30 K is due to a too coarse sampling of the velocity operator on a mesh 7×7×3, and disappears if a finer 15×15×11 mesh is employed (solid green line, which is also reported with the same color and style in Fig. 3.3.1).

The anharmonic linewidths appearing in Eq. (1.44) are the computationally most expensive part to evaluate (computing the linewidth distributions on a 7×7×3 $\boldsymbol{q}$-mesh requires about

60’000 core-hours on a modern supercomputer). Since the results reported in Fig. 3.A.1 suggest that the linewidths are converged on a 7×7×3 $\boldsymbol{q}$-point mesh, we employ an approximated strategy to evaluate the thermal conductivity expression (1.44) on a $\boldsymbol{q}$-mesh larger than 7×7×3 but relying on the anharmonic linewidths computed on the 7×7×3 $\boldsymbol{q}$-point mesh. Such a strategy is similar to that discussed by Garg and Marzari [243] and consists in: (i) approximating the linewidths as a single-valued function of frequency, $\Gamma(\boldsymbol{q})_s = f(\omega(\boldsymbol{q})_s)$; (ii) determining such a single-valued function from a fit or interpolation of the linewidths computed on a coarse $\boldsymbol{q}$-mesh (7×7×3 in our case); (iii) evaluating the thermal conductivity expression (1.44) on a dense $\boldsymbol{q}$-mesh (15×15×11 in our case) using as anharmonic linewidths those obtained from the function $f(\omega(\boldsymbol{q})_s)$.

We show in Fig. 3.A.3 the approximated interpolation functions at various temperatures (solid lines) employed to determine the linewidth of a vibrational mode from its frequency, $\Gamma(\boldsymbol{q})_s \approx f\big(\omega(\boldsymbol{q})_s\big)$. Specifically, the linewidth function $f\big(\omega(\boldsymbol{q})_s\big)$ is determined as follows: starting from the linewidths computed on a 7×7×3 $\boldsymbol{q}$-point mesh (circles in Fig. 3.A.3), we coarse-grain such a distribution into a set of discrete points equally spaced along the frequency axis (black crosses, with a spacing $\Delta\hbar\omega = 10\ \mathrm{cm}^{-1}$). The black crosses are computed performing a weighted average of the linewidths in a frequency window of 10 cm^{-1} and using weights $w[\Gamma(\boldsymbol{q})_s] = \frac{1}{[\Gamma(\boldsymbol{q})_s]^{1.8}}$:

$$f(\omega) = \frac{\sum_{\boldsymbol{q},s} \chi(\omega(\boldsymbol{q})_s, \omega, \Delta\omega)\cdot\Gamma(\boldsymbol{q})_s\cdot w[\Gamma(\boldsymbol{q})_s]}{\sum_{\boldsymbol{q},s} \chi(\omega(\boldsymbol{q})_s, \omega, \Delta\omega)\cdot w[\Gamma(\boldsymbol{q})_s]}, \tag{3.1}$$

where $\chi(\omega(\boldsymbol{q})_s, \omega, \Delta\omega)$ is an indicator function defined as

$$\chi(\omega(\boldsymbol{q})_s, \omega, \Delta\omega) = \begin{cases} 1 & \text{iff } \omega - \frac{\Delta\omega}{2} \le \omega(\boldsymbol{q})_s < \omega + \frac{\Delta\omega}{2}; \\ 0 & \text{otherwise.} \end{cases} \tag{3.2}$$

We also note that in the very low-frequency region (below 10 cm^{-1}), the $\boldsymbol{q}$-point mesh 7×7×3 does not sample any vibrational mode, thus the coarse-grained value for the linewidth distribution in this region is inferred by fitting the coarse-grained data $(\omega, f(\omega))$ with a 2-parameters (p_1, p_2) function $\frac{p_1}{\omega^{p_2}}$ over the frequency region from 15 to 105 cm^{-1} (the result of this fit at different temperatures are the dashed lines in Fig. 3.A.3).

We stress that this procedure contains several customary ingredients: the weights $\frac{1}{[\Gamma(\boldsymbol{q})_s]^{1.8}}$ for the average (3.1) and the form of the fitting function $\frac{p_1}{\omega^{p_2}}$ to extrapolate the low-frequency behavior of the linewidths have been chosen ad-hoc to reproduce as accurately as possible the SMA temperature-conductivity curve in the high-temperature regime ($\gtrsim$ 100 K) computed with the exact linewidths of the mesh 7×7×3 (see Fig. 3.A.2, where the dashed lines are conductivities computed using the exact linewidths, while the dotted lines are conductivities computed using this approximated interpolation on the same mesh).

Since this interpolation procedure allows to evaluate the linewidths at a negligible computa-

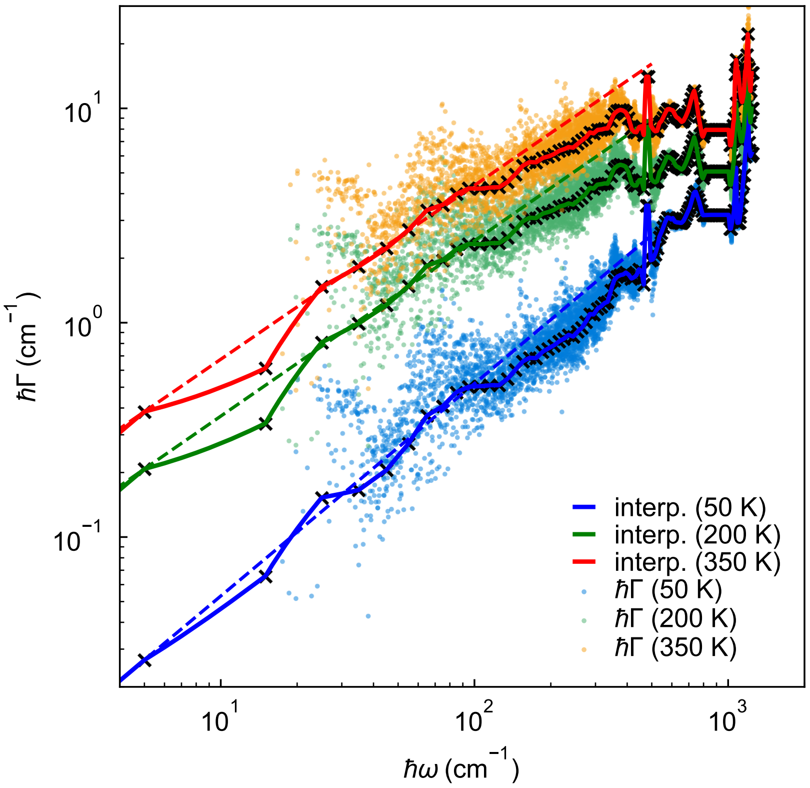

Figure 3.A.3 – **Approximated interpolation of the linewidths with frequency.** The phonon linewidth distributions (scatter points, with blue, green, and orange referring to a temperature of 50, 200, and 350 K, respectively) are approximated as a single-valued function of frequency (solid-lines), obtained interpolating linearly the weighted average (computed according to Eq. (3.1)) of the linewidths on frequency bins of 10 cm^{-1} (black crosses). In the low-frequency region (below 10 cm^{-1}) the coarse-grained value of the linewidths are inferred by fitting the black crosses with a 2-parameters (p_1, p_2) function $\frac{p_1}{\omega^{p_2}}$ over the frequency region from 15 to 105 cm^{-1} (the dashed lines are the result of these fits at different temperatures).

tional cost, we employ it to compute the conductivity tensor for meteoritic low tridymite on a denser $\boldsymbol{q}$-point mesh. In practice, we evaluate Eq. (1.44) on a 15×15×11 mesh, computing the linewidths with this approximated procedure (the computational cost for evaluating exactly the linewidths on such a dense mesh would be otherwise prohibitive), and all the other parameters exactly from the interatomic force constants. The results are reported in Fig. 3.A.2 (solid lines) and are different from those obtained using a coarser 7×7×3 $\boldsymbol{q}$-point mesh (dashed line) only at low temperatures ($\lesssim$ 100 K). Importantly, the results obtained employing this approximated interpolation procedure and a dense mesh display a monotonic decreasing trend for the conductivity along the eigenvector 2 of the conductivity tensor, suggesting that the minimum appearing in the conductivity along eigenvector 2 from the SMA calculation with the exact linewidths of the 7×7×3 mesh and around 30 K is a numerical artifact that disappears using denser meshes.

Due to the several approximations involved in the calculation of the conductivity of meteoritic low tridymite below 100 K, results obtained relying on these approximations are reported with dashed lines in Fig. 3.3.2.

The vibrational DOS reported in Fig. 3.2.1 is computed using the 7×7×3 $\boldsymbol{q}$-point mesh, and a Gaussian smearing of 15 cm^{-1} for the vibrational energies. All the results for α-quartz and vitreous silica reported in this chapter are exactly the same discussed in Chapter 2.

Thermal transport beyond Fourier

Part II

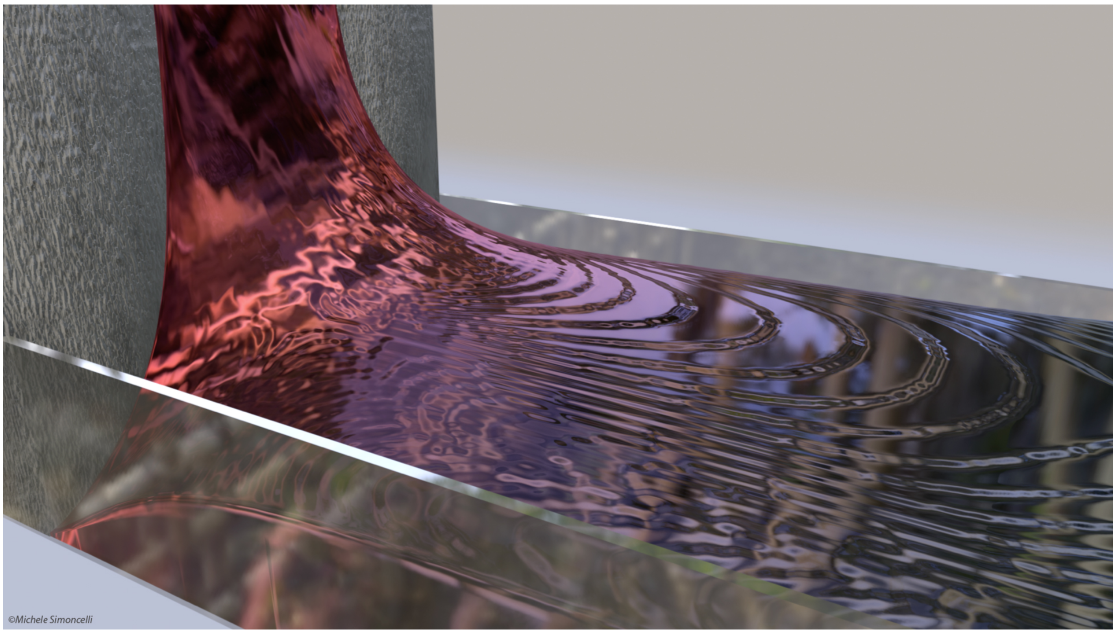
©Michele Simoncelli

Figure 3.1.4 – Hydrodynamic heat flow in a graphitic device, obtained from the solution of the viscous heat equations. Color is related to temperature, with red warmer than blue.

4 Generalization of Fourier's Law into Viscous Heat Equations

In 1822 Fourier formulated the well-known heat equation, which describes how temperature changes over space and time when heat flows in a solid material. Such an equation works well to describe conduction in macroscopic objects (several millimeters in size or larger) and at high temperatures. However, it does not describe hydrodynamic heat propagation, which can appear in electronic devices containing materials such as graphite and graphene.

Hydrodynamic heat-transport phenomena were discovered in the sixties and manifest themselves with heat propagating in a manner that deviates from the diffusive behavior predicted by Fourier's law. One of these heat-propagation phenomena is known as Poiseuille heat flow, in which the heat flux in a material assumes a profile analogous to the velocity field of a viscous fluid flowing inside a pipe (*i.e.* flowing faster at the center of the pipe and slower at the boundaries). Another phenomenon, called "second sound", takes place when heat propagates in a crystal in the form of a coherent temperature wave, which resembles the way in which sound spreads through the air.

These phenomena are not described by Fourier's equation. The microscopic Peierls-Boltzmann equation discussed in the previous chapters contains all the informations needed to describe them[1], but for most applications in engineering such a microscopic equation contains more informations than needed and is too complex to be solved quickly and straightforwardly.

In this chapter, we rely on the microscopic Peierls-Boltzmann equation to show that the thermal conductivity is not sufficient to describe heat hydrodynamics, but an additional parameter, thermal viscosity, must be taken into account. Then we use this microscopic insight to condense all the physics underlying hydrodynamic heat conduction into simpler, easily solvable, and accurate equations. The result is a set of "viscous heat equations", partial differential equations that are parametrized by thermal conductivity and viscosity, and describe both Fourier's diffusion and heat hydrodynamics.

---

[1] To date, these hydrodynamic phenomena have been observed only in simple crystals characterized by phonon interband spacings much larger than the linewidths (e.g., materials with a very ordered atomic structure and weak anharmonicity), for which the unified theory of thermal transport discussed in Chapter 1 becomes equivalent to the Peierls-Boltzmann equation.

We show that for graphitic devices the hydrodynamic behavior for heat predicted from the viscous heat equations lines up closely with recent experimental measurements [31]. We also discuss how chemical composition, size, and temperature of the material influence the appearance of heat hydrodynamics.

The formulation discussed here is relevant for technological applications, since hydrodynamic heat propagation emerges in materials for next-generation electronic devices such as graphene and graphite, and could potentially be exploited to overcome thermal challenges that limit miniaturization and efficiency. Finally, the methodology discussed in this chapter is general and provides insights on how microscopic (quasi) conservation laws can be exploited to coarse-grain a complex (integro-differential), microscopic transport equation into a set of much simpler but equally-accurate mesoscopic differential equations.

This chapter contains the postprint version of the article published in Physical Review X [66]. This work has been done under the supervision of my PhD advisor, Prof. Nicola Marzari, and in collaboration with Dr. Andrea Cepellotti (currently at Harvard University), and started from a discussion about the possibility to exploit the "relaxon kinetic theory for thermal transport" [39] to compute a quantity analogous to the viscosity for nearly ferromagnetic Fermi liquids [244]. I contributed to this work as a first author. In particular, I did the analytical and numerical calculations with inputs from Prof. Nicola Marzari and Dr. Andrea Cepellotti, and I wrote the first draft of the manuscript. In addition, I took care of the correspondence with the journal.

Full bibliographic reference: Michele Simoncelli, Nicola Marzari, Andrea Cepellotti
Generalization of Fourier's law into viscous heat equations. Physical Review X, **10** 011019 (2020)

DOI: https://doi.org/10.1103/PhysRevX.10.011019
URL: https://journals.aps.org/prx/abstract/10.1103/PhysRevX.10.011019
Copyright: 2020 American Physical Society

Generalization of Fourier's Law into Viscous Heat Equations

Michele Simoncelli*, [1], Nicola Marzari[1], Andrea Cepellotti[2]

4.1 Abstract

Heat conduction in dielectric crystals originates from the dynamics of atomic vibrations, whose evolution is well described by the linearized Boltzmann transport equation for the phonon populations. Recently, it was shown that thermal conductivity can be resolved exactly and in a closed form as a sum over relaxons, *i.e.* collective phonon excitations that are the eigenvectors of Boltzmann equation's scattering matrix [Cepellotti and Marzari, Phys. Rev. X **6**, 041013 (2016)]. Relaxons have a well-defined parity, and only odd relaxons contribute to the thermal conductivity. Here, we show that the complementary set of even relaxons determines another quantity — the thermal viscosity — that enters into the description of heat transport, and is especially relevant in the hydrodynamic regime, where dissipation of crystal momentum by Umklapp scattering phases out. We also show how the thermal conductivity and viscosity parametrize two novel viscous heat equations — two coupled equations for the temperature and drift-velocity fields — which represent the thermal counterpart of the Navier-Stokes equations of hydrodynamics in the linear, laminar regime. These viscous heat equations are derived from a coarse-graining of the linearized Boltzmann transport equation for phonons, and encompass both the limit of Fourier's law and that of second sound, taking place, respectively, in the regime of strong or weak momentum dissipation. Last, we introduce the Fourier deviation number as a descriptor that captures the deviations from Fourier's law due to hydrodynamic effects. We showcase these findings in a test case of a complex-shaped device made of graphite, obtaining a remarkable agreement with the recent experimental demonstration of hydrodynamic transport in this material, and also suggesting that hydrodynamic behavior can appear at room temperature in micrometer-sized diamond crystals. The present formulation rigorously generalizes Fourier's heat equation, extending the reach of physical and computational models for heat conduction also to the hydrodynamic regime.

4.2 Introduction

Thermal transport in insulating crystals takes place through the evolution and dynamics of the vibrations of atoms around their equilibrium positions. The first predictive theoretical framework to describe thermal transport was developed by Peierls in 1929 [11, 12, 14], who envisioned a microscopic theory in terms of a Boltzmann transport equation (BTE) for the propagation of vibrational excitations (phonon wavepackets). In the 1960s significant progress took place in this field, propelled by newly discovered hydrodynamic phenomena in crystals, with striking signatures such as Poiseuille-like heat flow [17] and second sound [18]. The former manifests itself with a heat flux that is akin to the flow of a fluid in a pipe (*i.e.* showing a parabolic-like profile with a maximum in the center and minimum at the boundaries, due to viscous effects); the latter instead results in heat propagation in the form of a coherent temperature wave, rather than a diffusing heat front. Second sound has been observed experimentally in a handful of solids; first, in solid helium [18], followed by sodium fluoride [245, 246], bismuth [247], sapphire [248], and strontium titanate [249, 250] – all at cryogenic conditions. Importantly, neither Poiseuille flow nor second sound can be described by the macroscopic Fourier's equation, which is limited to a diffusive description of heat propagation.

---

*Corresponding author: michele.simoncelli@epfl.ch

[1] Theory and Simulation of Materials (THEOS) and National Centre for Computational Design and Discovery of Novel Materials (MARVEL), École Polytechnique Fédérale de Lausanne, Lausanne, Switzerland.

[2] Department of Physics, University of California at Berkeley and Materials Sciences Division, Lawrence Berkeley National Laboratory, Berkeley, California 94720, USA

These experimental observations have been accompanied by several pioneering efforts aimed at providing a quantitative description of heat hydrodynamics at the mesoscopic level, *i.e.* in terms of partial differential equations (PDEs) that are simpler than the microscopic integro-differential BTE (we use "mesoscopic model" to denote any description requiring more fields or PDEs than the Fourier's PDE for the temperature field [251]). Sussmann and Thellung [23], starting from the linearized BTE (LBTE) in the absence of momentum-dissipating (Umklapp) phonon-phonon scattering events, derived mesoscopic equations in terms of the temperature and of the phonon drift velocity, *i.e.* the thermal counterparts of pressure and fluid velocity in liquids. Further advances came from Gurzhi [20, 21] and Guyer & Krumhansl [19, 22] who, including the effect of weak crystal momentum dissipation, obtained equations for damped second sound and for Poiseuille heat flow. Among early works, we also mention the discussions of phonon hydrodynamics in the framework of many-body theory, as in Refs. [252, 253, 254]. While correctly capturing the qualitative features of phonon hydrodynamics, all the theoretical investigations mentioned above assume simplified phonon dispersion relations (either power-law [20, 21] or linear isotropic [19, 22, 23]), or neglect momentum dissipation [23]. A more rigorous and general formulation — albeit valid only in the hydrodynamic regime of weak Umklapp scattering — was introduced by Hardy, who extended the study of second sound [24] and, together with Albers, of Poiseuille flow in terms of mesoscopic transport equations [25].

The turn of the century brought renewed interest in the theory of heat conduction; computational and algorithmic advances now allow to solve exactly the LBTE — employing iterative [34, 35, 36], variational [37], or exact diagonalization [38, 39] methods — and thus investigate the accuracy of the LBTE and the models derived from it. In addition, nowadays it is possible to solve the LBTE without any fitting parameter, deriving all quantities from first-principles; this has been shown to describe accurately the thermal properties of bulk crystals [7, 35, 41, 42, 43, 101, 161, 255, 256, 257, 258], provided phonon branches remain well-separated [67].

Further applications of the LBTE, combined with state-of-the-art first-principles simulations, have also recently predicted the existence of hydrodynamic phenomena at non-cryogenic temperatures in low-dimensional or layered materials such as graphene [255, 259, 260], other 2D materials [255], carbon nanotubes [261] and graphite [262]. Fittingly, and remarkably, these theoretical suggestions have now been confirmed by the experimental finding of second sound in graphite [31] at ~ 100 K.

In the hydrodynamic regime, where Poiseuille flow or second sound occur, Fourier's law fails [31, 263, 264, 265], depriving us of the most common tool used to predict the temperature profile in a device. The LBTE, in principle, allows to predict accurately thermal transport under these conditions, but its complexity prevents a straightforward application to materials with complex geometries (used in experiments and relevant for applications), thus posing limitations to the study of how a material's shape alters transport [256]. Recent research efforts have been directed at developing mesoscopic models that correct the shortcomings of Fourier's law and extend it at a lower computational cost than the solution of the full LBTE. Different strategies have been suggested; some approaches reduce the complexity of the LBTE by neglecting the effects of the phonon modes' repopulation due to scattering events (the so-called single-mode relaxation-time approximation (SMA)), thus allowing for analytical [266, 267, 268, 269] or asymptotic [270] solutions. From the LBTE in the SMA, mesoscopic models that generalize Fourier's law accounting for ultrafast thermal processes or ballistic effects have been derived [271, 272, 273, 274, 275]. Other works have derived mesoscopic models without relying on the LBTE [276], or have generalized the Guyer-Krumhansl equation to account for the effect of the boundaries on the heat flow [26, 27, 28, 29, 30]. A hydrodynamic transport model has been derived from the LBTE in the Callaway approximation, defining a phonon viscosity which can be computed from atomistic data [277].

Here, we provide a general and universal solution to the challenge of extending Fourier's law all the way to the hydrodynamic regime, deriving from the LBTE two novel coupled mesoscopic heat transport equations that cover exactly and on equal footing Fourier diffusion, hydrodynamic propagation, and all regimes in between.

To this aim, we first show that one can define the thermal viscosity of a crystal starting from an exact solution of the LBTE in terms of the eigenvectors of the scattering matrix (*i.e.* the relaxons introduced in Ref. [39] to determine thermal conductivity), and evaluate from it the crystal-momentum flux generated in response to a drift-velocity gradient. The relaxons' parity [39] highlights the complementary character of thermal conductivity and viscosity, with the former being determined by odd relaxons, and the latter by even relaxons.

Next, we use a coarse-graining procedure to derive two novel "viscous" heat equations: these are two coupled equations for the local temperature and drift-velocity fields, and are parametrized in terms of the thermal conductivity and viscosity. The viscous heat equations represent the thermal counterpart of the Navier-Stokes equations for fluids in the laminar regime, and, as mentioned, include Fourier's law and second sound in the limits of strong and weak crystal momentum dissipation, respectively.

Last, we introduce the Fourier deviation number (FDN), a dimensionless parameter that quantifies the deviation from Fourier's law due to hydrodynamic effects. We test this formalism on graphite, diamond and silicon, showing that the FDN predicts a temperature and size for the window of hydrodynamic thermal transport that replicates the explicit solution of the viscous heat equations, but at a negligible computational cost. Most importantly, the prediction of the present formulation for the hydrodynamic window of graphite is found to be in excellent agreement with recent, pioneering experiments [31]. In passing, we also predict that hydrodynamic behavior can appear in diamond at room temperature for micrometer-sized crystals.

4.3 Thermal viscosity

A microscopic description of thermal transport is given by the LBTE:

$$\frac{\partial n_\nu(\boldsymbol{r},t)}{\partial t} + \boldsymbol{v}_\nu \cdot \nabla n_\nu(\boldsymbol{r},t) = -\frac{1}{V}\sum_{\nu'} \Omega_{\nu\nu'} n_{\nu'}(\boldsymbol{r},t)\,, \tag{4.1}$$

where ν labels a phonon state (*i.e.* an index running on all the phonon wavevectors $\boldsymbol{q}$ and phonon branches s), $\boldsymbol{v}_\nu$ is the phonon group velocity, V is the crystal volume [1], and $\Omega_{\nu\nu'}$ is the phonon scattering matrix [39]. Eq. (4.1) governs the evolution of the deviation $n_\nu(\boldsymbol{r},t)$ of the phonon populations from equilibrium:

$$n_\nu(\boldsymbol{r},t) = N_\nu(\boldsymbol{r},t) - \bar{N}_\nu\,, \tag{4.2}$$

where $N_\nu(\boldsymbol{r},t)$ are the out-of-equilibrium phonon populations at position $\boldsymbol{r}$ and time t, $\bar{N}_\nu = (e^{\hbar\omega_\nu/(k_B\bar{T})}-1)^{-1}$ is the equilibrium Bose-Einstein distribution at temperature $\bar{T}$, and ω_ν are the phonon frequencies. From the solution of the LBTE one can derive the local lattice energy $E(\boldsymbol{r},t)=\frac{1}{V}\sum_\nu \hbar\omega_\nu N_\nu(\boldsymbol{r},t)$ and the total crystal momentum $\boldsymbol{P}(\boldsymbol{r},t)=\frac{1}{V}\sum_\nu \hbar\boldsymbol{q}N_\nu(\boldsymbol{r},t)$ [24]. The former is often studied in connection with the thermal conductivity [39], while the latter becomes relevant in the hydrodynamic regime of thermal transport [21, 23, 278]. We note in passing that this latter emerges only in "simple" crystals, *i.e.* those where phonon interbranch spacings are much larger than their linewidths [67].

The energy flux generated in response to a temperature gradient determines the thermal conductivity; correspondingly, the crystal-momentum flux generated in response to a perturbation of the drift velocity determines the thermal viscosity (for the analogous quantity in electronic transport, see Ref. [244]). Therefore, we start by considering a crystal in the hydrodynamic regime of thermal transport (*i.e.* carrying a finite amount of crystal momentum); the local equilibrium phonon distribution, obtained maximizing the local entropy under the constraints of fixed local energy and momentum [279], is the phonon drifting distribution [21]

$$N^D_\nu(T(\boldsymbol{r},t),\boldsymbol{u}(\boldsymbol{r},t)) = \frac{1}{e^{\frac{1}{k_B T(\boldsymbol{r},t)}(\hbar\omega_\nu - \hbar\boldsymbol{q}\cdot\boldsymbol{u}(\boldsymbol{r},t))}-1}\,. \tag{4.3}$$

The drifting distribution differs from the Bose-Einstein distribution due to the presence of the drift velocity $\boldsymbol{u}(\boldsymbol{r},t)$, a parameter expressing the amount of local momentum, just as the temperature $T(\boldsymbol{r},t)$ does for the local energy; formally, $T(\boldsymbol{r},t)$ and $\boldsymbol{u}(\boldsymbol{r},t)$ can be related to the Lagrange multipliers that enforce the constraints of fixed local energy and momentum, respectively. The drifting distribution (4.3) depends implicitly on $\boldsymbol{r},t$ through $T(\boldsymbol{r},t)$ and $\boldsymbol{u}(\boldsymbol{r},t)$. Next, we study the effect of small perturbations in the temperature and drift velocity. To this aim, we expand the deviation from equilibrium Eq. (4.2) in proximity of the local equilibrium Eq. (4.3) [24], finding

---

[1] $V=\mathcal{V}N_c$ *i.e.* the unit cell volume $\mathcal{V}$ times the number of unit cells that constitute the crystal N_c. N_c is also the number of wavevectors $\boldsymbol{q}$ used to sample the Brillouin zone

$$\begin{aligned} n_\nu(\boldsymbol{r},t) &= \frac{\partial N^D_\nu}{\partial T}\bigg|_{\mathrm{eq}}(T(\boldsymbol{r},t)-\bar{T}) + \frac{\partial N^D_\nu}{\partial \boldsymbol{u}}\bigg|_{\mathrm{eq}}\cdot \boldsymbol{u}(\boldsymbol{r},t) + n^\delta_\nu(\boldsymbol{r},t) \\ &= n^T_\nu(\boldsymbol{r},t) + n^D_\nu(\boldsymbol{r},t) + n^\delta_\nu(\boldsymbol{r},t), \end{aligned} \tag{4.4}$$

where n^T_ν arises from the local temperature [280], n^D_ν from the local drift velocity, and n^δ_ν accounts for all the information that cannot be mapped to a local equilibrium state; the subscript "eq" means that the derivatives are computed at equilibrium where $T(\boldsymbol{r},t)=\bar{T}$ and $\boldsymbol{u}(\boldsymbol{r},t)=0$ and to ease the notation this will be omitted in the following. In analogy with previous work [37, 39], we consider the steady-state case and linearize the LBTE around the constant temperature and drift-velocity gradients (*i.e.* n^δ_ν, ∇T, and $\nabla \boldsymbol{u}$ are constant). Then, we substitute Eq. (4.4) in Eq. (4.1) and, keeping only terms linear in the temperature and drift-velocity gradients, we obtain

$$\frac{\partial \bar{N}_\nu}{\partial T}\boldsymbol{v}_\nu\cdot\nabla T + \boldsymbol{v}_\nu\cdot\left(\frac{\partial N^D_\nu}{\partial \boldsymbol{u}}\cdot\nabla\boldsymbol{u}\right) = -\frac{1}{V}\sum_{\nu'}\Omega_{\nu\nu'}\left(n^T_{\nu'}(\boldsymbol{r},t) + n^D_{\nu'}(\boldsymbol{r},t) + n^\delta_{\nu'}\right). \tag{4.5}$$

We recast Eq. (4.5) in the symmetric (thus diagonalizable) form, *i.e.* in terms of $\tilde{\Omega}_{\nu\nu'} = \Omega_{\nu\nu'}\sqrt{\frac{\bar{N}_{\nu'}(\bar{N}_{\nu'}+1)}{\bar{N}_\nu(\bar{N}_\nu+1)}}$ and $\tilde{n}_\nu(\boldsymbol{r},t) = n_\nu(\boldsymbol{r},t)[\bar{N}_\nu(\bar{N}_\nu+1)]^{-\frac{1}{2}}$ with the goal of using the relaxon picture [39] to gain insight in the physics underlying transport. We then simplify the symmetrized Eq. (4.5) exploiting parity: we recall that a function f_ν is even if $f_\nu = f_{-\nu}$ (this is e.g. the case of the phonon energy $\hbar\omega_\nu = \hbar\omega_{-\nu}$), and odd if $f_\nu = -f_{-\nu}$ (e.g. the phonon group velocity $\boldsymbol{v}_\nu = -\boldsymbol{v}_{-\nu}$), and use the notation $-\nu = (-\boldsymbol{q},s)$. Therefore, $\frac{\partial \bar{N}_\nu}{\partial T}$ and thus $\tilde{n}^T_\nu(\boldsymbol{r},t)$ are even, whereas $\frac{\partial \bar{N}^D_\nu}{\partial \boldsymbol{u}}$ and thus $\tilde{n}^D_\nu(\boldsymbol{r},t)$ are odd.

Since the eigenvectors of the scattering matrix have a well-defined parity [24][2], we can split $\tilde{n}^\delta_\nu$ into $\tilde{n}^{\delta\mathrm{E}}_\nu + \tilde{n}^{\delta\mathrm{O}}_\nu$, separating the even ($\tilde{n}^{\delta\mathrm{E}}_\nu$) and odd ($\tilde{n}^{\delta\mathrm{O}}_\nu$) components. At steady state, Eq. (4.5) decouples into two equations, one for each parity. The equation for the odd part is

$$\frac{\boldsymbol{v}_\nu}{\sqrt{\bar{N}_\nu(\bar{N}_\nu+1)}}\cdot\left(\frac{\partial \bar{N}_\nu}{\partial T}\nabla T\right) = -\frac{1}{V}\sum_{\nu'}\tilde{\Omega}_{\nu\nu'}\tilde{n}^{\delta\mathrm{O}}_{\nu'} \tag{4.6}$$

and describes the response to a thermal gradient [37, 39], where $\tilde{n}^{\delta\mathrm{O}}_\nu$ is the odd out-of-equilibrium phonon population generated in response to a temperature gradient. In writing Eq. (4.6) we made the assumption that $\frac{1}{V}\sum_{\nu'}\tilde{\Omega}_{\nu\nu'}\left(\tilde{n}^D_{\nu'}(\boldsymbol{r},t)+\tilde{n}^{\delta\mathrm{O}}_{\nu'}\right) \simeq \frac{1}{V}\sum_{\nu'}\tilde{\Omega}_{\nu\nu'}\tilde{n}^{\delta\mathrm{O}}_{\nu'}$, as explained in Appendix 4.A. The solution of equation (4.6) can then be used to determine the heat flux and the thermal conductivity (see e.g. Refs. [37, 39]). The equation for the even part is

---

[2] This follows from the property $\tilde{\Omega}_{\nu\nu'} = \tilde{\Omega}_{-\nu,-\nu'}$

$$\frac{\boldsymbol{v}_\nu}{\sqrt{\bar{N}_\nu(\bar{N}_\nu+1)}} \cdot \left(\frac{\partial N^D_\nu}{\partial \boldsymbol{u}} \cdot \nabla \boldsymbol{u} \right) = -\frac{1}{V} \sum_{\nu'} \tilde{\Omega}_{\nu\nu'} \tilde{n}^{\delta \mathrm{E}}_{\nu'} \,, \tag{4.7}$$

and describes the response to a drift-velocity gradient, where $\tilde{n}^{\delta\mathrm{E}}_\nu$ is the even out-of-equilibrium phonon population generated in response to it. In writing Eq. (4.7) we used the property that $\tilde{n}^T_\nu(\boldsymbol{r},t)$ is an eigenvector of the scattering matrix with zero eigenvalue: $\frac{1}{V}\sum_{\nu'} \tilde{\Omega}_{\nu\nu'} \tilde{n}^T_{\nu'}(\boldsymbol{r},t) = 0$ (also detailed in Appendix 4.A).

The phonon deviation $\tilde{n}^{\delta\mathrm{E}}_\nu$ gives rise to a crystal momentum flux $\Pi^{ij}_{\delta\mathrm{E}} = \frac{1}{V}\sum_\nu \hbar q^i v^j_\nu \sqrt{\bar{N}_\nu(\bar{N}_\nu+1)}\, \tilde{n}^{\delta\mathrm{E}}_\nu$ [21, 24]. Analogously to the electronic case [244], the flux of crystal momentum allows to define the thermal viscosity as the 4th-rank tensor relating the local response $\Pi^{ij}_{\delta\mathrm{E}}(\boldsymbol{r},t)$ to the local perturbation $\nabla \boldsymbol{u}(\boldsymbol{r},t)$:

$$\Pi^{ij}_{\delta\mathrm{E}}(\boldsymbol{r},t) = -\sum_{kl} \eta^{ijkl} \frac{\partial u^k(\boldsymbol{r},t)}{\partial r^l} \,; \tag{4.8}$$

the uniform drift-velocity gradient is a special space-independent case of this local relationship. Eq. (4.7) has the same mathematical form of the steady-state LBTE linearized in the temperature gradient and used to compute the thermal conductivity. Therefore, we can readily solve it applying the methodology introduced in Ref. [39], and based on the eigenvectors of the scattering matrix (relaxons), to find a closed expression for $\tilde{n}^{\delta\mathrm{E}}_\nu$. Combining such solution with Eq. (4.8) we find, after symmetrizing, the following expression for the symmetrized thermal viscosity

$$\mu^{ijkl} = \frac{\eta^{ijkl} + \eta^{ilkj}}{2} = \sqrt{A^i A^k} \sum_{\alpha > 0} \frac{w^j_{i\alpha} w^l_{k\alpha} + w^l_{i\alpha} w^j_{k\alpha}}{2} \tau_\alpha \,, \tag{4.9}$$

where $A^i = \frac{\partial P^i}{\partial u^i}\big|_{\mathrm{eq}} = \frac{1}{k_B T V}\sum_\nu \bar{N}_\nu(\bar{N}_\nu+1)(\hbar q^i)^2$ is referred to as the specific momentum, τ_α is the relaxation time of relaxon α (*i.e.* the inverse eigenvalue associated to the eigenvector θ^α_ν of the symmetrized scattering matrix $\tilde{\Omega}_{\nu\nu'}$ [39]), and $w^j_{i\alpha}$ is the velocity tensor $w^j_{i\alpha} = \frac{1}{V}\sum_\nu \phi^i_\nu v^j_\nu \theta^\alpha_\nu$ for relaxon θ^α_ν and eigenvector ϕ^i_ν (see Appendix 4.B for a full demonstration). ϕ^i_ν are three special eigenvectors linked to the crystal momentum of the system; to see this, we first decompose the scattering matrix as $\tilde{\Omega}_{\nu\nu'} = \tilde{\Omega}^N_{\nu\nu'} + \tilde{\Omega}^U_{\nu\nu'}$, where $\tilde{\Omega}^N_{\nu\nu'}$ and $\tilde{\Omega}^U_{\nu\nu'}$ contain only momentum-conserving (normal) and momentum-dissipating (Umklapp) processes, respectively. Since the normal part of the scattering matrix conserves crystal momentum, there exists a set of 3 eigenvectors ϕ^i_ν ($i = 1, \ldots, 3$ where 3 is the dimensionality of the system) with zero eigenvalue for $\tilde{\Omega}^N_{\nu\nu'}$, which are associated to the conservation of crystal momentum in the 3 Cartesian directions. Because the viscosity describes the response of the crystal momentum flux to a change of drift velocity, it is not surprising that the eigenvectors ϕ^i_ν appear in its definition. In fact, the deviation-from-equilibrium distribution (Eq. (4.4)) is linear in the drift velocity, with the proportionality coefficients being these special eigenvectors (see Appendix 4.A for a proof), and therefore they appear in the viscosity as well, to describe a perturbation to the local equilibrium. We note in passing that the thermal viscosity defined in Eq. (4.9) has the dimensions of a dynamic viscosity (Pa·s) and satisfies the property $\mu^{ijkl} = \mu^{ilkj} = \mu^{kjil}$.

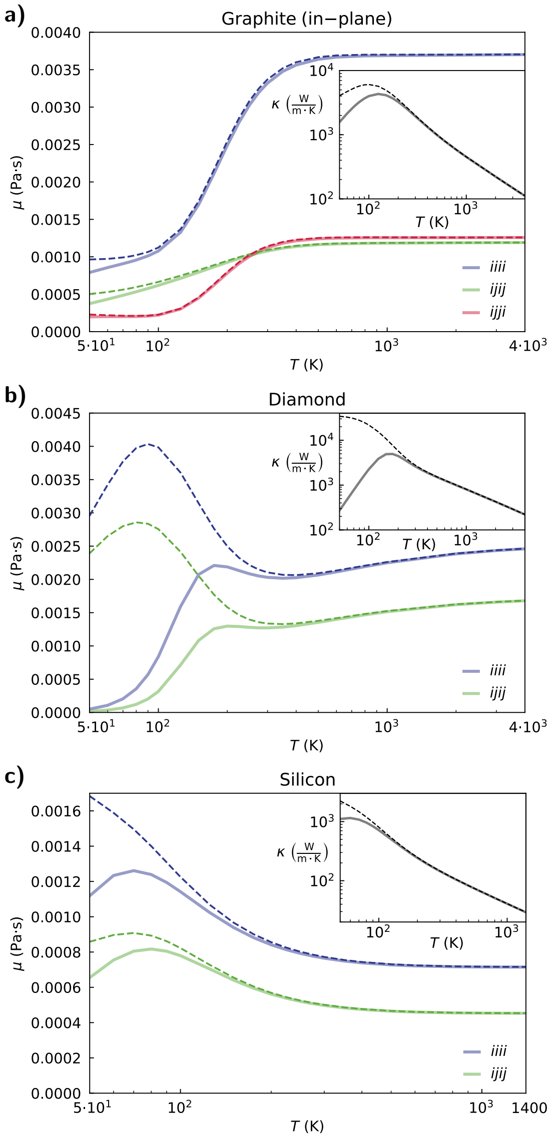

Figure 4.3.1 – Largest components of the 4th-order thermal viscosity tensor for graphite (a), diamond (b), and silicon (c), as a function of temperature (the off-plane tensor components for graphite are reported in Fig. 4.E.2). Insets: total thermal conductivities (in-plane components for graphite and diagonal components of the isotropic tensor for diamond and silicon) as a function of temperature. The dashed lines refer to the bulk materials (Eq. (4.9) for viscosity and Eq. (4.52) for conductivity); the solid lines show finite-size predictions computed using Eq. (4.57) and Eq. (4.58) for a sample having size (or grain size) 10 μm (see main text and Appendix 4.C; for diamond and silicon the component μ^{ijji} is negligible).

We report in Fig. 4.3.1 the first-principles estimates of the thermal viscosity for graphite, diamond, and silicon. We choose these three materials as prototypes for two different behaviors, the former two displaying hydrodynamic thermal transport [31, 37, 262, 264, 281, 282], as opposed to the more conventional case of silicon [37, 39]. We account for finite-size effects by combining the bulk viscosity in Eq. (4.9) with its ballistic limit via Matthiessen's rule for a sample having size (or grain size) of 10 μm; the same renormalization is applied also to the thermal conductivity (see Appendix 4.C for details). This is an approximate treatment of surface scattering effects, which provides an estimate of size effects at a much lower computational complexity compared to more refined models [281, 283]. In general, when samples' sizes become comparable or smaller than the carriers' diffusion lengths [29, 284, 285, 286, 287, 288], transport coefficients cannot be rigorously defined and a more accurate treatment is required, solving the much more complex and computationally expensive space-dependent LBTE [36, 256, 266, 289]. Matthiessen's approach is a good approximation when the values of thermal conductivity and viscosity do not differ significantly from their bulk counterparts, as is the case for the materials, sizes and temperatures considered in this work (e.g., in Fig. 4.3.1 the size renormalization is negligibly small in the temperature range considered for graphite and silicon, and becomes so above 300 K for diamond).

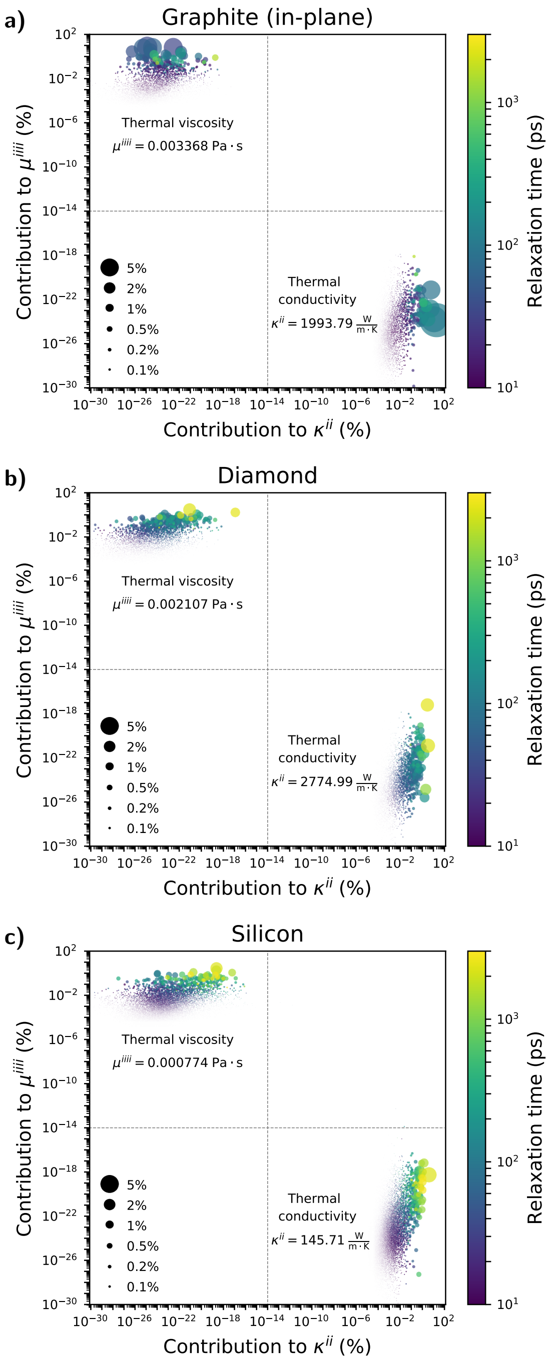

Figure 4.3.2 – Relaxons' contributions to the bulk thermal conductivity and to the thermal viscosity at 300 K for graphite (a, in-plane components), diamond (b) and silicon (c). Each dot represents a relaxon, with its color labeling its relaxation time, and its area being proportional to the sum of its percentage contributions to the thermal conductivity and viscosity. The dashed lines are plotted as a guide to the eye, to underscore how even and odd relaxons are fully decoupled. Odd relaxons, which determine the thermal conductivity, yield negligible (zero) contributions to the thermal viscosity; conversely, even relaxons determine the thermal viscosity and yield negligible (zero) contributions to thermal conductivity.

For graphite in the low-temperature ($\lesssim$100 K) regime, the bulk in-plane viscosity components are constant or slowly increasing with temperature; at higher temperatures, the viscosity components increase with temperature up to reaching their saturation values. For a graphite polycrystalline sample with a grain size of $10\mu m$, finite-size effects on viscosity (and on conductivity) are small. For diamond in the temperature regime below 90 K, the bulk values of the thermal viscosity increase with increasing temperature, then in the intermediate temperature regime (100 K $\lesssim T \lesssim$ 300 K) they decrease with temperature, and finally for increasingly higher temperatures they gently increase up to saturating to the high-temperature limiting values. However, size effects renormalize this behavior for temperatures below 300 K, leaving viscosity components that increase with temperature. In silicon, increasing temperature yields a decrease, up to a high-temperature saturation value, of the bulk thermal viscosity; size effect renormalize the viscosity below ~ 100 K yielding viscosity components that increase with temperature (*i.e.* a behavior analogous to that of diamond). We note that in the high-temperature limit, *i.e.* when the thermal conductivity decays as T^{-1} [14, 110], the viscosity components tend to constant values for all these three materials. The total bulk thermal conductivities are shown in the insets of Fig. 4.3.1 for comparison (we only show one component; for diamond and silicon the conductivity tensor is isotropic, for graphite we show the in-plane component). The off-plane transport coefficients for graphite are discussed in Fig. 4.E.2a. In graphite, the bulk thermal conductivity below 100 K does not increase monotonically as the temperature is decreased due to the presence of natural-abundance isotopic scattering. Natural-abundance isotopic scattering has been considered also for diamond and silicon, and the thermal conductivity at low temperatures is much lower than for isotopically-pure diamond [37, 164, 290, 291, 292, 293, 294] or silicon [295]. We have also verified that the effects of phonon coherences are negligible in these crystals [67]. We note in passing that, even if the thermal conductivities of diamond and silicon differ by more than one order of magnitude, their largest thermal-viscosity components differ only by a factor of 3. These results may be compared with the case of water, whose dynamic (shear) viscosity is $8.9{\cdot}10^{-4}$ Pa·s at room temperature, indicating that the thermal viscosity found here is comparable or larger. To a good approximation, water is an incompressible fluid, and thus viscosity component $ijkl$ with $j \neq k$ are negligible, this resulting in Navier-Stokes equations containing the Laplacian of the velocity multiplied by the "first viscosity" (or "shear viscosity") coefficient. For compressible fluids, the components of the viscosity tensor μ^{ijkl} with $j \neq k$ are non-negligible, resulting in Navier-Stokes equations containing mixed second-order derivatives of the velocity, as well as an additional parameter called "second viscosity" (or "volume viscosity") [296, 297, 298]. Here, the components of the viscosity tensor μ^{ijkl} with $j \neq k$ are needed to parametrize mixed second-order derivatives, and this elicits an analogy to a compressible fluid. It is important to mention that the present formulation may need further extension to deal with unstrained 2D materials, since their flexural phonon modes have a quadratic dispersion $\omega_\nu \propto q^2$ at $T = 0K$ [299]. Under these conditions, long-wavelength phonons lead to $\boldsymbol{q} \cdot \boldsymbol{u}$ being larger than ω_ν, causing negative values of the phonon drifting distribution which are not compatible with a semiclassical description of transport. Further work is needed to address this issue, for example considering the phonon renormalization due to coupling between bending and stretching degrees of freedom of the monolayer [300] or the presence of a substrate [301], or introducing the Wigner-function formalism [67, 302].

Finally, it is worth checking the complementary character of the thermal conductivity and viscosity that arises from their decoupled relaxons' contributions. As commented above, decomposing the thermal conductivity [39] and viscosity (4.9) in terms of single relaxons makes it possible to show that the thermal viscosity is uniquely determined by the even part of the relaxon spectrum, while the thermal conductivity is determined uniquely by the odd part of the relaxon spectrum [39]. In Fig. 4.3.2 we highlight the contributions of each relaxon to the total thermal conductivity and viscosity, confirming numerically this picture.

4.4 Viscous heat equations

We show here that heat conduction can be described by two novel viscous heat equations that cover on the same footing both the Fourier and hydrodynamic limits, and all intermediate regimes. These are two coupled equations in the temperature $T(\boldsymbol{r},t)$ and drift-velocity $\boldsymbol{u}(\boldsymbol{r},t)$ fields, which are parametrized by the thermal conductivity and viscosity. These equations represent the thermal counterpart of the Stokes equations of fluid dynamics — *i.e.* the Navier-Stokes equations in the linear regime, whose solution yields the laminar flow — where temperature takes the role of pressure and the phonon drift velocity that of the fluid velocity. In the kinetic regime, when momentum-dissipating (Umklapp) scattering processes dominate [255], these viscous heat equations become equivalent to Fourier's heat equation.

As underscored before, hydrodynamic thermal transport is characterized by energy conservation and crystal momentum quasi-conservation (the latter being exactly conserved only in absence of Umklapp processes [23]). Conserved quantities in the LBTE dynamics can be related to the eigenvectors of the full or normal scattering matrix with zero eigenvalues [24] (see also Appendix 4.A). Four of these eigenvectors (*i.e.* phonon distribution functions) can be identified. The first one is the Bose-Einstein eigenvector $\phi^0_\nu \propto \hbar\omega_\nu \propto \frac{\partial \bar{N}_\nu}{\partial T} \propto \tilde{n}^T_\nu$, which is the eigenvector of zero eigenvalue for the symmetrized full scattering matrix $\tilde{\Omega}_{\nu\nu'}$; its zero eigenvalue is associated to energy conservation in scattering events (both normal and Umklapp). The other three eigenvectors are the drift eigenvectors $\phi^i_\nu \propto \hbar q^i \propto \frac{\partial N^D_\nu}{\partial u^i} \propto \tilde{n}^D_\nu$, $i = 1,2,3$ (where 3 is the dimensionality of the system) already introduced for the evaluation of the viscosity; these ϕ^i_ν are eigenvectors with zero eigenvalue for the normal part of the scattering matrix $\tilde{\Omega}^N_{\nu\nu'}$ and are associated to the conservation of crystal momentum by normal scattering events [22, 23, 24]. We note that these four eigenvectors constitute the first two terms of the phonon distribution expansion in Eq. (4.4). We can thus derive the mesoscopic equations that govern the evolution of the temperature ($T(\boldsymbol{r},t)$) and drift velocity ($\boldsymbol{u}(\boldsymbol{r},t)$) fields projecting the microscopic LBTE in the subspaces spanned by ϕ^0_ν and by ϕ^i_ν ($i = 1,\ldots,3$). In order to derive a closed-form equation for the drift velocity, when projecting in the subspace spanned by ϕ^i_ν we consider the effects of momentum dissipation only within that subspace. The result is the following set of equations (see Appendix 4.D for a detailed derivation):

$$C\frac{\partial T(\boldsymbol{r},t)}{\partial t}+\sum_{i,j=1}^{3} W^{i}_{0j}\sqrt{\bar{T}A^{j}C}\frac{\partial u^{j}(\boldsymbol{r},t)}{\partial r^{i}}-\sum_{i,j=1}^{3}\kappa^{ij}\frac{\partial^{2}T(\boldsymbol{r},t)}{\partial r^{i}\partial r^{j}}=0\,, \tag{4.10}$$

$$A^{i}\frac{\partial u^{i}(\boldsymbol{r},t)}{\partial t}+\sqrt{\frac{CA^{i}}{\bar{T}}}\sum_{j=1}^{3}W^{j}_{i0}\frac{\partial T(\boldsymbol{r},t)}{\partial r^{j}}-\sum_{j,k,l=1}^{3}\mu^{ijkl}\frac{\partial^{2}u^{k}(\boldsymbol{r},t)}{\partial r^{j}\partial r^{l}}=-\sum_{j=1}^{3}\sqrt{A^{i}A^{j}}D^{ij}_{U}u^{j}(\boldsymbol{r},t)\,, \tag{4.11}$$

where $C=\frac{1}{k_B\bar{T}^2V}\sum_\nu \bar{N}_\nu\big(\bar{N}_\nu+1\big)(\hbar\omega_\nu)^2$ is the specific heat, $W^i_{0j}=\frac{1}{V}\sum_\nu \phi^0_\nu v^i_\nu \phi^j_\nu$ is a velocity tensor that arises from the non-diagonal form of the diffusion operator in the basis of the eigenvectors of the normal part of the scattering matrix (see Appendix 4.D), $\bar{T}$ is the reference (equilibrium) temperature on which a perturbation is applied (see Sec. 4.6 and Appendix 4.A.1), A^i is the specific momentum in direction i (defined in Sec. 4.3), μ^{ijkl} is the thermal viscosity tensor, κ^{ij} is the thermal conductivity tensor [39], and D^{ij}_U is the momentum dissipation rate; the latter is caused both by the presence of Umklapp processes as well as boundary scattering (*i.e.* D^{ij}_U is sensitive to size effects like the thermal conductivity and viscosity). Treating boundary scattering as in Ref. [281], the momentum-dissipating phonon collisions described by the matrix $\tilde{\Omega}^U_{\nu\nu'}$ can be rewritten as $\tilde{\Omega}^U_{\nu\nu'}=\tilde{\Omega}^{U,\text{bulk}}_{\nu\nu'}+\tilde{\Omega}^{U,\text{boundary}}_{\nu\nu'}(L_S)$, where $\tilde{\Omega}^{U,\text{bulk}}_{\nu\nu'}$ accounts for umklapp scattering in the bulk and $\tilde{\Omega}^{U,\text{boundary}}_{\nu\nu'}(L_S)$ approximates the momentum-dissipating scattering of phonons with boundaries at a distance L_S. Therefore, we compute D^{ij}_U as $D^{ij}_U=D^{ij}_{U,\text{bulk}}+D^{ij}_{U,\text{boundary}}(L_S)$, where

$$\begin{aligned}D^{ij}_{U,\text{bulk}}&=\frac{1}{V^2}\sum_{\nu\nu'}\phi^i_\nu\tilde{\Omega}^{U,\text{bulk}}_{\nu\nu'}\phi^j_{\nu'};\\ D^{ij}_{U,\text{boundary}}(L_S)&=\frac{1}{V^2}\sum_{\nu\nu'}\phi^i_\nu\tilde{\Omega}^{U,\text{boundary}}_{\nu\nu'}(L_S)\phi^j_{\nu'}=\frac{1}{V}\sum_\nu\phi^i_\nu\frac{|\boldsymbol{v}_\nu|}{L_S}\phi^j_\nu.\end{aligned} \tag{4.12}$$

The scalar equation (4.10) and the vectorial (3-components) equation (4.11) rule the coupled evolution of the scalar temperature field and of the vector drift-velocity field; they constitute the main result of this work and we name these "viscous heat equations". These transport equations are reminiscent of the linearized Stokes equations for fluids: to see this more clearly, we note that local energy $E(\boldsymbol{r},t)$ and crystal momentum $\boldsymbol{P}(\boldsymbol{r},t)$ are proportional to temperature and drift velocity respectively ($E(\boldsymbol{r},t)=C\,T(\boldsymbol{r},t)$ and $P^i(\boldsymbol{r},t)=A^i\,u^i(\boldsymbol{r},t)$, where C is the specific heat and $\boldsymbol{A}$ is the specific momentum). Exploiting these relationships, it is possible to rewrite the viscous heat equations in a more familiar form, namely as energy E and momentum P^i balance equations:

$$\frac{\partial E(\boldsymbol{r},t)}{\partial t}+\nabla\cdot\Big(\boldsymbol{Q}^{\delta}(\boldsymbol{r},t)+\boldsymbol{Q}^{D}(\boldsymbol{r},t)\Big)=0\,, \tag{4.13}$$

$$\frac{\partial P^i(\boldsymbol{r},t)}{\partial t}+\sum_j\left(\frac{\partial\Pi^{ij}_T(\boldsymbol{r},t)}{\partial r^j}+\frac{\partial\Pi^{ij}_{\delta\text{E}}(\boldsymbol{r},t)}{\partial r^j}\right)=-\frac{\partial P^i(\boldsymbol{r},t)}{\partial t}\bigg|_{\text{Umkl}}, \tag{4.14}$$

where, on the basis of the phonon population expansion in Eq. (4.4), we distinguish the drifting heat flux into the contributions from the local temperature gradient $Q^{\delta,i}(\boldsymbol{r},t) = -\sum_j \kappa^{ij}\nabla^j T(\boldsymbol{r},t)$ and from the drift velocity field $Q^{D,i}(\boldsymbol{r},t) = \sum_j W^i_{0j}\sqrt{\bar{T}A^j C}u^j(\boldsymbol{r},t)$. Similarly, the non-equilibrium momentum flux receives separate contributions from the local temperature $\Pi^{ij}_T(\boldsymbol{r},t) = \sqrt{CA^i/\bar{T}}\;W^j_{i0}[T(\boldsymbol{r},t)-\bar{T}]$ and from variations of the drift velocity through Eq. (4.8). Finally, $\frac{\partial P^i}{\partial t}\big|_{\text{Umkl}}$ accounts for the dissipation of crystal momentum by Umklapp processes or scattering with boundaries; further details can be found in Appendix 4.D. The distinction between temperature-driven and drifting components of the heat flux ($\boldsymbol{Q}^{\delta}(\boldsymbol{r},t)$ and $\boldsymbol{Q}^{D}(\boldsymbol{r},t)$, respectively) is essential for hydrodynamic transport. We will show in Sec. 4.7 that Fourier's law is recovered in the limiting case where crystal momentum dissipation dominates over viscous effects and is the fastest timescale of the phonon dynamics.

It is worth mentioning that the viscous heat equations introduced here differ from the Stokes equations for fluids in two major ways. First, there is no analogy with the mass conservation satisfied by Stokes equations, since the total phonon number is not a constant of motion (e.g. a phonon coalescence event decreases the number of phonons in the system). Second, while collisions between molecules in the fluid conserve momentum, scattering among phonons does not conserve crystal momentum in presence of Umklapp processes.

The most relevant feature of the viscous heat equations is their capability to describe hydrodynamic thermal transport in terms of mesoscopic quantities, *i.e.* temperature and drift velocity, resulting in a much simpler and computationally less expensive approach than the microscopic LBTE. The parameters entering Eqs. (4.10, 4.11) can be determined from first-principles calculations or, possibly less accurately, from classical potentials, and are tabulated in Appendix 4.E for graphite, diamond and silicon.

In order to be solved, the viscous heat equations require appropriate boundary conditions on the temperature and drift velocity. Boundary conditions on temperature have been widely studied in conjunction with Fourier's heat equation [303]: typically, one makes assumptions on the system's capability to exchange heat at the boundaries, and on the temperature at those boundaries (Neumann and Dirichlet boundary conditions, respectively [303]). In the next section 4.6 we consider a system in which the temperature is fixed at some boundaries, while the others are assumed to be adiabatic (that is, the heat flux across these boundaries is zero). In contrast, boundary conditions on the drift velocity, *i.e.* on crystal momentum at the sample's borders, have not been studied as extensively. Since crystal momentum is not conserved at boundaries [23], we impose a no-slip condition of zero drift velocity $\boldsymbol{u}(\boldsymbol{r},t)$ on all boundaries, ensuring thus zero drifting heat $\boldsymbol{Q}^{D}(\boldsymbol{r},t) \propto \boldsymbol{u}(\boldsymbol{r},t)$. As discussed in past work [14, 256], more comprehensive boundary conditions require quantifying phonon reflection at surfaces, and are beyond the scope of this work.

The viscous heat equations (4.10,4.11) improve upon past work on different levels. First, they are valid for general dispersion relations for phonons, and thus overcome the limitations — pointed out by Hardy and Albers [25] already in 1974 — of the pioneering mesoscopic models developed in the 1960s by Guyer-Krumhansl [19, 22] or Gurzhi [21], which assumed linear-isotropic or power-law phonon dispersion relations, respectively (assumptions which arose from the hypothesis that hydrodynamic phenomena would occur at cryogenic temperatures only). The limitations of the Guyer-Krumhansl [19, 22] and Gurzhi [21] models were overcome in 1974 by Hardy and Albers [25], who derived from the LBTE a set of mesoscopic equations for energy and crystal momentum valid for a general phonon dispersion relation (*i.e.* not necessarily linear-isotropic). Hardy and Albers' formulation relies on the hydrodynamic approximation — *i.e.* that the fastest timescale of phonon dynamics is that of normal processes — that is valid only within the hydrodynamic regime, where Umklapp collisions are rare events. In fact, Hardy and Albers' equations are limited just to the hydrodynamic regime and do not incorporate Fourier's law as a limit (and thus any intermediate regimes). The viscous heat equations address exactly this issue, and Fourier's law emerges when crystal momentum dissipation (due to Umklapp processes or scattering with boundaries) dominates over viscous effects and is the fastest timescale of the phonon dynamics (see Sec. 4.7). Finally, the viscous heat equations take into account the entire collision matrix, at variance with recent mesoscopic models derived from the LBTE either in the SMA [28] or in the Callaway approximation [277].

4.5 Second sound

Second sound is the coherent propagation of a temperature wave [19, 23, 24, 31, 253, 260, 304, 305, 306, 307], and it is an effect properly described by the viscous heat equations. From a phenomenological point of view, second sound appears when the temperature field satisfies the following damped wave equation [24] (we define x as the second sound propagation direction):

$$\frac{\partial^2 T(x,t)}{\partial t^2} + \frac{1}{\tau_{ss}}\frac{\partial T(x,t)}{\partial t} - v_{ss}^2 \frac{\partial^2 T(x,t)}{\partial x^2} = 0\,, \tag{4.15}$$

where τ_{ss} and v_{ss} are the second-sound relaxation time and propagation velocity, yet to be determined. In contrast to Fourier's law, which has the form of a classical (non-relativistic) diffusion equation and states that a temperature-gradient variation causes an instantaneous variation of the heat flux, Eq. (4.15) has the physical property that a sudden localized change of temperature propagates in space with a finite speed (*i.e.* it is not felt instantly everywhere in space) [251, 308, 309, 310]. The temperature profile that solves Eq. (4.15) has the form of a damped wave:

$$T(x,t) = \bar{T} + \delta T\, e^{i(kx-\tilde{\omega}(k)t)} e^{-t/2\tau_{ss}}\,, \tag{4.16}$$

where the second sound frequency $\tilde{\omega}(k)$ depends on the second-sound wavevector k. In Appendix 4.F we derive the second-sound equation from the viscous heat equations (4.10,4.11) following two different approaches (bottom-up and top-down). In the first bottom-up approach we find the conditions for which the damped wave equation (4.15) emerges from the viscous heat equations Eq. (4.10,4.11). When this happens, the solution of Eq. (4.15) is the damped wave equation for temperature (4.16) shown above, with the second-sound dispersion relation given by $\tilde{\omega}(k) = \sqrt{v_{ss}^2 k^2 - (2\tau_{ss})^{-2}}$ (this can be easily verified substituting Eq. (4.16) into Eq. (4.15)). This allows to express τ_{ss} and v_{ss} in terms of the parameters appearing in the viscous heat equations; in particular, $\tau_{ss} = \frac{C(W^x_{x0})^2}{\kappa^{xx}(D^{xx}_U)^2 + D^{xx}_U C(W^x_{x0})^2}$ and $v_{ss} = \frac{\kappa^{xx} D^{xx}_U + C(W^x_{x0})^2}{C W^x_{x0}}$. The propagation velocity of second sound is affected by damping and depends on the wavevector k: it is given by the group velocity $v_g(k) = \frac{\partial \bar{\omega}(k)}{\partial k} = k v_{ss}[k^2 - (2\tau_{ss} v_{ss})^{-2}]^{-\frac{1}{2}}$, and we note that it reduces to the undamped propagation velocity v_{ss} in the undamped limit $\tau_{ss} \to \infty$.

These results are consistent with empirical expectations on second sound: in the limit of weak crystal momentum dissipation the second-sound relaxation time increases, while the velocity becomes smaller, making second sound more likely to be observed in the hydrodynamic regime [19, 24]. In fact, when $D^{xx}_U \to 0$ we find that $\tau_{ss} \to (D^{xx}_U)^{-1}$ and $v_{ss} \to W^x_{x0}$. We note that the viscous heat equations describe not only the propagation of the temperature field, but also that of the drift velocity. In Appendix 4.F we show that when second sound emerges the drift-velocity field propagates as a damped wave as well (*i.e.* similar to Eq. (4.16)), with the same relaxation time and velocity of temperature, but with a phase shift. Phase shifts between hydrodynamic and resistive components of the frequency-dependent heat flux have also been discussed recently in the context of an improved Callaway approximation for the LBTE [279, 311].

As an alternative, we took inspiration from Ref. [260], which derived the second-sound dispersion relations by taking advantage of the Laplace transform of the LBTE, to identify solutions in the form of a damped wave following a top-down approach. In particular, we take a damped-wave ansatz for temperature, Eq. (4.16) with $\bar{\omega}(k)$ replaced by $\hat{\omega}(k)$ and τ_{ss} by $\hat{\tau}_{ss}$ (we use the hat to distinguish the results for the top-down approach from those of the bottom-up approach), and a similar one for the drift-velocity field (with the same frequency and decay time of temperature); we substitute these into the viscous heat equations (4.10,4.11) and determine the conditions under which these are acceptable solutions. As detailed in Appendix 4.F, we find that the dispersion relations of second sound in the long-wavelength limit reduce to $\hat{\omega}(k) - \frac{i}{2\hat{\tau}_{ss}} \approx \sqrt{k^2\left[(W^x_{0x})^2 + D^{xx}_U \kappa^{xx}/2C - \mu^{xxxx} D^{xx}_U/2A^x\right] - \left(D^{xx}_U/2\right)^2} - iD^{xx}_U/2$. In this long wavelength limit and in the hydrodynamic regime $D^{xx}_U \to 0$, we have $\hat{\tau}_{ss} \approx \frac{1}{D^{xx}_U}$ and $\hat{v}_g(k) \approx W^x_{0x}$, which is consistent with the first bottom-up approach presented to derive the equations for second sound. We further stress that the LBTE can only rigorously describe second sound in the long-wavelength limit $k \to 0$ in order for the temperature to be slowly varying (for which the two approaches shown in this section provide the same result); for smaller wavelengths, the definition of temperature itself becomes questionable [312].

We also recall that Enz [253] and Hardy [24] distinguished between "drifting" and "driftless" second sound. The former emerges when normal processes dominate and is described in terms of balance equations for energy and momentum; the latter is determined by a uniform energy flux that decays exponentially. The second sound discussed here is of the drifting kind, as it emerges from a set of balance equations for energy and crystal momentum derived from the LBTE.

4.6 Case study

We showcase the solution for the viscous heat equations for graphite around the equilibrium temperature $\bar{T} = 70$ K in the geometry shown in Fig. 4.6.1, often used as an illustrative example in textbooks on fluid dynamics.

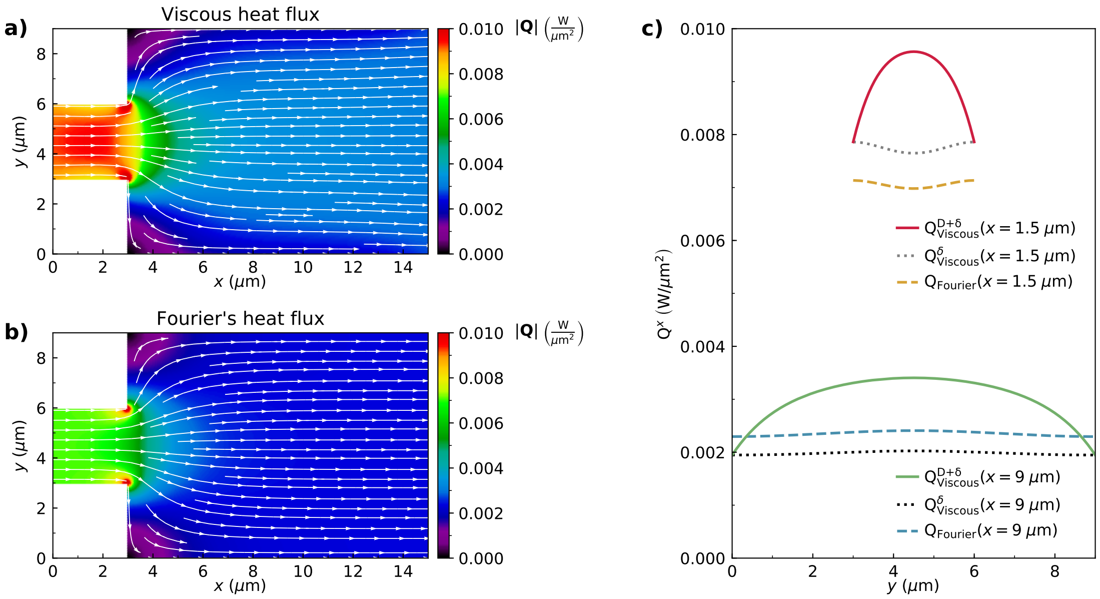

Figure 4.6.1 – In-plane $(x-y)$ heat fluxes in graphite around $\bar{T} = 70$ K, for a sample infinite in the z direction (the z direction of the sample coincides with the off-plane direction of graphite). Panel a) shows the total heat flux ($\boldsymbol{Q}^D + \boldsymbol{Q}^\delta$) obtained from the viscous heat equations (4.10, 4.11). Panel b) shows instead the Fourier heat flux ($Q^i_{\text{Fourier}}(\boldsymbol{r}, t) = -\sum_j \kappa^{ij} \nabla^j T(\boldsymbol{r}, t)$) obtained solving the steady-state Fourier equation $\sum_{ij} \kappa^{ij} \frac{\partial^2 T(\boldsymbol{r},t)}{\partial r^i \partial r^j} = 0$. Boundary conditions are as follows: the temperature is set at 80 K (60 K) on the left and right boundaries, a zero total heat flux is imposed at the other boundaries, and zero drift velocity is imposed on all boundaries (no-slip boundary condition). With this choice of boundary conditions, the phonon distribution reduces to the Bose-Einstein distribution on the left and right boundaries, where the temperature is fixed. Despite having local equilibrium at the left/right boundaries, a non-zero drift velocity is present in the material as a consequence of the coupling in Eq. (4.10) between drift velocity and temperature. Panel c) shows the x-component of the heat flux along sections taken at $x = 1.5\ \mu m$ (orange, gray, red) and $x = 9.0\ \mu m$ (black, blue, green); solid lines are the results obtained from the viscous heat equations, dashed lines are the results from Fourier's law, and dotted lines are the heat fluxes due to the temperature gradient within the viscous heat equations ($\boldsymbol{Q}^\delta$).

The equations are solved numerically using a finite-element solver implemented in Mathematica [313], imposing a temperature of 80 K on the left side ($x = 0\ \mu m$) and of 60 K on the right side ($x = 15\ \mu m$), assuming all boundaries at $x \neq 0$ and $x \neq 15\ \mu m$ to be adiabatic, and imposing a no-slip condition on $\boldsymbol{u}$ at all boundaries.

We show in Fig. 4.6.1 the total viscous heat flux $\boldsymbol{Q}^{\delta}+\boldsymbol{Q}^{D}$, and the flux predicted by Fourier's law $\boldsymbol{Q}_{\text{Fourier}}$ [Figs. 4.6.1(a) and 4.6.1(b), respectively] and contrast the Fourier and viscous heat flux components across two different sections [Fig. 4.6.1(c)].

We stress that Fourier's law lacks a description of the contribution to the heat flux derived from the local drift velocity [23, 306, 314]. As a result, Fourier's law misses qualitative and quantitative properties of the heat flux profile. The largest differences are observed in proximity of spatial inhomogeneities, such as boundaries or corners. For example, $\boldsymbol{Q}^{D}$ quickly increases (decreases) in proximity of the thermal reservoir on the hot (left) [cold (right)] side of the sample; these changes in $\boldsymbol{Q}^{D}$ determine opposite changes in $\boldsymbol{Q}^{\delta}$. Microscopically, these variations are caused by the rapid transition of the phonon distribution from the Bose-Einstein equilibrium distribution imposed at the boundaries to an out-of-equilibrium distribution carrying non-zero total crystal momentum (*i.e.* a drift velocity) inside the sample.

We report in Fig. 4.6.1c the total heat flux profiles along two transversal sections of the sample, contrasting the prediction from the viscous heat equations (solid lines) with that of Fourier's law (dashed lines). Along these sections, Fourier's law predicts a flat heat flux profile, while the viscous heat equations yield a Poiseuille-like profile. The results from the viscous heat equations are thus substantially different from Fourier's predictions, and the behavior of the heat flux can be understood from a simple analytical 1D solution of the viscous heat equations in the absence of Umklapp processes [23]: as discussed in Appendix 4.G, the flux is described by hyperbolic functions with a characteristic length scale $\lambda=\sqrt{\frac{\mu\kappa}{ACW^2}}$ (an estimate of the friction lengths, see Ref. [256]). At distances from the surface larger than λ we recover the flat behavior typical of the bulk. We also note that these results mimic those from the (computationally very expensive) space-dependent solution of the LBTE (either in the frequency-dependent SMA approximation [289] or considering the full scattering operator [256]), which generates a minimum flux on surfaces and maximum at the sample's center. We further note that, at variance with classical fluid dynamics and as pointed out in Ref. [256], the total heat flux does not drop to zero at the boundaries: the no-slip condition sets the drifting heat flux $\boldsymbol{Q}^{D}$ to zero, but the temperature-driven component $\boldsymbol{Q}^{\delta}$ is still allowed to be nonzero.

In Fig. 4.6.2 we plot the difference between the temperature profile predicted by Fourier's law and the viscous heat equations along transversal [Fig. 4.6.2(a)] and longitudinal [Fig. 4.6.2(b)] directions. The insets in Fig. 4.6.2b show the results of the viscous equations (solid blue line) and Fourier's law (dashed red line) along the section $y=4.5\ \mu m$. Along the transversal direction (Fig. 4.6.2a), Fourier's law and Eqs. (4.10, 4.11) predict temperature profiles which are substantially different in the presence of variations of the sample's shape (green line corresponding to $x=3.3\ \mu m$), while they are merely shifted by a positive or negative offset away from these; the precise amount depends on the distance from the fixed-temperature boundaries. These differences become more clear by inspecting the longitudinal direction (Fig. 4.6.2b), where the discrepancy between the temperature predicted by Fourier's law and Eqs. (4.10, 4.11) is largest at $x\simeq 3\ \mu m$, *i.e.* where the sample of Fig. 4.6.1 changes geometry. We show in the inset of Fig. 4.6.2b that also the longitudinal temperature profile (for $y=4.5\ \mu m$)

changes when going from Fourier's law (dashed red line) to the viscous heat equations (solid blue line). The difference is maximized close to variations of the sample's shape at $x = 3\ \mu m$ and at the boundaries $x = 0$ and $x = 15\ \mu m$; in this latter case, the viscous heat equations predict steeper-than-Fourier's law or non-linear temperature gradients that are reminiscent of those obtained in molecular dynamics simulations [125, 188, 315, 316, 317, 318, 319, 320, 321, 322] and in explicit solutions of the LBTE [256].

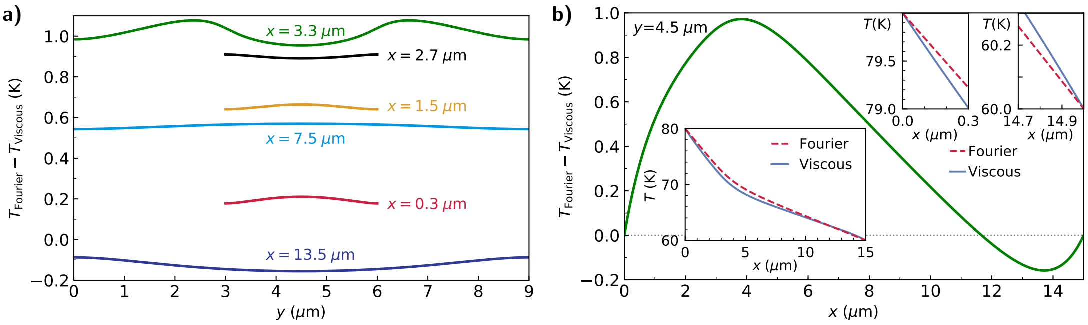

Figure 4.6.2 – Difference between the temperature profiles predicted by Fourier's law and by the viscous heat equations, plotted in the left panel a) along y for various values of x and in the right panel b) along x for $y = 4.5\ \mu m$. The insets of panel b) show the temperature profile along x for $y = 4.5\ \mu m$; the result of the viscous heat equations (4.10, 4.11) is solid/blue, Fourier's law prediction is dashed/red.

4.7 Fourier Deviation Number

In this section, we introduce a descriptor that parametrizes the conditions under which hydrodynamic heat conduction is observed; we will refer to this as the "Fourier deviation number" (FDN). In particular, we aim at distinguishing the diffusive regime from the hydrodynamic regime: in the former case the viscous heat equations become equivalent to Fourier's law, while in the latter case Fourier's law no longer holds and the viscous heat equations are required. In order to investigate how the hydrodynamic deviations from Fourier's law depend on the sample's sizes and reference temperature $\bar{T}$, we solve the viscous heat equations and Fourier's equation for several samples having different dimensions, and at various reference temperatures $\bar{T}$. We perform this analysis for graphite (Fig. 4.7.1a), diamond (Fig. 4.7.1b) and silicon (Fig. 4.7.1c). In particular, we consider samples that are similar — in the geometric sense — to the reference sample shown in Fig. 4.6.1, *i.e.* we generate samples of different dimensions starting from the reference sample of Fig. 4.6.1 and varying the sizes via a uniform scaling. Following this protocol, we vary the sample's length $l_{\rm TOT}$, reported on the y−axis of Fig. 4.7.1a-c, from 0.1 to 100 μm (e.g. the reference sample of Fig. 4.6.1 corresponds to $y = 15\ \mu m$, $y = 100\ \mu m$ corresponds to a sample obtained magnifying uniformly by a factor of $100/15 \simeq 6.66$ the sizes of the reference sample). The color in Fig. 4.7.1a-c represents the normalized $\mathscr{L}^2$ distance between the temperature profile predicted by Fourier's law and the viscous heat equations for a given sample length $l_{\rm TOT}$ and reference temperature $\bar{T}$:

$$\mathscr{L}^2[T_{\rm Fourier} - T_{\rm Viscous}](l_{\rm TOT}, \bar{T}) = \sqrt{\frac{\int_G [T_{\rm Fourier}(x,y) - T_{\rm Viscous}(x,y)]^2 dxdy}{\int_G dxdy}}\,, \tag{4.17}$$

and in order to ease the qualitative interpretation of these results later, we evaluate $\mathscr{L}^2$ in the spatially-homogeneous region G defined by $x > \frac{1}{5} l_{\rm TOT}$. We also inspected the effects of shape on the deviation $\mathscr{L}^2$, finding that the magnitude of $\mathscr{L}^2$ is larger for geometries with spatial non-homogeneities that imply larger values of the drift velocity's second derivative; nevertheless, the dependence of $\mathscr{L}^2$ on $l_{\rm TOT}$ and $\bar{T}$ is qualitatively unchanged for different shapes.

Results in Figs. 4.7.1a-c have been computed accounting for finite-size effects as discussed in Secs. 4.3 and 4.4. Additionally, to better compare with the experimental results of Ref. [31], we make the hypothesis of working with polycrystalline graphite with an average crystal grain size of 10 μm as in Ref. [31]: as a result, the transport coefficients of graphite are renormalized by the system size for $l_{\rm TOT} < 10\ \mu m$, and by the grain size for $l_{\rm TOT} > 10\ \mu m$ (therefore, for $l_{\rm TOT} > 10\ \mu m$ size effects are given only by the boundary conditions' effects on the temperature and drift-velocity fields). In graphite, the difference between Fourier's law and the viscous heat equations is largest in the temperature range 60-80 K and for sizes $10 \mu m \lesssim l_{\rm TOT} \lesssim 20 \mu m$.

Turning our attention to diamond, we first recall that it is characterized by a very large thermal conductivity, which originates from having large group velocities and weak Umklapp scattering [164, 290, 291, 292, 293, 294]; the latter condition being favorable to the emergence of hydrodynamic effects. This is confirmed by the results shown in Fig. 4.7.1b, with the hydrodynamic deviation being largest around room temperature and dimension $l_{\rm TOT} \gtrsim 1\ \mu m$ (we note in passing that, at this temperature and size, the finite-size renormalization of transport coefficients is small and well compatible with the mesoscopic approach described in this work). These results suggest that a hydrodynamic window exists also for diamond, and that therefore hydrodynamic behavior (e.g. second sound) might be measurable in this material at temperatures even larger than graphite.

For silicon, instead, the deviation from Fourier's law is smaller and takes place at lower temperatures. Silicon is an example of a material for which the thermal conductivity computed within the SMA approximation is very close to the conductivity computed from the exact solution of the LBTE [35, 37, 39, 68], and it is known that the SMA works reasonably well in systems where momentum-dissipating (Umklapp) scattering events dominate over those conserving crystal momentum (normal) [68, 101]. Therefore, the negligible magnitude of hydrodynamic effects predicted by the viscous heat equations for silicon is consistent with the predominance of Umklapp over normal scattering events known to occur in this material. We last remark that, in contrast to graphite, results for diamond and silicon have been computed for single crystals, *i.e.* transport coefficients are not limited by grains' size.

In order to capture intuitively and inexpensively all these trends we introduce an approach

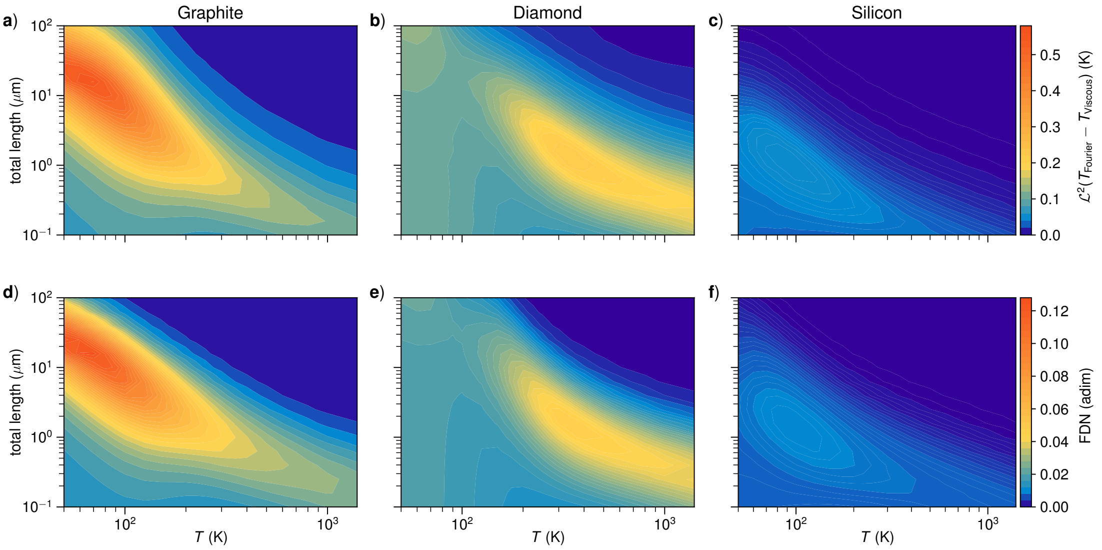

Figure 4.7.1 – Top row, $\mathscr{L}^2$ distance (see text) between the temperature profile predicted by Fourier's law and that of the viscous heat equations (4.10, 4.11), shown as a function of temperature and total length of a sample similar (in the geometric sense) to the shape of Fig. 4.6.1 for the cases of graphite (a), diamond (b) and silicon (c). The color quantifies the $\mathscr{L}^2$ distance between the temperature profiles predicted by Fourier's law ($T_{\text{Fourier}}(x,y)$) and the viscous heat equations (4.10, 4.11) ($T_{\text{Viscous}}(x,y)$), computed over the region G corresponding to points with $x > \frac{1}{5} l_{\text{TOT}}$ where l_{TOT} is the total length of the sample geometrically similar to that in Fig. 4.6.1 (see main text for details). Bottom row, Fourier Deviation Number (FDN, as defined in Eq. (4.24)) for the same materials as a function of temperature and total length of the sample (for the geometry of Fig. 4.6.1, the characteristic size L appearing in FDN is the shortest length-scale, *i.e.* 1/5 of the total length l_{TOT}). It is apparent that the FDN correctly identifies the deviations between the solutions of Fourier's equation and the viscous heat equations.

inspired by the definition of the Reynolds number, and we rewrite the viscous heat equations (4.10, 4.11) in adimensional form (we follow the standard procedure used e.g. in fluid dynamics, which is also called "Buckingham Pi theorem" [323, 324]). First, we extract the magnitudes of the tensors appearing in the viscous heat equations, factorizing the largest component: $A^i = A_{\text{m}}\text{a}^i$, where $A_{\text{m}} = \max_i(|A^i|)$ and $\text{a}^i = A^i/A_{\text{m}}$ is an adimensional tensor with the largest component having modulus equal to 1. Similarly, we factorize the largest component of all other tensors: $\kappa^{ij} = \kappa_{\text{m}}\text{k}^{ij}$ (with $\kappa_{\text{m}} = \max_{i,j}(|\kappa^{ij}|)$ and $\text{k}^{ij} = \kappa^{ij}/\kappa_{\text{m}}$); $W^j_{i0} = W_{\text{m}}\text{w}^j_i$ (with $W_{\text{m}} = \max_{i,j}(|W^j_{i0}|)$ and $\text{w}^j_i = W^j_{i0}/W_{\text{m}}$); $D^{ij}_U = D_{U,\text{m}}\text{d}^{ij}$ (with $D_{U,\text{m}} = \max_{i,j}(|D^{ij}_U|)$ and $\text{d}^{ij} = D^{ij}_U/D_{U,\text{m}}$); $\mu^{ijkl} = \mu_{\text{m}}\text{m}^{ijkl}$ (with $\mu_{\text{m}} = \max_{i,j,k,l}(|\mu^{ijkl}|)$ and $\text{m}^{ijkl} = \mu^{ijkl}/\mu_{\text{m}}$). Then, we define a set of dimensionless variables $\boldsymbol{r}^* = \boldsymbol{r}/L$, $\boldsymbol{u}^* = \boldsymbol{u}/u_0$, and $T^* = T/\delta T$, where L, u_0 and δT are a characteristic size, drift velocity and temperature perturbation (more on these later). Substituting these variables in Eqs. (4.10, 4.11), and limiting ourselves to the steady-state regime, we obtain:

$$\pi_1 \sum_{i,j=1}^{3} \frac{\mathsf{w}_j^i \sqrt{\mathsf{a}^j}}{g(\mathsf{w}\cdot\sqrt{\mathsf{a}})_2} \frac{\partial u^{*j}(\boldsymbol{r}^*)}{\partial r^{*i}} - \sum_{i,j=1}^{3} \frac{\mathsf{k}^{ij}}{g(\mathsf{k})_2} \frac{\partial^2 T^*(\boldsymbol{r}^*)}{\partial r^{*i} \partial r^{*j}} = 0\,, \tag{4.18}$$

$$\pi_2 \sqrt{\mathsf{a}^i} \sum_{j=1}^{3} \frac{\mathsf{w}_i^j}{g^i(\mathsf{w})_1} \frac{\partial T^*(\boldsymbol{r}^*)}{\partial r^{*j}} - \pi_3 \sum_{j,k,l=1}^{3} \frac{\mathsf{m}^{ijkl}}{g^i(\mathsf{m})_3} \frac{\partial^2 u^{*k}(\boldsymbol{r}^*)}{\partial r^{*j} \partial r^{*l}} = -\sum_{j=1}^{3} \frac{\sqrt{\mathsf{a}^i \mathsf{a}^j}\,\mathsf{d}^{ij}}{g^i(\sqrt{\mathsf{a}\otimes\mathsf{a}}\cdot\mathsf{d})_1} u^{*j}(\boldsymbol{r}^*)\,, \tag{4.19}$$

where we have introduced the quantities
$g(\mathsf{w}\cdot\sqrt{\mathsf{a}})_2 = (\max_{ij}[\mathsf{w}_j^i \sqrt{\mathsf{a}^j}])^{-1} \sum_{ij} \mathsf{w}_j^i \sqrt{\mathsf{a}^j}$,
$g(\mathsf{k})_2 = (\max_{ij}[\mathsf{k}^{ij}])^{-1} \sum_{ij} \mathsf{k}^{ij}$,
$g^i(\mathsf{w})_1 = (\max_j[\mathsf{w}_j^i])^{-1} \sum_j \mathsf{w}_j^i$,
$g^i(\sqrt{\mathsf{a}\otimes\mathsf{a}}\cdot\mathsf{d})_1 = (\max_j[\sqrt{\mathsf{a}^i \mathsf{a}^j}\,\mathsf{d}^{ij}])^{-1} \sum_j \sqrt{\mathsf{a}^i \mathsf{a}^j}\,\mathsf{d}^{ij}$,
$g^i(\mathsf{m})_3 = (\max_{jkl}[\mathsf{m}^{ijkl}])^{-1} \sum_{jkl} \mathsf{m}^{ijkl}$. The role of these parameters is to account for the correct order of magnitude of the five summations appearing in Eqs. (4.18,4.19); they carry a Cartesian superscript i whenever they may depend on direction, and their subscripts indicate the number of indexes summed in their definition. For example, for a 3×3 isotropic tensor $\chi^{ij} = \chi_{\mathrm{m}} \delta^{ij}$ (where χ_{m} is a constant and δ^{ij} is the Kronecker tensor), $g(\chi)_2 = (\chi_{\mathrm{m}})^{-1} \sum_{ij} \chi^{ij} = 3$ and $g^i(\chi)_1 = (\chi_{\mathrm{m}})^{-1} \sum_j \chi^{ij} = 1\ \forall\ i$. Because we are computing the FDN for the planar geometry discussed in Fig. 4.6.1, we can discard the z component (*i.e.* the Cartesian direction indexed by 3) from Eqs. (4.18,4.19). Then, for diamond, silicon and in-plane graphite, transport properties are isotropic (*i.e.* all the 2nd-rank tensors appearing in Eq. (4.18) and Eq. (4.19) are diagonal). From this it follows that $g(\mathsf{w}\cdot\sqrt{\mathsf{a}})_2 = 2$; $g(\mathsf{k})_2 = 2$; $g^i(\mathsf{w})_1 = 1\ \forall\ i = 1,2$; and $g^i(\sqrt{\mathsf{a}\otimes\mathsf{a}}\cdot\mathsf{d})_1 = 1\ \forall\ i = 1,2$. Finally, the tensor m^{ijkl} is not isotropic (because the thermal viscosity tensor from which it is derived is not isotropic), and from the values in Fig. 4.3.1 it follows that $g^i(\mathsf{m})_1 = 1 + \frac{\mu^{xyxy}}{\mu^{xxxx}}\,\forall i = 1,2,3$ for diamond and silicon, and $g^i(\mathsf{m})_1 = 1 + \frac{\mu^{xyxy}}{\mu^{xxxx}} + 2\frac{\mu^{xyyx}}{\mu^{xxxx}}\ \forall\ i = 1,2$ for graphite.

The final expressions for the dimensionless parameters π_1, π_2, π_3 are thus:

$$\pi_1 = \frac{\sqrt{\bar{T} A_{\mathrm{m}} C} W_{\mathrm{m}} u_0 L}{\kappa_{\mathrm{m}}\, \delta T} \frac{g(\mathsf{w}\cdot\sqrt{\mathsf{a}})_2}{g(\mathsf{k})_2}\,, \tag{4.20}$$

$$\pi_2 = \sqrt{\frac{C}{A_{\mathrm{m}} \bar{T}}} \frac{W_{\mathrm{m}} \delta T}{L D_{U,\mathrm{m}} u_0} \frac{g^i(\mathsf{w})_1}{g^i(\sqrt{\mathsf{a}\otimes\mathsf{a}}\cdot\mathsf{d})_1}\,, \tag{4.21}$$

$$\pi_3 = \frac{\mu_{\mathrm{m}}}{D_{U,\mathrm{m}} L^2 A_{\mathrm{m}}} \frac{g^i(\mathsf{m})_3}{g^i(\sqrt{\mathsf{a}\otimes\mathsf{a}}\cdot\mathsf{d})_1}\,. \tag{4.22}$$

From the derivation of these parameters, it is clear that they can be interpreted in terms of average values (we indicate with $\langle\ldots\rangle$ the average over space) of physical quantities: $\pi_1 \sim \langle Q^D\rangle / \langle Q^\delta\rangle$, $\pi_2 \sim \langle\frac{\partial \Pi_T}{\partial r}\rangle / \langle\frac{\partial P}{\partial t}\big|_{\mathrm{Umkl}}\rangle$ and $\pi_3 \sim \langle\frac{\partial \Pi_{\delta \mathrm{E}}}{\partial r}\rangle / \langle\frac{\partial P}{\partial t}\big|_{\mathrm{Umkl}}\rangle$. Still, to evaluate these parameters we need to know the characteristic size L and temperature perturbation δT, and estimate the characteristic values of the drift velocity u_0. Focusing on the setup discussed in the previous section (Fig. 4.6.1), we have $L = \frac{1}{5} l_{\mathrm{TOT}}$ (corresponding to the shortest length scale of the geometry considered, which has total length l_{TOT} along x) and δT=10K. As shown in Appendix 4.H, the characteristic drift velocity u_0 is found by interpolating the asymptotic behavior at low (u_L) and high (u_H) temperatures $u_0^{-1} = u_L^{-1} + u_H^{-1}$. In the low-temperature limit, where Umklapp scattering is frozen, viscous effects determine the drift velocity, and one can show that $u_L = \frac{3}{7}\sqrt{\frac{CA^x}{\bar{T}} \frac{W^x_{x0}\,\delta T\,L}{\mu^{xxxx}+\mu^{xyxy}}}$. In the high temperature limit, the drift velocity is mainly determined by the crystal momentum dissipation rate and $u_H = \sqrt{\frac{C}{\bar{T}A^x} \frac{W^x_{x0}}{D^{xx}_U} \frac{2}{7} \frac{\delta T}{L}}$. We can therefore estimate the values of all the π_1, π_2, and π_3 factors.

Looking at the definition of π_1, π_2 and π_3, it is straightforward to identify the conditions for which the viscous heat equations reduce to Fourier's law. When $\pi_3 \ll 1$, *i.e.* for crystal momentum dissipation dominating over viscous effects and/or very large characteristic size L, the temperature gradient in Eq. (4.19) is proportional to the drift velocity: $\pi_2 \sum_j \frac{\mathrm{w}^j_i}{g^i(\mathrm{w})_1} \frac{\partial T^*(\boldsymbol{r}^*)}{\partial r^{*j}} \simeq -\sum_j \frac{\sqrt{\mathrm{a}}^j \mathrm{d}^{ij}}{g^i(\sqrt{\mathrm{a}\otimes\mathrm{a}}\cdot\mathrm{d})_1} u^{*j}(\boldsymbol{r}^*)$. While it is intuitive to understand the emergence of Fourier's law when crystal momentum dissipation (e.g. due to Umklapp scattering) dominates over viscous effects, the Fourier-like behavior of large-size samples can be rationalized qualitatively recalling the simple analytical 1D solution of the viscous heat equations in the absence of Umklapp processes discussed in Appendix 4.G: the heat flux is described by hyperbolic functions with a characteristic length scale $\lambda = \sqrt{\frac{\mu_{\mathrm{m}}\kappa_{\mathrm{m}}}{A_{\mathrm{m}} C (W_{\mathrm{m}})^2}}$, and for a characteristic size $L \gg \lambda$, a flat Fourier-like heat flux profile is recovered. It is worth mentioning that $\pi_3 \ll 1$ — and thus Fourier-like behavior — can also emerge for very small (sub-micrometer) length scales, where ballistic effects are relevant and strongly renormalize the transport coefficients, as discussed in Appendix 4.C. The emergence of Fourier-like behavior in the ballistic regime (with a size-dependent thermal conductivity alike to that employed here) has been explained in a recent work [325], confirming that the results for sub-micrometer sizes obtained with the aforementioned approximated treatment of boundary scattering are qualitatively correct. If we insert the condition $\pi_3 \ll 1$ in Eq. (4.18), we obtain a Fourier-like equation for the temperature:

$$\sum_{i,j} \left[\left(\pi_1 \pi_2 \frac{g(\mathrm{k})_2 g^i(\sqrt{\mathrm{a}\otimes\mathrm{a}}\cdot\mathrm{d})_1}{g(\mathrm{w}\cdot\sqrt{\mathrm{a}})_2 g^i(\mathrm{w})_1} \sum_{k,l} \mathrm{w}^i_k (\mathrm{d}^{-1})^{kl} \mathrm{w}^j_l \right) + \mathrm{k}^{ij} \right] \frac{\partial^2 T^*(\boldsymbol{r}^*)}{\partial r^{*i} \partial r^{*j}} = 0 \,. \tag{4.23}$$

So, the thermal conductivity is corrected by a term proportional to $\pi_1\pi_2$ (since in all the setups considered here, $\frac{g(\mathrm{k})_2 g^i(\sqrt{\mathrm{a}\otimes\mathrm{a}}\cdot\mathrm{d})_1}{g(\mathrm{w}\cdot\sqrt{\mathrm{a}})_2 g^i(\mathrm{w})_1} = 1$), but the qualitative behavior is that of Fourier's law. Numerically, we find that $\pi_1\pi_2 \ll 1$ for graphite in the high-temperature limit (see Fig. 4.7.2a), so that the viscous heat flux is well approximated by Fourier's flux; the same limiting behavior is observed also in diamond and silicon. On the other hand, deviations from the temperature profile predicted by Fourier's law appear when both π_1 and π_3 are large. In fact, $\pi_3 \gtrsim 1$ implies that the temperature gradient in Eq. (4.19) is coupled to the second derivative of the drift velocity, and one can not obtain a Fourier-like equation as before; large values of π_1 imply that the drift velocity affects the evolution of temperature in Eq. (4.18). It follows that Fourier's law is mathematically recovered for crystal momentum dissipation dominating over viscous effects and/or large characteristic size ($\pi_3 \ll 1$), but deviations between the viscous and Fourier temperature profile can be small even when viscous effects dominate over crystal momentum dissipation ($\pi_3 \gg 1$) if the coupling between drift velocity and temperature in Eq. (4.18) is small ($\pi_1 \ll 1$). We note in passing that while this reasoning has been made here at steady state, it can be straightforwardly extended to the time-dependent case, considering time variations of the drifting velocity slow compared to the crystal momentum dissipation timescale.

On the basis of this reasoning, it is convenient to introduce a Fourier deviation number (FDN) as:

$$\mathrm{FDN} = \left(\frac{1}{\pi_1} + \frac{1}{\pi_3}\right)^{-1}, \tag{4.24}$$

which provides a simple estimate of the deviations from Fourier's law: the larger the FDN, the larger the deviations from Fourier's law.

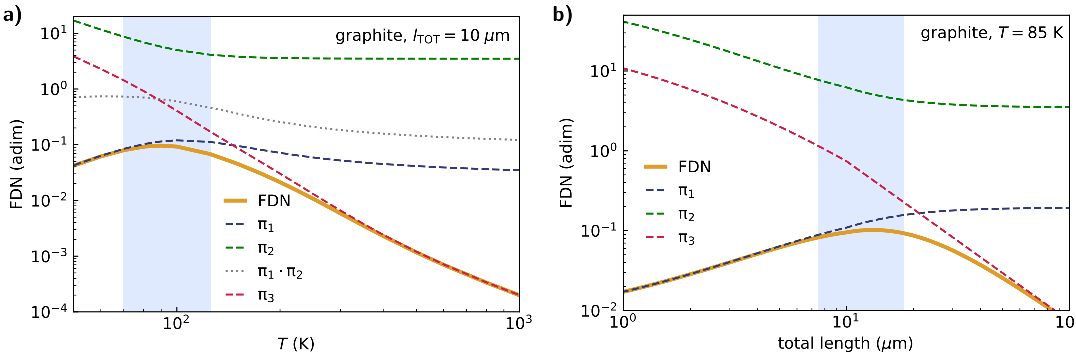

Figure 4.7.2 – Fourier Deviation Number (FDN, solid line) and its different contributions π_1 and π_3 [Eq. (4.24)] for a graphite sample of fixed length $l_{\mathrm{TOT}} = 10\mu m$ as a function of temperature (panel a), and at fixed $\bar{T}$=85 K as a function of sample's length l_{TOT} (panel b). The shaded areas are the hydrodynamic (second-sound) windows measured at 10μm (panel a) or 85 K (panel b) by Huberman *et al.* [31]. The terms π_2 and $\pi_1\pi_2$ are also reported in panel a) because in the high-temperature limit Fourier's law is recovered when $\pi_1\pi_2 \ll 1$ (see main text for details). Notably, FDN predicts hydrodynamic effects to be largest at temperatures and sizes that are in excellent agreement with these observed in the experiments.

In Fig. 4.7.1d-f, we plot the FDN for graphite, diamond and silicon as a function of sample's total length l_{TOT} and reference temperature $\bar{T}$. Remarkably, the FDN captures the trends of the exact solution of the viscous heat equations (Fig. 4.7.1a-c), thus identifying accurately the regime where hydrodynamic behavior emerges. The magnitude of FDN is directly proportional to the magnitude of hydrodynamic effects: a larger FDN implies a larger difference between the Fourier and viscous temperature profiles. A detailed analysis of the π terms as a function of temperature for a graphite sample geometrically similar to that in Fig. 4.6.1 and with a fixed total length $l_{\mathrm{TOT}} = 10\mu$m is shown in Fig. 4.7.2a, where $l_{\mathrm{TOT}} = 10\mu$m has been chosen to match the length fixed in the experiments by Huberman *et al.* [31] to investigate the magnitude of hydrodynamic effects as a function of temperature. Importantly, the FDN at fixed $l_{\mathrm{TOT}} = 10\mu$m predicts hydrodynamic effects to be largest at temperatures that match very well those measured in recent experiments for second sound in graphite [31]. Then, we rationalize the trend of FDN as a function of temperature in terms of the π terms entering in Eq. (4.24): π_1 increases with temperature for T$\lesssim$ 100 K and saturates to a constant value at high temperature and π_3 decreases asymptotically like T^{-2}. Fig. 4.7.2b shows the analysis of FDN as a function of the sample's size l_{TOT} (varied according to the aforementioned protocol) at fixed temperature 85 K, *i.e.* the temperature fixed in the experiments by Huberman *et al.* [31] to investigate the magnitude of hydrodynamic effects as a function of size. Also in this case, FDN predicts hydrodynamic effects to be largest in a size range that matches very well the sizes at which hydrodynamic effects have been measured. We thus conclude that the present model is capable of describing quantitatively the hydrodynamic window that has been recently measured in graphite. In Appendix 4.I, we also show that for diamond extending the sizes in Fig. 4.7.1e up to 10 mm yields an increase of FDN for temperatures around 50-60 K and dimensions ~ 1 mm. This result is in qualitative agreement with the predictions for diamond's second sound window performed using the reduced isotropic crystal model or the Callaway model [264]. Finally, the parameters entering in the π_i $(i = 1, 2, 3)$ are exactly the same used for the numerical solutions of the viscous heat equations in Fig. 4.7.1a-c.

4.8 Conclusions

We have introduced a framework to describe heat conduction beyond Fourier's law and to capture in the process the hydrodynamic transport regime where the phonon gas assumes a drift velocity and heat propagation resembles fluid dynamics. Just as a perturbation of the temperature generates an energy flux that is proportional to thermal conductivity, a perturbation of the drift velocity generates a crystal momentum flux, with the proportionality tensor coefficient between the two being a thermal viscosity. We have shown that thermal conductivity and viscosity can be determined exactly and in a closed form as a sum over relaxons (*i.e.* the eigenvectors of the phonon scattering matrix). Relaxons have a well-defined parity and even relaxons contribute exclusively to the thermal viscosity (odd relaxons contribute exclusively to the thermal conductivity [39]).

Most importantly, the microscopic LBTE has been coarse-grained into two novel mesoscopic viscous heat equations, which are coupled equations parametrized by the thermal conductivity and viscosity that govern the evolution of the temperature and drift-velocity fields. The viscous heat equations provide a general description of heat transfer encompassing both the Fourier and the hydrodynamic regimes, and all intermediate cases, allowing for the emergence of second sound, and of Poiseuille-like heat flow associated to a temperature profile deviating from Fourier's law. In addition, these viscous heat equations show that the thermal conductivity is not sufficient to describe thermal transport in general terms, but also its complementary quantity, the thermal viscosity, must be taken into account.

We have characterized the hydrodynamic behavior in terms of the Fourier deviation number (FDN), a dimensionless parameter that quantifies hydrodynamic deviations from Fourier's law. At a negligible computational cost, the FDN enables to study the temperature-and-size window at which hydrodynamic phenomena such as second sound emerge.

The full solution of the viscous heat equations allows to predict measurable temperature and heat flux profiles in complex shaped devices in the mesoscopic heat transport regime at a much reduced cost, and more transparently, than solving the full LBTE, therefore paving the way towards understanding shape and size effects in complex and microscopic devices, and especially when novel physics arises, such is the case in phononic devices [326, 327, 328, 329, 330, 331, 332, 333, 334, 335, 336, 337, 338]. These results are particularly relevant for the emerging field of materials that display hydrodynamic thermal transport, often characterized by large thermal conductivities [31, 255, 259, 260, 261, 262, 263, 264, 265]. Such behavior has been investigated in devices made either of graphite, diamond or silicon. For graphite, the present formulation predicts the hydrodynamic windows (as a function of temperature for a fixed size, or as a function of size for a fixed temperature) in excellent agreement with recent experimental findings [31], while suggesting that hydrodynamic behavior can also appear in diamond at room temperature for micrometer-sized crystals.

Finally, we remark that the present methodology can be adapted to describe viscous phenomena for electronic conduction [339, 340, 341, 342], or any other transport phenomena described by a linearized Boltzmann equation.

Appendix

4.A Eigenvectors of the scattering matrix

The scattering matrix $\Omega_{\nu\nu'}$ appearing in Eq. (4.1) is not symmetric, but it can be recast in a symmetric (and thus diagonalizable) form by means of the the following transformation [24, 38, 39]:

$$\tilde{\Omega}_{\nu\nu'} = \Omega_{\nu\nu'} \sqrt{\frac{\bar{N}_{\nu'}(\bar{N}_{\nu'}+1)}{\bar{N}_{\nu}(\bar{N}_{\nu}+1)}} \,, \tag{4.25}$$

$$\tilde{n}_{\nu}(\boldsymbol{r},t) = \frac{n_{\nu}(\boldsymbol{r},t)}{\sqrt{\bar{N}_{\nu}(\bar{N}_{\nu}+1)}} \,, \tag{4.26}$$

where also the distribution $n_{\nu}(\boldsymbol{r},t)$ appearing in Eqs. (4.6,4.7) has to be transformed for consistency. The symmetrized scattering operator $\tilde{\Omega}_{\nu\nu'}$ is real and symmetric, and can thus be diagonalized [24, 38, 39]:

$$\frac{1}{V}\sum_{\nu'} \tilde{\Omega}_{\nu\nu'} \theta^{\alpha}_{\nu'} = \frac{1}{\tau_{\alpha}} \theta^{\alpha}_{\nu} \,, \tag{4.27}$$

where θ^{α}_{ν} denotes a relaxon (*i.e.* an eigenvector), α is the relaxon index and the inverse eigenvalue τ_{α} is the relaxon lifetime. We also define a scalar product [39]:

$$\langle \alpha | \alpha' \rangle = \frac{1}{V}\sum_{\nu} \theta^{\alpha}_{\nu} \theta^{\alpha'}_{\nu} = \delta_{\alpha,\alpha'} \,, \tag{4.28}$$

used to normalize eigenvectors.

In order to show that eigenvectors with zero eigenvalues are related to conserved quantities in the LBTE dynamics, we rewrite the scattering operator distinguishing scattering events that conserve crystal momentum – normal (N) – from those that do not – Ukmlapp (U):

$$\tilde{\Omega}_{\nu\nu'} = \tilde{\Omega}^{N}_{\nu\nu'} + \tilde{\Omega}^{U}_{\nu\nu'} \,. \tag{4.29}$$

As stated in the main text, there are four eigenvectors with zero eigenvalues, that we will discuss in the next sections.

4.A.1 Bose-Einstein eigenvector: local temperature

Applying the transformation (4.26) to Eq. (4.5) and considering the steady-state conditions, one obtains the following equation for the even part (see below for the odd part):

$$\frac{\boldsymbol{v}_\nu}{\sqrt{\bar{N}_\nu(\bar{N}_\nu+1)}}\cdot\left(\frac{\partial N^D_\nu}{\partial \boldsymbol{u}}\cdot\nabla\boldsymbol{u}\right)=-\frac{1}{V}\sum_{\nu'}\tilde{\Omega}_{\nu\nu'}\left(\tilde{n}^T_{\nu'}(\boldsymbol{r},t)+\tilde{n}^{\delta\mathrm{E}}_{\nu'}\right). \tag{4.30}$$

The distribution $\tilde{n}^T_\nu(\boldsymbol{r},t)$ is obtained applying the symmetrization (4.26) to the distribution $n^T_\nu(\boldsymbol{r},t)$ appearing in equation (4.4) and it is thus evident that $\tilde{n}^T_\nu(\boldsymbol{r},t)\propto\omega_\nu(T(\boldsymbol{r},t)-\bar{T})$. From the energy conservation in scattering events (both normal and Umklapp), it follows that [24, 93]

$$\begin{aligned}&\frac{1}{V}\sum_{\nu'}\tilde{\Omega}_{\nu\nu'}\tilde{n}^T_{\nu'}(\boldsymbol{r},t)=\\&\frac{1}{V}\sum_{\nu'}\tilde{\Omega}_{\nu\nu'}\frac{1}{\sqrt{\bar{N}_{\nu'}(\bar{N}_{\nu'}+1)}}\frac{\partial\bar{N}_{\nu'}}{\partial T}[T(\boldsymbol{r},t)-\bar{T}]=\\&\frac{1}{V}\sum_{\nu'}\tilde{\Omega}_{\nu\nu'}\sqrt{\bar{N}_{\nu'}(\bar{N}_{\nu'}+1)}\frac{\hbar\omega_{\nu'}}{k_B\bar{T}^2}(T(\boldsymbol{r},t)-\bar{T})=0\,.\end{aligned} \tag{4.31}$$

As a result, we identify $\frac{\partial\bar{N}_\nu}{\partial T}$ as an eigenvector θ^0_ν with zero eigenvalue, that, after normalization, is

$$\theta^0_\nu=\sqrt{\frac{\bar{N}_\nu(\bar{N}_\nu+1)}{k_B\bar{T}^2C}}\hbar\omega_\nu=\sqrt{\frac{k_B\bar{T}^2}{C\bar{N}_\nu(\bar{N}_\nu+1)}}\frac{\partial\bar{N}_\nu}{\partial T}\,, \tag{4.32}$$

where the specific heat C is

$$C=\left.\frac{\partial E}{\partial T}\right|_{\mathrm{eq}}=\frac{1}{k_B\bar{T}^2V}\sum_\nu\bar{N}_\nu\left(\bar{N}_\nu+1\right)(\hbar\omega_\nu)^2\,. \tag{4.33}$$

From equation (4.31), it follows that $\tilde{n}^T_\nu(\boldsymbol{r},t)$ disappears from Eq. (4.30). Therefore, Eq. (4.30) gives Eq. (4.7) in the main text. In the context of the decomposition (4.29), the Bose-Einstein eigenvector (4.32) is an eigenvector to both the normal and Umklapp scattering operator, and will be denoted as ϕ^0_ν when we will later consider the basis of eigenvectors of the normal scattering operator in Appendix 4.D. We conclude by noting that these considerations approximately hold also when the approximate treatment of scattering with boundaries discussed in Sec. 4.4 ($\tilde{\Omega}^{U,\mathrm{boundary}}_{\nu\nu'}$) is included as $\tilde{\Omega}^U_{\nu\nu'}=\tilde{\Omega}^{U,\mathrm{bulk}}_{\nu\nu'}+\tilde{\Omega}^{U,\mathrm{boundary}}_{\nu\nu'}$, provided the phenomenological boundary-scattering term—which does not strictly conserve energy—is small compared to the bulk umklapp scattering matrix; this happens e.g. in the mesoscopic regime where the finite-size renormalization of transport coefficients is small and the viscous heat equations are valid.

4.A.2 Drift eigenvectors: local drift velocity

Starting from Eq. (4.5) at the steady-state, one obtains the following equation for the odd part:

$$\frac{\boldsymbol{v}_\nu}{\sqrt{\bar{N}_\nu(\bar{N}_\nu+1)}}\cdot\left(\frac{\partial\bar{N}_\nu}{\partial T}\nabla T\right)=-\frac{1}{V}\sum_{\nu'}\tilde{\Omega}_{\nu\nu'}\left(\tilde{n}^D_{\nu'}(\boldsymbol{r},t)+\tilde{n}^{\delta O}_{\nu'}\right). \tag{4.34}$$

The distribution $\tilde{n}^D_\nu(\boldsymbol{r},t)$ is obtained applying the symmetrization (4.26) to the distribution $n^D_\nu(\boldsymbol{r},t)$ appearing in equation (4.4). We note in particular that $\tilde{n}^D_\nu(\boldsymbol{r},t)\propto\sum_{i=1}^3 q^i\cdot u^i(\boldsymbol{r},t)$.

The drifting distribution $\tilde{n}^D_\nu(\boldsymbol{r},t)$ is the stationary distribution for a system conserving crystal momentum. Therefore, recalling the decomposition (4.29), we have that

$$\frac{1}{V}\sum_{\nu'}\tilde{\Omega}^N_{\nu\nu'}\tilde{n}^D_{\nu'}(\boldsymbol{r},t)=\frac{1}{V}\sum_{\nu'}\tilde{\Omega}^N_{\nu\nu'}\sqrt{\bar{N}_{\nu'}(\bar{N}_{\nu'}+1)}\frac{\hbar}{k_B\bar{T}}\boldsymbol{q'}\cdot\boldsymbol{u}(\boldsymbol{r},t)=0\,, \tag{4.35}$$

since $\tilde{\Omega}^N_{\nu\nu'}$ accounts only for Normal scattering events that conserve crystal momentum [22, 23, 24]. From Eq. (4.35) it is possible to identify three eigenvectors of $\tilde{\Omega}^N_{\nu\nu'}$ with zero eigenvalues [24]:

$$\phi^i_\nu=\frac{1}{\sqrt{\bar{N}_\nu(\bar{N}_\nu+1)}}\sqrt{\frac{k_B\bar{T}}{A^i}}\frac{\partial N^D_\nu}{\partial u^i}=\sqrt{\frac{\bar{N}_\nu(\bar{N}_\nu+1)}{k_B\bar{T}A^i}}\hbar q^i\,, \tag{4.36}$$

where $i=1,2,3$ and A^i is a normalization constant. The drift eigenvectors (4.36) are, in general, not orthogonal [25]. Nevertheless, we work in a Cartesian coordinate system for $\boldsymbol{q'}$ and $\boldsymbol{u}(\boldsymbol{r},t)$, so that these 3 eigenvectors are orthogonal and can also be normalized, choosing A^i from the condition $\langle\phi^i|\phi^i\rangle=1$. In computing the normalization constants A^i, we note that they can be expressed in terms of physically meaningful quantities. In particular, we note that the crystal momentum density associated to the drifting distribution is:

$$\boldsymbol{P}=\frac{1}{V}\sum_\nu N^D_\nu\hbar\boldsymbol{q}, \tag{4.37}$$

and its derivative with respect to the drift velocity is:

$$\begin{aligned}\left.\frac{\partial P^i}{\partial u^j}\right|_{\text{eq}}&=\frac{1}{V}\sum_\nu\left.\frac{\partial N^D_\nu}{\partial u^j}\right|_{\text{eq}}\hbar q^i\\&=\frac{1}{k_B\bar{T}V}\sum_\nu\bar{N}_\nu(\bar{N}_\nu+1)\hbar q^i\hbar q^j\,.\end{aligned} \tag{4.38}$$

Comparing Eq. (4.36) with Eq. (4.38) we note that

$$A^i=\frac{\partial P^i}{\partial u^i}\Big|_{\text{eq}}=\frac{1}{k_B\bar{T}V}\sum_\nu\bar{N}_\nu(\bar{N}_\nu+1)(\hbar q^i)^2\,, \tag{4.39}$$

and $\frac{\partial P^i}{\partial u^j}\Big|_{\text{eq}}=0 \iff i\neq j$. Therefore, we will refer to A^i as the specific momentum, due to its formal similarity with specific heat. It can be shown that in the high temperature limit, $A^i(T\to\infty)\propto T$ (see also Appendix 4.E).

Finally, it is worth mentioning that in going from equation (4.5) to equation (4.6), the term $n^D_\nu(\boldsymbol{r},t)$ has disappeared due to the following approximation:

$$\begin{aligned}
&\frac{1}{V}\sum_{\nu'}\tilde{\Omega}_{\nu\nu'}(\tilde{n}^D_{\nu'}(\boldsymbol{r},t)+\tilde{n}^{\delta\mathrm{O}}_{\nu'}) = \\
&\frac{1}{V}\sum_{\nu'}(\tilde{\Omega}^N_{\nu\nu'}+\tilde{\Omega}^U_{\nu\nu'})(\tilde{n}^D_{\nu'}(\boldsymbol{r},t)+\tilde{n}^{\delta\mathrm{O}}_{\nu'}) = \\
&\frac{1}{V}\sum_{\nu'}\tilde{\Omega}^U_{\nu\nu'}\tilde{n}^D_{\nu'}(\boldsymbol{r},t)+\frac{1}{V}\sum_{\nu'}\tilde{\Omega}_{\nu\nu'}\tilde{n}^{\delta\mathrm{O}}_{\nu'} \simeq \\
&\frac{1}{V}\sum_{\nu'}\tilde{\Omega}_{\nu\nu'}\tilde{n}^{\delta\mathrm{O}}_{\nu'}\,.
\end{aligned} \tag{4.40}$$

This is correct both at high and low temperatures, because at high temperatures the strong crystal momentum dissipation ensures $\tilde{n}^D_{\nu'}(\boldsymbol{r},t)\propto \boldsymbol{u}(\boldsymbol{r},t)\approx \boldsymbol{0}$ (see also Fig. 4.H.1), and at low temperatures Umklapp processes are much less frequent than normal processes ($\tilde{\Omega}^U_{\nu\nu'}\ll\tilde{\Omega}^N_{\nu\nu'}$).

4.A.3 Local equilibrium

From Eq. (4.31) and Eq. (4.40) it follows that, in the hydrodynamic regime, the distributions $\tilde{n}^T_\nu(\boldsymbol{r},t)$ and $\tilde{n}^D_\nu(\boldsymbol{r},t)$ are left unchanged by the dynamics described by the LBTE; therefore, these are local equilibrium distributions. It follows that $\tilde{n}^T_\nu(\boldsymbol{r},t)$ and $\tilde{n}^D_\nu(\boldsymbol{r},t)$ do not appear in Eq. (4.6) and Eq. (4.7) and thus do not contribute to the thermal conductivity and viscosity, which respectively describe the response to a perturbation of the local temperature and drift velocity. It is worth mentioning that, in the kinetic regime, $\tilde{n}^D_\nu(\boldsymbol{r},t)$ vanishes and $\tilde{n}^T_\nu(\boldsymbol{r},t)$ is still a stationary distribution for the LBTE.

4.B Thermal viscosity

The total crystal momentum flux tensor Π^{ij}_{tot}[24] is defined as

$$\Pi^{ij}_{\mathrm{tot}}(\boldsymbol{r},t)=\frac{1}{V}\sum_\nu \hbar q^i v^j_\nu N_\nu(\boldsymbol{r},t)\,. \tag{4.41}$$

Due to the odd parity of q^i and v^j_ν, only the even part of the phonon distribution contributes to the crystal momentum flux. Using the decomposition (4.4) introduced in the main text, we identify three contributions to the crystal momentum flux:

$$\begin{aligned}
\Pi^{ij}_{\mathrm{tot}}(\boldsymbol{r},t)&=\frac{1}{V}\sum_\nu \hbar q^i v^j_\nu[\bar{N}_\nu+n^T_\nu(\boldsymbol{r},t)+n^{\delta\mathrm{E}}_\nu(\boldsymbol{r},t)]\\
&=\bar{\Pi}^{ij}+\Pi^{ij}_T(\boldsymbol{r},t)+\Pi^{ij}_{\delta\mathrm{E}}(\boldsymbol{r},t)\,,
\end{aligned} \tag{4.42}$$

where $\bar{\Pi}^{ij}$ is the equilibrium (constant) crystal momentum flux, which is not affected by the LBTE's dynamics; $\Pi^{ij}_T(\boldsymbol{r},t)$ is the momentum flux related to the local equilibrium temperature and $\Pi^{ij}_{\delta\mathrm{E}}(\boldsymbol{r},t)$ is the out-of-equilibrium momentum flux generated in response to deviations from local equilibrium conditions and is further discussed below.

As stated by Eq. (4.8), the unsymmetrized thermal viscosity tensor η^{ijkl} relates a drift velocity perturbation to the momentum flux generated as a response to that perturbation. Eq. (4.8) is valid in the mesoscopic regime mentioned in Sec. 4.3 and 4.6, where the thermal viscosity is space-independent and nonhomogeneities arise mainly from variations of the local temperature and local drift velocity. In particular, η^{ijkl} is determined by deviations from local equilibrium and thus depends only on $\tilde{n}^{\delta\mathrm{E}}$. To determine the distribution $\tilde{n}^{\delta\mathrm{E}}$, we must solve the LBTE linearized in the drift velocity gradient Eq. (4.7). To this aim, we first symmetrize the LBTE using the transformations (4.25) and (4.26), finding

$$\frac{\boldsymbol{v}_\nu}{\sqrt{\bar{N}_\nu(\bar{N}_\nu+1)}}\cdot\left(\frac{\partial N^D_\nu}{\partial \boldsymbol{u}}\cdot\nabla\boldsymbol{u}\right)=-\frac{1}{V}\sum_{\nu'}\tilde{\Omega}_{\nu\nu'}\tilde{n}^{\delta\mathrm{E}}_{\nu'}\,. \tag{4.43}$$

Next, using the relaxon approach discussed in Ref. [39] for thermal conductivity, we write the response to the perturbation $\nabla\boldsymbol{u}$ as a linear combination of even eigenvectors:

$$\tilde{n}^{\delta\mathrm{E}}_\nu=\sum_{ij,\beta>0}f^{ij}_\beta\theta^\beta_\nu\frac{\partial u^i}{\partial r^j}\,, \tag{4.44}$$

where the summation does not involve the Bose eigenvector ($\beta=0$) since, as discussed in the Appendix for Eqs. (4.31) and (4.42), the Bose eigenvector is related to the local-equilibrium temperature and does not contribute to the out-of-equilibrium response to a drift-velocity perturbation. Substituting this relation in the LBTE, and noting that the left term is related to the eigenvector ϕ^i_ν of the normal scattering matrix [Eq. (4.36)], we obtain

$$v^j_\nu\sqrt{\frac{A^i}{k_B\bar{T}}}\phi^i_\nu=-\sum_{\beta>0}\frac{1}{\tau_\beta}f^{ij}_\beta\theta^\beta_\nu\,. \tag{4.45}$$

Taking the scalar product with a generic eigenvector θ^α_ν (with $\alpha>0$), we find

$$\sqrt{\frac{A^i}{k_B\bar{T}}}w^j_{i\alpha}=-\frac{f^{ij}_\alpha}{\tau_\alpha}\,, \tag{4.46}$$

where $w^j_{i\alpha}$ is a velocity tensor given by

$$w^j_{i\alpha}=\frac{1}{V}\sum_\nu\phi^i_\nu v^j_\nu\theta^\alpha_\nu\,. \tag{4.47}$$

Thanks to the odd parity of ϕ^i_ν and v^j_ν, the velocity $w^j_{i\alpha}$ is different from zero only for even eigenvectors α; Eq. (4.46) can thus be trivially solved for f^{ij}_α.

With the knowledge of the LBTE solution f^{ij}_α at hand, the crystal momentum flux tensor is readily computed. We thus express $\Pi^{ij}_{\delta\mathrm{E}}$ in the relaxon basis, finding

$$\begin{aligned}\Pi^{ij}_{\delta\mathrm{E}} &= \frac{1}{V}\sum_{\nu} n^{\delta\mathrm{E}}_{\nu}\hbar q^{i} v^{j}_{\nu} \\ &= \frac{1}{V}\sum_{\nu} \tilde{n}^{\delta\mathrm{E}}_{\nu}\sqrt{\bar{N}_{\nu}(\bar{N}_{\nu}+1)}\hbar q^{i} v^{j}_{\nu} \\ &= \frac{1}{V}\sum_{kl,\nu,\alpha>0} f^{kl}_{\alpha}\theta^{\alpha}_{\nu}\frac{\partial u^{k}}{\partial r^{l}}\sqrt{\bar{N}_{\nu}(\bar{N}_{\nu}+1)}\hbar q^{i} v^{j}_{\nu} \\ &= \sqrt{k_B\bar{T}A^{i}}\sum_{kl,\alpha>0} f^{kl}_{\alpha} w^{j}_{i\alpha}\frac{\partial u^{k}}{\partial r^{l}}\,. \end{aligned} \tag{4.48}$$

Substituting Eq. (4.46) in Eq. (4.48), we obtain the expression for the asymmetric thermal viscosity tensor:

$$\eta^{ijkl} = \sqrt{A^{i}A^{k}}\sum_{\alpha>0} w^{j}_{i\alpha} w^{l}_{k\alpha}\tau_{\alpha}. \tag{4.49}$$

The tensor η^{ijkl} is, in general, not symmetric under exchange of indexes $j \leftrightarrow l$. We will show later that, in a way analogous to fluids, only the sum over the spatial derivatives of the momentum flux tensor is relevant for the mesoscopic description of hydrodynamic thermal transport:

$$\sum_{j}\frac{\partial\Pi^{ij}_{\delta\mathrm{E}}(\boldsymbol{r},t)}{\partial r^{j}} = -\sum_{jkl}\eta^{ijkl}\frac{\partial^2 u^{k}(\boldsymbol{r},t)}{\partial r^{j}\partial r^{l}} = -\sum_{jkl}\mu^{ijkl}\frac{\partial^2 u^{k}(\boldsymbol{r},t)}{\partial r^{j}\partial r^{l}}\,, \tag{4.50}$$

where in the last term of Eq. (4.50) we have rewritten the divergence of the momentum flux tensor using the symmetrized viscosity tensor μ^{ijkl}:

$$\mu^{ijkl} = \frac{\eta^{ijkl}+\eta^{ilkj}}{2}\,. \tag{4.51}$$

It is worth drawing a parallel between thermal viscosity and conductivity, where the latter can be written as [39]

$$\kappa^{ij} = C\sum_{\alpha} w^{i}_{0\alpha} w^{j}_{0\alpha}\tau_{\alpha}\,. \tag{4.52}$$

Notably, $w^{i}_{0\alpha}$ is different from zero only for odd eigenvectors. As a result, thermal conductivity and viscosity are two quantities describing the transport due to the odd and even part of the spectrum respectively, *i.e.* energy and crystal momentum.

4.B.1 Single-mode relaxation-time approximation

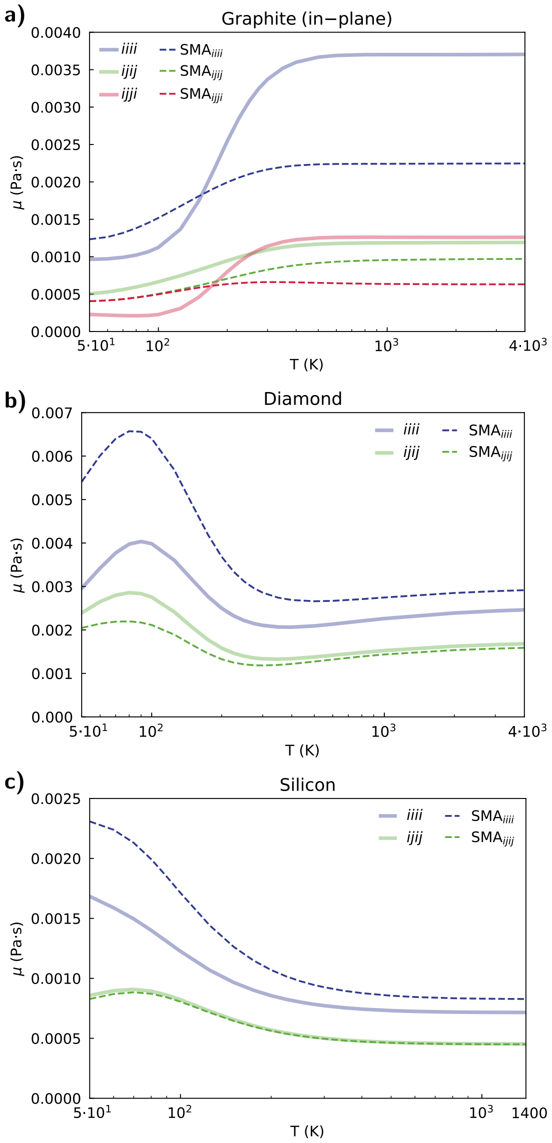

Figure 4.B.1 – Comparison between the exact bulk thermal viscosity (solid lines) and the SMA bulk thermal viscosity (dashed line) for in-plane graphite (a), diamond (b) and silicon (c).

In this section we derive the expression for thermal viscosity within the single-mode relaxation-time approximation (SMA). Using the SMA, the LBTE at Eq. (4.43) becomes

$$\frac{\boldsymbol{v}_\nu}{\sqrt{\bar{N}_\nu(\bar{N}_\nu+1)}}\cdot\left(\frac{\partial N^D_\nu}{\partial \boldsymbol{u}}\cdot\nabla\boldsymbol{u}\right)=-\frac{\tilde{n}^{\delta\mathrm{E}}_\nu}{\tau^{\mathrm{SMA}}_\nu}\,. \tag{4.53}$$

The deviation from equilibrium $\tilde{n}_\nu^{\delta\mathrm{E}}$ is readily found as

$$\tilde{n}_\nu^{\delta\mathrm{E}} = -\frac{\boldsymbol{v}_\nu}{\sqrt{\bar{N}_\nu(\bar{N}_\nu+1)}} \cdot \left(\frac{\partial N_\nu^D}{\partial \boldsymbol{u}} \cdot \nabla \boldsymbol{u}\right) \tau_\nu^{\mathrm{SMA}} . \tag{4.54}$$

We insert this result in the definition of momentum flux, obtaining

$$\Pi^{ij}_{\delta\mathrm{E,SMA}} = \frac{1}{V}\sum_\nu n_\nu^{\delta\mathrm{E}} \hbar q^i v_\nu^j = -\frac{1}{V}\sum_{\nu,kl} \hbar^2 q^i v_\nu^j q^k v_\nu^l \frac{\bar{N}_\nu\left(\bar{N}_\nu+1\right)}{k_B \bar{T}} \tau_\nu^{\mathrm{SMA}} \frac{\partial u^k}{\partial r^l} . \tag{4.55}$$

where we stress that, due to the lack of energy conservation in phonon collisions within the SMA treatment [280], in Eq. (4.55) it has not been possible to separate, as in Eq. (4.42), the momentum flux generated from a local temperature from that arising from a drift-velocity perturbation.

From the definition of the thermal viscosity (4.8), the SMA thermal viscosity is therefore

$$\mu^{ijkl}_{\mathrm{SMA}} = \frac{\eta^{ijkl}_{\mathrm{SMA}} + \eta^{ilkj}_{\mathrm{SMA}}}{2} = \frac{1}{V}\sum_\nu \hbar^2 q^i v_\nu^j q^k v_\nu^l \frac{\bar{N}_\nu\left(\bar{N}_\nu+1\right)}{k_B \bar{T}} \tau_\nu^{\mathrm{SMA}} , \tag{4.56}$$

where we highlight the fact that in the SMA approximation $\eta^{ijkl}_{\mathrm{SMA}} = \mu^{ijkl}_{\mathrm{SMA}}$, since in the SMA the viscosity tensor $\eta^{ijkl}_{\mathrm{SMA}}$ has the $j \leftrightarrow l$ symmetry. A comparison between the exact bulk thermal viscosity (4.9) and the SMA bulk thermal viscosity (4.56) is shown in Fig. 4.B.1. We highlight how the SMA approximation — which neglects the off-diagonal elements of the scattering operator and works well when Umklapp processes dominate over normal processes [22, 37, 101] — overestimates the largest component of the thermal viscosity, especially at low temperatures. This overestimation is more pronounced in diamond compared to silicon, in agreement with results from previous works where the SMA approximation was reported to yield quite accurate results for the thermal conductivity of silicon [39] but not for diamond [37].

4.C Size effects on the thermal conductivity and viscosity

In order to obtain a simple estimate of size effects, we compute the total effective thermal conductivity and viscosity using a Matthiessen sum of the bulk and ballistic limit:

$$\frac{1}{\kappa^{ij}} = \frac{1}{\kappa^{ij}_{\mathrm{bulk}}} + \frac{1}{\kappa^{ij}_{\mathrm{ballistic}}} , \tag{4.57}$$

$$\frac{1}{\mu^{ijkl}} = \frac{1}{\mu^{ijkl}_{\mathrm{bulk}}} + \frac{1}{\mu^{ijkl}_{\mathrm{ballistic}}} . \tag{4.58}$$

The ballistic conductivity and viscosity are computed for a sample of size L_S as $\kappa^{ij}_{\text{ballistic}} = K^{ij}_S \cdot L_S$ and $\mu^{ijkl}_{\text{ballistic}} = M^{ijkl} \cdot L_S$, where the prefactors K_S and M^{ijkl} are

$$K^{ij}_S = \frac{1}{V}\sum_\nu (\hbar\omega_\nu)^2 \frac{\bar{N}_\nu(\bar{N}_\nu+1)}{k_B \bar{T}^2} v^i_\nu v^j_\nu \frac{1}{|\boldsymbol{v}_\nu|}\,, \tag{4.59}$$

$$M^{ijkl} = \frac{1}{V}\sum_\nu \hbar^2 q^i v^j_\nu q^k v^l_\nu \frac{\bar{N}_\nu\big(\bar{N}_\nu+1\big)}{k_B \bar{T}} \frac{1}{|\boldsymbol{v}_\nu|}\,. \tag{4.60}$$

These prefactors are obtained after setting $\tau_\nu = \frac{L_S}{|\boldsymbol{v}_\nu|}$ in the SMA expressions of κ and μ. L_S is the length that determines boundary effects, *i.e.* the sample's size for a single crystal or the grain size for a polycrystalline sample. The numerical values of K^{ij}_S and M^{ijkl} can be computed from first-principles and are tabulated in Tabs. 4.E.1, 4.E.2, 4.E.3.

4.D Viscous heat equations

In this section we derive an extension to Fourier's law from the LBTE, which describes mesoscopic hydrodynamic thermal transport in terms of the temperature $T(\boldsymbol{r},t)$ and drift velocity $\boldsymbol{u}(\boldsymbol{r},t)$ fields. We focus on the mesoscopic regime where transport coefficients are well-defined (*i.e.* the finite-size renormalization of transport coefficients is small) and non-homogeneities arise from variations of the temperature and drift velocity. In contrast to Sec. 4.3, here the temperature and drift velocity gradients are space-dependent, and consequently the LBTE is not linearized in the temperature and drift velocity gradients. We start recalling that hydrodynamic thermal transport emerges when most collisions between phonon wavepackets conserve the crystal momentum. This can happen, for example, when the mean free path for normal collisions Λ^N is much smaller than the boundary scattering's length L_S (for a single crystal L_S is the sample's size, in the case of a polycrystalline sample L_S is the size of the grains) or the mean free path for Umklapp collisions Λ^U: $\Lambda^N \ll L_S, \Lambda^U$ [21, 255]. Under these conditions, the local equilibrium is expressed in terms of the four special eigenvectors ϕ^0_ν (also denoted θ^0_ν, since this is a common eigenvector for the full and normal scattering operator, see Appendix 4.A), ϕ^i_ν $(i = 1,2,3)$ described in Sec. (4.A.1,4.A.2), and of the local temperature $T(\boldsymbol{r},t)$ and drift velocity $\boldsymbol{u}(\boldsymbol{r},t)$ fields. As explained in Sec. (4.A.1,4.A.2), these four special eigenvectors do not contribute to thermal conductivity and viscosity, since these latter coefficients only describe the response to a perturbation of the local equilibrium.

In order to exploit the relationship between the drift velocity $\boldsymbol{u}(\boldsymbol{r},t)$ and the drift eigenvectors ϕ^i_ν, we choose to work with the basis of eigenvectors of the normal scattering matrix $\tilde{\Omega}^N_{\nu\nu'}$. To this aim, we diagonalize $\tilde{\Omega}^N_{\nu\nu'}$ as

$$\frac{1}{V}\sum_{\nu'} \tilde{\Omega}^N_{\nu\nu'}\phi^\beta_{\nu'} = \frac{1}{\tau^N_\beta}\phi^\beta_\nu\,, \tag{4.61}$$

where $\beta \geq 0$ is an an integer that labels the eigenvectors ϕ^β_ν and eigenvalues $\frac{1}{\tau^N_\beta}$. Among these eigenvectors, we know the analytic expression for the 4 of them associated with energy and momentum conservation, which we label with $\beta = 0$ for the energy eigenvector (in this section we will use ϕ^0_ν to label the Bose-Einstein eigenvector (4.32)), and $\beta = 1, \ldots, 3$ for the momentum eigenvectors, Eq. (4.36).

Noting that the set of "normal" eigenvectors $\{\phi^\beta_\nu\}$ ("normal" in the sense that they diagonalize $\tilde{\Omega}^N_{\nu\nu'}$, the part of the scattering matrix that accounts for normal processes only) is a complete basis set [22], we write the deviation from equilibrium $\tilde{n}_\nu(\boldsymbol{r}, t)$ as a linear combination of these eigenvectors:

$$\tilde{n}_\nu(\boldsymbol{r}, t) = \sum_\beta z_\beta(\boldsymbol{r}, t)\phi^\beta_\nu \,. \tag{4.62}$$

After symmetrizing the LBTE [Eq. (4.1)] according to Eq. (4.25) and (4.26), we use Eq. (4.62) to write the LBTE in the basis of the eigenvectors of the normal scattering operator

$$\sum_\beta \frac{\partial z_\beta(\boldsymbol{r}, t)}{\partial t}\phi^\beta_\nu + \boldsymbol{v}_\nu \cdot \left(\sum_\beta \nabla z_\beta(\boldsymbol{r}, t)\phi^\beta_\nu \right) = -\sum_{\beta>3} \frac{z_\beta(\boldsymbol{r}, t)}{\tau^N_\beta}\phi^\beta_\nu - \frac{1}{V}\sum_{\nu',\beta>0} z_\beta(\boldsymbol{r}, t)\tilde{\Omega}^U_{\nu\nu'}\phi^\beta_{\nu'} \,. \tag{4.63}$$

This equation is formally equivalent to the LBTE, but allows us to take advantage of the knowledge of the first 4 eigenvectors to derive mesoscopic equations.

4.D.1 The projection of the LBTE on the 1^{st} (Bose-Einstein) eigenvector: energy moment

Here we show how to obtain an energy balance equation. First, we note from Eq. (4.4) that the phonon population expansion of Eq. (4.62) can be recast as

$$\begin{aligned}\tilde{n}_\nu(\boldsymbol{r}, t) &= \tilde{n}^T_\nu(\boldsymbol{r}, t) + \tilde{n}^D_\nu(\boldsymbol{r}, t) + \tilde{n}^\delta_\nu(\boldsymbol{r}, t) \\ &= \sqrt{\frac{C}{k_B \bar{T}^2}}\phi^0_\nu(T(\boldsymbol{r}, t) - \bar{T}) + \sum_{i=1}^{3}\sqrt{\frac{A^i}{k_B \bar{T}}}\phi^i_\nu u^i(\boldsymbol{r}, t) + \sum_{\beta>3}\phi^\beta_\nu z_\beta(\boldsymbol{r}, t) \,.\end{aligned} \tag{4.64}$$

The coefficients z_β in front of the 4 special eigenvectors of $\tilde{\Omega}^N_{\nu\nu'}$ are associated to temperature and drift velocity, which fully determine local equilibrium; in detail

$$z_0(\boldsymbol{r}, t) = \sqrt{\frac{C}{k_B \bar{T}^2}}(T(\boldsymbol{r}, t) - \bar{T}) \,, \tag{4.65}$$

$$z_i(\boldsymbol{r}, t) = \sqrt{\frac{A^i}{k_B \bar{T}}}u^i(\boldsymbol{r}, t), \; i = 1, 2, 3 \,. \tag{4.66}$$

We now project the LBTE (4.63) in the subspace spanned by the Bose-Einstein eigenvector ϕ^0_ν, *i.e.* we take the scalar product of Eq. (4.63) with ϕ^0_ν, finding

$$\frac{\partial z_0(\boldsymbol{r}, t)}{\partial t} + \sum_{\beta>0} \boldsymbol{W}_{0\beta} \cdot \nabla z_\beta(\boldsymbol{r}, t) = 0 \,, \tag{4.67}$$

where we used the fact that ϕ^0_ν is an eigenvector of zero eigenvalue to $\tilde{\Omega}^U_{\nu\nu'}$ (see Sec. (4.A.1)) and we defined the velocity tensor

$$W^j_{\alpha\beta} = \frac{1}{V}\sum_\nu \phi^\alpha_\nu v^j_\nu \phi^\beta_\nu \,. \tag{4.68}$$

Note that the velocity $W^j_{\alpha\beta}$ differs from the velocity $w^j_{\alpha\beta}$ introduced in Sec. (4.3) for thermal viscosity; the difference arises from the use in Eq. (4.68) of the "normal" eigenvectors (of $\tilde{\Omega}^N_{\nu\nu'}$) rather than the general eigenvectors of $\tilde{\Omega}_{\nu\nu'}$ ($W^j_{\alpha\beta} \neq w^j_{\alpha\beta}$ in presence of Umklapp processes).

Substituting Eqs. (4.65, 4.66) in (4.67) we obtain

$$\sqrt{\frac{C}{k_B\bar{T}^2}}\frac{\partial T(\boldsymbol{r},t)}{\partial t} + \sum_{i,j=1}^{3}\sqrt{\frac{A^i}{k_B\bar{T}}}W^j_{0i}\frac{\partial u^i(\boldsymbol{r},t)}{\partial r^j} + \sum_{\beta>3}\boldsymbol{W}_{0\beta}\cdot\nabla z_\beta(\boldsymbol{r},t) = 0\,. \tag{4.69}$$

To elucidate the meaning of this equation, we note that the harmonic heat flux can be written as [16]:

$$\begin{aligned} \boldsymbol{Q}(\boldsymbol{r},t) &= \frac{1}{V}\sum_\nu \boldsymbol{v}_\nu \hbar\omega_\nu N_\nu(\boldsymbol{r},t) \\ &= \frac{1}{V}\sum_\nu \boldsymbol{v}_\nu \hbar\omega_\nu \big(n^D_\nu(\boldsymbol{r},t) + n^{\delta O}_\nu(\boldsymbol{r},t)\big)\,, \end{aligned} \tag{4.70}$$

where we used the fact that only odd components of the phonon distribution contribute to the heat flux. Therefore, the heat flux receives contributions from both the drift velocity [314] and the temperature gradient [39]. In the basis of "normal" eigenvectors, the drifting contribution can be written as

$$\begin{aligned} Q^{D,i}(\boldsymbol{r},t) &= \frac{1}{V}\sum_\nu v^i_\nu \hbar\omega_\nu n^D_\nu(\boldsymbol{r},t) = \\ &= \frac{1}{V}\sum_\nu v^i_\nu \hbar\omega_\nu \frac{\partial N^D_\nu}{\partial \boldsymbol{u}}\cdot\boldsymbol{u}(\boldsymbol{r},t) \\ &= \frac{1}{V}\sum_{\nu,j} v^i_\nu \theta^0_\nu \sqrt{\bar{T}A^j C}\phi^j_\nu u^j(\boldsymbol{r},t) \\ &= \sum_j \sqrt{\bar{T}A^j C}W^i_{0j}u^j(\boldsymbol{r},t)\,, \end{aligned} \tag{4.71}$$

while for the contribution from the deviation from local equilibrium $n^{\delta\mathrm{O}}_\nu(\boldsymbol{r},t)$, we find

$$\begin{aligned}
Q^{\delta\mathrm{O},i}(\boldsymbol{r},t) &= \frac{1}{V}\sum_\nu v^i_\nu \hbar\omega_\nu n^{\delta\mathrm{O}}_\nu(\boldsymbol{r},t) \\
&= \frac{1}{V}\sum_\nu v^i_\nu \hbar\omega_\nu \sqrt{\bar{N}_\nu(\bar{N}_\nu+1)}\,\tilde{n}^{\delta\mathrm{O}}_\nu(\boldsymbol{r},t) \\
&= \frac{\sqrt{Ck_B\bar{T}^2}}{V}\sum_{\beta>3}\sum_\nu z_\beta(\boldsymbol{r},t)\phi^0_\nu v^i_\nu \phi^\beta_\nu \\
&= \sqrt{Ck_B\bar{T}^2}\sum_{\beta>3} W^i_{0\beta} z_\beta(\boldsymbol{r},t)\,,
\end{aligned} \tag{4.72}$$

where only odd eigenvectors contribute ($W^i_{0\beta}=0$ for even β eigenvectors). As explained in Sec. (4.A.3), the thermal conductivity is determined only from odd eigenvectors that are not related to local equilibrium (that is, all the odd eigenvectors minus the three drift eigenvectors). At this point it is crucial to recall that the relaxons have a well defined parity (even or odd), deriving from the symmetries of the full scattering operator $\tilde{\Omega}_{\nu\nu'}=\tilde{\Omega}_{-\nu,-\nu'}$ [24, 343]. Because the same symmetries apply to $\tilde{\Omega}^N_{\nu\nu'}$, also the eigenvectors of the normal scattering operator have a well defined parity [24, 25, 343]. The odd component of the heat flux (and hence the thermal conductivity) is determined only from the odd part of the LBTE's solution $\tilde{n}^{\delta\mathrm{O}}_\nu(\boldsymbol{r},t)$ [39, 343], and this can be written either as a linear combination of odd relaxons (as done in Ref. [39]) or, equivalently, as a linear combination of odd eigenvectors of the normal scattering matrix, as done here. From the completeness of these basis sets it follows that the heat flux (4.72) arising from the odd out-of-equilibrium phonon distribution determined from equation (4.6), and described as a linear combination of odd eigenvectors of the normal scattering matrix, is equivalent to the heat flux of Ref. [39] that is written as a linear combination of odd relaxons (eigenvectors of the full scattering matrix). In an equivalent way, the equation for the odd part of the LBTE (4.6) is equivalent to the equation used to determine the thermal conductivity in Ref. [39], the only difference being the basis chosen for the decomposition of the solution (the relaxons in Ref. [39] and in the computation of the thermal viscosity reported in Fig. 4.3.1, and the eigenvectors of the normal scattering matrix here). The choice of the basis set does not affect the resulting local odd heat flux, which can therefore be related to the local temperature gradient via the thermal conductivity [39]:

$$Q^{\delta\mathrm{O},i}(\boldsymbol{r},t) = -\sum_{j=1}^{3}\kappa^{ij}\nabla^j T(\boldsymbol{r},t)\,. \tag{4.73}$$

In Eq. (4.73) the thermal conductivity is space-independent, *i.e.* Eq. (4.73) is valid in the mesoscopic regime where the thermal conductivity and viscosity are space-independent and non-homogeneities arise solely from variations of the local temperature and local drift velocity. Eqs. (4.72) and (4.73) can be used to rewrite Eq. (4.69) in terms of the local temperature and drift velocity fields, obtaining Eq. (4.10) of the main text:

$$C\frac{\partial T(\boldsymbol{r},t)}{\partial t}+\sum_{i,j=1}^{3}W_{0j}^{i}\sqrt{\bar{T}A^{j}C}\frac{\partial u^{j}(\boldsymbol{r},t)}{\partial r^{i}}-\sum_{i,j=1}^{3}\kappa^{ij}\frac{\partial^{2}T(\boldsymbol{r},t)}{\partial r^{i}\partial r^{j}}=0\,. \tag{4.74}$$

Eq. (4.74) is clearly not sufficient to fully describe the hydrodynamic heat conduction problem in which both $T(\boldsymbol{r},t)$ and $\boldsymbol{u}(\boldsymbol{r},t)$ are nonzero. In the next section we will derive a complementary set of equations that completes the formulation.

4.D.2 The projection of the LBTE on the $2^{\text{nd}}/3^{\text{rd}}/4^{\text{th}}$ eigenvectors: the momentum eigenspace

In this section, we derive a set of balance equations for crystal momentum. We start by recalling from Eq. (4.42) that the momentum flux receives contributions from three different terms. Of these three, the first term is a constant related to the equilibrium temperature, and thus is not changed by the LBTE. Therefore, we focus only on the momentum flux related to the local equilibrium temperature $\Pi_{T}^{ij}(\boldsymbol{r},t)$ and the out-of-equilibrium momentum flux generated in response to a drift velocity gradient $\Pi_{\delta\mathrm{E}}^{ij}(\boldsymbol{r},t)$. Using the expression of the four special eigenvectors discussed in Sec. (4.A.1, 4.A.2), we rewrite these two momentum fluxes in the basis of eigenvectors of the normal scattering matrix, finding:

$$\begin{aligned}\Pi_{T}^{ij}(\boldsymbol{r},t)&=\frac{1}{V}\sum_{\nu}\hbar q^{i}v_{\nu}^{j}n_{\nu}^{T}(\boldsymbol{r},t)\\&=\frac{1}{V}\sum_{\nu}\frac{\partial\bar{N}_{\nu}}{\partial T}\hbar q^{i}v_{\nu}^{j}[T(\boldsymbol{r},t)-\bar{T}]\\&=\sqrt{\frac{CA^{i}}{\bar{T}}}\frac{1}{V}\sum_{\nu}\phi_{\nu}^{0}v_{\nu}^{j}\phi_{\nu}^{i}[T(\boldsymbol{r},t)-\bar{T}]\\&=\sqrt{\frac{CA^{i}}{\bar{T}}}W_{i0}^{j}[T(\boldsymbol{r},t)-\bar{T}]\end{aligned} \tag{4.75}$$

and

$$\begin{aligned}\Pi_{\delta E}^{ij}(\boldsymbol{r},t)&=\frac{1}{V}\sum_{\nu}\hbar q^{i}v_{\nu}^{j}n_{\nu}^{\delta E}(\boldsymbol{r},t)\\&=\frac{\sqrt{k_{B}\bar{T}A^{i}}}{V}\sum_{\nu,\beta>3}\phi_{\nu}^{\beta}v_{\nu}^{j}\phi_{\nu}^{i}z_{\beta}(\boldsymbol{r},t)\\&=\sqrt{k_{B}\bar{T}A^{i}}\sum_{\beta>3}W_{i\beta}^{j}z_{\beta}(\boldsymbol{r},t)\,,\end{aligned} \tag{4.76}$$

where we used the velocity tensor defined in Eq. (4.68).

Next, as in the previous section, we take the scalar product of Eq. (4.63) with ϕ_{ν}^{i} $(i=1,2,3)$, obtaining the following three equations indexed by $i = 1,2,3$

$$\frac{\partial z_i(\boldsymbol{r},t)}{\partial t} + \boldsymbol{W}_{i0}\cdot\nabla z_0(\boldsymbol{r},t) + \sum_{\beta>3} \boldsymbol{W}_{i\beta}\cdot\nabla z_\beta(\boldsymbol{r},t) = -\sum_{j=1}^{3} z_j(\boldsymbol{r},t)D_U^{ij} - \sum_{\beta>3} z_\beta(\boldsymbol{r},t)D_U^{i\beta}\,, \tag{4.77}$$

where we used the fact that ϕ_ν^i are eigenvectors of $\tilde{\Omega}^N_{\nu\nu'}$ with zero eigenvalues and we defined

$$D_U^{i\beta} = \frac{1}{V^2}\sum_{\nu,\nu'}\phi_\nu^i\tilde{\Omega}^U_{\nu\nu'}\phi_{\nu'}^\beta\,. \tag{4.78}$$

From the property $\tilde{\Omega}^U_{\nu\nu'} = \tilde{\Omega}^U_{-\nu,-\nu'}$ it can be shown that $D_U^{i\beta}$ vanishes when β indexes an even eigenvector. Since the coefficients $z_\beta(\boldsymbol{r},t)$ for the first four eigenvectors ($\beta = 0,1,2,3$) are known, it is convenient to rewrite Eq. (4.77) as:

$$\frac{\partial z_i(\boldsymbol{r},t)}{\partial t} + \boldsymbol{W}_{i0}\cdot\nabla z_0(\boldsymbol{r},t) + \sum_{\beta>3}\left(\boldsymbol{W}_{i\beta}\cdot\nabla + D_U^{i\beta}\right)z_\beta(\boldsymbol{r},t) = -\sum_{j=1}^{3} z_j(\boldsymbol{r},t)D_U^{ij}\,, \tag{4.79}$$

In the hydrodynamic regime, Umklapp momentum dissipation is weak and thus $D_U^{i\beta}\to 0$ (ϕ_ν^i is approximately an eigenvector with a vanishing eigenvalue for $\tilde{\Omega}^U_{\nu\nu'}$). Therefore, we simplify Eq. (4.79) noting that

$$\left|\sum_{\beta>3}\boldsymbol{W}_{i\beta}\cdot\nabla z_\beta(\boldsymbol{r},t)\right| \gg \left|\sum_{\beta>3} D_U^{i\beta} z_\beta(\boldsymbol{r},t)\right|\,. \tag{4.80}$$

Then, we use the expression of the coefficients $z_\beta(\boldsymbol{r},t)$ ($\beta = 0,1,2,3$), and substitute Eqs. (4.65,4.66) in the simplified Eq. (4.79), obtaining:

$$\sqrt{\frac{A^i}{k_B\bar{T}}}\frac{\partial u^i(\boldsymbol{r},t)}{\partial t} + \sqrt{\frac{C}{k_B\bar{T}^2}}\sum_{j=1}^{3} W_{i0}^j\frac{\partial T(\boldsymbol{r},t)}{\partial r^j} + \frac{1}{\sqrt{k_B\bar{T}A^i}}\sum_j\frac{\partial \Pi^{ij}_{\delta\mathrm{E}}(\boldsymbol{r},t)}{\partial r^j} = -\sum_{j=1}^{3}\sqrt{\frac{A^j}{k_B\bar{T}}}D_U^{ij}u^j(\boldsymbol{r},t)\,. \tag{4.81}$$

Next, we note that only even eigenvectors different from the Bose-Einstein eigenvector determine the even distribution $n_\nu^{\delta\mathrm{E}}(\boldsymbol{r},t)$ appearing in the expression for the out-of-equilibrium momentum flux tensor (4.76). As shown in Eq. (4.50), in the mesoscopic regime the sum over the spatial derivatives of $\Pi^{ij}_{\delta\mathrm{E}}(\boldsymbol{r},t)$ can be expressed in terms of the viscosity and second derivative of the drift velocity. We thus find

$$A^i\frac{\partial u^i(\boldsymbol{r},t)}{\partial t} + \sqrt{\frac{CA^i}{\bar{T}}}\sum_{j=1}^{3} W_{i0}^j\frac{\partial T(\boldsymbol{r},t)}{\partial r^j} - \sum_{j,k,l=1}^{3}\mu^{ijkl}\frac{\partial^2 u^k(\boldsymbol{r},t)}{\partial r^j\partial r^l} = -\sum_{j=1}^{3}\sqrt{A^iA^j}D_U^{ij}u^j(\boldsymbol{r},t)\,. \tag{4.82}$$

Combining this with Eq. (4.74) we obtain 4 equations to be solved in terms of temperature $T(\boldsymbol{r},t)$ and drift velocity $\boldsymbol{u}(\boldsymbol{r},t)$; these are the viscous heat equations at the core of this work and that are further discussed in the main text.

As a final remark it is worth mentioning that in the kinetic regime, characterized by strong crystal momentum dissipation, the inequality (4.80) may not be valid. Nevertheless, in such a regime umklapp processes are the most frequent and crystal-momentum dissipation prevails over crystal-momentum redistribution ($\max_{i,j=1}^{3}[D_U^{ij}] \gg \max_{i\in[1,2,3];\beta>3}[D_U^{i\beta}]$), thus yielding the following (stronger) inequality

$$\left|\frac{\partial z_i(\boldsymbol{r},t)}{\partial t} + \sum_{\beta>3}\left(\boldsymbol{W}_{i\beta}\cdot\nabla + D_U^{i\beta}\right) z_\beta(\boldsymbol{r},t)\right| \ll \left| -\sum_{j=1}^{3} z_j(\boldsymbol{r},t) D_U^{ij}\right|, \tag{4.83}$$

implying that the viscous heat equations reduce to Fourier's law, as discussed in Sec. 4.7.

From a mathematical point of view, the projection of the LBTE in the Bose-Einstein subspace, performed computing the scalar product between the LBTE in the normal eigenvectors basis (4.63) and the Bose-Einstein eigenvector (4.32) $\propto \omega_\nu$, is equivalent to calculating the energy moment of the LBTE. Analogously, the projection in the momentum subspace, performed calculating the scalar product between the LBTE (4.63) and the momentum eigenvectors (4.36) $\propto q^i$, is equivalent to computing the momentum moment of the LBTE.

4.E Parameters entering the viscous heat equations.

We report in this section the numerical values of the parameters needed to solve the viscous heat equations. Due to the crystal symmetries of the materials considered, several components of vectors and tensors are equivalent. 2nd-rank tensors such as thermal conductivity (κ^{ij}), momentum dissipation (D_U^{ij}) and velocity (W_{0i}^{j}) are isotropic and diagonal for diamond and silicon; for graphite they are isotropic and diagonal for in-plane (x, y) directions (as used in the geometry of Fig. 4.6.1). Similarly, the specific momentum A^i is isotropic for diamond and silicon, and independent from the in-plane direction in graphite ($A^x = A^y$). The values of $D_{U,\text{bulk}}^{ij}$, A^i, C and W_{0i}^{j} as a function of temperature are plotted in Fig. 4.E.1 (we only report the in-plane or isotropic components, indexes are omitted). The numerical values of these parameters can be found in Tabs. 4.E.1, 4.E.2, 4.E.3; in addition, these tables contain also the prefactors discussed in Sec. 4.3, 4.4 and Appendix 4.C needed to compute the thermal conductivity and viscosity in the ballistic limit ($\kappa_{\text{ballistic}}^{ij}$ and $\mu_{\text{ballistic}}^{ijkl}$, respectively). In particular, the parameters K_S^{ij} and M^{ijkl} are defined as $K_S^{ij} = \kappa_{\text{ballistic}}^{ij}/L_S$ and $M^{ijkl} = \mu_{\text{ballistic}}^{ijkl}/L_S$, where L_S is the length that determines surface effects, *i.e.* the sample's size for a single crystal or the grain size for a polycrystalline sample. Similarly, the parameter F_U^{ij} are defined as $F_U^{ij} = D_{U,\text{boundary}}^{ij}(L_S) \cdot L_S$. In the tables, we report the populations' (κ_P^{ij}) and coherences' (κ_C^{ij}) contributions to the total bulk conductivity ($\kappa_{\text{bulk}}^{ij} = \kappa_P^{ij} + \kappa_C^{ij}$ [67]) and the non-zero irreducible components of the bulk thermal viscosity tensor, limiting graphite to in-plane components.

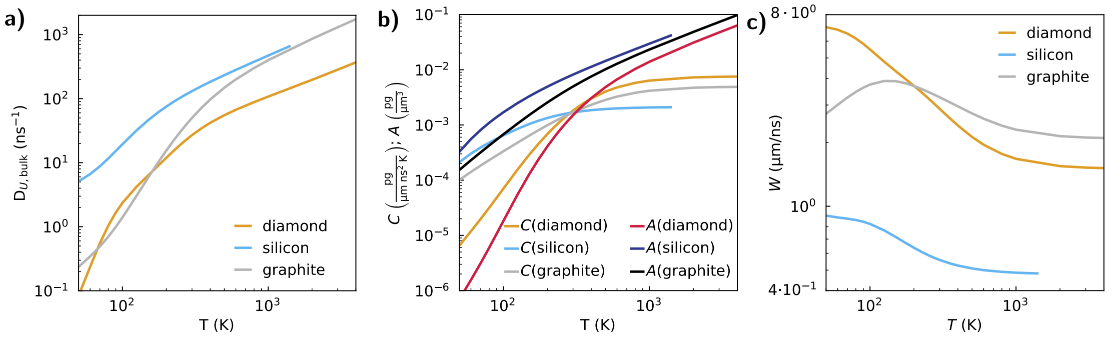

Figure 4.E.1 – Trends as a function of the temperature of various quantities reported in Tabs. 4.E.1, 4.E.2, 4.E.3. Panel a), values of the bulk momentum dissipation inverse timescale $D_{U,\text{bulk}}(T)$ (Eq. (4.12)); panel b), specific heat $C(T)$ (Eq. (4.33)) and specific momentum $A(T)$ (Eq. (4.39)) ; panel c), values of the velocity $W(T)$ (Eq. (4.68)).

Additionally, Fig. 4.E.2 shows the off-plane transport coefficients (panel a) and the off-plane non-negligible values of A^i, $D_{U,\text{bulk}}^{ij}$, and W_{0i}^{j} (panel b) for graphite; these parameters are not relevant for the geometry studied in Sec. 4.6 and are reported for completeness.

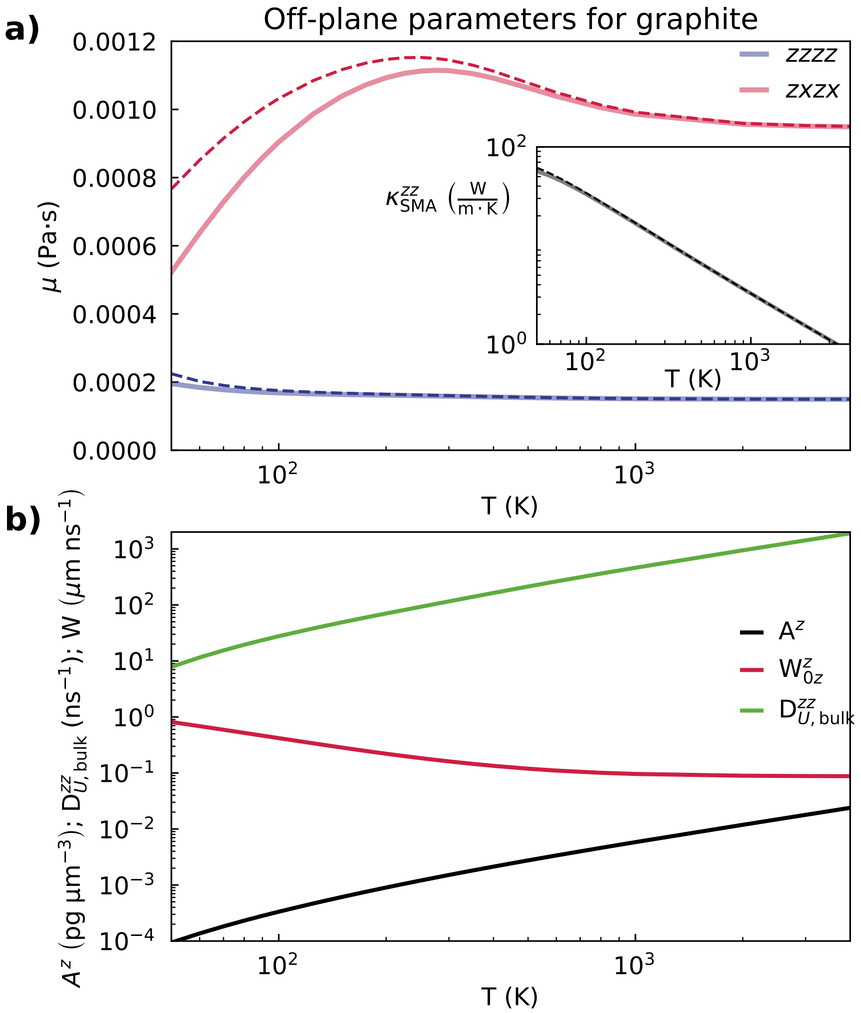

Figure 4.E.2 – Panel a), off-plane thermal viscosity (Eq. (4.9)) and off-plane SMA thermal conductivity (inset, Eq. (1.46)) of graphite for a sample having a grain size of 10 μm (solid line) or for the bulk case (dashed line). The other components of the viscosity tensor involving off-plane directions are negligible (at least one order of magnitude smaller than the largest component reported here). Panel b), specific momentum A^z (Eq. (4.39)), component W^z_{0z} of the velocity tensor (Eq. (4.68)), and component $D^{zz}_{U,\mathrm{bulk}}$ (Eq. (4.12)) of the momentum dissipation tensor of graphite.

Table 4.E.1 – Parameters entering the viscous heat equations for graphite. We report here only the in-plane components of the tensors needed to perform the calculation of Fig. 4.6.1: $\kappa_{\mathrm{P}}^{ij} = \kappa_{\mathrm{P}}\delta^{ij}$, $\kappa_{\mathrm{C}}^{ij} = \kappa_{\mathrm{C}}\delta^{ij}$, $K_S^{ij} = K_S\delta^{ij}$, $D_{U,\mathrm{bulk}}^{ij} = D_{U,\mathrm{bulk}}\delta^{ij}$, $F_U^{ij} = F_U\delta^{ij}$, $A = A^i \ \forall \ i$, $W_{0i}^{j} = W_{i0}^{j} = W\delta^{ij}$, where the indexes i, j represent the in-plane directions x, y only ($i, j = 1,2$ and $i \neq j$).

T [K]	$\kappa_{\mathrm{P}}\,[\frac{\mathrm{W}}{\mathrm{m\cdot K}}]$	$\kappa_{\mathrm{C}}\,[\frac{\mathrm{W}}{\mathrm{m\cdot K}}]$	$K_S\,[\frac{\mathrm{W}}{\mathrm{m^2\cdot K}}]$	$\mu_{\mathrm{bulk}}^{iiii}$ [Pa·s]	$\mu_{\mathrm{bulk}}^{ijij}$ [Pa·s]	$\mu_{\mathrm{bulk}}^{ijji}$ [Pa·s]	$M^{iiii}\,[\frac{\mathrm{Pa\cdot s}}{\mathrm{m}}]$	$M^{ijij}\,[\frac{\mathrm{Pa\cdot s}}{\mathrm{m}}]$	$M^{ijji}\,[\frac{\mathrm{Pa\cdot s}}{\mathrm{m}}]$	$D_{U,\mathrm{bulk}}\,[\mathrm{ns}^{-1}]$	$F_U\,[\frac{\mathrm{m}}{\mathrm{s}}]$	A $[\frac{\mathrm{pg}}{\mu\mathrm{m}^3}]$	$C\,[\frac{\mathrm{pg}}{\mu\mathrm{m\cdot ns^2\cdot K}}]$	W $[\frac{\mu\mathrm{m}}{\mathrm{ns}}]$
50	4.05937e+03	1.68603e-04	2.57075e+08	9.64173e-04	5.02673e-04	2.28503e-04	4.39176e+02	1.46638e+02	1.46269e+02	2.35602e-01	4.26877e+03	1.53433e-04	1.00900e-04	2.72761e+00
60	4.71660e+03	2.57901e-04	3.95197e+08	9.71961e-04	5.28685e-04	2.19176e-04	7.15578e+02	2.39244e+02	2.38166e+02	3.43827e-01	4.59801e+03	2.29498e-04	1.41101e-04	3.00647e+00
70	5.30227e+03	3.86737e-04	5.59073e+08	9.91550e-04	5.60889e-04	2.12711e-04	1.07264e+03	3.59308e+02	3.56660e+02	4.90888e-01	4.88642e+03	3.20256e-04	1.84524e-04	3.25249e+00
80	5.73508e+03	5.99494e-04	7.45726e+08	1.02183e-03	5.95233e-04	2.10580e-04	1.51011e+03	5.07190e+02	5.01440e+02	6.99024e-01	5.13608e+03	4.25102e-04	2.30997e-04	3.45924e+00
85	5.88316e+03	7.64389e-04	8.46709e+08	1.04140e-03	6.12652e-04	2.11623e-04	1.75824e+03	5.91502e+02	5.83334e+02	8.33461e-01	5.24694e+03	4.82650e-04	2.55380e-04	3.54681e+00
90	5.98509e+03	9.89803e-04	9.52360e+08	1.06450e-03	6.30069e-04	2.14443e-04	2.02532e+03	6.82640e+02	6.71286e+02	9.92275e-01	5.34894e+03	5.43532e-04	2.80534e-04	3.62371e+00
100	6.05968e+03	1.70592e-03	1.17648e+09	1.12368e-03	6.64594e-04	2.26760e-04	2.61392e+03	8.85020e+02	8.64331e+02	1.39551e+00	5.52812e+03	6.75030e-04	3.33160e-04	3.74625e+00
125	5.68808e+03	6.19470e-03	1.79932e+09	1.36901e-03	7.47169e-04	3.08284e-04	4.37038e+03	1.50275e+03	1.43336e+03	3.03975e+00	5.85614e+03	1.05685e-03	4.77779e-04	3.89427e+00
150	4.95001e+03	1.68525e-02	2.48830e+09	1.74338e-03	8.22466e-04	4.58198e-04	6.46259e+03	2.26630e+03	2.09701e+03	5.82976e+00	6.06477e+03	1.50504e-03	6.38359e-04	3.88637e+00
175	4.19048e+03	3.54534e-02	3.21691e+09	2.16305e-03	8.89217e-04	6.35206e-04	8.81058e+03	3.15609e+03	2.82509e+03	9.95230e+00	6.20314e+03	2.00676e-03	8.09822e-04	3.80167e+00
200	3.53715e+03	6.22028e-02	3.96223e+09	2.54485e-03	9.46684e-04	7.98006e-04	1.13505e+04	4.15136e+03	3.59604e+03	1.54740e+01	6.30063e+03	2.54990e-03	9.86974e-04	3.68920e+00
225	3.00949e+03	9.60903e-02	4.70645e+09	2.85177e-03	9.94791e-04	9.28042e-04	1.40336e+04	5.23216e+03	4.39558e+03	2.23622e+01	6.37337e+03	3.12432e-03	1.16581e-03	3.57259e+00
250	2.59110e+03	1.35378e-01	5.43687e+09	3.08241e-03	1.03413e-03	1.02427e-03	1.68237e+04	6.38073e+03	5.21448e+03	3.05105e+01	6.43012e+03	3.72211e-03	1.34366e-03	3.46122e+00
275	2.25923e+03	1.78035e-01	6.14489e+09	3.25018e-03	1.06572e-03	1.09285e-03	1.96938e+04	7.58209e+03	6.04680e+03	3.97658e+01	6.47577e+03	4.33732e-03	1.51881e-03	3.35792e+00
300	1.99378e+03	2.22075e-01	6.82487e+09	3.37078e-03	1.09079e-03	1.14103e-03	2.26238e+04	8.82402e+03	6.88860e+03	4.99551e+01	6.51324e+03	4.96554e-03	1.69010e-03	3.26300e+00
350	1.60318e+03	3.07855e-01	8.08784e+09	3.52011e-03	1.12596e-03	1.19869e-03	2.86057e+04	1.13924e+04	8.59058e+03	7.24549e+01	6.57048e+03	6.24865e-03	2.01775e-03	3.09612e+00
400	1.33509e+03	3.83750e-01	9.21271e+09	3.59939e-03	1.14751e-03	1.22790e-03	3.46848e+04	1.40297e+04	1.03064e+04	9.68155e+01	6.61114e+03	7.55350e-03	2.32135e-03	2.95575e+00
500	9.98702e+02	4.95975e-01	1.10594e+10	3.66770e-03	1.16905e-03	1.25159e-03	4.69490e+04	1.93852e+04	1.37502e+04	1.47964e+02	6.66215e+03	1.01896e-02	2.84581e-03	2.73866e+00
600	7.99431e+02	5.63451e-01	1.24444e+10	3.69035e-03	1.17775e-03	1.25863e-03	5.92022e+04	2.47475e+04	1.71850e+04	1.99654e+02	6.69043e+03	1.28283e-02	3.26054e-03	2.58552e+00
800	5.75423e+02	6.24987e-01	1.42502e+10	3.70056e-03	1.18356e-03	1.26080e-03	8.34395e+04	3.53375e+04	2.39875e+04	3.00624e+02	6.71747e+03	1.80581e-02	3.82784e-03	2.39757e+00
1000	4.52004e+02	6.47048e-01	1.52910e+10	3.70106e-03	1.18535e-03	1.26010e-03	1.07299e+05	4.57299e+04	3.07007e+04	3.97914e+02	6.72894e+03	2.32138e-02	4.16766e-03	2.29514e+00
2000	2.21503e+02	6.74660e-01	1.69581e+10	3.70084e-03	1.18829e-03	1.25838e-03	2.23610e+05	9.61271e+04	6.35592e+04	8.57330e+02	6.74228e+03	4.83715e-02	4.73019e-03	2.13973e+00
3000	1.47397e+02	6.92956e-01	1.73097e+10	3.70278e-03	1.18973e-03	1.25860e-03	3.38143e+05	1.45600e+05	9.59938e+04	1.30189e+03	6.74440e+03	7.31498e-02	4.85155e-03	2.10827e+00
4000	1.10542e+02	7.11733e-01	1.74364e+10	3.70441e-03	1.19062e-03	1.25896e-03	4.52156e+05	1.94803e+05	1.28304e+05	1.74234e+03	6.74511e+03	9.78154e-02	4.89550e-03	2.09705e+00

Table 4.E.2 – Parameters entering the viscous heat equations for diamond. As discussed above, due to the symmetries of diamond's crystal, $\kappa_{\mathrm{P}}^{ij} = \kappa_{\mathrm{P}}\delta^{ij}$, $\kappa_{\mathrm{C}}^{ij} = \kappa_{\mathrm{C}}\delta^{ij}$, $K_S^{ij} = K_S\delta^{ij}$, $D_{U,\mathrm{bulk}}^{ij} = D_{U,\mathrm{bulk}}\delta^{ij}$, $F_U^{ij} = F_U\delta^{ij}$, $A = A^i \ \forall \ i$, $W_{0i}^{j} = W_{i0}^{j} = W\delta^{ij}$, where $i, j = 1, \cdots, 3$ and $i \neq j$.

T [K]	$\kappa_{\mathrm{P}}\,[\frac{\mathrm{W}}{\mathrm{m\cdot K}}]$	$\kappa_{\mathrm{C}}\,[\frac{\mathrm{W}}{\mathrm{m\cdot K}}]$	$K_S\,[\frac{\mathrm{W}}{\mathrm{m^2\cdot K}}]$	$\mu_{\mathrm{bulk}}^{iiii}$ [Pa·s]	$\mu_{\mathrm{bulk}}^{ijij}$ [Pa·s]	$M^{iiii}\,[\frac{\mathrm{Pa\cdot s}}{\mathrm{m}}]$	$M^{ijij}\,[\frac{\mathrm{Pa\cdot s}}{\mathrm{m}}]$	$D_{U,\mathrm{bulk}}\,[\mathrm{ns}^{-1}]$	$F_U\,[\frac{\mathrm{m}}{\mathrm{s}}]$	A $[\frac{\mathrm{pg}}{\mu\mathrm{m}^3}]$	$C\,[\frac{\mathrm{pg}}{\mu\mathrm{m\cdot ns^2\cdot K}}]$	W $[\frac{\mu\mathrm{m}}{\mathrm{ns}}]$
50	3.43111e+04	2.07528e-05	2.73909e+07	2.95594e-03	2.39102e-03	5.06687e+00	1.68663e+00	8.37822e-02	1.20887e+04	6.98185e-07	6.53393e-06	6.98908e+00
60	3.28294e+04	4.82483e-05	4.87721e+07	3.42258e-03	2.65063e-03	1.10924e+01	3.61332e+00	2.36470e-01	1.17603e+04	1.55771e-06	1.18825e-05	6.79196e+00
70	3.05315e+04	9.23559e-05	7.95828e+07	3.77282e-03	2.80007e-03	2.16728e+01	7.01404e+00	5.51176e-01	1.13049e+04	3.15801e-06	1.99510e-05	6.51375e+00
80	2.77912e+04	1.57229e-04	1.22126e+08	3.97491e-03	2.85772e-03	3.90900e+01	1.27110e+01	1.04179e+00	1.07756e+04	5.98689e-06	3.16787e-05	6.17705e+00
90	2.48308e+04	2.52625e-04	1.78772e+08	4.03466e-03	2.83659e-03	6.62241e+01	2.18227e+01	1.66305e+00	1.02476e+04	1.07215e-05	4.80997e-05	5.82219e+00
100	2.18775e+04	3.96722e-04	2.51659e+08	3.98459e-03	2.75499e-03	1.06364e+02	3.57240e+01	2.35506e+00	9.77500e+03	1.81905e-05	7.02007e-05	5.48421e+00
125	1.54475e+04	1.17600e-03	5.13987e+08	3.60462e-03	2.41425e-03	2.85397e+02	1.01522e+02	4.21125e+00	8.92029e+03	5.47561e-05	1.55097e-04	4.80253e+00
150	1.08162e+04	3.12615e-03	8.93341e+08	3.14294e-03	2.05193e-03	6.09964e+02	2.29408e+02	6.31694e+00	8.41644e+03	1.26987e-04	2.86510e-04	4.32960e+00
175	7.74443e+03	7.08919e-03	1.37511e+09	2.76384e-03	1.77050e-03	1.10184e+03	4.34626e+02	8.87028e+00	8.09518e+03	2.43489e-04	4.63817e-04	3.97834e+00
200	5.78523e+03	1.38027e-02	1.93367e+09	2.49842e-03	1.58204e-03	1.76124e+03	7.22624e+02	1.19199e+01	7.86336e+03	4.07776e-04	6.82343e-04	3.69265e+00
225	4.53806e+03	2.36643e-02	2.54139e+09	2.32532e-03	1.46502e-03	2.57437e+03	1.09085e+03	1.53786e+01	7.67879e+03	6.19378e-04	9.35200e-04	3.44745e+00
250	3.72328e+03	3.66215e-02	3.17342e+09	2.21560e-03	1.39570e-03	3.52071e+03	1.53178e+03	1.91087e+01	7.52304e+03	8.75213e-04	1.21427e-03	3.23270e+00
275	3.16907e+03	5.21840e-02	3.80954e+09	2.14710e-03	1.35666e-03	4.57803e+03	2.03552e+03	2.29796e+01	7.38778e+03	1.17073e-03	1.51104e-03	3.04395e+00
300	2.77499e+03	6.95343e-02	4.43449e+09	2.10528e-03	1.33661e-03	5.72518e+03	2.59170e+03	2.68886e+01	7.26885e+03	1.50073e-03	1.81740e-03	2.87843e+00
350	2.25727e+03	1.05819e-01	5.61142e+09	2.06829e-03	1.32779e-03	8.21663e+03	3.82299e+03	3.45670e+01	7.07083e+03	2.24339e-03	2.43160e-03	2.60738e+00
400	1.93101e+03	1.39434e-01	6.65793e+09	2.06410e-03	1.33876e-03	1.08779e+04	5.16074e+03	4.18582e+01	6.91554e+03	3.06547e-03	3.01541e-03	2.40095e+00
500	1.53218e+03	1.92815e-01	8.33667e+09	2.09261e-03	1.37770e-03	1.64273e+04	7.98902e+03	5.51336e+01	6.69637e+03	4.83923e-03	4.01807e-03	2.12089e+00
600	1.28760e+03	2.33780e-01	9.54694e+09	2.13344e-03	1.41760e-03	2.20429e+04	1.08752e+04	6.69946e+01	6.55639e+03	6.67950e-03	4.78618e-03	1.94940e+00
800	9.89166e+02	2.97535e-01	1.10517e+10	2.20690e-03	1.48108e-03	3.30993e+04	1.65761e+04	8.81536e+01	6.39925e+03	1.03530e-02	5.78811e-03	1.76384e+00
1000	8.07834e+02	3.45553e-01	1.18801e+10	2.26142e-03	1.52541e-03	4.38462e+04	2.21156e+04	1.07517e+02	6.31958e+03	1.39372e-02	6.35996e-03	1.67254e+00
2000	4.26034e+02	4.74596e-01	1.31490e+10	2.38976e-03	1.62563e-03	9.50713e+04	4.84227e+04	1.96731e+02	6.20573e+03	3.09257e-02	7.26149e-03	1.54525e+00
3000	2.90112e+02	5.43241e-01	1.34078e+10	2.43788e-03	1.66217e-03	1.44824e+05	7.38984e+04	2.83004e+02	6.18362e+03	4.73219e-02	7.44892e-03	1.52096e+00
4000	2.20060e+02	5.95281e-01	1.35003e+10	2.46306e-03	1.68105e-03	1.94151e+05	9.91319e+04	3.68665e+02	6.17580e+03	6.35407e-02	7.51621e-03	1.51241e+00

Table 4.E.3 – Parameters entering the viscous heat equations for silicon. As discussed above, due to the symmetries of silicon's crystal, $\kappa_{\mathrm{P}}^{ij}=\kappa_{\mathrm{P}}\delta^{ij}$, $\kappa_{\mathrm{C}}^{ij}=\kappa_{\mathrm{C}}\delta^{ij}$, $K_S^{ij}=K_S\delta^{ij}$, $D_{U,\mathrm{bulk}}^{ij}=D_{U,\mathrm{bulk}}\delta^{ij}$, $F_U^{ij}=F_U\delta^{ij}$, $A=A^i\ \forall\ i$, $W_{0i}^{j}=W_{i0}^{j}=W\delta^{ij}$, where $i,j=1,\cdots,3$ and $i\neq j$.

T [K]	$\kappa_{\mathrm{P}}\ [\frac{\mathrm{W}}{\mathrm{m\cdot K}}]$	$\kappa_{\mathrm{C}}\ [\frac{\mathrm{W}}{\mathrm{m\cdot K}}]$	$K_S\ [\frac{\mathrm{W}}{\mathrm{m^2\cdot K}}]$	$\mu_{\mathrm{bulk}}^{iiii}$ [Pa·s]	$\mu_{\mathrm{bulk}}^{ijij}$ [Pa·s]	$M^{iiii}\ [\frac{\mathrm{Pa\cdot s}}{\mathrm{m}}]$	$M^{ijij}\ [\frac{\mathrm{Pa\cdot s}}{\mathrm{m}}]$	$D_{U,\mathrm{bulk}}\ [\mathrm{ns}^{-1}]$	$F_U\ [\frac{\mathrm{m}}{\mathrm{s}}]$	A $[\frac{\mathrm{pg}}{\mu\mathrm{m}^3}]$	$C\ [\frac{\mathrm{pg}}{\mu\mathrm{m\cdot ns^2\cdot K}}]$	W $[\frac{\mu\mathrm{m}}{\mathrm{ns}}]$
50	2.23795e+03	4.59329e-02	2.20201e+08	1.68379e-03	8.58240e-04	3.33315e+02	2.76288e+02	5.11570e+00	2.70364e+03	3.27665e-04	2.11441e-04	9.02735e-01
60	1.81398e+03	7.09541e-02	3.15143e+08	1.58868e-03	8.96618e-04	5.52469e+02	4.76459e+02	6.62366e+00	2.71505e+03	5.54460e-04	3.02489e-04	8.85284e-01
70	1.47266e+03	9.57185e-02	4.08143e+08	1.49577e-03	9.08048e-04	8.04123e+02	7.07599e+02	8.78307e+00	2.72606e+03	8.14113e-04	3.91395e-04	8.73874e-01
80	1.19453e+03	1.18329e-01	4.97327e+08	1.40019e-03	8.93142e-04	1.07864e+03	9.57983e+02	1.16582e+01	2.73491e+03	1.09495e-03	4.77916e-04	8.61085e-01
90	9.74026e+02	1.37274e-01	5.82183e+08	1.30833e-03	8.61466e-04	1.36970e+03	1.22015e+03	1.52308e+01	2.74122e+03	1.38989e-03	5.62856e-04	8.44738e-01
100	8.03719e+02	1.51720e-01	6.62519e+08	1.22579e-03	8.22564e-04	1.67298e+03	1.48947e+03	1.94247e+01	2.74509e+03	1.69464e-03	6.46690e-04	8.25091e-01
125	5.32796e+02	1.69276e-01	8.42648e+08	1.06829e-03	7.27720e-04	2.46564e+03	2.17760e+03	3.19146e+01	2.74649e+03	2.48348e-03	8.49829e-04	7.69340e-01
150	3.87535e+02	1.70507e-01	9.92662e+08	9.66838e-04	6.55421e-04	3.28405e+03	2.87136e+03	4.60065e+01	2.74093e+03	3.29333e-03	1.03633e-03	7.16183e-01
175	3.02197e+02	1.66898e-01	1.11455e+09	9.00619e-04	6.04637e-04	4.11081e+03	3.56215e+03	6.06265e+01	2.73283e+03	4.11117e-03	1.19918e-03	6.71955e-01
200	2.47534e+02	1.63344e-01	1.21236e+09	8.55850e-04	5.69080e-04	4.93707e+03	4.24698e+03	7.52349e+01	2.72447e+03	4.92977e-03	1.33675e-03	6.36972e-01
225	2.09966e+02	1.60900e-01	1.29062e+09	8.24499e-04	5.43728e-04	5.75879e+03	4.92514e+03	8.96094e+01	2.71681e+03	5.74536e-03	1.45094e-03	6.09681e-01
250	1.82675e+02	1.59448e-01	1.35343e+09	8.01853e-04	5.25234e-04	6.57443e+03	5.59687e+03	1.03682e+02	2.71013e+03	6.55621e-03	1.54510e-03	5.88350e-01
275	1.61970e+02	1.58683e-01	1.40415e+09	7.85055e-04	5.11434e-04	7.38370e+03	6.26280e+03	1.17454e+02	2.70443e+03	7.36173e-03	1.62269e-03	5.71533e-01
300	1.45710e+02	1.58355e-01	1.44545e+09	7.72310e-04	5.00922e-04	8.18690e+03	6.92362e+03	1.30950e+02	2.69961e+03	8.16196e-03	1.68684e-03	5.58128e-01
350	1.21755e+02	1.58409e-01	1.50744e+09	7.54699e-04	4.86338e-04	9.77722e+03	8.23261e+03	1.57251e+02	2.69211e+03	9.74789e-03	1.78475e-03	5.38497e-01
400	1.04880e+02	1.58914e-01	1.55067e+09	7.43511e-04	4.77032e-04	1.13499e+04	9.52838e+03	1.82836e+02	2.68671e+03	1.13174e-02	1.85414e-03	5.25164e-01
500	8.25113e+01	1.60439e-01	1.60486e+09	7.30895e-04	4.66472e-04	1.44577e+04	1.20928e+04	2.32571e+02	2.67977e+03	1.44204e-02	1.94232e-03	5.08869e-01
600	6.82316e+01	1.62305e-01	1.63594e+09	7.24532e-04	4.61092e-04	1.75321e+04	1.46339e+04	2.81113e+02	2.67571e+03	1.74906e-02	1.99348e-03	4.99732e-01
800	5.08841e+01	1.66661e-01	1.66806e+09	7.18968e-04	4.56298e-04	2.36251e+04	1.96779e+04	3.76331e+02	2.67145e+03	2.35755e-02	2.04682e-03	4.90446e-01
1000	4.06552e+01	1.71502e-01	1.68337e+09	7.16939e-04	4.54479e-04	2.96784e+04	2.46951e+04	4.70285e+02	2.66941e+03	2.96202e-02	2.07239e-03	4.86079e-01
1200	3.38805e+01	1.76561e-01	1.69180e+09	7.16146e-04	4.53716e-04	3.57109e+04	2.96982e+04	5.63606e+02	2.66828e+03	3.56437e-02	2.08651e-03	4.83688e-01
1400	2.90538e+01	1.81710e-01	1.69692e+09	7.15858e-04	4.53394e-04	4.17311e+04	3.46933e+04	6.56567e+02	2.66759e+03	4.16548e-02	2.09512e-03	4.82240e-01

4.F Second sound

In this section we show that drifting second sound [19, 24, 31, 260], *i.e.* thermal transport in terms of a temperature damped wave, is described by the viscous heat equations. We will first show the emergence of second sound following a bottom-up approach, *i.e.* analyzing the conditions under which the two viscous heat equations decouple with the first equation (4.10) reducing to a damped wave equations for the temperature field. Afterwards, we will analyze second sound within the viscous heat equations following a top-down approach, *i.e.* requiring the temperature field to have the mathematical form of a damped wave and analyzing if and under which conditions this can emerge from the viscous heat equations.

4.F.1 Second sound from the viscous heat equations (bottom-up approach)

For simplicity we consider an isotropic system whose tensors appearing in the viscous heat equations (4.10,4.11) are proportional to the identity; the general derivation can be obtained straightforwardly generalizing the procedure reported here. Without loss of generality, we consider $\hat{x}$ as the direction of second sound propagation. In an isotropic system, the drifting heat flux $\boldsymbol{Q}^D(\boldsymbol{r},t)$ is collinear with the drift velocity and the heat flux due to local temperature changes $\boldsymbol{Q}^\delta(\boldsymbol{r},t)$ is collinear with the temperature gradient. Thus, it follows that the only nonzero component of the drift velocity must be along the second sound propagation direction $u^x=u$ (for simplicity we omit all tensor indexes in the rest of this section, since the only the component having all the indexes equal to x is needed for this discussion). With these conditions, the viscous heat equations (4.10,4.11) become:

$$C\frac{\partial T(x,t)}{\partial t}+W\sqrt{\bar{T}AC}\frac{\partial u(x,t)}{\partial x}-\kappa\frac{\partial^2 T(x,t)}{\partial x^2}=0\,, \tag{4.84}$$

$$A\frac{\partial u(x,t)}{\partial t}+\sqrt{\frac{CA}{\bar{T}}}W\frac{\partial T(x,t)}{\partial x}-\mu\frac{\partial^2 u(x,t)}{\partial x^2}=-A\,D_U u(x,t)\,. \tag{4.85}$$

In order to observe second sound, temperature changes need to propagate following a damped wave equation. To this aim, we require that drift velocity and temperature are related as

$$W\sqrt{\bar{T}AC}\frac{\partial u(x,t)}{\partial x}=C\tau_{ss}(1-f)\frac{\partial^2 T(x,t)}{\partial t^2}-Cf\frac{\partial T(x,t)}{\partial t}\,. \tag{4.86}$$

where τ_{ss} is the second sound relaxation time and $0<|f|<1$ is a constant, both to be determined. To better understand this requirement, we insert Eq. (4.86) in Eq. (4.84), finding the desired temperature damped-wave equation:

$$\frac{\partial^2 T(x,t)}{\partial t^2}+\frac{1}{\tau_{ss}}\frac{\partial T(x,t)}{\partial t}-\frac{\kappa}{C\tau_{ss}(1-f)}\frac{\partial^2 T(x,t)}{\partial x^2}=0\,. \tag{4.87}$$

Next, we show that condition (4.86) implies that also the drift velocity field follows a damped-wave equation. To this aim, we take the derivative with respect to x of Eq. (4.86), finding

$$W\sqrt{\bar{T}AC}\frac{\partial^2 u(x,t)}{\partial^2 x}=\underbrace{\left(C\tau_{ss}(1-f)\frac{\partial^2}{\partial t^2}-Cf\frac{\partial}{\partial t}\right)}_{\hat{O}}\frac{\partial T(x,t)}{\partial x}\,, \tag{4.88}$$

where $\hat{O}$ is a differential operator. Next, by applying the operator $\hat{O}$ to both sides of equation (4.85) and using condition (4.88), we obtain

$$\begin{aligned}&\frac{\partial^3 u(x,t)}{\partial t^3}-\frac{f}{1-f}\frac{1}{\tau_{ss}}\frac{\partial^2 u(x,t)}{\partial t^2}+\frac{W^2}{\tau_{ss}(1-f)}\frac{\partial^2 u(x,t)}{\partial x^2}-\frac{\mu}{A}\frac{\partial^4 u(x,t)}{\partial t^2\partial x^2}+\frac{f}{1-f}\frac{1}{\tau_{ss}}\frac{\mu}{A}\frac{\partial^3 u(x,t)}{\partial t\partial x^2}\\&=-D_U\left(\frac{\partial^2 u(x,t)}{\partial t^2}-\frac{f}{1-f}\frac{1}{\tau_{ss}}\frac{\partial u(x,t)}{\partial t}\right)\,.\end{aligned} \tag{4.89}$$

If we consider only the lowest-order derivatives in Eq. (4.89), we obtain a simplified equation that holds in the close-to-equilibrium regime where variations in space and time are small. In particular, neglecting higher-than-second order derivatives gives:

$$\frac{\partial^2 u(x,t)}{\partial t^2}+\underbrace{\frac{D_U f}{f-(1-f)\tau_{ss}D_U}}_{c_1}\frac{\partial u(x,t)}{\partial t}-\underbrace{\frac{W^2}{f-(1-f)\tau_{ss}D_U}}_{c_2}\frac{\partial^2 u(x,t)}{\partial x^2}=0\,. \tag{4.90}$$

Therefore, if

$$f>\frac{\tau_{ss}D_U}{1+\tau_{ss}D_U}\,, \tag{4.91}$$

then both constants c_1 and c_2 are positive and the evolution of the drift velocity is that of a damped wave equation like the one for temperature.

The coefficients τ_{ss} and f are determined solving Eqs. (4.87,4.90) and imposing the second sound condition (4.86). The solutions are of the form

$$T(x,t) = \frac{1}{2\pi}\int C_T(k) e^{-\frac{t}{2\tau_{ss}}} e^{i(kx-\bar{\omega}(k)t)} dk \tag{4.92}$$

and

$$u(x,t) = \frac{1}{2\pi}\int C_u(k) e^{-\frac{t}{2\tau_{ss}}} e^{i(kx-\bar{\omega}(k)t)} dk \tag{4.93}$$

with:

$$\bar{\omega}(k) = \sqrt{v_{ss}^2 k^2 - \frac{1}{4\tau_{ss}^2}}\,; \tag{4.94}$$

$$v_g(k) = \frac{\partial \bar{\omega}(k)}{\partial k} = \frac{k v_{ss}}{\sqrt{k^2 - (2\tau_{ss} v_{ss})^{-2}}}\,; \tag{4.95}$$

$$f = D_U \tau_{ss}\,; \tag{4.96}$$

$$\tau_{ss} = \frac{CW^2}{\kappa (D_U)^2 + D_U C W^2}\,; \tag{4.97}$$

$$v_{ss} = \frac{\kappa D_U + CW^2}{CW}\,. \tag{4.98}$$

The condition (4.96) is derived from the requirement $c_1 = \frac{1}{\tau_{ss}}$, and is consistent with the damped wave requirement (4.91); condition (4.97) is derived from the requirement that $c_2 = \frac{\kappa}{C\tau_{ss}(1-f)}$ and the second sound velocity (4.98) has been obtained substituting Eq. (4.96) and Eq. (4.97) into Eq. (4.87). We note that for $D_U \to 0$ (that is, negligible crystal momentum dissipation) $v_g(k) \to v_{ss} \to W$, *i.e.* the second sound propagation velocity approaches the drifting second sound velocity defined by Hardy [24]) and $\tau_{ss} \to (D_U)^{-1}$. Finally, the second sound condition (4.86) imposes the following relation between the coefficients:

$$C_u(k) = \frac{-i}{k}\left\{\frac{\tau_{ss}}{W}\sqrt{\frac{C}{\bar{T}A}}\left[(1-\tau_{ss}D_U)\left(\frac{1}{2\tau_{ss}} + i\bar{\omega}(k)\right)^2 + D_U\left(\frac{1}{2\tau_{ss}} + i\bar{\omega}(k)\right)\right]\right\} C_T(k) \tag{4.99}$$

$C_T(k)$ must be set according to initial conditions and the form of $C_u(k)$ follows from equation (4.99). We note from Eq. (4.99) that, when second sound occur, temperature and drift velocity are both damped waves that are characterized by a phase shift.

4.F.2 Second sound from the viscous heat equations (top-down approach)

In the previous section, we obtained second sound properties by finding the conditions under which the viscous equation for temperature (Eq. (4.10)) becomes a damped wave equation. However, we can also obtain a second sound equation taking inspiration from the approach outlined in Ref. [260], *i.e.* by looking for the conditions upon which the microscopic degrees of freedom of the transport equation evolve as a damped wave. In particular, we want to find the conditions such that the solution of Eqs. (4.10,4.11) are

$$T(x,t) = \bar{T} + \delta T e^{i(kx-\hat{\omega}(k)t)} e^{-t/2\hat{\tau}_{ss}}, \tag{4.100}$$

$$u(x,t) = u_0 e^{i(kx-\hat{\omega}(k)t)} e^{-t/2\hat{\tau}_{ss}}, \tag{4.101}$$

where δT and u_0 are in general complex numbers to allow for a phase difference between the two waves. We note in particular that this guess for solution requires that both temperature and drift velocity oscillate at the same frequency and decay with the same rate, which is consistent with the conditions (4.92,4.93) obtained in the previous section.

Using this guess for the solution, the derivation of the dispersion relation and the decay time easily follows. To this aim, we substitute Eqs. (4.100,4.101) in the viscous heat equations (4.10,4.11) and introducing the complex frequency $\tilde{\omega}(k) = \hat{\omega}(k) - i/2\hat{\tau}_{ss}$ to simplify the calculation, we find

$$-iC\tilde{\omega}(k)\delta T + W\sqrt{\bar{T}AC}\,iku_0 + \kappa k^2 \delta T = 0, \tag{4.102}$$

$$-iA\tilde{\omega}(k)u_0 + \sqrt{\frac{CA}{\bar{T}}}Wik\delta T + \mu k^2 u_0 = -AD_U u_0. \tag{4.103}$$

Next, we rewrite Eq. (4.103) as:

$$u_0 = -\delta T \frac{ik\sqrt{\frac{CA}{\bar{T}}}W}{\mu k^2 + AD_U - iA\tilde{\omega}(k)}, \tag{4.104}$$

and substitute this expression into Eq. (4.102), finding

$$-iC\tilde{\omega}(k) + \frac{CAW^2k^2}{\mu k^2 + AD_U - iA\tilde{\omega}(k)} + \kappa k^2 = 0, \tag{4.105}$$

that gives:

$$(-iC\tilde{\omega}(k) + \kappa k^2)(AD_U + \mu k^2 - iA\tilde{\omega}(k)) + CAW^2k^2 = 0. \tag{4.106}$$

This is a quadratic equation that determines the dispersion relations for $\tilde{\omega}(k)$, given by:

$$\tilde{\omega}^2(k) + i\tilde{\omega}(k)\left[\left(\frac{\mu}{A} + \frac{\kappa}{C}\right)k^2 + D_U\right] - \left(W^2 + \frac{\kappa D_U}{C} + \frac{\kappa\mu k^2}{CA}\right)k^2 = 0. \tag{4.107}$$

This equation can be solved to obtain the complex frequency $\tilde{\omega}(k)$ and thus the oscillation frequency and decay time of second sound as a function of the wavevector k. Solving for this quadratic equation, we obtain:

$$\tilde{\omega}(k) = -\frac{i}{2}\left(\frac{\mu}{A}k^2 + D_U + \frac{\kappa}{C}k^2\right) \pm \frac{1}{2}\left[-\left(\frac{\mu}{A}k^2 + D_U + \frac{\kappa}{C}k^2\right)^2 + 4\left(W^2k^2 + \frac{D_U\kappa k^2}{C} + \frac{\kappa\mu k^4}{AC}\right)\right]^{\frac{1}{2}}. \tag{4.108}$$

In order to compare this result with the expression for second sound derived in the previous section, it is worth recalling that the semiclassical description of thermal transport used throughout this work holds for long-wavelength perturbations. Therefore, we simplify the previous expression retaining terms to smallest order in k, finding:

$$\tilde{\omega}(k) \approx -\frac{iD_U}{2} \pm \sqrt{-\left(\frac{D_U}{2}\right)^2 + k^2\left(W^2 + \frac{D_U \kappa}{2C} - \frac{\mu D_U}{2A}\right)}\,.$$

Choosing for convenience the solution with positive real part, we can readily see that $\hat{\omega}(k) = \sqrt{k^2(W^2 + D_U\kappa/2C - \mu D_U/2A) - (D_U/2)^2}$ and $\hat{\tau}_{ss} = 1/D_U$, that is, the second sound's decay time is set by the crystal-momentum dissipation rate. In the limit of decreasingly smaller crystal-momentum dissipation ($D_U \to 0$), we find $\hat{\omega}(k) \approx W\,k$, that is, second sound disperses linearly with k, and has a velocity $\hat{v}_g(k) = \partial\hat{\omega}(k)/\partial k \approx W$. These limiting approximations ($\hat{v}_g(k) \approx W$ and $\hat{\tau}_{ss} \approx \frac{1}{D_U}$) are consistent with the results found in the previous section.

4.G Analytical 1D example

The viscous heat equations (4.10,4.11) can be solved analytically in a handful of toy models. Here, for simplicity, we neglect dissipation of momentum by Umklapp processes ($D_U^{ij} = 0$) and consider steady-state heat diffusion along the transversal direction of a thin film, so that the problem becomes effectively a 1D problem, with x labeling the orthogonal direction position. In addition, since we are considering a 1D geometry, we label $A = A^x$, $W = W_{0x}^x$, $\mu = \mu^{xxxx}$ and assume that temperature and velocity fields depend only on the position x. Under these considerations the viscous heat equations (4.10,4.11) reduce to:

$$\sqrt{\bar{T}AC}W\frac{\partial u(x)}{\partial x} - \kappa\frac{\partial^2 T(x)}{\partial x^2} = 0\,, \tag{4.109}$$

$$\sqrt{\frac{CA}{\bar{T}}}W\frac{\partial T(x)}{\partial x} - \mu\frac{\partial^2 u(x)}{\partial x^2} = 0\,. \tag{4.110}$$

To solve the problem, we specify the following no-slip boundary conditions on a 1D geometry having length $2l$:

$$u(x = \pm l) = 0\,, \tag{4.111}$$

and

$$T(x = \pm l) = \bar{T} \pm \delta T\,, \tag{4.112}$$

that is, we assume boundaries at thermal equilibrium.

We look for solutions of the form:

$$u(x) = d\cosh(bl) + a\cosh(bx)\,, \tag{4.113}$$

$$T(x) = \bar{T} + c\sinh(bx)\,. \tag{4.114}$$

After some algebra, one finds the solution

$$u(x) = \delta T \sqrt{\frac{\kappa}{\mu \bar{T}}} \left(\frac{\cosh(bx)}{\sinh(bl)} - \coth(bl) \right) , \tag{4.115}$$

$$T(x) = \bar{T} + \delta T \frac{\sinh(bx)}{\sinh(bl)} , \tag{4.116}$$

$$b = \sqrt{\frac{ACW^2}{\mu \kappa}} = \lambda^{-1} . \tag{4.117}$$

This analytical solution shares several qualitative similarities with the numerical example discussed in the main text, and more clearly highlights how the factor $\lambda = 1/b$ represents a length scale at which surface scattering affects thermal transport, which is in turn dependent on both conductivity and viscosity. Moreover, we note that the mathematical form of the solution has the same qualitative behavior of the problem studied by Sussmann and Thellung [23], which serves as a verification of the present model. At variance with their work however, the prefactors introduced here allow us to go beyond the Debye approximation for the phonon dispersion.

4.H Estimate of the characteristic drift velocity

In this Appendix, we estimate the characteristic value of the drift velocity (u_0) in the high- (u_H) and low-temperature (u_L) regimes. These characteristic values are determined substituting in the viscous heat equations (4.10, 4.11) the characteristic values of the temperature (and related derivatives) and solving them approximatively for the velocity. With this aim, we start estimating the characteristic temperature gradient in the setup of Fig. 4.6.1 when a temperature difference $\bar{T} \pm \delta T$ is imposed on the two opposite sides (at $x = 0$ and $x = 15\ \mu m$). For a sample geometrically similar to that in Fig. 4.6.1 with total length l_{TOT} (e.g., $l_{\text{TOT}} = 15\mu\text{m}$ for the sample in Fig. 4.6.1), we choose its shortest lengthscale, $L = l_{\text{TOT}}/5$, as a length unit.

In this setup we clearly distinguish two regions. The left region has length $l_L = 1\ L$ and width $w_L = 1\ L$, while the right region has length $l_R = 4\ L$ and width $w_R = 3\ L$. Energy conservation requires that the current in the left side must be equal to that in the right side. Since the temperature gradient is mainly along the x direction, the x component of the heat flux on the left side Q^x_L must be 3 times the heat flux on the right side, $Q^x_L = 3Q^x_R$. Using Fourier's law, and supposing that the thermal conductivity tensor is isotropic and constant throughout the sample, it follows that $Q^x = -\kappa^{xx}\nabla^x T$ and the temperature gradients in the two regions are related as $\nabla^x T_L = 3\nabla^x T_R$. Requiring the total temperature drop to be equal to the temperature difference imposed by the boundary conditions, we can write

$$-2\delta T = \Delta T^x_L + \Delta T^x_R = l_L \nabla^x T_L + l_R \nabla^x T_R = 7L\, \nabla^x T_R , \tag{4.118}$$

where ΔT^x_L and ΔT^x_R are the temperature drops over the left and right regions, respectively.

Focusing from now on on the larger region on the right, it follows that the temperature drop taking place over this region is approximately given by $\Delta T_R = -\frac{8}{7}\delta T$.

To determine a characteristic value of drift velocity u_0, we substitute $\nabla T_R^x \simeq \frac{\Delta T_R}{l_R}$ in Eq. (4.11) and for simplicity consider isotropic symmetry, valid e.g. for silicon, diamond and for graphite in the in-plane directions. u_0 can be determined focusing on the steady state limit of Eq. (4.11). We simplify its estimate considering separately the limits of low and high temperatures.

In the high temperature limit, the term related to momentum dissipation ($\propto D_U^{ij}$) is much larger than the viscous term ($\propto \mu^{ijkl}$) (see Fig. 4.E.1), therefore Eq. (4.11) can be approximated as:

$$\sqrt{\frac{CA^x}{\bar{T}}} W_{x0}^x \nabla^x T^x \simeq -A^x D_U^{xx} u^x \,. \tag{4.119}$$

Using the estimated temperature gradient $\nabla T_R^x \simeq \frac{\Delta T_R}{l_R}$, the high-temperature characteristic value of drift velocity u_H is found to be

$$u_H = \sqrt{\frac{C}{\bar{T}A^x}} \frac{W_{x0}^x}{D_U^{xx}} \frac{2}{7} \frac{\delta T}{L} \,. \tag{4.120}$$

At low temperatures, viscous effects dominate over momentum dissipation (see Figs. 4.3.1 and 4.E.1), so that Eq. (4.11) is approximated as

$$\sqrt{\frac{CA^x}{\bar{T}}} W_{x0}^x \frac{\partial T(x,y)}{\partial x} \simeq \mu^{xxxx} \frac{\partial^2 u^x(x,y)}{\partial x^2} + \mu^{xyxy} \frac{\partial^2 u^x(x,y)}{\partial y^2} \,, \tag{4.121}$$

where we considered only the two largest components of the viscosity tensor. To estimate the average value of these second derivatives, we note that, as shown in Fig. 4.6.1, $\boldsymbol{u}(x,y)$ has a bell-like profile in the sample interior, which vanishes at the boundaries. We thus proceed with a few assumptions that allow us to make an estimate of u_L. First, we suppose that the average values of the second derivatives of the drift velocity in Eq. 4.121 are of the same order of magnitude, that is $\langle \frac{\partial^2 u^x}{\partial x^2} \rangle \sim \langle \frac{\partial^2 u^x}{\partial y^2} \rangle$, which can be checked numerically. It follows that Eq. (4.121) can be simplified as:

$$\langle \frac{\partial^2 u^x}{\partial y^2} \rangle \simeq \sqrt{\frac{CA^x}{\bar{T}}} \frac{W_{x0}^x \nabla^x T_R}{\mu^{xxxx} + \mu^{xyxy}} = -a \,. \tag{4.122}$$

Next, we note that the variation of $\boldsymbol{u}$ is stronger along the y coordinate. To mimic the Poiseuille-like shape, we assume the velocity profile to be constant along the x direction, and parabolic along the y direction with vanishing velocity at the boundaries ($y = 0\ \mu m$ and $y = w_R$), so that $\boldsymbol{u}(x,y) \simeq [-a \cdot y(y - w_R), 0, 0]$.

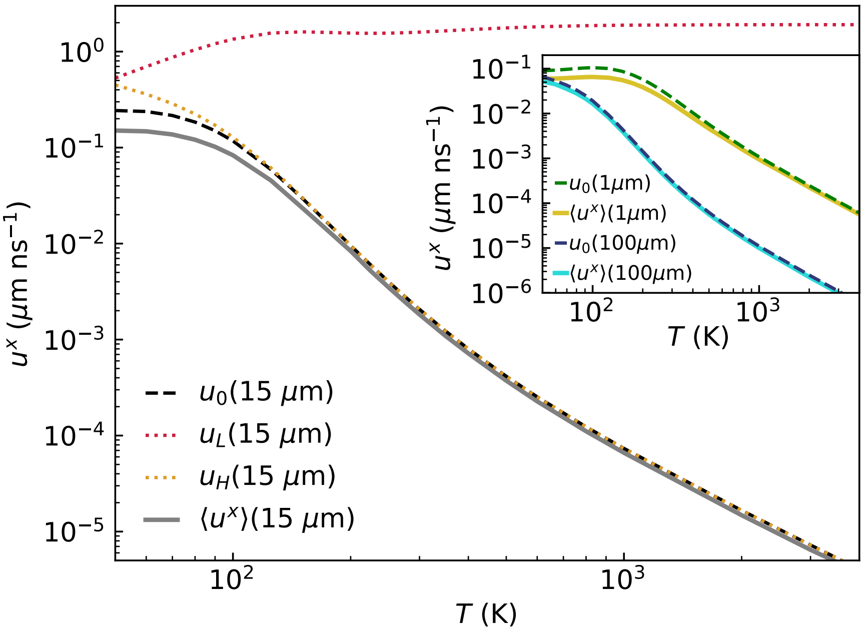

Figure 4.H.1 – Estimates of the characteristic value of the drift velocity u_0 (dashed lines) as combination of the asymptotic trends given by u_H (Eq. (4.120), dotted orange) and u_L (Eq. (4.124), dotted red) for graphite samples having total length $l_{\mathrm{TOT}} = l_L + l_R = 15\ \mu$m (main plot), 1 μm and 100 μm (inset). $\langle u^x\rangle$ (solid lines) is the average value of the drift velocity computed from the numerical solution of the viscous heat equations in the region $l_L < x < (l_L + l_R)$.

With these approximations, we can estimate the average value of the parabolic velocity profile, i.e. the characteristic value of the drift velocity at low temperatures u_L, as:

$$u_L = \frac{1}{w_R}\int_0^{w_R} u^x(y)dy = \frac{a\,w_R^2}{6} = \tag{4.123}$$

$$= \frac{3}{7}\sqrt{\frac{CA^x}{\bar{T}}}\,\frac{W^x_{x0}\delta T L}{\mu^{xxxx}+\mu^{xyxy}} \tag{4.124}$$

where we used $w_R = 3\,L$ and $l_R = 4\,L$. We thus recover the expression for u_L given in section 4.7 in the main text. The characteristic value of the drift velocity u_0 is obtained interpolating the high- and low-temperature limiting values as $u_0^{-1} = u_H^{-1} + u_L^{-1}$. The estimates of u_H, u_L and u_0 for graphite are reported in Fig. 4.H.1. We also compare this rough estimate with the average value of $u^x(x, y)$ computed from the numerical solution of the viscous heat equations on the region $x > \frac{1}{5} l_{\mathrm{TOT}}$ of the geometry discussed in the main text and denoted denoted with $\langle u^x\rangle$. Despite the qualitative arguments used to derive u_0, the estimate is able to capture qualitative trends and approximately reproduce average results from the numerical solution of the viscous heat equations.

4.I Hydrodynamic behavior in macroscopic diamond samples

In this section we show how extending the sizes in Fig. 4.7.1e up to 10 mm yields another peak for FDN for dimensions around 1 mm and temperatures around 50-60 K. This result has been confirmed by full solutions of the viscous heat equations similar to these reported in Fig. 4.7.1b. The increase of FDN at low temperature and large size reported in Fig. 4.I.1 is in qualitative agreement with the predictions for the second-sound window performed using the reduced isotropic crystal model or the Callaway model [264]. However, in contrast with this work, Ref. [264] reports that an isotopic concentration much lower than the natural isotope abundance is necessary for the observation of second sound in diamond.

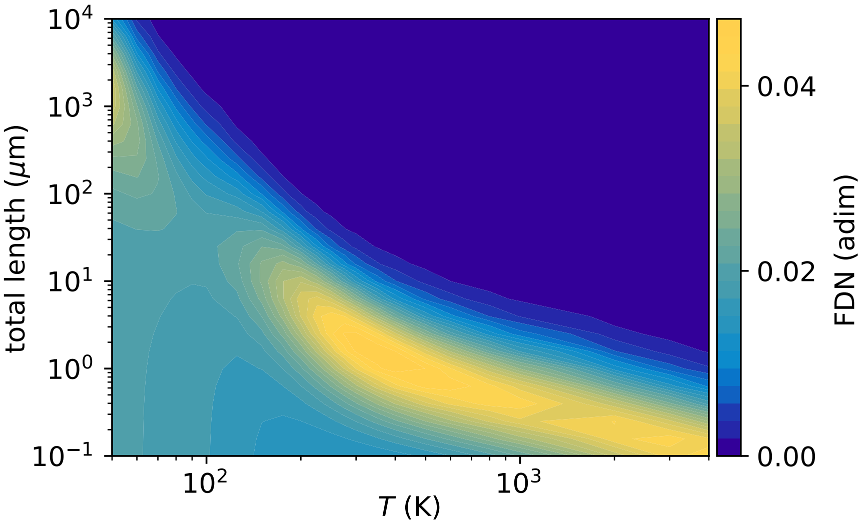

Figure 4.I.1 – Hydrodynamic behavior in crystalline diamond at natural isotopic abundance: increasing the dimension of the diamond sample can yield an increase of the hydrodynamic effects at low temperatures.

The analysis here and in Fig. 4.7.1 are limited to a minimum reference temperature of $\bar{T} = 50$ K because, for lower temperatures, anharmonicity becomes decreasingly smaller while size effects become increasingly larger, resulting in convergence issues for the numerical calculations (which would also require a refined, computationally-expensive, treatment of surface effects [256]). Most importantly, the temperature and size ranges reported in Fig. 4.7.1 highlight the most accessible experimental conditions under which hydrodynamic behavior can appear in diamond, namely micrometer-sized diamond samples (thus much less expensive than millimeter-sized samples) and non-cryogenic temperatures.

4.J Computational details

First-principles calculations are performed with the Quantum ESPRESSO distribution [149, 344]. For all the materials analyzed, the the local-density approximation (LDA) for the exchange-correlation energy functional is employed due to its capability to accurately describe the structural and vibrational [40] properties of graphite [281], diamond [37] and silicon [39], and its compatibility with the D3Q code [41, 161] for first-principles calculations of anharmonic (third-order) interatomic force constants. Details on the computation of the second- and third-order interatomic force constants are reported in Ref. [39] for silicon, in Ref. [37] for diamond and in Ref. [281] for graphite. The LBTE's scattering matrix $\Omega_{\nu\nu'}$ is computed as in Ref. [37] and accounts for third-order anharmonicity [41] and isotopic disorder [33, 137] at natural abundance. Thermal conductivity and viscosity calculations for silicon and diamond are performed using $27\times27\times27$ q-point grids and a Gaussian smearing of 2 cm^{-1} and 8 cm^{-1}, respectively. Thermal conductivity and viscosity calculations for graphite are performed using a $49\times49\times3$ q-point grid and a Gaussian smearing of 8 cm^{-1}. The use of an odd, Gamma-centered q-points mesh is crucial to correctly account for the parity symmetries of the scattering operator.

5 Hydrodynamic heat transport in hBN

This chapter focuses on materials science and discusses preliminary results on the emergence of heat hydrodynamics in hexagonal boron nitride (hBN). Specifically, we compute from first-principles thermal conductivity and viscosity for hBN, and relying on the Fourier Deviation Number (FDN) introduced in Chapter 4, we predict heat hydrodynamics to appear in hBN devices having sizes around 10 μm and at temperatures around 75 K. Relying on the viscous heat equations, we discuss how signatures of heat-hydrodynamic effects are influenced by the isotopic mass disorder of boron. We predict that isotopically pure samples (containing the isotope ^{11}B only) display hydrodynamic effects and deviations from Fourier's law stronger than isotopically disordered samples (with an isotopic disorder corresponding to natural isotopic abundance of boron, 19.9% ^{10}B and 80.1% ^{11}B).

5.1 Introduction

Hexagonal boron nitride (hBN) is a layered material with a structure analogous to that of graphite, but with a wide band gap[1]. It has recently received great attention due to the possibility to be used in combination with graphene or graphite to form heterostructures (see e.g. Refs. [336, 346, 347]).

Thermal transport in graphite has been extensively studied (e.g. Refs. [262, 281] and references therein), and as discussed extensively in Chapter 4, heat hydrodynamics in graphite around 100 K [31] has been recently measured and explained by the viscous heat equations. Conversely, studies on hBN are at an earlier stage. hBN has been shown to have a high room-temperature thermal conductivity ($\gtrsim$ 400 W/m K [347, 348]), which suggests that most of the collisions between phonons are conserving the crystal momentum (*i.e.* normal collisions are much more frequent than Umklapp collisions [14]) — a condition that favors the emergence of heat hydrodynamics.

These observations motivate us to investigate the emergence of hydrodynamic heat transport in hBN, performing on this materials a theoretical analysis based on the viscous heat equations similar to that discussed in Chapter 4.

---

[1] hBN has an indirect band gap equal to 5.95 eV [345].

5.2 Transport coefficients of hBN

hBN is a simple crystal characterized by a 4-atom primitive cell and weak anharmonicity, and we recall that in this regime the Wigner-Boltzmann transport equation (WBTE, Eq. (1.34)) reduces to the linearized Boltzmann transport equation (LBTE, Eq. (1.41)). This statement is demonstrated quantitatively in Tab. 5.B.1 and Tab. 5.B.2, where it is shown that the populations' conductivity computed from an exact variational solution of the populations' equation (1.41) (which is exactly equivalent to the LBTE, see Chapter 1) is at least three orders or magnitude larger than the coherences' conductivity. Therefore, as discussed in Chapter 4, for the description of the simple crystal hBN it is sufficient to consider the Peierls-Boltzmann limit of the WBTE, and this will be the strategy employed in this chapter.

5.2.1 Thermal conductivity

We report in Fig. 5.2.1 the predictions for the in-plane thermal conductivity of hBN obtained from the exact solution of the LBTE (1.41), showing predictions in hBN containing boron at natural isotopic concentration (left, h$^{\text{nat}}$BN) or in monoisotopic hBN containing exclusively the isotope ^{11}B of boron (right, h^{11}BN). We highlight that the presence of isotopic mass disorder for boron causes a significant reduction of the conductivity at low temperature.

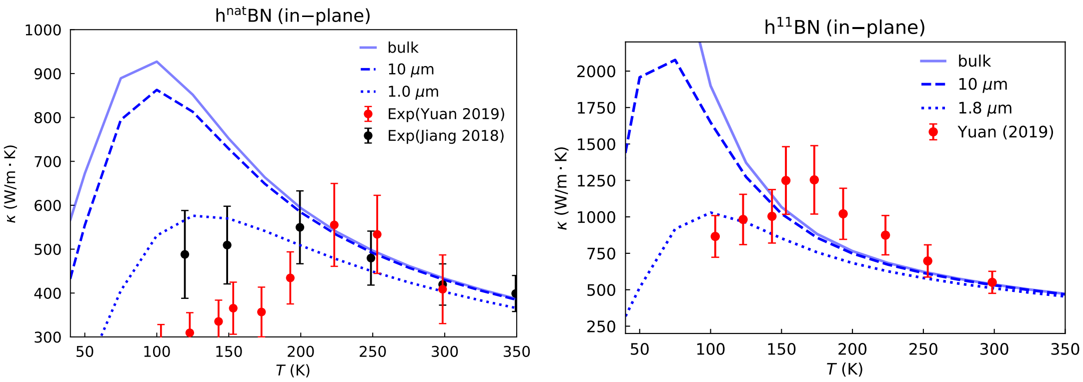

Figure 5.2.1 – **In-plane thermal conductivity of h$^{\text{nat}}$BN (left) and h^{11}BN (right).** Solid lines are predictions for a bulk, defect-free crystal; dashed and dotted lines are predictions that account for finite-size effects, such as scattering with sample's boundaries or grains' boundaries, with a characteristic length around the micrometer (see the legends for details, these extrinsic scattering effects are taken into account following the approximated Matthiessen method discussed in Appendix 4.C). Experimental data are taken from Yuan *et al.* [348] and Jiang *et al.* [347].

We note that theoretical predictions for a bulk crystal (solid lines) are in reasonable agreement with experiments [347, 348] at temperatures larger than 200 K in $h^{nat}BN$ and at temperatures larger than 150 K in $h^{11}BN$. At low temperature, the conductivity is very sensitive to extrinsic scattering of phonons with sample's boundaries, grains' boundaries, and crystal defects such as dislocations, vacancies and carbon impurities (Ref. [348] shows with dark-field transmission electron microscopy images that these extrinsic scattering sources are present in the samples on which the conductivity is measured). Dashed and dotted lines in Fig. 5.2.1 show corrections to the conductivity due to extrinsic scattering sources with different typical lengths (computed according to the approximated Matthiessen method discussed in Appendix 4.C); these corrections explain, at least qualitatively, the trend of the conductivity observed in experiments.

The off-plane conductivity of hBN (Fig. 5.2.2) is about two orders of magnitude lower than the in-plane conductivity, and it is not significantly affected either by the presence of isotopic disorder or by extrinsic scattering sources.

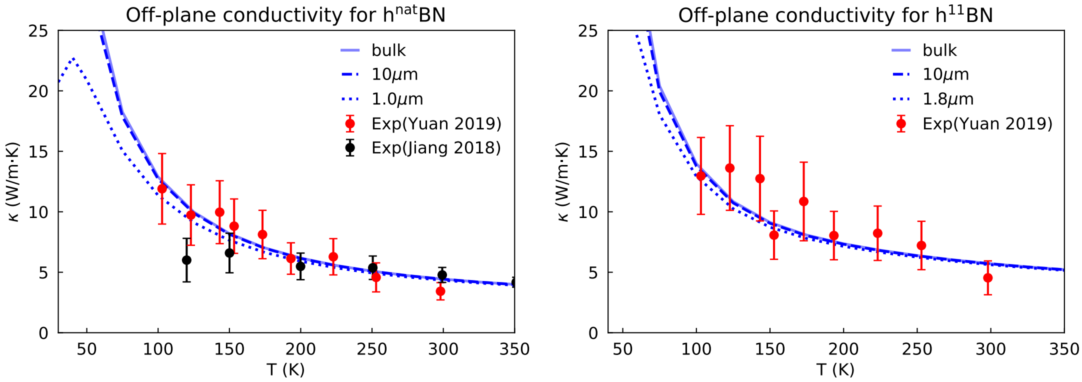

Figure 5.2.2 – **Off-plane thermal conductivity of $h^{nat}BN$ (left) and $h^{11}BN$ (right).** We present results obtained solving exactly the LBTE. Solid lines are predictions for a bulk, defect-free crystal; dashed and dotted lines are predictions that account for finite-size effects, such as scattering with sample's boundaries or grains' boundaries, with a characteristic length around the micrometer (see the legends of the plots for details, these extrinsic scattering effects are taken into account relying on the approximated Matthiessen method discussed in Appendix 4.C). Experimental data are taken from Yuan *et al.* [348] and Jiang *et al.* [347].

5.2.2 Thermal viscosity

We show in Fig. 5.2.3 the first-principles estimates for the in-plane thermal viscosity components of hBN with isotopic mass disorder at natural abundance for boron, or in the presence of monoisotopic ^{11}B only. We see that the presence of isotopic mass disorder has a weak effect on the viscosity (this in contrast with the conductivity, which is strongly affected by the presence of isotopic mass disorder for boron, as shown in Fig. 5.2.1). We note that the viscosity-temperature curves in hBN show an increase with temperature (reminiscent to that observed in graphite, see Fig. 4.3.1), and they are negligibly affected by finite-size effects. We note that the viscosities of hBN are in general smaller (of about a factor 1.5 or 2) than those of graphite.

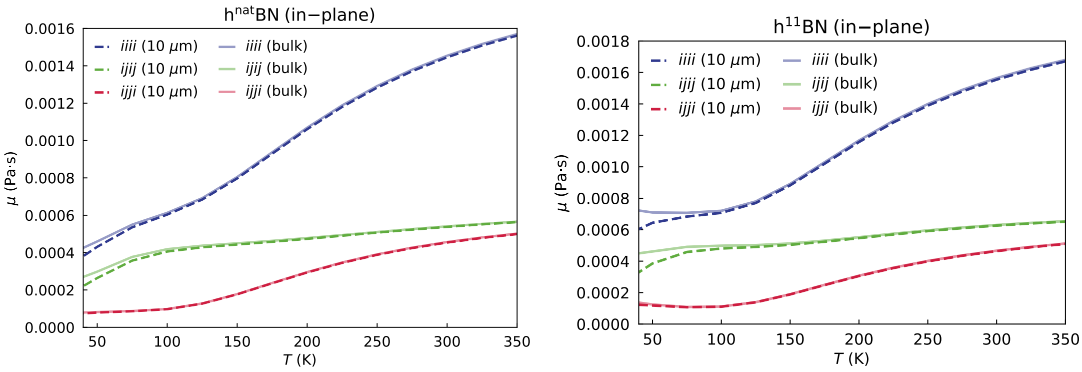

Figure 5.2.3 – **In-plane components of the thermal viscosity of h^{nat}BN (left) and h^{11}BN (right).** Solid lines are predictions for a bulk, defect-free crystal; dashed lines are predictions that account for extrinsic scattering with grain boundaries, for grains having a typical size of 10 micrometers (these extrinsic scattering sources are taken into account following the approximated Matthiessen method discussed in Appendix 4.C).

The off-plane components of the viscosity tensor for hBN are shown for completeness in Fig. 5.2.4, they are lower (roughly of at least a factor of 5) than the in-plane components, and negligibly affected by finite-size effects.

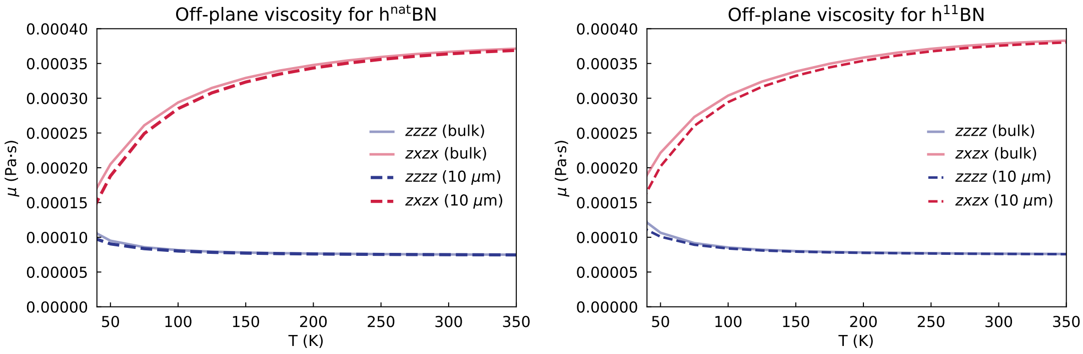

Figure 5.2.4 – **Off-plane components of the thermal viscosity of h^{nat}BN (left) and h^{11}BN (right).** Solid lines are predictions for a bulk, defect-free crystal; dashed lines are predictions that account for extrinsic scattering with grain boundaries, for grains having a typical size of 10 micrometers (these extrinsic scattering effects are taken into account according to the approximated Matthiessen method discussed in Appendix 4.C).

5.3 Heat hydrodynamics in hBN

In Chapter 4 we have introduced the Fourier Deviation Number (FDN, see Sec. 4.7), a descriptor that quantifies deviations from Fourier's law due to heat-hydrodynamic effects. Here, we rely on this descriptor to investigate the emergence of hydrodynamic heat transport in hBN. Specifically, we use the first-principles estimates of thermal conductivity, viscosity, and other parameters entering in the viscous heat equations (see Appendix 5.B) to compute the FDN for devices made of hBN and having exactly the shape discussed in Chapter 4 (Fig. 4.6.1), and thus predict the devices' sizes and temperatures at which hydrodynamic deviations from Fourier's law are maximized. We note that hBN is structurally analogous to graphite, and the tensor coefficients for hBN (e.g. thermal conductivity and viscosity) have exactly the same symmetries of those for graphite discussed in Chapter 4. Therefore, we perform here an analysis for hBN completely analogous to that performed in Chapter 4 for graphite (we refer the reader to Sec. 4.7 for details).

We report in Fig. 5.3.1 the results for FDN in $h^{nat}BN$ and $h^{11}BN$, which predict thermal hydrodynamic effects to be relevant in devices having size of about 10^1 μm and at temperatures around $50-80$ K in both these materials. We note that FDN predicts heat-hydrodynamic effects in monoisotopic $h^{11}BN$ to be stronger and to survive in larger devices compared to $h^{nat}BN$.

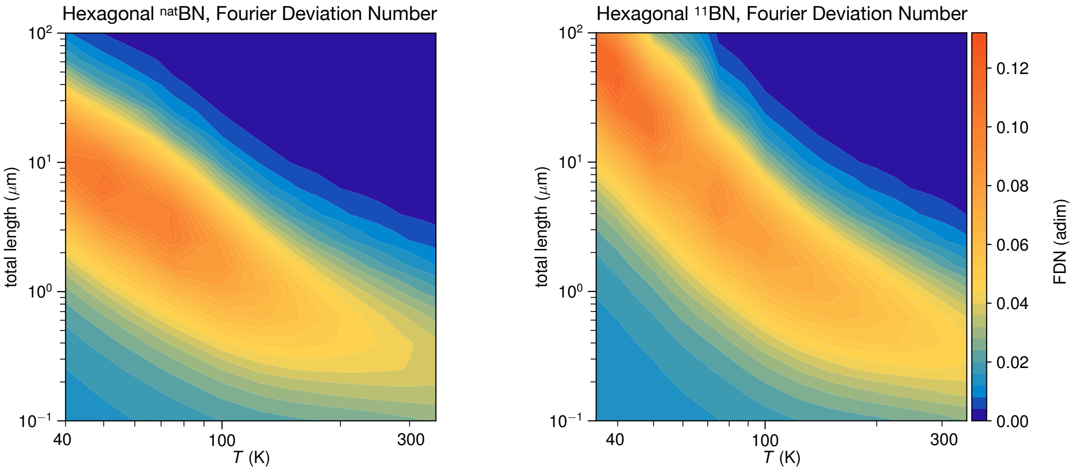

Figure 5.3.1 – **Deviations from Fourier's law in $h^{nat}BN$ and $h^{11}BN$.** The deviations from Fourier's law due to hydrodynamic effects are predicted relying on the Fourier Deviation Number, computed according to Eq. (4.24) for $h^{nat}BN$ (left) and $h^{11}BN$ (right) as a function of temperature and total length of the sample (we employ here the same geometry of Fig. 4.6.1, for which the characteristic size L appearing in FDN is the shortest length-scale, *i.e.* 1/5 of the total length l_{TOT}). We identify the total length $l_{TOT} = 10\mu m$ and temperature $T = 75\ K$ as conditions under which heat-hydrodynamic effects are expected to be relevant in both $h^{nat}BN$ and $h^{11}BN$.

We note that the plots for FND in hBN reported in Fig. 5.3.1 differ from those for graphite reported in Fig. 4.7.1 not only because of the material-dependent values entering in the expression for FDN (Eq. (4.24)), but also because they have been computed relying on different hypothesis concerning the presence of grain-boundary scattering. More precisely, the plots for graphite have been computed considering the presence of grains with typical size 10 μm, to match the experimental conditions of Ref. [31], while the plots for hBN have been computed assuming a single crystal (this because we have not found any experimental result on heat hydrodynamics in a hBN device with a specific grain size and with which we can compare our predictions).

From Fig. 5.3.1 we identify the size of 10 μm and the temperature of 75 K as conditions under which hydrodynamic deviations from Fourier's law are expected to be relevant in both h^{11}BN and h^{nat}BN. Therefore, in the next sections we will investigate the magnitude of these deviations in a device having a characteristic size of 10 μm and at an average temperature of 75 K.

5.3.1 Solution of the viscous heat equations in hBN

We solve the viscous heat equations for a device having the same shape of that discussed in Fig. 4.6.1 in Chapter 4, since such a geometry has been proved to be adequate to show the appearance of heat-hydrodynamic effects. The equations are solved numerically using a finite-element solver implemented in the software Mathematica [313], and the source code used to obtain these solutions has been also made available as a part of the Mathematica software documentation [349]. Fig. 5.3.2 shows the temperature and drift-velocity fields resulting from the numerical solution of the viscous heat equations. We have imposed boundary conditions similar to those discussed for graphite in Chapter 4: temperature is fixed to 85 on the left side ($x = 0\ \mu m$) and to 65 K on the right side ($x = 10\ \mu m$), all boundaries at $x \neq 0$ and $x \neq 10\ \mu m$ are assumed to be adiabatic, and a no-slip condition for the drift velocity ($\boldsymbol{u} = \mathbf{0}$) is imposed at all boundaries. We highlight how in monoisotopic h^{11}BN the drift velocity is larger than in isotopically disordered h^{nat}BN.

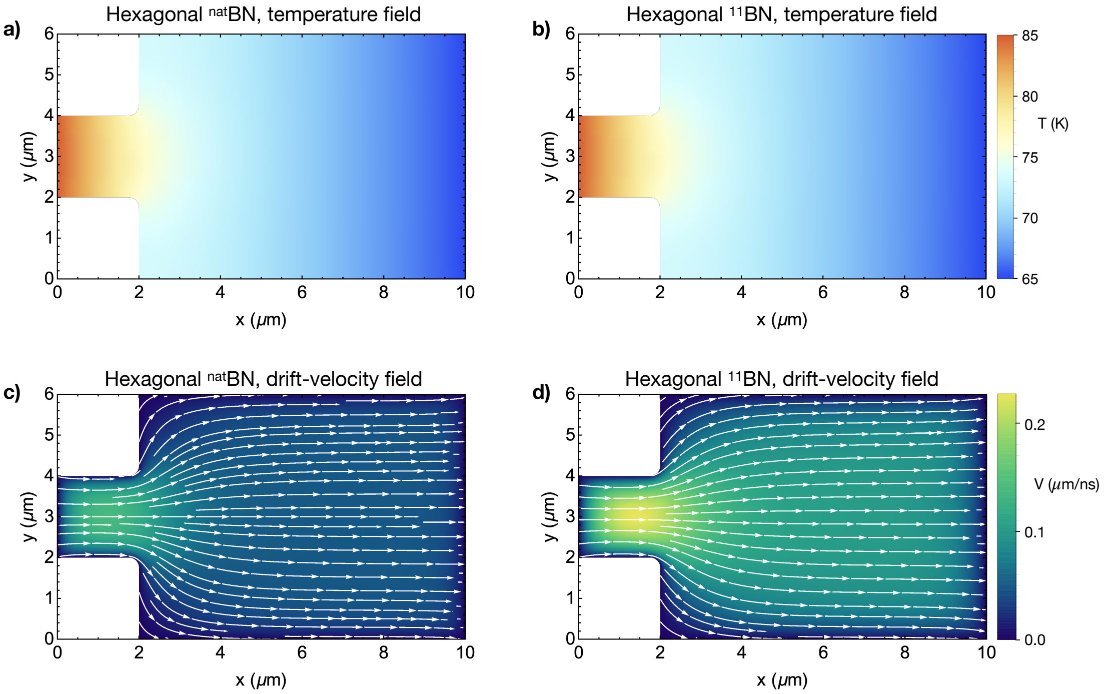

Figure 5.3.2 – **Solution of the viscous heat equations in isotopically disordered or monoisotopic hBN.** The viscous heat equations (4.10, 4.11) are solved imposing the temperature at 85 K (65 K) on the left and right boundaries, a zero total heat flux is imposed at the other boundaries, and zero drift velocity is imposed on all boundaries (no-slip boundary condition). Top row: temperature field obtained from the solution of the viscous heat equations in hBN containing boron isotopes at natural abundance (left, h$^{\text{nat}}$BN) and containing only ^{11}B (right, h^{11}BN). Bottom row, drift-velocity field in h$^{\text{nat}}$BN (left) and in h^{11}BN (right). We highlight that the drift velocity field assumes larger values in h^{11}BN compared to h$^{\text{nat}}$BN, suggesting the appearance of stronger heat-hydrodynamic effects in h^{11}BN.

The total heat flux obtained from the solution of the viscous heat equations as a sum of the heat flux originating from the temperature gradient and that originating from the drift velocity (see Sec. 4.6 in Chapter 4) is shown in Fig. 5.3.3. The heat flux is larger in monoisotopic h^{11}BN compared to h$^{\text{nat}}$BN, this because the former material has higher thermal conductivity (see Fig. 5.2.1) and higher drift velocity (see Fig. 5.3.2) than the latter. These considerations are shown quantitatively in Fig. 5.3.4, where the x-component of the heat flux in the device of Fig. 5.3.3 is shown at $x = 1\ \mu m$ (orange, red) and $x = 6.0\ \mu m$ (blue, green).

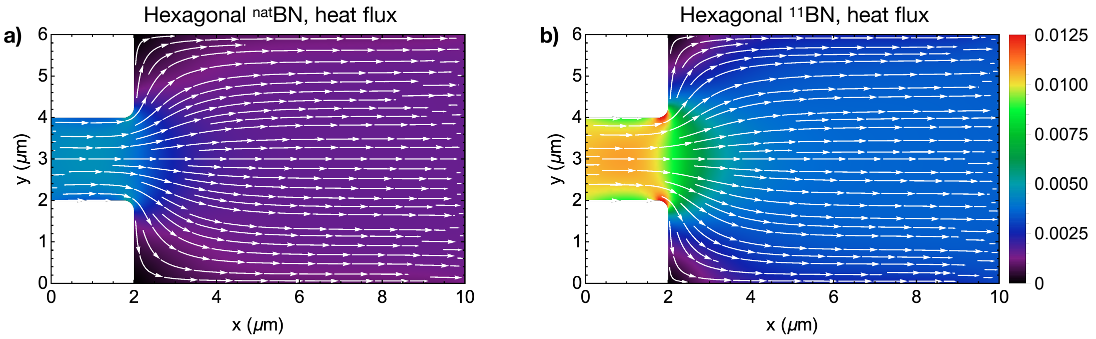

Figure 5.3.3 – **Viscous heat flux in hBN.** In-plane $(x - y)$ heat flux in a device made of $h^{nat}BN$ (left) and $h^{11}BN$ (right) and having applied a temperature of 85 K at $x = 0$ μm and of 65 K at $x = 10$ μm, for a sample infinite in the z direction (the z direction of the sample coincides with the off-plane direction of hBN). We show the total heat flux $(\boldsymbol{Q}^D + \boldsymbol{Q}^\delta)$ obtained from the viscous heat equations (4.10, 4.11).

Fig. 5.3.4 clearly shows the emergence of a Poiseuille-like heat flux profile in hBN devices, a signature of hydrodynamic heat transport. We highlight how such a Poiseuille-like profile is more pronounced in monoisotopic $h^{11}BN$ compared to $h^{nat}BN$, this because the former features larger values of the drift-velocity field compared to the latter (see Fig. 5.3.2), and the drift velocity is linearly related to the drifting component of the heat flux $\boldsymbol{Q}^D$, see Eq. (4.71).

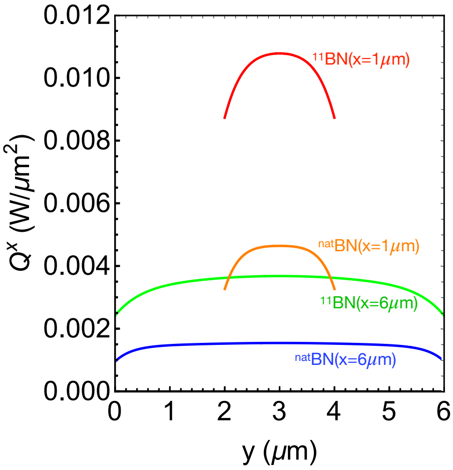

Figure 5.3.4 – **Poiseuille heat flux in hBN.** x-component of the heat flux obtained solving the viscous heat equation for the device of Fig. 5.3.3, shown along the sections $x = 1$ μm (orange, red) and $x = 6.0$ μm (blue, green). The paraboliclike profile for the heat flux is a signature of heat hydrodynamics [19].

5.3.2 Hydrodynamic deviations from Fourier's law

In this section we discuss the effects of hydrodynamic deviations from Fourier's law on the temperature field. In Fig. 5.3.5 we plot the difference between the temperature profile predicted by Fourier's law and the viscous heat equations. Similarly to the case of graphite discussed in Chapter 4, deviations from Fourier's law are maximized in proximity of variations of the sample's shape, with Fourier's law predicting a warmer temperature in these regions. We also note that the stronger hydrodynamic effects observed in the drift velocity and total heat flux of h^{11}BN compared to h$^{\mathrm{nat}}$BN, result here in a stronger temperature deviation (between Fourier's law and viscous heat equations) in h^{11}BN compared to h$^{\mathrm{nat}}$BN.

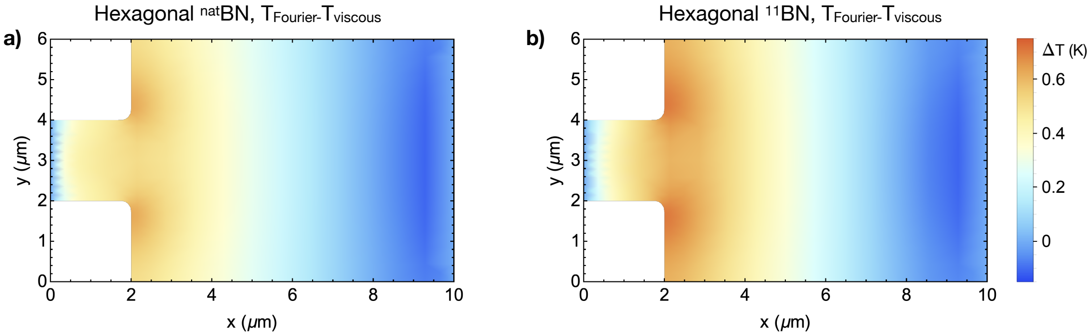

Figure 5.3.5 – **Temperature deviations from Fourier's law in h$^{\mathrm{nat}}$BN and h^{11}BN.** The color map shows the difference between the temperature field predicted by Fourier's law and that predicted by the viscous heat equations. Deviations from Fourier's law are larger in h^{11}BN than in h$^{\mathrm{nat}}$BN.

5.4 Conclusions

We have computed from first-principles the thermal conductivity, viscosity, and other parameters entering in the viscous heat equations for hBN at various isotopic concentration of boron (*i.e.* natural concentration of isotopes and monoisotopic ^{11}B). We have used these parameters to compute the Fourier Deviation Number (FDN) and predict the temperatures and devices' sizes at which heat-hydrodynamic effects are maximized. We have predicted hydrodynamic deviations from Fourier's law to appear in hBN devices having sizes around 10 μm and at temperatures around 75 K, and to be larger in monoisotopic hBN containing ^{11}B only.

Appendix

5.A Computational details

First-principles calculations have been performed with the Quantum ESPRESSO distribution [149, 344] using the the local-density approximation (LDA) for the exchange-correlation energy functional, since it has been shown to accurately describe the vibrational and thermal properties of hBN [347, 348, 350]. The pseudopotentials have been taken from the pseudo Dojo library [351] (specifically, we have used norm-conserving and scalar-relativistic pseudopotentials with accuracy "stringent" and of type ONCVPSP v0.4). The crystal structure of hBN has been taken from [352] (Crystallographic Open Database [159] id 2016170). Kinetic energy cutoffs of 90 and 360 Ry have been used for the wave functions and for the charge density; the Brillouin zone (BZ) is integrated with a Monkhorst-Pack mesh of 8×8×3 points, with a (1,1,1) shift. The equilibrium crystal structure has been computed performing a "vc-relax" calculation with Quantum ESPRESSO and the DFT-optimized lattice parameters are $a = 2.489089$ Å and $c/a = 2.604045$. Second-order force constants have been computed on a 8×8×3 mesh using density-functional perturbation theory [40] and accounting for the non-analytic term correction due to the dielectric tensor and Born effective charges. Third-order force constants have been computed using the finite-difference method implemented in ShengBTE [68], on a 4×4×2 supercell, integrating the BZ with a 2×2×1 Monkhorst-Pack mesh, and considering interactions up to 3.944 Å (which corresponds to the 6th nearest neighbor). Then, anharmonic force constants have been converted from SHENGBTE format to `mat3R` format using the interconversion software `d3_import_shengbte.x` provided with the D3Q package [41, 161], including interactions up to the second neighbouring cell for the re-centering of the third-order force constants (parameter NFAR=2). Thermal conductivity calculations have been performed as in Ref. [39, 66], using a q-point mesh equal to 49×49×3 and a Gaussian smearing of 6 cm^{-1}. The use of an odd, Gamma-centered q-points mesh is crucial to correctly account for the parity symmetries of the scattering operator. Third-order anharmonicity is calculated as detailed in Refs. [37, 39]. Scattering due to isotopic mass disorder is taken into account as detailed in Refs. [33, 137]. The effect of the mass of boron has been taken into account also in the computation of the dynamical matrix (1.19), and we show in Fig. 5.A.1 that changing the mass of boron from the natural-abundance weighted average (10.811 u) to the mass of isotopically pure ^{11}B (11.009 u) has a weak but visible effect on the phonon dispersion.

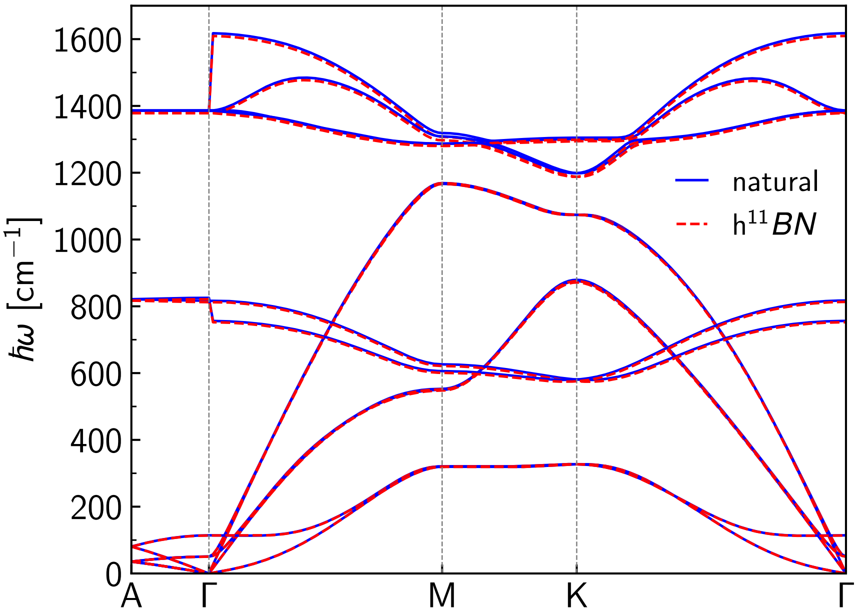

Figure 5.A.1 – **Phonon dispersion relation of hBN.** Blue lines are the phonon bands obtained using the natural-abundance isotopic average mass of boron (10.811 u), while dashed red lines are obtained using the mass of isotopically pure ^{11}B (11.009 u).

5.B Parameters entering in the viscous heat equations for hBN

In this appendix we report the parameters computed from first-principles that enter in the viscous heat equations. Numerical values for the in-plane parameters are reported in Tab. 5.B.1 and Tab. 5.B.2, and a plot of these parameters is shown in Fig. 5.B.1.

Finally, the off-plane parameters (not used in this chapter) are reported for completeness in Fig. 5.B.2.

Table 5.B.1 – Parameters entering the viscous heat equations for h$^{\mathrm{nat}}$BN . We report here only the in-plane components of the tensors needed to perform the calculations of this chapter: $\kappa_{\mathrm{P}}^{ij} = \kappa_{\mathrm{P}}\delta^{ij}$, $\kappa_{\mathrm{C}}^{ij} = \kappa_{\mathrm{C}}\delta^{ij}$, $K_S^{ij} = K_S\delta^{ij}$, $D_{U,\mathrm{bulk}}^{ij} = D_{U,\mathrm{bulk}}\delta^{ij}$, $F_U^{ij} = F_U\delta^{ij}$, $A = A^i\ \forall\ i$, $W_{0i}^{j} = W_{i0}^{j} = W\delta^{ij}$, where the indexes i, j represent the in-plane directions x, y only ($i, j = 1,2$ and $i \neq j$).

T [K]	$\kappa_{\mathrm{P}}\ [\frac{\mathrm{W}}{\mathrm{m\cdot K}}]$	$\kappa_{\mathrm{C}}\ [\frac{\mathrm{W}}{\mathrm{m\cdot K}}]$	$K_S\ [\frac{\mathrm{W}}{\mathrm{m^2\cdot K}}]$	$\mu_{\mathrm{bulk}}^{iiii}$ [Pa·s]	$\mu_{\mathrm{bulk}}^{ijij}$ [Pa·s]	$\mu_{\mathrm{bulk}}^{ijji}$ [Pa·s]	$M^{iiii}\ [\frac{\mathrm{Pa\cdot s}}{\mathrm{m}}]$	$M^{ijij}\ [\frac{\mathrm{Pa\cdot s}}{\mathrm{m}}]$	$M^{ijji}\ [\frac{\mathrm{Pa\cdot s}}{\mathrm{m}}]$	$D_{U,\mathrm{bulk}}$ [ns^{-1}]	$F_U\ [\frac{\mathrm{m}}{\mathrm{s}}]$	A $[\frac{\mathrm{pg}}{\mu\mathrm{m}^3}]$	$C\ [\frac{\mathrm{pg}}{\mu\mathrm{m\cdot ns^2\cdot K}}]$	W $[\frac{\mu\mathrm{m}}{\mathrm{ns}}]$
40	5.67154e+02	2.65369e-04	1.84499e+08	4.25337e-04	2.69685e-04	7.92792e-05	3.62741e+02	1.21147e+02	1.20797e+02	1.48608e+00	3.47818e+03	1.54296e-04	9.52842e-05	2.18733e+00
50	6.72272e+02	4.93959e-04	3.16604e+08	4.59689e-04	2.98115e-04	8.18756e-05	6.90538e+02	2.31011e+02	2.29761e+02	2.13504e+00	3.71653e+03	2.70383e-04	1.48212e-04	2.40589e+00
75	8.89306e+02	1.59667e-03	7.45117e+08	5.49953e-04	3.76979e-04	8.72434e-05	2.02339e+03	6.81105e+02	6.71099e+02	4.66381e+00	4.02352e+03	7.12520e-04	3.02610e-04	2.71303e+00
100	9.27156e+02	4.90182e-03	1.24293e+09	6.13010e-04	4.18581e-04	9.78760e-05	3.89572e+03	1.32585e+03	1.28476e+03	1.03142e+01	4.11088e+03	1.32868e-03	4.69695e-04	2.80149e+00
125	8.51774e+02	1.29586e-02	1.78072e+09	6.91607e-04	4.37306e-04	1.27753e-04	6.08263e+03	2.10636e+03	1.98769e+03	2.03117e+01	4.14043e+03	2.05466e-03	6.41591e-04	2.79201e+00
150	7.51849e+02	2.65701e-02	2.35094e+09	8.04663e-04	4.49990e-04	1.77875e-04	8.46251e+03	2.99492e+03	2.73289e+03	3.40018e+01	4.16174e+03	2.84839e-03	8.18582e-04	2.73903e+00
175	6.63624e+02	4.45417e-02	2.94131e+09	9.37165e-04	4.63196e-04	2.37450e-04	1.09762e+04	3.97531e+03	3.49888e+03	5.01522e+01	4.18488e+03	3.68679e-03	9.99455e-04	2.67099e+00
200	5.93644e+02	6.51044e-02	3.53653e+09	1.06894e-03	4.78169e-04	2.95770e-04	1.35898e+04	5.03229e+03	4.27633e+03	6.78115e+01	4.21005e+03	4.55615e-03	1.18160e-03	2.60159e+00
225	5.39251e+02	8.68080e-02	4.12317e+09	1.18840e-03	4.94280e-04	3.47368e-04	1.62800e+04	6.15078e+03	5.06110e+03	8.64099e+01	4.23571e+03	5.44754e-03	1.36263e-03	2.53587e+00
250	4.96383e+02	1.08706e-01	4.69140e+09	1.29190e-03	5.10555e-04	3.90899e-04	1.90288e+04	7.31703e+03	5.85112e+03	1.05618e+02	4.26050e+03	6.35478e-03	1.54077e-03	2.47490e+00
275	4.61690e+02	1.30249e-01	5.23477e+09	1.37982e-03	5.26209e-04	4.26964e-04	2.18220e+04	8.51936e+03	6.64520e+03	1.25220e+02	4.28357e+03	7.27347e-03	1.71476e-03	2.41843e+00
300	4.32798e+02	1.51134e-01	5.74943e+09	1.45407e-03	5.40758e-04	4.56745e-04	2.46483e+04	9.74827e+03	7.44244e+03	1.45054e+02	4.30451e+03	8.20042e-03	1.88359e-03	2.36599e+00
325	4.08115e+02	1.71203e-01	6.23338e+09	1.51676e-03	5.53981e-04	4.81423e-04	2.74988e+04	1.09963e+04	8.24213e+03	1.64981e+02	4.32322e+03	9.13327e-03	2.04641e-03	2.31723e+00
350	3.86584e+02	1.90374e-01	6.68593e+09	1.56985e-03	5.65828e-04	5.01991e-04	3.03664e+04	1.22577e+04	9.04362e+03	1.84888e+02	4.33976e+03	1.00702e-02	2.20253e-03	2.27192e+00

Table 5.B.2 – Parameters entering the viscous heat equations for $h^{11}BN$. We report here only the in-plane components of the tensors needed to perform the calculations of this chapter: $\kappa_P^{ij} = \kappa_P\delta^{ij}$, $\kappa_C^{ij} = \kappa_C\delta^{ij}$, $K_S^{ij} = K_S\delta^{ij}$, $D_{U,\mathrm{bulk}}^{ij} = D_{U,\mathrm{bulk}}\delta^{ij}$, $F_U^{ij} = F_U\delta^{ij}$, $A = A^i\ \forall\ i$, $W_{0i}^{j} = W_{i0}^{j} = W\delta^{ij}$, where the indexes i, j represent the in-plane directions x, y only ($i, j = 1,2$ and $i \neq j$).

T [K]	$\kappa_P\,[\frac{W}{m\cdot K}]$	$\kappa_C\,[\frac{W}{m\cdot K}]$	$K_S\,[\frac{W}{m^2\cdot K}]$	$\mu_{\mathrm{bulk}}^{iiii}$ [Pa·s]	$\mu_{\mathrm{bulk}}^{ijij}$ [Pa·s]	$\mu_{\mathrm{bulk}}^{ijji}$ [Pa·s]	$M^{iiii}\,[\frac{Pa\cdot s}{m}]$	$M^{ijij}\,[\frac{Pa\cdot s}{m}]$	$M^{ijji}\,[\frac{Pa\cdot s}{m}]$	$D_{U,\mathrm{bulk}}$ [ns^{-1}]	$F_U\,[\frac{m}{s}]$	A $[\frac{pg}{\mu m^3}]$	$C\,[\frac{pg}{\mu m\cdot ns^2\cdot K}]$	W $[\frac{\mu m}{ns}]$
40	6.48174e+03	2.43778e-04	1.85577e+08	7.21973e-04	4.49708e-04	1.36473e-04	3.66676e+02	1.22462e+02	1.22106e+02	1.03061e-01	3.47088e+03	1.56256e-04	9.59673e-05	2.18404e+00
50	5.08496e+03	4.39299e-04	3.18233e+08	7.09609e-04	4.61623e-04	1.24381e-04	6.97634e+02	2.33387e+02	2.32121e+02	3.15987e-01	3.70983e+03	2.73574e-04	1.49113e-04	2.40299e+00
75	2.87382e+03	1.19669e-03	7.48233e+08	7.07296e-04	4.91045e-04	1.08615e-04	2.04154e+03	6.87240e+02	6.77105e+02	1.93310e+00	4.01963e+03	7.19449e-04	3.03986e-04	2.71119e+00
100	1.89907e+03	2.58860e-03	1.24792e+09	7.20155e-04	4.98382e-04	1.11402e-04	3.92792e+03	1.33705e+03	1.29525e+03	5.71441e+00	4.10962e+03	1.33990e-03	4.71727e-04	2.79944e+00
125	1.37164e+03	5.21646e-03	1.78806e+09	7.79727e-04	5.01978e-04	1.39347e-04	6.13109e+03	2.12395e+03	2.00311e+03	1.19136e+01	4.14080e+03	2.07076e-03	6.44647e-04	2.78843e+00
150	1.06699e+03	9.66905e-03	2.36077e+09	8.91251e-04	5.12533e-04	1.89739e-04	8.52906e+03	3.02013e+03	2.75353e+03	2.02022e+01	4.16302e+03	2.86999e-03	8.22855e-04	2.73368e+00
175	8.83008e+02	1.62740e-02	2.95342e+09	1.02915e-03	5.30428e-04	2.49625e-04	1.10622e+04	4.00902e+03	3.52496e+03	3.01303e+01	4.18665e+03	3.71435e-03	1.00492e-03	2.66425e+00
200	7.65123e+02	2.51062e-02	3.55061e+09	1.16741e-03	5.52319e-04	3.07683e-04	1.36961e+04	5.07502e+03	4.30804e+03	4.13328e+01	4.21210e+03	4.58997e-03	1.18813e-03	2.59391e+00
225	6.83803e+02	3.60584e-02	4.13896e+09	1.29214e-03	5.74869e-04	3.58660e-04	1.64072e+04	6.20280e+03	5.09861e+03	5.35343e+01	4.23792e+03	5.48778e-03	1.37008e-03	2.52756e+00
250	6.23329e+02	4.88988e-02	4.70873e+09	1.39919e-03	5.95930e-04	4.01553e-04	1.91773e+04	7.37844e+03	5.89459e+03	6.65173e+01	4.26281e+03	6.40150e-03	1.54901e-03	2.46616e+00
275	5.75413e+02	6.33176e-02	5.25353e+09	1.48916e-03	6.14491e-04	4.37170e-04	2.19921e+04	8.59015e+03	6.69477e+03	8.01021e+01	4.28596e+03	7.32669e-03	1.72367e-03	2.40940e+00
300	5.35638e+02	7.89685e-02	5.76951e+09	1.56429e-03	6.30300e-04	4.66758e-04	2.48404e+04	9.82843e+03	7.49827e+03	9.41385e+01	4.30696e+03	8.26014e-03	1.89306e-03	2.35678e+00
325	5.01567e+02	9.55019e-02	6.25468e+09	1.62704e-03	6.43502e-04	4.91475e-04	2.77130e+04	1.10858e+04	8.30433e+03	1.08503e+02	4.32573e+03	9.19946e-03	2.05633e-03	2.30792e+00
350	4.71776e+02	1.12591e-01	6.70835e+09	1.67963e-03	6.54418e-04	5.12263e-04	3.06029e+04	1.23564e+04	9.11232e+03	1.23095e+02	4.34233e+03	1.01428e-02	2.21279e-03	2.26256e+00

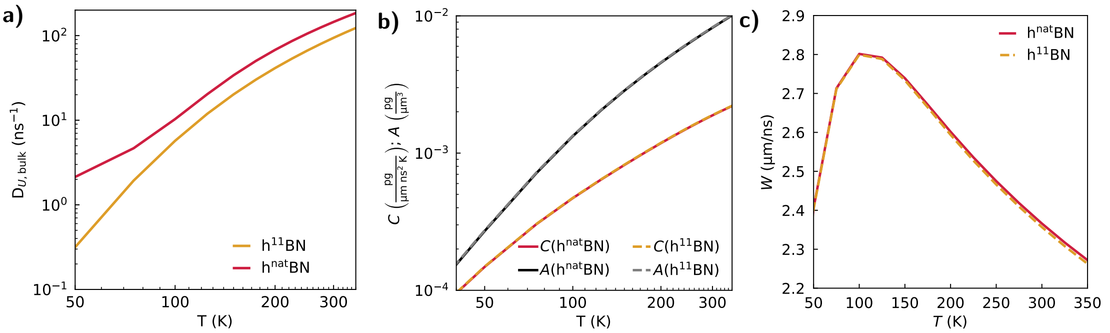

Figure 5.B.1 – **Trends as a function of the temperature of various quantities reported in Tabs. 5.B.1, 5.B.2.** Panel a), values of the bulk momentum dissipation inverse timescale $D_{U,\mathrm{bulk}}(T)$ (Eq. (4.12) with i=j=1); we highlight how the presence of isotopes of boron at natural abundance results in a stronger dissipation of crystal momentum (*i.e.* a larger $D_{U,\mathrm{bulk}}(T)$). Panel b), specific heat $C(T)$ (Eq. (4.33)) and specific momentum $A(T)$ (Eq. (4.39) with i=1). Panel c), values of the velocity $W(T)$ (Eq. (4.68) with j=1, α=1, β=0).

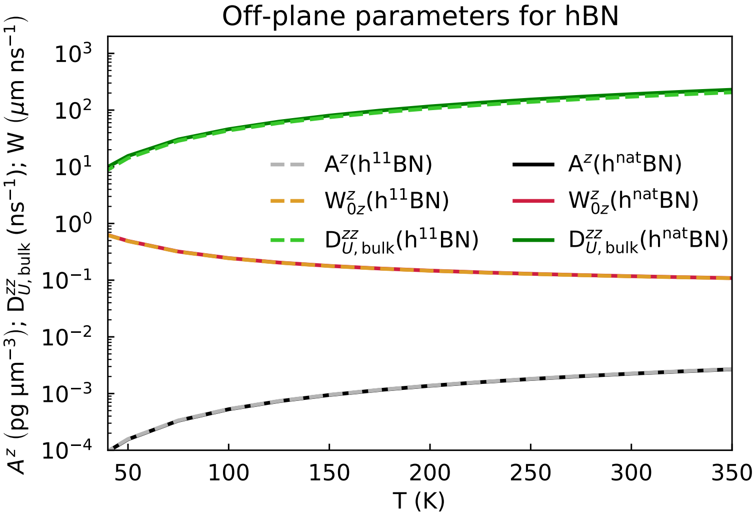

Figure 5.B.2 – **Off-plane parameters entering in the viscous heat equations for hBN.** We use “h$^{\mathrm{nat}}$BN” and “h^{11}BN” to refer to layered hexagonal boron nitride containing boron at natural isotopic concentration (19.9% ^{10}B and 80.1% ^{11}B) or only the isotope ^{11}B, respectively. We recall that the off-plane direction (z) is indexed with the number 3. We show the component of the specific momentum A^z (dashed gray for h^{11}B and solid black for h$^{\mathrm{nat}}$B, computed from Eq. (4.39) with i=3), the velocity-tensor component W^z_{0z} (dashed orange for h^{11}B and solid red for h$^{\mathrm{nat}}$BN, computed from Eq. (4.68) with j=3, α=0, β=3), and the momentum-dissipation-tensor component $D^{zz}_{U,\mathrm{bulk}}$ (dashed light green for h^{11}BN and solid dark green for h$^{\mathrm{nat}}$BN, computed from Eq. (4.12) with i=j=3).

Conclusions Part III

Conclusions

In this thesis we have investigated the physics underlying thermal transport both at the microscopic and mesoscopic level, *i.e.* at the levels where atomic vibrations can be resolved and where only the evolution of statistical averages (e.g. temperature) are relevant, respectively. We have elucidated how the macroscopic Fourier's heat equation for the temperature and the microscopic Peierls-Boltzmann equation for the quantum atomic vibrational excitations (phonons) can be extended to enlarge their domain of applicability.

Specifically, starting from the Wigner formulation of quantum mechanics, we have derived a microscopic equation that describes thermal transport in very general terms and covers on the same footing crystalline, amorphous, and glassy materials. This novel Wigner transport equation generalizes the Peierls-Boltzmann transport equation introduced in 1929, and naturally adds a tunnelling term to the diffusion and scattering of phonon wavepackets. We have shown that tunnelling is essential to describe correctly transport in materials that are engineered to be poor thermal conductors, such as thermoelectrics and thermal barrier coatings. We have shown the predictive accuracy of this formulation by calculating from first-principles the thermal conductivity of complex zirconates (used for thermal barrier coatings) and perovskites (used for thermoelectric devices), highlighting the agreement with experiments at increasing temperatures, where the tunnelling term dominates and offsets the incorrect T^{-1} decay of Peierls-Boltzmann conductivity. We have shown that it is necessary to adopt an appropriated ("Wallace" [76]) phase convention for the Wigner distribution in order to obtain a size-consistent conductivity.

We have relied on the Wigner transport equation to investigate how the interplay between the quantum statistics of atomic vibrations, disorder, and anharmonicity affects the thermal properties of disordered solids, analyzing vitreous silica as a paradigmatic case of a glass. At low temperatures, the quantum Bose-Einstein statistics of vibrations determines the increasing trend of the conductivity with temperature, and in this regime theoretical predictions reproduce the trend observed in experiments. Increasing temperature (and thus the anharmonic linewidths), the conductivity predicted from the Wigner transport equation displays a trend that saturates with temperature, while the temperature-conductivity curve measured in experiments shows an increasing trend. Such a discrepancy at high temperatures might be due to not accounting for radiative energy transfer in the Wigner formulation derived and employed here, and the investigation of such an effect will be subject of future theoretical

work.
We have shown that in vitreous silica the conductivity predicted from the harmonic Allen-Feldman theory is compatible with predictions from the anharmonic Wigner transport equation introduced in this thesis. This is not surprising at low temperatures, where anharmonicity phases out and the Wigner conductivity formula reduces analytically to the harmonic Allen-Feldman conductivity. Instead, in the high temperature regime, we have shown that the anharmonic linewidths become larger but have a negligible effect on the conductivity of vitreous silica. We have rationalized such a negligible effect, showing that at high temperature the conductivity of glasses can be resolved in terms of a Lorentzian weighted average of couplings (off-diagonal elements of the velocity operator) between vibrational eigenstates with different energy. Since in this average the broadening of the Lorentzian is given by the anharmonic linewidths, increasing temperature corresponds to use a broader Lorentzian distribution[2], which weights more velocity-operator elements with larger energy differences when determining the conductivity. We have shown that for vitreous silica the velocity-operator elements are approximately constant with respect to the energy difference between the eigenstates coupled, implying that their Lorentzian weighted average is not significantly affected by the broadening, thus by anharmonicity.
We have introduced an "anharmonic thermal diffusivity", a quantity that allows to interpret heat conduction in glasses microscopically and accounting for anharmonicity, disorder, and the quantum Bose-Einstein statistics of atomic vibrations. Finally, we have discussed how the anharmonic diffusivity allows to characterize the microscopic length scale of heat transport in disordered materials, finding the signature of a phonon liquid in vitreous silica, with vibrations' mean free paths determined by the disorder length scale and thus independent from energy. Future work will focus on studying the trend of the temperature-conductivity curve of amorphous systems at cryogenic temperatures (below 30 K) combining the methodology discussed here with state-of-the-art models of amorphous silicon [214, 215, 353].

We have discussed the emergence of an exotic trend for the temperature-conductivity curve in the silica polymorph meteoritic low tridymite, predicting a trend intermediate between the decreasing trend of the crystalline polymorph α-quartz and the increasing trend of the glassy polymorph vitreous silica. This prediction, which awaits experimental confirmation, suggests future studies on the possibility to engineer the trend of the temperature-conductivity curve in materials by varying their structural disorder (*i.e.* the size of their primitive cell).

The microscopic insights presented here, on the interplay between anharmonicity and disorder in determining the thermal properties of materials, will potentially be relevant to the following technological applications: (i) for thermoelectric energy harvesting, allowing e.g. to investigate how to enhance the efficiency of devices used for thermoelectric conversion of waste heat into electricity; (ii) for thermal barrier coatings, since the microscopic theory developed here could be combined with high-throughput computational screening and provide novel design strategies for materials with ultralow thermal conductivity; (iii) for gas storage technologies, where porous materials with ultralow conductivity [118] are employed, and thermal properties are very important for managing the energy exchanged during the adsorption and desorption processes [119]; (iv) for devices relying on “phase-change materials”, *i.e.* materials in which heat is used to change the atomic structure from crystalline to glassy (and vice-versa), and the change of the electrical resistance between the crystalline and glassy structure is used for memory storage or neuro-inspired computing [354, 355, 356, 357]; (v) in piezoelectric sensors at high temperature, since these sensors are made of complex crystals having ultralow thermal conductivity and for which the microscopic theory discussed in this thesis has been shown to be relevant [120, 121].

---

[2] We recall that increasing temperature yields an increase in the linewidths

In the second part of this thesis we have focused on the hydrodynamic regime of thermal transport, where heat propagation resembles fluid dynamics. Signatures of an hydrodynamic behavior for heat are the appearance of second sound (*i.e.* heat propagation as a temperature wave) or Poiseuille heat flow (*i.e.* heat flow having a paraboliclike profile akin to the profile of the velocity field of a fluid flowing in a pipe); importantly, Fourier’s heat equation is limited to a diffusive description of heat transfer and fails to describe these phenomena. The hydrodynamic regime appears in simple crystals characterized by phonon interband spacings much larger than the linewidths, conditions under which the microscopic Wigner transport equation becomes equivalent to the Peierls-Boltzmann equation. Therefore, we have considered the Peierls-Boltzmann limit of the microscopic Wigner transport equation, and we have relied on the recently introduced relaxon kinetic theory for thermal transport [39] to show that a viscosity for heat emerges from the solution of the microscopic Peierls-Boltzmann equation, and it has a complementary role to the thermal conductivity, since the former is determined exclusively from the even part of the microscopic solution, while the latter is determined exclusively from the odd part of the microscopic solution. We have exploited microscopic (quasi) conservation laws to condense the physics described by the complex (integro-differential) microscopic Peierls-Boltzmann equation into a set of much simpler but equally-accurate mesoscopic differential equations, called “viscous heat equations”, which generalize Fourier’s equation accounting for both heat diffusion and hydrodynamics. We have introduced the Fourier deviation number, a descriptor that captures the deviations between the viscous heat equations and Fourier’s law due to hydrodynamic effects. We have shown that for graphitic devices the hydrodynamic behavior for heat predicted from the viscous heat equations lines up closely with recent experimental measurements [31]. We have also discussed how the appearance of signatures of hydrodynamic heat transport in a device is influenced by its chemical composition, size, and temperature. Importantly, we have predicted that hydrodynamic behavior for heat could potentially emerge in devices made of layered hexagonal boron nitride (in the in-plane direction), at sizes around 10 μm and at temperatures around 75 K. Finally, the viscous heat equations could be relevant for technological applications, since hydrodynamic heat propagation emerges in materials for next-generation electronic devices such as graphene and graphite, and could potentially be exploited to overcome thermal challenges that limit miniaturization and efficiency.

Bibliography

[1] Pop, E., Sinha, S. & Goodson, K. E. Heat Generation and Transport in Nanometer-Scale Transistors. *Proc. IEEE* **94**, 1587–1601 (2006).

[2] Balandin, A. A. *et al.* Superior thermal conductivity of single-layer graphene. *Nano Lett.* **8**, 902–907 (2008).

[3] Balandin, A. A. Thermal properties of graphene and nanostructured carbon materials. *Nat. Mater.* **10** (2011).

[4] Snyder, G. J. & Toberer, E. S. Complex thermoelectric materials. *Nat. Mater.* **7**, 105–114 (2008).

[5] Ali, R., Shehbaz, T. & Bemporad, E. Investigation on failure in thermal barrier coatings on gas turbine first-stage rotor blade. *J. Fail. Anal. Prev.* **18**, 1062–1072 (2018).

[6] Southwest airlines engine explosion linked to prior accident. *BBC news article* URL https://www.bbc.com/news/world-us-canada-43818752.

[7] Cahill, D. G. *et al.* Nanoscale thermal transport. ii. 2003–2012. *Appl. Phys. Rev.* **1**, 011305 (2014).

[8] Zou, L. *et al.* Current approaches of photothermal therapy in treating cancer metastasis with nanotherapeutics. *Theranostics* **6**, 762 (2016).

[9] Aristotle, i. & commentary by W. D. Ross. *Aristotle's Metaphysics* (Oxford: Clarendon Press, 1924.).

[10] Fourier, J. *Theorie analytique de la chaleur* (Chez Firmin Didot, père et fils, 1822).

[11] Peierls, R. E. Zur kinetischen theorie der wärmeleitung in kristallen. *Annalen der Physik* **395**, 1055–1101 (1929).

[12] Peierls, R. E. *Quantum theory of solids* (Oxford Classics Series, 2001).

[13] Ashcroft, N. W. & Mermin, N. D. *Solid State Physics* (Holt-Saunders, 1976).

[14] Ziman, J. M. *Electrons and phonons: the theory of transport phenomena in solids* (Oxford Univ. Press, Oxford, 1960).

[15] Iafrate, G. J., Sokolov, V. N. & Krieger, J. B. Quantum transport and the wigner distribution function for bloch electrons in spatially homogeneous electric and magnetic fields. *Phys. Rev. B* **96**, 144303 (2017).

[16] Hardy, R. J. Energy-Flux Operator for a Lattice. *Phys. Rev.* **132**, 168–177 (1963).

[17] Mezhov-Deglin, L. Measurement of the thermal conductivity of crystalline He^4. *Soviet Phys. JETP* **22** (1966).

[18] Ackerman, C. C., Bertman, B., Fairbank, H. A. & Guyer, R. A. Second sound in solid helium. *Phys. Rev. Lett.* **16**, 789–791 (1966).

[19] Guyer, R. A. & Krumhansl, J. A. Thermal conductivity, second sound, and phonon hydrodynamic phenomena in nonmetallic crystals. *Phys. Rev.* **148**, 778–788 (1966).

[20] Gurzhi, R. Thermal conductivity of dielectrics and ferrodielectrics at low temperatures. *J. Exp. Theor. Phys.* **46** (1964).

[21] Gurzhi, R. N. Hydrodynamic effects in solids at low temperature. *Sov. Phys. Uspekhi* **11**, 255–270 (1968).

[22] Guyer, R. A. & Krumhansl, J. A. Solution of the linearized phonon boltzmann equation. *Phys. Rev.* **148**, 766–778 (1966).

[23] Sussmann, J. A. & Thellung, A. Thermal Conductivity of Perfect Dielectric Crystals in the Absence of Umklapp Processes. *Proc. Phys. Soc.* **81**, 1122 (1963).

[24] Hardy, R. J. Phonon boltzmann equation and second sound in solids. *Phys. Rev. B* **2**, 1193 (1970).

[25] Hardy, R. J. & Albers, D. L. Hydrodynamic approximation to the phonon boltzmann equation. *Phys. Rev. B* **10**, 3546–3551 (1974).

[26] Alvarez, F., Jou, D. & Sellitto, A. Phonon hydrodynamics and phonon-boundary scattering in nanosystems. *J. Appl. Phys.* **105**, 014317 (2009).

[27] Guo, Y. & Wang, M. Phonon hydrodynamics and its applications in nanoscale heat transport. *Phys. Rep.* **595**, 1–44 (2015).

[28] Guo, Y. & Wang, M. Phonon hydrodynamics for nanoscale heat transport at ordinary temperatures. *Phys. Rev. B* **97**, 035421 (2018).

[29] Ziabari, Amirkoushyar and Torres, Pol and Vermeersch, Bjorn and Xuan, Yi and Cartoixà, Xavier and Torelló, Alvar and Bahk, Je-Hyeong and Koh, Yee Rui and Parsa, Maryam and Ye, Peide D. and Alvarez, F. Xavier and Shakouri, Ali. Full-field thermal imaging of quasiballistic crosstalk reduction in nanoscale devices. *Nat. Commun.* **9**, 255 (2018).

[30] Torres, P. *et al.* Emergence of hydrodynamic heat transport in semiconductors at the nanoscale. *Phys. Rev. Materials* **2**, 076001 (2018).

[31] Huberman, S. *et al.* Observation of second sound in graphite at temperatures above 100 K. *Science* **364**, 375–379 (2019).

[32] Machida, Y., Matsumoto, N., Isono, T. & Behnia, K. Phonon hydrodynamics and ultrahigh–room-temperature thermal conductivity in thin graphite. *Science* **367**, 309–312 (2020).

[33] Garg, J., Bonini, N., Kozinsky, B. & Marzari, N. Role of Disorder and Anharmonicity in the Thermal Conductivity of Silicon-Germanium Alloys: A First-Principles Study. *Phys. Rev. Lett.* **106**, 045901 (2011).

[34] Omini, M. & Sparavigna, A. An iterative approach to the phonon Boltzmann equation in the theory of thermal conductivity. *Physica B: Condens. Matter* **212**, 101 – 112 (1995).

[35] Broido, D., Malorny, M., Birner, G., Mingo, N. & Stewart, D. Intrinsic lattice thermal conductivity of semiconductors from first principles. *Appl. Phys. Lett.* **91**, 231922 (2007).

[36] Carrete, J. *et al.* almaBTE : A solver of the space–time dependent Boltzmann transport equation for phonons in structured materials. *Comput. Phys. Commun.* **220**, 351 – 362 (2017).

[37] Fugallo, G., Lazzeri, M., Paulatto, L. & Mauri, F. Ab initio variational approach for evaluating lattice thermal conductivity. *Phys. Rev. B* **88**, 045430 (2013).

[38] Chaput, L. Direct Solution to the Linearized Phonon Boltzmann Equation. *Phys. Rev. Lett.* **110**, 265506 (2013).

[39] Cepellotti, A. & Marzari, N. Thermal Transport in Crystals as a Kinetic Theory of Relaxons. *Phys. Rev. X* **6**, 041013 (2016).

[40] Baroni, S., de Gironcoli, S., Dal Corso, A. & Giannozzi, P. Phonons and related crystal properties from density-functional perturbation theory. *Rev. Mod. Phys.* **73**, 515–562 (2001).

[41] Paulatto, L., Mauri, F. & Lazzeri, M. Anharmonic properties from a generalized third-order ab initio approach: Theory and applications to graphite and graphene. *Phys. Rev. B* **87**, 214303 (2013).

[42] Esfarjani, K., Chen, G. & Stokes, H. T. Heat transport in silicon from first-principles calculations. *Phys. Rev. B* **84**, 085204 (2011).

[43] Luckyanova, M. N. *et al.* Coherent phonon heat conduction in superlattices. *Science* **338**, 936–939 (2012).

[44] Allen, P. B. & Feldman, J. L. Thermal Conductivity of Glasses: Theory and Application to Amorphous Si. *Phys. Rev. Lett.* **62**, 645–648 (1989).

[45] Li, W. & Mingo, N. Ultralow lattice thermal conductivity of the fully filled skutterudite $YbFe_4Sb_{12}$ due to the flat avoided-crossing filler modes. *Phys. Rev. B* **91**, 144304 (2015).

[46] Lee, W. *et al.* Ultralow thermal conductivity in all-inorganic halide perovskites. *Proc. Natl. Acad. Sci. U. S. A.* **114**, 8693–8697 (2017).

[47] Chen, X. *et al.* Twisting phonons in complex crystals with quasi-one-dimensional substructures. *Nat. Commun.* **6**, 6723 (2015).

[48] Weathers, A. *et al.* Glass-like thermal conductivity in nanostructures of a complex anisotropic crystal. *Phys. Rev. B* **96**, 214202 (2017).

[49] Lory, P.-F. *et al.* Direct measurement of individual phonon lifetimes in the clathrate compound $Ba_{7.81}Ge_{40.67}Au_{5.33}$. *Nat. Commun.* **8**, 491 (2017).

[50] Mukhopadhyay, S. and Parker, D. S. and Sales, B. C. and Puretzky, A. A. and McGuire, M. A. and Lindsay, L. Two-channel model for ultralow thermal conductivity of crystalline Tl_3VSe_4. *Science* **360**, 1455–1458 (2018).

[51] Shenogin, S., Bodapati, A., Keblinski, P. & McGaughey, A. J. Predicting the thermal conductivity of inorganic and polymeric glasses: The role of anharmonicity. *J. Appl. Phys.* **105**, 034906 (2009).

[52] Allen, P. B., Feldman, J. L., Fabian, J. & Wooten, F. Diffusons, locons and propagons: Character of atomic vibrations in amorphous Si. *Philos. Mag. B* **79**, 1715–1731 (1999).

[53] Donadio, D. & Galli, G. Atomistic Simulations of Heat Transport in Silicon Nanowires. *Phys. Rev. Lett.* **102**, 195901 (2009).

[54] Glassbrenner, C. J. & Slack, G. A. Thermal Conductivity of Silicon and Germanium from 3°K to the Melting Point. *Phys. Rev.* **134**, A1058–A1069 (1964).

[55] Suresh, G., Seenivasan, G., Krishnaiah, M. & Srirama Murti, P. Investigation of the thermal conductivity of selected compounds of gadolinium and lanthanum. *J. Nucl. Mater.* **249**, 259–261 (1997).

[56] Vassen, R., Cao, X., Tietz, F., Basu, D. & Stöver, D. Zirconates as New Materials for Thermal Barrier Coatings. *J. Am. Ceram. Soc.* **83**, 2023–2028 (2000).

[57] Chen, H., Gao, Y., Tao, S., Liu, Y. & Luo, H. Thermophysical properties of lanthanum zirconate coating prepared by plasma spraying and the influence of post-annealing. *J. Alloy Compd.* **486**, 391–399 (2009).

[58] Wan, C. *et al.* Glass-like thermal conductivity in ytterbium-doped lanthanum zirconate pyrochlore. *Acta Mater.* **58**, 6166–6172 (2010).

[59] Yang, J., Wan, C., Zhao, M., Shahid, M. & Pan, W. Effective blocking of radiative thermal conductivity in La2Zr2O7/LaPO4 composites for high temperature thermal insulation applications. *J. Eur. Ceram. Soc.* **36**, 3809–3814 (2016).

[60] Luo, Y., Yang, X., Feng, T., Wang, J. & Ruan, X. Vibrational hierarchy leads to dual-phonon transport in low thermal conductivity crystals. *Nat. Commun.* **11**, 1–10 (2020).

[61] Xia, Y., Pal, K., He, J., Ozoliņš, V. & Wolverton, C. Particlelike Phonon Propagation Dominates Ultralow Lattice Thermal Conductivity in Crystalline Tl_3VSe_4. *Phys. Rev. Lett.* **124**, 065901 (2020).

[62] Xia, Y., Ozoliņš, V. & Wolverton, C. Microscopic Mechanisms of Glasslike Lattice Thermal Transport in Cubic $Cu_{12}Sb_4S_{13}$ Tetrahedrites. *Phys. Rev. Lett.* **125**, 085901 (2020).

[63] Jain, A. Multichannel thermal transport in crystalline Tl_3VSe_4. *Phys. Rev. B* **102**, 201201 (2020).

[64] Wigner, E. On the quantum correction for thermodynamic equilibrium. *Phys. Rev.* **40**, 749–759 (1932).

[65] Moyal, J. E. Quantum mechanics as a statistical theory. In *Mathematical Proceedings of the Cambridge Philosophical Society*, vol. 45, 99–124 (Cambridge University Press, 1949).

[66] Simoncelli, M., Marzari, N. & Cepellotti, A. Generalization of fourier's law into viscous heat equations. *Phys. Rev. X* **10**, 011019 (2020).

[67] Simoncelli, M. and Marzari, N. and Mauri, F. Unified theory of thermal transport in crystals and glasses. *Nat. Phys.* **15**, 809–813 (2019).

[68] Li, W., Carrete, J., Katcho, N. A. & Mingo, N. ShengBTE: A solver of the Boltzmann transport equation for phonons. *Comput. Phys. Commun.* **185**, 1747 – 1758 (2014).

[69] Eriksson, F., Fransson, E. & Erhart, P. The hiphive package for the extraction of high-order force constants by machine learning. *Adv. Theory Simul.* **2**, 1800184 (2019).

[70] Togo, A., Chaput, L. & Tanaka, I. Distributions of phonon lifetimes in brillouin zones. *Phys. Rev. B* **91**, 094306 (2015).

[71] Kittel, C. Interpretation of the Thermal Conductivity of Glasses. *Phys. Rev.* **75**, 972–974 (1949).

[72] Freeman, J. J. & Anderson, A. C. Thermal conductivity of amorphous solids. *Phys. Rev. B* **34**, 5684–5690 (1986).

[73] Allen, P. B. & Feldman, J. L. Thermal conductivity of disordered harmonic solids. *Phys. Rev. B* **48**, 12581–12588 (1993).

[74] Marcolongo, A., Umari, P. & Baroni, S. Microscopic theory and quantum simulation of atomic heat transport. *Nat. Phys.* **12**, 80 (2016).

[75] Ercole, L., Marcolongo, A., Umari, P. & Baroni, S. Gauge invariance of thermal transport coefficients. *J. Low Temp. Phys.* **185**, 79–86 (2016).

[76] Wallace, D. C. *Thermodynamics of crystals* (Wiley, 1972).

[77] Maradudin, A. A. & Vosko, S. H. Symmetry properties of the normal vibrations of a crystal. *Rev. Mod. Phys.* **40**, 1–37 (1968).

[78] Blum, K. *Density matrix theory and applications* (Springer Science & Business Media, 2013).

[79] Di Ventra, M. *Electrical transport in nanoscale systems* (Cambridge University Press, 2008).

[80] Frensley, W. R. Boundary conditions for open quantum systems driven far from equilibrium. *Rev. Mod. Phys.* **62**, 745–791 (1990).

[81] Rossi, F. *Theory of semiconductor quantum devices: microscopic modeling and simulation strategies* (Springer Science & Business Media, 2011).

[82] Breuer, H.-P. & Petruccione, F. *The theory of open quantum systems* (Oxford University Press, 2002).

[83] Zak, J. Lattice operators in crystals for Bravais and reciprocal vectors. *Phys. Rev. B* **12**, 3023–3026 (1975).

[84] Weyl, H. Quantenmechanik und gruppentheorie. *Zeitschrift für Physik* **46**, 1–46 (1927).

[85] Groenewold, H. J. On the principles of elementary quantum mechanics. In *On the Principles of Elementary Quantum Mechanics*, 1–56 (Springer, 1946).

[86] Imre, K., Özizmir, E., Rosenbaum, M. & Zweifel, P. Wigner method in quantum statistical mechanics. *J. Math. Phys.* **8**, 1097–1108 (1967).

[87] Hillery, M., O'Connell, R. F., Scully, M. O. & Wigner, E. P. Distribution functions in physics: fundamentals. *Phys. Rep.* **106**, 121–167 (1984).

[88] Srivastava, G. P. *The physics of phonons* (Taylor & Francis Group, 1990).

[89] Iotti, R. C., Ciancio, E. & Rossi, F. Quantum transport theory for semiconductor nanostructures: A density-matrix formulation. *Phys. Rev. B* **72**, 125347 (2005).

[90] Rossi, F. & Kuhn, T. Theory of ultrafast phenomena in photoexcited semiconductors. *Rev. Mod. Phys.* **74**, 895–950 (2002).

[91] Vasko, F. T. & Raichev, O. E. *Quantum Kinetic Theory and Applications: Electrons, Photons, Phonons* (Springer Science & Business Media, 2006).

[92] Cohen-Tannoudji, C., Dupont-Roc, J., Grynberg, G. & Thickstun, P. *Atom-photon interactions: basic processes and applications* (Wiley Online Library, 2004).

[93] Spohn, H. The phonon Boltzmann equation, properties and link to weakly anharmonic lattice dynamics. *J. Stat. Phys.* **124**, 1041–1104 (2006).

[94] Lepri, S. *Thermal transport in low dimensions: from statistical physics to nanoscale heat transfer*, vol. 921 (Springer, 2016).

[95] Ordonez-Miranda, J., Yang, R., Volz, S. & Alvarado-Gil, J. J. Steady state and modulated heat conduction in layered systems predicted by the analytical solution of the phonon boltzmann transport equation. *J. Appl. Phys.* **118**, 075103 (2015).

[96] Hinch, E. J. *Perturbation methods* (Cambridge university press, 1991).

[97] Trovato, M. & Reggiani, L. Quantum maximum entropy principle for a system of identical particles. *Phys. Rev. E* **81**, 021119 (2010).

[98] Trovato, M. & Reggiani, L. Quantum maximum-entropy principle for closed quantum hydrodynamic transport within a wigner function formalism. *Phys. Rev. E* **84**, 061147 (2011).

[99] Tadano, T., Gohda, Y. & Tsuneyuki, S. Anharmonic force constants extracted from first-principles molecular dynamics: applications to heat transfer simulations. *J. Phys. Condens. Matter* **26**, 225402 (2014).

[100] Callaway, J. *Quantum theory of the solid state* (Academic Press, 1991).

[101] Lindsay, L. First Principles Peierls-Boltzmann Phonon Thermal Transport: A Topical Review. *Nanoscale and Microscale Thermophys. Eng.* **20**, 67–84 (2016).

[102] Krieger, J. B. & Iafrate, G. J. Quantum transport for bloch electrons in a spatially homogeneous electric field. *Phys. Rev. B* **35**, 9644–9658 (1987).

[103] Hübner, R. and Graham, R. Landau-Zener transitions and dissipation in a mesoscopic ring. *Phys. Rev. B* **53**, 4870–4885 (1996).

[104] Kané, G., Lazzeri, M. & Mauri, F. Zener tunneling in the electrical transport of quasimetallic carbon nanotubes. *Phys. Rev. B* **86**, 155433 (2012).

[105] Gebauer, R. & Car, R. Current in open quantum systems. *Phys. Rev. Lett.* **93**, 160404 (2004).

[106] Gebauer, R. & Car, R. Kinetic theory of quantum transport at the nanoscale. *Phys. Rev. B* **70**, 125324 (2004).

[107] Alon, O. E. & Cederbaum, L. S. Hellmann-Feynman theorem at degeneracies. *Phys. Rev. B* **68**, 033105 (2003).

[108] Zhang, J., Guo, X., Jung, Y.-G., Li, L. & Knapp, J. Lanthanum zirconate based thermal barrier coatings: A review. *Surf. Coat. Technol.* **323**, 18–29 (2017).

[109] Such a nonlinear function yields a visual representation of conduction along the (one-dimensional) line $K-\Gamma-L$ with a number of green and blue pixels proportional to the conductivities κ_P and κ_C, respectively.

[110] Sun, T. & Allen, P. B. Lattice thermal conductivity: Computations and theory of the high-temperature breakdown of the phonon-gas model. *Phys. Rev. B* **82**, 224305 (2010).

[111] Wang, Y. *et al.* Cation dynamics governed thermal properties of lead halide perovskite nanowires. *Nano Lett.* **18**, 2772–2779 (2018).

[112] Cahill, D. G., Watson, S. K. & Pohl, R. O. Lower limit to the thermal conductivity of disordered crystals. *Phys. Rev. B* **46**, 6131–6140 (1992).

[113] Voneshen, D. *et al.* Suppression of thermal conductivity by rattling modes in thermoelectric sodium cobaltate. *Nat. Mater.* **12**, 1028–1032 (2013).

[114] Cepellotti, A. & Kozinsky, B. Interband tunneling effects on materials transport properties using the first principles Wigner distribution. *Mater. Today Phys.* 100412 (2021).

[115] Dangić, Đ., Hellman, O., Fahy, S. & Savić, I. The origin of the lattice thermal conductivity enhancement at the ferroelectric phase transition in GeTe. *arXiv preprint arXiv:2012.08414* (2020).

[116] Isaeva, L., Barbalinardo, G., Donadio, D. & Baroni, S. Modeling heat transport in crystals and glasses from a unified lattice-dynamical approach. *Nat. Commun.* **10**, 3853 (2019).

[117] Semwal, B. S. & Sharma, P. K. Thermal conductivity of an anharmonic crystal. *Phys. Rev. B* **5**, 3909–3914 (1972).

[118] Babaei, H. & Wilmer, C. E. Mechanisms of Heat Transfer in Porous Crystals Containing Adsorbed Gases: Applications to Metal-Organic Frameworks. *Phys. Rev. Lett.* **116**, 025902 (2016).

[119] Kapil, V. , Wieme, J., Vandenbrande, S., Lamaire, A., Van Speybroeck, V., and Ceriotti, M. Modeling the Structural and Thermal Properties of Loaded Metal–Organic Frameworks. An Interplay of Quantum and Anharmonic Fluctuations. *J. Chem. Theory Comput.* **15**, 3237–3249 (2019).

[120] Damjanovic, D. Materials for high temperature piezoelectric transducers. *Curr. Opin. Solid State Mater. Sci.* **3**, 469–473 (1998).

[121] Kugaenko, O. *et al.* Basic thermophysical parameters of langasite ($La_3Ga_5SiO_{14}$), langatate ($La_3Ta_{0.5}Ga_{5.5}O_{14}$), and catangasite ($Ca_3TaGa_3Si_2O_{14}$) single crystals in a temperature range of 25 to 1000 C. *Bull. Russ. Acad. Sci.: Phys.* **76**, 1258–1263 (2012).

[122] Xia, Y. *et al.* High-throughput study of lattice thermal conductivity in binary rocksalt and zinc blende compounds including higher-order anharmonicity. *Phys. Rev. X* **10**, 041029 (2020).

[123] Tadano, T. & Saidi, W. A. First-principles phonon quasiparticle theory applied to a strongly anharmonic halide perovskite. *arXiv* 2103.00745 (2021).

[124] Kac, M., Uhlenbeck, G. & Hemmer, P. On the van der waals theory of the vapor-liquid equilibrium. i. discussion of a one-dimensional model. *J. Math. Phys.* **4**, 216–228 (1963).

[125] Iubini, S., Di Cintio, P., Lepri, S., Livi, R. & Casetti, L. Heat transport in oscillator chains with long-range interactions coupled to thermal reservoirs. *Phys. Rev. E* **97**, 032102 (2018).

[126] Gonze, X. & Lee, C. Dynamical matrices, born effective charges, dielectric permittivity tensors, and interatomic force constants from density-functional perturbation theory. *Phys. Rev. B* **55**, 10355–10368 (1997).

[127] Marzari, N., Mostofi, A. A., Yates, J. R., Souza, I. & Vanderbilt, D. Maximally localized wannier functions: Theory and applications. *Rev. Mod. Phys.* **84**, 1419–1475 (2012).

[128] Bamler, R. *Phase-Space Berry Phases in Chiral Magnets: Skyrmion Charge, Hall Effect, and Dynamics of Magnetic Skyrmions.* Ph.D. thesis, Universität zu Köln (2016).

[129] Blount, E. Formalisms of band theory. In *Solid state physics*, vol. 13, 305–373 (Elsevier, 1962).

[130] Demeio, L., Barletti, L., Bertoni, A., Bordone, P. & Jacoboni, C. Wigner-function approach to multiband transport in semiconductors. *Physica B: Condens. Matter* **314**, 104–107 (2002).

[131] Giovanni Borgioli and Giovanni Frosali and Paul F. Zweifel . Wigner Approach to the Two-Band Kane Model for a Tunneling Diode. *Transport Theor. Stat. Phys.* **32**, 347–366 (2003).

[132] Wong, C. H. & Tserkovnyak, Y. Quantum kinetic equation in phase-space textured multiband systems. *Phys. Rev. B* **84**, 115209 (2011).

[133] Messiah, A. *Quantum Mechanics two volumes bound as one* (Dover, 2014).

[134] Louisell, W. H. & Louisell, W. H. *Quantum statistical properties of radiation*, vol. 7 (Wiley New York, 1973).

[135] Landau, L. D. & Lifshitz, E. M. *Course of theoretical physics. Statistical physics, vol. 5.*, vol. 5 (Pergamon press, 1980).

[136] Levinson, I. Translational invariance in uniform fields and the equation for the density matrix in the wigner representation. *Sov. Phys. JETP* **30**, 362–367 (1970).

[137] Tamura, S.-i. Isotope scattering of dispersive phonons in Ge. *Phys. Rev. B* **27**, 858–866 (1983).

[138] Carruthers, P. & Zachariasen, F. Quantum collision theory with phase-space distributions. *Rev. Mod. Phys.* **55**, 245–285 (1983).

[139] Rosati, R., Dolcini, F., Iotti, R. C. & Rossi, F. Wigner-function formalism applied to semiconductor quantum devices: Failure of the conventional boundary condition scheme. *Phys. Rev. B* **88**, 035401 (2013).

[140] Nedjalkov, M., Querlioz, D., Dollfus, P. & Kosina, H. *Wigner Function Approach*, 289–358 (Springer New York, New York, NY, 2011).

[141] Zak, J. Finite translations in solid-state physics. *Phys. Rev. Lett.* **19**, 1385–1387 (1967).

[142] Zak, J. Dynamics of Electrons in Solids in External Fields. *Phys. Rev.* **168**, 686–695 (1968).

[143] Zak, J. & Birman, J. L. kq representation in lattice dynamics. *Phys. Rev. B* **10**, 1315–1318 (1974).

[144] Marder, M. P. *Condensed matter physics* (John Wiley & Sons, 2010).

[145] Rammer, J. & Smith, H. Quantum field-theoretical methods in transport theory of metals. *Rev. Mod. Phys.* **58**, 323–359 (1986).

[146] Auerbach, A. & Allen, P. B. Universal high-temperature saturation in phonon and electron transport. *Phys. Rev. B* **29**, 2884–2890 (1984).

[147] Jain, A. *et al.* The Materials Project: A materials genome approach to accelerating materials innovation. *APL Materials* **1**, 011002 (2013).

[148] Persson, K. Materials Data on La2Zr2O7 (SG:227) by Materials Project (2014). URL https://materialsproject.org/materials/mp-4974/#.

[149] Giannozzi, P. *et al.* Advanced capabilities for materials modelling with Quantum ESPRESSO. *J. Phys. Condens. Matter* **29**, 465901 (2017).

[150] Dal Corso, A. Pseudopotentials periodic table: From H to Pu. *Comput. Mater. Sci.* **95**, 337–350 (2014).

[151] Garrity, K. F., Bennett, J. W., Rabe, K. M. & Vanderbilt, D. Pseudopotentials for high-throughput DFT calculations. *Comput. Mater. Sci.* **81**, 446 – 452 (2014).

[152] Grimme, S. Semiempirical GGA-type density functional constructed with a long-range dispersion correction. *J. Comput. Chem* **27**, 1787–1799 (2006).

[153] Lejaeghere, K. *et al.* Reproducibility in density functional theory calculations of solids. *Science* **351**, aad3000 (2016).

[154] Prandini, G., Marrazzo, A., Castelli, I. E., Mounet, N. & Marzari, N. Precision and efficiency in solid-state pseudopotential calculations. *Npj Comput. Mater.* **4**, 1–13 (2018).

[155] Subramanian, M., Aravamudan, G. & Rao, G. S. Oxide pyrochlores—a review. *Prog. Solid. State Ch.* **15**, 55–143 (1983).

[156] Togo, A. & Tanaka, I. First principles phonon calculations in materials science. *Scr. Mater.* **108**, 1–5 (2015).

[157] Chernatynskiy, A. & Phillpot, S. R. Phonon Transport Simulator (PhonTS). *Comput. Phys. Commun.* **192**, 196–204 (2015).

[158] Stoumpos, Constantinos C. and Malliakas, Christos D. and Peters, John A. and Zhifu Liu and Maria Sebastian and Jino Im and Chasapis, Thomas C. and Wibowo, Arief C. and Chung, Duck Young and Freeman, Arthur J and Wessels, Bruce W. and Kanatzidis, Mercouri G. Crystal growth of the perovskite semiconductor CsPbBr3: A new material for high-energy radiation detection. *Cryst. Growth Des.* **13**, 2722–2727 (2013).

[159] Gražulis, S. *et al.* Crystallography Open Database – an open-access collection of crystal structures. *J. Appl. Crystallogr.* **42**, 726–729 (2009).

[160] Momma, K. & Izumi, F. VESTA 3 for three-dimensional visualization of crystal, volumetric and morphology data. *J. Appl. Crystallogr.* **44**, 1272–1276 (2011).

[161] Paulatto, L., Errea, I., Calandra, M. & Mauri, F. First-principles calculations of phonon frequencies, lifetimes, and spectral functions from weak to strong anharmonicity: The example of palladium hydrides. *Phys. Rev. B* **91**, 054304 (2015).

[162] Miyata, K. *et al.* Large polarons in lead halide perovskites. *Sci. Adv.* **3** (2017).

[163] Feldman, J. L., Kluge, M. D., Allen, P. B. & Wooten, F. Thermal conductivity and localization in glasses: Numerical study of a model of amorphous silicon. *Phys. Rev. B* **48**, 12589–12602 (1993).

[164] Wei, L., Kuo, P. K., Thomas, R. L., Anthony, T. R. & Banholzer, W. F. Thermal conductivity of isotopically modified single crystal diamond. *Phys. Rev. Lett.* **70**, 3764–3767 (1993).

[165] Berman, R., Hudson, P. & Martinez, M. Nitrogen in diamond: evidence from thermal conductivity. *J. Phys. C Solid State. Phys.* **8**, L430 (1975).

[166] Ho, C. Y., Powell, R. W. & Liley, P. E. *Thermal conductivity of the elements: a comprehensive review* (National Standard Reference Data System, 1974).

[167] Zink, B. L., Pietri, R. & Hellman, F. Thermal conductivity and specific heat of thin-film amorphous silicon. *Phys. Rev. Lett.* **96**, 055902 (2006).

[168] Cahill, D. G., Katiyar, M. & Abelson, J. R. Thermal conductivity of a-Si:H thin films. *Phys. Rev. B* **50**, 6077–6081 (1994).

[169] Inyushkin, A., Taldenkov, A., Gibin, A., Gusev, A. & Pohl, H.-J. On the isotope effect in thermal conductivity of silicon. *Phys. Status Solidi (C)* **1**, 2995–2998 (2004).

[170] Eucken, A. Über die temperaturabhängigkeit der wärmeleitfähigkeit fester nichtmetalle. *Ann. Phys.* **339**, 185–221 (1911).

[171] Birch, A. F. & Clark, H. The thermal conductivity of rocks and its dependence upon temperature and composition. *Am. J. Sci.* **238**, 529–558 (1940).

[172] Knapp, W. J. Thermal conductivity of nonmetallic single crystals. *J. Am. Ceram. Soc.* **26**, 48–55 (1943).

[173] Zeller, R. C. & Pohl, R. O. Thermal Conductivity and Specific Heat of Noncrystalline Solids. *Phys. Rev. B* **4**, 2029–2041 (1971).

[174] Kanamori, H., Fujii, N. & Mizutani, H. Thermal diffusivity measurement of rock-forming minerals from 300 to 1100 K. *J. Geophys. Res.* **73**, 595–605 (1968).

[175] Wray, K. L. & Connolly, T. J. Thermal conductivity of clear fused silica at high temperatures. *J. Appl. Phys.* **30**, 1702–1705 (1959).

[176] Touloukian, Y., Powell, R., Ho, C. & Klemens, P. Thermophysical properties of matter - the TPRC data series. Volume 2. Thermal conductivity - nonmetallic solids. Tech. Rep., Thermophysical and Electronic Properties Information Analysis Center (1971).

[177] Sergeev, O., Shashkov, A. & Umanskii, A. Thermophysical properties of quartz glass. *J. Eng. Phys.* **43**, 1375–1383 (1982).

[178] Cahill, D. G. Thermal conductivity measurement from 30 to 750 K: the 3ω method. *Rev. Sci. Instrum.* **61**, 802–808 (1990).

[179] Abdulagatov, I. *et al.* Thermal conductivity of fused quartz and quartz ceramic at high temperatures and high pressures. *J. Phys. Chem. Solids* **61**, 779–787 (2000).

[180] Yang, S. T., Matthews, M. J., Elhadj, S., Draggoo, V. G. & Bisson, S. E. Thermal transport in CO_2 laser irradiated fused silica: In situ measurements and analysis. *J. Appl. Phys.* **106**, 103106 (2009).

[181] Heraeus. Data sheet: Quartz glass for optics - data and properties (2010). URL https://www.heraeus.com/media/media/hca/doc_hca/products_and_solutions_8/optics/Data_and_Properties_Optics_fused_silica_EN.pdf.

[182] Alexander, S., Entin-Wohlman, O. & Orbach, R. Phonon-fracton anharmonic interactions: The thermal conductivity of amorphous materials. *Phys. Rev. B* **34**, 2726–2734 (1986).

[183] Nakayama, T., Yakubo, K. & Orbach, R. L. Dynamical properties of fractal networks: Scaling, numerical simulations, and physical realizations. *Rev. Mod. Phys.* **66**, 381–443 (1994).

[184] Bernasconi, A., Sleator, T., Posselt, D., Kjems, J. K. & Ott, H. R. Dynamic properties of silica aerogels as deduced from specific-heat and thermal-conductivity measurements. *Phys. Rev. B* **45**, 10363–10376 (1992).

[185] Larkin, J. M. & McGaughey, A. J. H. Thermal conductivity accumulation in amorphous silica and amorphous silicon. *Phys. Rev. B* **89**, 144303 (2014).

[186] Lv, W. & Henry, A. Non-negligible contributions to thermal conductivity from localized modes in amorphous silicon dioxide. *Sci. Rep.* **6**, 35720 (2016).

[187] Carbogno, C., Ramprasad, R. & Scheffler, M. Ab Initio Green-Kubo Approach for the Thermal Conductivity of Solids. *Phys. Rev. Lett.* **118**, 175901 (2017).

[188] Puligheddu, M., Gygi, F. & Galli, G. First-principles simulations of heat transport. *Phys. Rev. Mater* **1**, 060802 (2017).

[189] Jund, P. & Jullien, R. Molecular-dynamics calculation of the thermal conductivity of vitreous silica. *Phys. Rev. B* **59**, 13707–13711 (1999).

[190] Tian, Y. *et al.* Thermal conductivity of vitreous silica from molecular dynamics simulations: The effects of force field, heat flux and system size. *J. Chem. Phys.* **146**, 054504 (2017).

[191] Ercole, L., Marcolongo, A. & Baroni, S. Accurate thermal conductivities from optimally short molecular dynamics simulations. *Sci. Rep.* **7**, 1–11 (2017).

[192] Simoncelli, M. et al. Quantum thermal transport in solids from Wigner's phase-space formalism. *In preparation (Chapter 1 of this thesis)* .

[193] Ida, T., Ando, M. & Toraya, H. Extended pseudo-Voigt function for approximating the Voigt profile. *J. Appl. Crystallogr.* **33**, 1311–1316 (2000).

[194] Pasquarello, A., Hybertsen, M. S. & Car, R. Interface structure between silicon and its oxide by first-principles molecular dynamics. *Nature* **396**, 58 (1998).

[195] Kotz, F. *et al.* Three-dimensional printing of transparent fused silica glass. *Nature* **544**, 337–339 (2017).

[196] Niu, H., Piaggi, P. M., Invernizzi, M. & Parrinello, M. Molecular dynamics simulations of liquid silica crystallization. *Proc. Natl. Acad. Sci. USA* **115**, 5348–5352 (2018).

[197] Hu, Y.-J. *et al.* Predicting densities and elastic moduli of SiO_2-based glasses by machine learning. *Npj Comput. Mater.* **6**, 1–13 (2020).

[198] Feldman, J. & Kluge, M. D. Realistic model calculations based on the kubo theory for the thermal conductivity of amorphous insulators. *Philos. Mag. B* **71**, 641–647 (1995).

[199] Ercole, L. *et al.* ab initio Simulation of Heat Transport in Silica Glass. *PhD thesis, SISSA* (2018).

[200] Kingery, W. Thermal conductivity: Xii, temperature dependence of conductivity for single-phase ceramics. *J. Am. Ceram. Soc.* **38**, 251–255 (1955).

[201] Bouchut, P., Decruppe, D. & Delrive, L. Fused silica thermal conductivity dispersion at high temperature. *J. Appl. Phys.* **96**, 3221–3227 (2004).

[202] Giacomazzi, L., Umari, P. & Pasquarello, A. Medium-range structure of vitreous SiO_2 obtained through first-principles investigation of vibrational spectra. *Phys. Rev. B* **79**, 064202 (2009).

[203] Gurevich, V. L., Parshin, D. A. & Schober, H. R. Anharmonicity, vibrational instability, and the boson peak in glasses. *Phys. Rev. B* **67**, 094203 (2003).

[204] Anderson, P. W., Halperin, B. & Varma, C. M. Anomalous low-temperature thermal properties of glasses and spin glasses. *Philos. Mag.* **25**, 1–9 (1972).

[205] Feldman, J. L., Allen, P. B. & Bickham, S. R. Numerical study of low-frequency vibrations in amorphous silicon. *Phys. Rev. B* **59**, 3551–3559 (1999).

[206] Charpentier, T., Kroll, P. & Mauri, F. First-principles nuclear magnetic resonance structural analysis of vitreous silica. *J. Phys. Chem. C* **113**, 7917–7929 (2009).

[207] Munde, M. S., Gao, D. Z. & Shluger, A. L. Diffusion and aggregation of oxygen vacancies in amorphous silica. *J. Phys. Condens. Matter* **29**, 245701 (2017).

[208] Anderson, P. W. Absence of Diffusion in Certain Random Lattices. *Phys. Rev.* **109**, 1492–1505 (1958).

[209] Wehinger, B. *et al.* Lattice dynamics of α-cristobalite and the boson peak in silica glass. *J. Phys. Condens. Matter* **27**, 305401 (2015).

[210] Baldi, G., Giordano, V. M., Ruta, B. & Monaco, G. On the nontrivial wave-vector dependence of the elastic modulus of glasses. *Phys. Rev. B* **93**, 144204 (2016).

[211] Ferry, D. & Goodnick, S. M. *Transport in nanostructures.* 6 (Cambridge university press, 1999).

[212] Jeans, J. *An introduction to the kinetic theory of gases* (Cambridge University Press, 1967).

[213] Bartók, A. P., Payne, M. C., Kondor, R. & Csányi, G. Gaussian approximation potentials: The accuracy of quantum mechanics, without the electrons. *Phys. Rev. Lett.* **104**, 136403 (2010).

[214] Bartók, A. P., Kermode, J., Bernstein, N. & Csányi, G. Machine learning a general-purpose interatomic potential for silicon. *Phys. Rev. X* **8**, 041048 (2018).

[215] Deringer, V. L. Bernstein, N., Csányi, G., Mahmoud, C. B., Ceriotti, M., Wilson, M., Drabold, D. A., and Elliott, S. R. Origins of structural and electronic transitions in disordered silicon. *Nature* **589**, 59–64 (2021).

[216] Beltukov, Y. M., Fusco, C., Parshin, D. A. & Tanguy, A. Boson peak and Ioffe-Regel criterion in amorphous siliconlike materials: The effect of bond directionality. *Phys. Rev. E* **93**, 023006 (2016).

[217] Pompe, G. & Hegenbarth, E. Thermal Conductivity of Amorphous Si at Low Temperatures. *Phys. Status Solidi (B)* **147**, 103–108 (1988).

[218] Fu, C. L. & Ho, K. M. First-principles calculation of the equilibrium ground-state properties of transition metals: Applications to Nb and Mo. *Phys. Rev. B* **28**, 5480–5486 (1983).

[219] Marzari, N. Ab-initio molecular dynamics for metallic systems. *PhD thesis, Cambridge University* (1996).

[220] Marzari, N., Vanderbilt, D., De Vita, A. & Payne, M. C. Thermal Contraction and Disordering of the Al(110) Surface. *Phys. Rev. Lett.* **82**, 3296–3299 (1999).

[221] de Gironcoli, S. Lattice dynamics of metals from density-functional perturbation theory. *Phys. Rev. B* **51**, 6773–6776 (1995).

[222] Richet, P., Bottinga, Y., Denielou, L., Petitet, J. & Tequi, C. Thermodynamic properties of quartz, cristobalite and amorphous SiO_2: drop calorimetry measurements between 1000 and 1800 K and a review from 0 to 2000 K. *Geochim. Cosmochim. Acta* **46**, 2639–2658 (1982).

[223] Bianco, R., Errea, I., Paulatto, L., Calandra, M. & Mauri, F. Second-order structural phase transitions, free energy curvature, and temperature-dependent anharmonic phonons in the self-consistent harmonic approximation: Theory and stochastic implementation. *Phys. Rev. B* **96**, 014111 (2017).

[224] Aseginolaza, U. *et al.* Phonon collapse and second-order phase transition in thermoelectric snse. *Phys. Rev. Lett.* **122**, 075901 (2019).

[225] Horbach, J., Kob, W. & Binder, K. Specific heat of amorphous silica within the harmonic approximation. *J. Phys. Chem. B* **103**, 4104–4108 (1999).

[226] Hill, V. G. and Roy, Rustum. Silica Structure Studies: V, The Variable Inversion in Cristobalite. *J. Am. Ceram. Soc.* **41**, 532–537 (1958).

[227] Kunugi, M., Soga, N., Sawa, H. & Konishi, A. Thermal conductivity of cristobalite. *J. Am. Ceram. Soc.* **55**, 580–580 (1972).

[228] Hay, H., Ferlat, G., Casula, M., Seitsonen, A. P. & Mauri, F. Dispersion effects in SiO_2 polymorphs: An ab initio study. *Phys. Rev. B* **92**, 144111 (2015).

[229] Brueckner, R. Properties and structure of vitreous silica. I. *J. Non-Cryst. Solids* **5**, 123–175 (1970).

[230] Pluth, J. J., Smith, J. V. & Faber, J. Crystal structure of low cristobalite at 10, 293, and 473 K: Variation of framework geometry with temperature. *J. Appl. Phys.* **57**, 1045–1049 (1985).

[231] Downs, R. T. & Palmer, D. The pressure behavior of α cristobalite. *Am. Mineral.* **79**, 9–14 (1994).

[232] Tucker, M., Keen, D. & Dove, M. A detailed structural characterization of quartz on heating through the α–β phase transition. *Mineral. Mag.* **65**, 489–507 (2001).

[233] Rumble, J. *CRC handbook of chemistry and physics*, vol. 100 (CRC press, 2014).

[234] Giacomazzi, L., Umari, P. & Pasquarello, A. Medium-range structure of vitreous SiO_2. *Materials Cloud Archive* (2019). URL https://doi.org/10.24435/materialscloud:2019.0086/v1.

[235] Carpenter, J. M. & Price, D. L. Correlated motions in glasses studied by coherent inelastic neutron scattering. *Phys. Rev. Lett.* **54**, 441–443 (1985).

[236] Buchenau, U. *et al.* Low-frequency modes in vitreous silica. *Phys. Rev. B* **34**, 5665–5673 (1986).

[237] Le Roux, S. & Jund, P. Ring statistics analysis of topological networks: New approach and application to amorphous GeS_2 and SiO_2 systems. *Comput. Mater. Sci.* **49**, 70–83 (2010).

[238] Silvestrelli, P. L., Marzari, N., Vanderbilt, D. & Parrinello, M. Maximally-localized wannier functions for disordered systems: Application to amorphous silicon. *Solid State Commun.* **107**, 7–11 (1998).

[239] Mizokami, K., Togo, A. & Tanaka, I. Lattice thermal conductivities of two SiO_2 polymorphs by first-principles calculations and the phonon Boltzmann transport equation. *Phys. Rev. B* **97**, 224306 (2018).

[240] Keskar, N. R. & Chelikowsky, J. R. Structural properties of nine silica polymorphs. *Phys. Rev. B* **46**, 1–13 (1992).

[241] Dollase, W., & WH, B. The superstructure of meteoritic low tridymite solved by computer simulation. *Am. Mineral.* **61**, 971–978 (1976).

[242] Grant, R. W. New data on tridymite. *Am. Mineral.* **52**, 536–541 (1967).

[243] Garg, J. *Thermal conductivity from first-principles in bulk, disordered, and nanostructured materials.* Ph.D. thesis, Massachusetts Institute of Technology (2011).

[244] Rice, M. J. Theory of Viscosity in Nearly Ferromagnetic Fermi Liquids. *Phys. Rev.* **162**, 189 (1967).

[245] Jackson, H. E., Walker, C. T. & McNelly, T. F. Second Sound in NaF. *Phys. Rev. Lett.* **25**, 26–28 (1970).

[246] Pohl, D. W. & Irniger, V. Observation of Second Sound in NaF by Means of Light Scattering. *Phys. Rev. Lett.* **36**, 480–483 (1976).

[247] Narayanamurti, V. & Dynes, R. C. Observation of Second Sound in Bismuth. *Phys. Rev. Lett.* **28**, 1461–1465 (1972).

[248] Danil'Chenko, B., Poroshin, V. & Sarbei, O. An observation of second sound in sapphire. *JETP Lett.* **30** (1979).

[249] Hehlen, B., Pérou, A.-L., Courtens, E. & Vacher, R. Observation of a Doublet in the Quasielastic Central Peak of Quantum-Paraelectric $SrTiO_3$. *Phys. Rev. Lett.* **75**, 2416–2419 (1995).

[250] Koh, Y. K. & Cahill, D. G. Frequency dependence of the thermal conductivity of semiconductor alloys. *Phys. Rev. B* **76**, 075207 (2007).

[251] Bergamasco, L. *et al.* Mesoscopic moment equations for heat conduction: characteristic features and slow–fast mode decomposition. *Entropy* **20**, 126 (2018).

[252] Griffin, A. On the detection of second sound in crystals by light scattering. *Phys. Lett.* **17**, 208–210 (1965).

[253] Enz, C. P. One-particle densities, thermal propagation, and second sound in dielectric crystals. *Ann. Phys.* **46**, 114–173 (1968).

[254] Beck, H., Meier, P. & Thellung, A. Phonon hydrodynamics in solids. *Phys. Status Solidi (A)* **24**, 11–63 (1974).

[255] Cepellotti, A. *et al.* Phonon hydrodynamics in two-dimensional materials. *Nat. Commun.* **6**, 6400 (2015).

[256] Cepellotti, A. & Marzari, N. Boltzmann transport in nanostructures as a friction effect. *Nano Lett.* **17**, 4675–4682 (2017).

[257] Omini, M. & Sparavigna, A. Beyond the isotropic-model approximation in the theory of thermal conductivity. *Phys. Rev. B* **53**, 9064–9073 (1996).

[258] McGaughey, A. J., Jain, A., Kim, H.-Y. & Fu, B. Phonon properties and thermal conductivity from first principles, lattice dynamics, and the boltzmann transport equation. *J. Appl. Phys.* **125**, 011101 (2019).

[259] Lee, S., Broido, D., Esfarjani, K. & Chen, G. Hydrodynamic phonon transport in suspended graphene. *Nat. Commun.* **6**, 6290 (2015).

[260] Cepellotti, A. & Marzari, N. Transport waves as crystal excitations. *Phys. Rev. Materials* **1**, 045406 (2017).

[261] Lee, S. & Lindsay, L. Hydrodynamic phonon drift and second sound in a (20,20) single-wall carbon nanotube. *Phys. Rev. B* **95** (2017).

[262] Ding, Z. *et al.* Phonon Hydrodynamic Heat Conduction and Knudsen Minimum in Graphite. *Nano Lett.* **18**, 638–649 (2018).

[263] Martelli, V., Jiménez, J. L., Continentino, M., Baggio-Saitovitch, E. & Behnia, K. Thermal Transport and Phonon Hydrodynamics in Strontium Titanate. *Phys. Rev. Lett.* **120** (2018).

[264] Khodusov, V. & Naumovets, A. Second sound waves in diamond. *Diam. Relat. Mater.* **21**, 92 – 98 (2012).

[265] Machida, Y. *et al.* Observation of Poiseuille flow of phonons in black phosphorus. *Science Advances* **4** (2018).

[266] Hua, C. & Minnich, A. J. Analytical Green's function of the multidimensional frequency-dependent phonon Boltzmann equation. *Phys. Rev. B* **90**, 214306 (2014).

[267] Vermeersch, B., Carrete, J., Mingo, N. & Shakouri, A. Superdiffusive heat conduction in semiconductor alloys. I. Theoretical foundations. *Phys. Rev. B* **91**, 085202 (2015).

[268] Maznev, A. A., Johnson, J. A. & Nelson, K. A. Onset of nondiffusive phonon transport in transient thermal grating decay. *Phys. Rev. B* **84**, 195206 (2011).

[269] Yang, F. & Dames, C. Heating-frequency-dependent thermal conductivity: An analytical solution from diffusive to ballistic regime and its relevance to phonon scattering measurements. *Phys. Rev. B* **91**, 165311 (2015).

[270] Péraud, J.-P. M. & Hadjiconstantinou, N. G. Extending the range of validity of Fourier's law into the kinetic transport regime via asymptotic solution of the phonon Boltzmann transport equation. *Phys. Rev. B* **93**, 045424 (2016).

[271] Chen, G. Ballistic-diffusive heat-conduction equations. *Phys. Rev. Lett.* **86**, 2297–2300 (2001).

[272] Anderson, C. V. D. R. & Tamma, K. K. Novel Heat Conduction Model for Bridging Different Space and Time Scales. *Phys. Rev. Lett.* **96**, 184301 (2006).

[273] Ordonez-Miranda, J., Yang, R. & Alvarado-Gil, J. A constitutive equation for nano-to-macro-scale heat conduction based on the boltzmann transport equation. *J. Appl. Phys.* **109**, 084319 (2011).

[274] Ramu, A. T. & Ma, Y. An enhanced fourier law derivable from the boltzmann transport equation and a sample application in determining the mean-free path of nondiffusive phonon modes. *J. Appl. Phys.* **116**, 093501 (2014).

[275] Hua, C., Lindsay, L., Chen, X. & Minnich, A. Experimental demonstration of a generalized Fourier's Law for non-diffusive thermal transport. *arXiv preprint arXiv:1902.10020* (2019).

[276] Cao, B.-Y. & Guo, Z.-Y. Equation of motion of a phonon gas and non-Fourier heat conduction. *J. Appl. Phys.* **102**, 053503 (2007).

[277] Li, X. & Lee, S. Role of hydrodynamic viscosity on phonon transport in suspended graphene. *Phys. Rev. B* **97**, 094309 (2018).

[278] Klemens, P. G. & Simon, F. E. The thermal conductivity of dielectric solids at low temperatures (theoretical). *Proc. Royal Soc. Lond. Series A.* **208**, 108–133 (1951).

[279] Allen, P. B. Improved Callaway model for lattice thermal conductivity. *Phys. Rev. B* **88**, 144302 (2013).

[280] Allen, P. B. & Perebeinos, V. Temperature in a Peierls-Boltzmann treatment of nonlocal phonon heat transport. *Phys. Rev. B* **98**, 085427 (2018).

[281] Fugallo, G. *et al.* Thermal Conductivity of Graphene and Graphite: Collective Excitations and Mean Free Paths. *Nano Lett.* **14**, 6109–6114 (2014).

[282] Gandolfi, M., Benetti, G., Glorieux, C., Giannetti, C. & Banfi, F. Accessing temperature waves: A dispersion relation perspective. *Int. J. Heat Mass Transf.* **143**, 118553 (2019).

[283] Torres, P. *et al.* First principles kinetic-collective thermal conductivity of semiconductors. *Phys. Rev. B* **95**, 165407 (2017).

[284] Heron, J., Fournier, T., Mingo, N. & Bourgeois, O. Mesoscopic size effects on the thermal conductance of silicon nanowire. *Nano Lett.* **9**, 1861–1865 (2009).

[285] Siemens, M. E. *et al.* Quasi-ballistic thermal transport from nanoscale interfaces observed using ultrafast coherent soft x-ray beams. *Nat. Mater.* **9**, 26 (2010).

[286] Johnson, J. A. *et al.* Direct measurement of room-temperature nondiffusive thermal transport over micron distances in a silicon membrane. *Phys. Rev. Lett.* **110**, 025901 (2013).

[287] Regner, K. T. *et al.* Broadband phonon mean free path contributions to thermal conductivity measured using frequency domain thermoreflectance. *Nat. Commun.* **4**, 1640 (2013).

[288] Wilson, R. B. & Cahill, D. G. Anisotropic failure of Fourier theory in time-domain thermoreflectance experiments. *Nat. Commun.* **5**, 5075 (2014).

[289] Péraud, J.-P. M. & Hadjiconstantinou, N. G. Efficient simulation of multidimensional phonon transport using energy-based variance-reduced Monte Carlo formulations. *Phys. Rev. B* **84**, 205331 (2011).

[290] Berman, R. Thermal conductivity of isotopically enriched diamonds. *Phys. Rev. B* **45**, 5726–5728 (1992).

[291] Onn, D. G., Witek, A., Qiu, Y. Z., Anthony, T. R. & Banholzer, W. F. Some aspects of the thermal conductivity of isotopically enriched diamond single crystals. *Phys. Rev. Lett.* **68**, 2806–2809 (1992).

[292] Olson, J. R. *et al.* Thermal conductivity of diamond between 170 and 1200 K and the isotope effect. *Phys. Rev. B* **47**, 14850–14856 (1993).

[293] Ward, A., Broido, D. A., Stewart, D. A. & Deinzer, G. Ab initio theory of the lattice thermal conductivity in diamond. *Phys. Rev. B* **80**, 125203 (2009).

[294] Broido, D. A., Lindsay, L. & Ward, A. Thermal conductivity of diamond under extreme pressure: A first-principles study. *Phys. Rev. B* **86**, 115203 (2012).

[295] Inyushkin, A. V. *et al.* Ultrahigh thermal conductivity of isotopically enriched silicon. *J. Appl. Phys.* **123**, 095112 (2018).

[296] Landau, L. D. & Lifshitz, E. M. *Fluid Mechanics. Course of theoretical physics. Vol. 6* (Pergamon Press, Oxford, 1984).

[297] Lifshitz, E. M. & Pitaevskii, L. P. *Physical Kinetics. Course of theoretical physics. Vol. 10* (Pergamon Press, Oxford, 1980).

[298] Batchelor, C. K. & Batchelor, G. *An introduction to fluid dynamics* (Cambridge university press, 2000).

[299] Bonini, N., Garg, J. & Marzari, N. Acoustic phonon lifetimes and thermal transport in free-standing and strained graphene. *Nano Lett.* **12**, 2673–2678 (2012).

[300] Mariani, E. & von Oppen, F. Flexural Phonons in Free-Standing Graphene. *Phys. Rev. Lett.* **100**, 076801 (2008).

[301] Ong, Z.-Y. & Pop, E. Effect of substrate modes on thermal transport in supported graphene. *Phys. Rev. B* **84**, 075471 (2011).

[302] Weinbub, J. & Ferry, D. K. Recent advances in Wigner function approaches. *Appl. Phys. Rev.* **5**, 041104 (2018).

[303] Logan, J. D. *Applied partial differential equations* (Springer, 2014).

[304] Kwok, P. C. Dispersion and damping of second sound in non-isotropic solids. *Physics Physique Fizika* **3**, 221 (1967).

[305] Ackerman, C. & Guyer, R. Temperature pulses in dielectric solids. *Ann. Phys. (N. Y.)* **50**, 128–185 (1968).

[306] Maris, H. J. Second sound and heat flow in anisotropic solids. *Phys. Rev. B* **24**, 1205–1208 (1981).

[307] Chester, M. Second sound in solids. *Phys. Rev.* **131**, 2013–2015 (1963).

[308] Cattaneo, C. Sulla conduzione del calore. *Atti Sem. Mat. Fis. Univ. Modena* **3**, 83–101 (1948).

[309] Joseph, D. D. & Preziosi, L. Heat waves. *Rev. Mod. Phys.* **61**, 41–73 (1989).

[310] Tzou, D. Y. The generalized lagging response in small-scale and high-rate heating. *Int. J. Heat Mass Transf.* **38**, 3231–3240 (1995).

[311] Majee, A. K. & Aksamija, Z. Dynamical thermal conductivity of suspended graphene ribbons in the hydrodynamic regime. *Phys. Rev. B* **98**, 024303 (2018).

[312] Lepri, S., Livi, R. & Politi, A. Thermal conduction in classical low-dimensional lattices. *Phys. Rep.* **377**, 1–80 (2003).

[313] Wolfram research. *Mathematica, Version 12.0* Champaign, IL (2019).

[314] Simons, S. The relation between the heat current and the phonon drift velocity. *Am. J. Phys.* **51**, 457–458 (1983).

[315] Schelling, P. K., Phillpot, S. R. & Keblinski, P. Comparison of atomic-level simulation methods for computing thermal conductivity. *Phys. Rev. B* **65**, 144306 (2002).

[316] Zhang, Y.-Y., Pei, Q.-X., Liu, H.-Y. & Wei, N. Thermal conductivity of a h-BCN monolayer. *Phys. Chem. Chem. Phys.* **19**, 27326–27331 (2017).

[317] Khadem, M. H. & Wemhoff, A. P. Comparison of Green–Kubo and NEMD heat flux formulations for thermal conductivity prediction using the Tersoff potential. *Comput. Mater. Sci.* **69**, 428–434 (2013).

[318] He, Y., Savić, I., Donadio, D. & Galli, G. Lattice thermal conductivity of semiconducting bulk materials: atomistic simulations. *Phys. Chem. Chem. Phys.* **14**, 16209–16222 (2012).

[319] Zhou, X. W., Aubry, S., Jones, R. E., Greenstein, A. & Schelling, P. K. Towards more accurate molecular dynamics calculation of thermal conductivity: Case study of gan bulk crystals. *Phys. Rev. B* **79**, 115201 (2009).

[320] Fan, Z. *et al.* Thermal conductivity decomposition in two-dimensional materials: Application to graphene. *Phys. Rev. B* **95**, 144309 (2017).

[321] Allen, P. B. Analysis of nonlocal phonon thermal conductivity simulations showing the ballistic to diffusive crossover. *Phys. Rev. B* **97**, 134307 (2018).

[322] Li, Z. *et al.* Influence of Boundaries and Thermostatting on Nonequilibrium Molecular Dynamics Simulations of Heat Conduction in Solids. *arXiv preprint arXiv:1905.11024* (2019).

[323] Buckingham, E. On physically similar systems; illustrations of the use of dimensional equations. *Phys. Rev.* **4**, 345–376 (1914).

[324] White, F. M. Fluid mechanics. 5th edition. *Boston: McGraw-Hill Book Company* (2003).

[325] Maassen, J. & Lundstrom, M. Steady-state heat transport: Ballistic-to-diffusive with Fourier's law. *J. Appl. Phys.* **117**, 035104 (2015).

[326] Terraneo, M., Peyrard, M. & Casati, G. Controlling the energy flow in nonlinear lattices: A model for a thermal rectifier. *Phys. Rev. Lett.* **88**, 094302 (2002).

[327] Li, B., Wang, L. & Casati, G. Thermal diode: Rectification of heat flux. *Phys. Rev. Lett.* **93**, 184301 (2004).

[328] Chang, C. W., Okawa, D., Majumdar, A. & Zettl, A. Solid-state thermal rectifier. *Science* **314**, 1121–1124 (2006).

[329] Hu, J., Ruan, X. & Chen, Y. P. Thermal conductivity and thermal rectification in graphene nanoribbons: a molecular dynamics study. *Nano Lett.* **9**, 2730–2735 (2009).

[330] Wang, Y. *et al.* Phonon lateral confinement enables thermal rectification in asymmetric single-material nanostructures. *Nano Lett.* **14**, 592–596 (2014).

[331] Anufriev, R. & Nomura, M. Thermal conductance boost in phononic crystal nanostructures. *Phys. Rev. B* **91**, 245417 (2015).

[332] Volz, S. *et al.* Nanophononics: state of the art and perspectives. *Eur. Phys. J. B* **89**, 15 (2016).

[333] Wang, H. *et al.* Experimental study of thermal rectification in suspended monolayer graphene. *Nat. Commun.* **8**, 15843 (2017).

[334] Liu, Y., Xu, Y., Zhang, S.-C. & Duan, W. Model for topological phononics and phonon diode. *Phys. Rev. B* **96**, 064106 (2017).

[335] Chen, S., Donadio, D., Benenti, G. & Casati, G. Efficient thermal diode with ballistic spacer. *Phys. Rev. E* **97**, 030101 (2018).

[336] Felix, I. M. & Pereira, L. F. C. Thermal conductivity of graphene-hbn superlattice ribbons. *Sci. Rep.* **8**, 2737 (2018).

[337] Sood, A. *et al.* An electrochemical thermal transistor. *Nat. Commun.* **9**, 4510 (2018).

[338] De Luca, M. *et al.* Phonon engineering in twinning superlattice nanowires. *Nano Lett.* **19**, 4702–4711 (2019).

[339] Levitov, L. & Falkovich, G. Electron viscosity, current vortices and negative nonlocal resistance in graphene. *Nat. Phys.* **12**, 672 (2016).

[340] Bandurin, D. A. *et al.* Negative local resistance caused by viscous electron backflow in graphene. *Science* **351**, 1055–1058 (2016).

[341] Moll, P. J., Kushwaha, P., Nandi, N., Schmidt, B. & Mackenzie, A. P. Evidence for hydrodynamic electron flow in $PdCoO_2$. *Science* **351**, 1061–1064 (2016).

[342] Scaffidi, T., Nandi, N., Schmidt, B., Mackenzie, A. P. & Moore, J. E. Hydrodynamic electron flow and hall viscosity. *Phys. Rev. Lett.* **118**, 226601 (2017).

[343] Hardy, R. J. Lowest-order contribution to the lattice thermal conductivity. *J. Math. Phys.* **6**, 1749–1761 (1965).

[344] Giannozzi, P. *et al.* QUANTUM ESPRESSO: a modular and open-source software project for quantum simulations of materials. *J. Phys. Condens. Matter* **21**, 395502 (2009).

[345] Cassabois, G., Valvin, P. & Gil, B. Hexagonal boron nitride is an indirect bandgap semiconductor. *Nat. Photonics* **10**, 262–266 (2016).

[346] Haigh, S. *et al.* Cross-sectional imaging of individual layers and buried interfaces of graphene-based heterostructures and superlattices. *Nat. Mater.* **11**, 764–767 (2012).

[347] Jiang, P., Qian, X., Yang, R. & Lindsay, L. Anisotropic thermal transport in bulk hexagonal boron nitride. *Phys. Rev. Mater* **2**, 064005 (2018).

[348] Yuan, C. *et al.* Modulating the thermal conductivity in hexagonal boron nitride via controlled boron isotope concentration. *Commun. Phys.* **2**, 1–8 (2019).

[349] Simoncelli, M., Marzari, N. & Cepellotti, A. Generalization of Fourier's Law into Viscous Heat Equations (2020). URL https://www.wolframcloud.com/obj/github-cloud/blobs/99db255de7ebfd5e2542d952d4ef84496b640efb.

[350] Cuscó, R. *et al.* Isotopic effects on phonon anharmonicity in layered van der waals crystals: Isotopically pure hexagonal boron nitride. *Phys. Rev. B* **97**, 155435 (2018).

[351] Van Setten, M. *et al.* The pseudodojo: Training and grading a 85 element optimized norm-conserving pseudopotential table. *Comput. Phys. Commun.* **226**, 39–54 (2018).

[352] Kurakevych, O. O. & Solozhenko, V. L. Rhombohedral boron subnitride, B_13N_2, by X-ray powder diffraction. *Acta Crystallogr., Sect. C* **63**, i80–i82 (2007).

[353] Deringer, V. L. , Bernstein, N., Bartók, A. P , Cliffe, M. J., Kerber, R. N., Marbella, L. E. , Grey, C. P., Elliott, S. R., and Csányi, G. Realistic atomistic structure of amorphous silicon from machine-learning-driven molecular dynamics. *J. Phys. Chem. Lett.* **9**, 2879–2885 (2018).

[354] Raoux, S., Xiong, F., Wuttig, M. & Pop, E. Phase change materials and phase change memory. *MRS bulletin* **39**, 703–710 (2014).

[355] Koelmans, W. W. *et al.* Projected phase-change memory devices. *Nat. Commun.* **6**, 1–7 (2015).

[356] Zhang, W., Mazzarello, R., Wuttig, M. & Ma, E. Designing crystallization in phase-change materials for universal memory and neuro-inspired computing. *Nat. Rev. Mater.* **4**, 150–168 (2019).

[357] Campi, D. and Paulatto, L. and Fugallo, G. and Mauri, F. and Bernasconi, M. First-principles calculation of lattice thermal conductivity in crystalline phase change materials: GeTe, Sb_2Te_3, and $Ge_2Sb_2Te_5$. *Phys. Rev. B* **95**, 024311 (2017).

Michele Simoncelli | Curriculum Vitae

Personal information

NAME	Michele Simoncelli
BIRTH DATE	5 July 1992
ADDRESS	EPFL STI IMX THEOS MED 2 1020 (Bâtiment MED) Station 9 CH-1015 Lausanne
TELEPHONE	+41 77 908 29 53
E-MAIL	michele.simoncelli@epfl.ch
ORCID ID	`https://orcid.org/0000-0002-7052-4286`
GOOGLE SCHOLAR ID	`https://scholar.google.com/citations?user=hwEqZ0kAAAAJ&hl=en&oi=ao`

Education

Sep 2016–: PhD, École Polytechnique Fédérale de Lausanne (Switzerland).
Research topic: condensed matter physics and materials science, with a focus on the fundamental theory of thermal transport in solids. Supervisor: Prof. Nicola Marzari.

Sep 2014–Jul 2016: International Master in Physics of Complex Systems, 110/110 with honor.
Excellence program involving SISSA (Trieste), Politecnico di Torino, ENS Cachan (Paris), Universities Paris 6,7,11. Competitive admission limited to 20 students. Thesis: Molecular simulation of aqueous electrolytes in nanoporous carbons: blue energy and water desalination. Supervisor: Prof. Mathieu Salanne.

Sep 2011–Jul 2014: Bachelor's degree in Physics, University of Trento (Italy), 110/110 with honor.
Thesis: Numerical investigation of dispersion and nonlinear effects on the temporal evolution of wave packets. Supervisor: Prof. Giovanni Garberoglio. Excellence study program, completed with a final project on "Chaotic systems and fractals".

Sep 2006–Jul 2011: High School I.T.I. G. Marconi, Rovereto (Italy), 100/100 with honor.

Institutional responsibilities

Jan 2018-: Responsible of the organization of the master projects at the Laboratory of Theory and Simulation of Materials (THEOS) at EPFL (`http://theossrv1.epfl.ch/Main/Projects`).

Teaching and supervision

Apr 2020 - Jan 2021: Co-supervision of student Enrico Di Lucente in his master thesis work on *"Thermal properties of skutterudites: a competition between particle-like and wave-like heat conduction"*.

Sep 2019 - Jan 2020: Teaching assistant, EPFL master course "Fundamentals of solid-state materials".

Feb 2018 - May 2018: Teaching assistant, EPFL master course "Atomistic and quantum simulations of materials".

Mar 2017 - Sep 2017: Co-supervision of student Norma Rivano in her master thesis work *"Thermal transport in one-dimensional carbon chains: a first principle relaxon approach"*.

Memberships in scientific societies

Sep 2019: Member of the EUCYS alumni Network `https://www.eucysalumni.net/team`

Mar 2019: Member of the jury at the Italian high school scientific contest "I giovani e le scienze".

Member of the Swiss Physical Society (Membership number: 4090)

Member of the American Physical Society (Account number: 61298882)

Prizes and awards

Oct 2020: Weizmann Institute of Science (Israel). Dimitris N. Chorafas Foundation Award. (5'000 USD)

Sep 2018: Best poster award a the International Workshop on Computational Design and Discovery of Novel Materials, Lausanne (Switzerland).

Feb 2018: École Polytechnique Fédérale de Lausanne (Switzerland), Computational thinking award. (1'000 CHF)

Sep 2017: Poster award at the Paris International School on Advanced Computational Materials Science.

Sep 2015: Université Paris-Saclay (France). Paris-Saclay scholarship. (10'000 EUR)

Dec 2014: Cassa Rurale di Lizzana (Italy), Merit prize for the academic year 2013-2014.

Sep 2014: University of Trento (Italy), Merit prize for the academic years 2011-2014. (4'000 EUR)

May 2013: International Sustainable World Energy, Engineering, Environment Project Olympiad, Houston (TX), USA. Participation with the project "Static Sun Detector", Bronze Medal.

Dec 2012: Cassa Rurale di Lizzana (Italy), Merit prize for the academic year 2011-2012.

Sep 2012: European Union Contest for Young Scientists (EUCYS), Bratislava (Slovakia). Intel ISEF award.

Apr 2012: I giovani e le scienze 2012, Milan (Italy). First Prize and qualification to the European contest EUCYS.

Jul 2011: Italian national prize for excellence in high school, awarded to top 0.9% students.

Invited talks & Seminars

Jul 2020: Quantum Matter Institute, University of British Columbia (Canada). “Unified theory of thermal transport in crystals and glasses”.

Feb 2020: Cavendish Laboratory, University of Cambridge (United Kingdom). “Thermal transport beyond Fourier, and beyond Boltzmann”.

Jun 2019: Conference on Nanophononics, Bridging Statistical Physics, Molecular Modeling and Experiments. ICTP Trieste (Italy). “Unified theory of thermal transport in crystals and glasses & viscous heat hydrodynamics”.

Contributed talks & posters

Nov 2020: International conference on electron-phonon coupling and thermoelectric efficiency. University of the Basque Country (Spain). “Generalization of Fourier's law into viscous heat equations”.

Jan 2020: International Conference on Molecular-Scale Charge and Thermal Transport. Engelberg, Switzerland. Talk “A unified theory of thermal transport in crystal and glasses, and a generalization of Fourier's law to heat hydrodynamics”.

Mar 2019: APS March Meeting 2019. Boston (U.S.A.). Talk “Unified theory of thermal transport in crystals and disordered solids”.

Jan 2019: 19th International Workshop on Computational Physics and Material Science: Total Energy and Force Methods. ICTP, Trieste (Italy). Poster “Unified theory of thermal transport in crystals and disordered solids”.

Sep 2018: COMDI Conference. Lausanne (Switzerland). Poster on “Thermal transport in 2D transition metal dichalcogenides within the relaxon picture”, best poster award.

Apr 2018: DPG Conference, Berlin. Talk “Thermal transport in 2D transition metal dichalcogenides”.

Sep 2017: Paris International School on Advanced Computational Materials Science. Université Pierre et Marie Curie (Paris). Poster “Thermal transport in layered and 2D materials within the relaxons picture”, poster award.

May 2013: Intel International Science and Engineering Fair, Phoenix (AZ), U.S.A. Participation with the project "CNC milling machine".

Outreach

Feb 2020: The viscous heat equations developed during my PhD have been included as an example in the Wolfram Mathematica documentation. `https://www.wolframcloud.com/obj/github-cloud/blobs/99db255de7ebfd5e2542d952d4ef84496b640efb`

Feb 2018: “Molecular dynamics in a supercapacitor” first prize award talk at the "computational thinking contest", on the use of digital visualization techniques to present scientific data in an engaging way (`https://acces.epfl.ch/index-html/page-74894-en-html/page-115220-en-html/page-143465-en-html/contest_2017/`)

Jan 2012: Presentation of the project “CNC milling machine” at the TV program "Geo scienza" (Rai3, `https://www.youtube.com/watch?v=xwijHDY3eAY`).

Personal skills

LANGUAGES: English (working knowledge), Italian (mother tongue), French (fluent).

TECHNICAL AND PROGRAMMING SKILLS: C, C++, C#, PYTHON, FORTRAN, R, MATLAB, MATHEMATICA, BLENDER, LaTeX, MPI.

Publications

1. Simoncelli, M., Marzari, N., & Cepellotti, A. (2020). Generalization of Fourier’s law into viscous heat equations. Physical Review X **10**, 011019.
2. Simoncelli, M., Marzari, N., & Mauri, F. (2019). Unified theory of thermal transport in crystals and glasses. Nature Physics **15**, 809.
3. Simoncelli, M., Ganfoud, N., Sene, A., Haefele, M., Daffos, B., Taberna, P. L., Salanne, M., Simon, P., & Rotenberg, B. (2018). Blue energy and desalination with nanoporous carbon electrodes: capacitance from molecular simulations to continuous models. Physical Review X **8**, 021024. HPCwire Readers’ & Editors’ Choice Award.

Up-to-date publication list and bibliometric indices can be found on Google Scholar:
`https://scholar.google.com/citations?user=hwEqZ0kAAAAJ&hl=en&oi=ao`